Université de Paris

Ecole doctorale STEP'UP – ED n° 560

Institut de Physique du Globe de Paris

Dynamique des éruptions pliniennes : réévaluation de l'aléa volcanique en Martinique

Par Audrey Michaud-Dubuy

Thèse de doctorat de Sciences de la Terre et de l'Environnement

Dirigée par Edouard Kaminski

Présentée et soutenue publiquement le 18 décembre 2019

Devant un jury composé de :

Costanza Bonadonna, Professor, Université de Genève, rapportrice
Tomaso Esposti Ongaro, Assistant Professor, INGV Pisa, rapporteur
Anne Le Friant, Directrice de recherche, Université de Paris, examinatrice
Hélène Balcone-Boissard, Maître de conférences, Sorbonne Université, examinatrice
Edouard Kaminski, Professeur, Université de Paris, directeur de thèse
Guillaume Carazzo, Physicien-adjoint, Université de Paris, co-encadrant de thèse

THÈSE de DOCTORAT
de l'UNIVERSITÉ DE PARIS

Spécialité : Sciences de la Terre et de l'Environnement

présentée par

Audrey MICHAUD-DUBUY

pour obtenir le titre de

DOCTEURE DE L'UNIVERSITÉ DE PARIS

Sujet de la thèse :

Dynamique des éruptions pliniennes : réévaluation de l'aléa volcanique en Martinique

Soutenue le 18 décembre 2019, devant le jury composé de

Costanza BONADONNA .... Rapportrice
Tomaso ESPOSTI ONGARO .... Rapporteur
Hélène BALCONE-BOISSARD .... Examinatrice
Anne LE FRIANT .... Examinatrice
Edouard KAMINSKI .... Directeur de thèse
Guillaume CARAZZO .... Co-encadrant de thèse

Équipe de Dynamique des Fluides Géologiques
Institut de Physique du Globe de Paris
1, rue Jussieu - 75005 Paris

Mais un jour la terre s'ouvre

Et le volcan n'en peut plus

Le sol se rompt

On découvre des richesses inconnues

La mer à son tour divague

De violence inemployée

Me voilà comme une vague

Vous ne serez pas noyés

Une sorcière comme les autres - Anne Sylvestre

Remerciements

Un immense merci tout d'abord à Guillaume Carazzo et Edouard Kaminski, mes directeurs de thèse, pour m'avoir proposé ce formidable sujet qui me permettait de revenir vers la Pelée, mon volcan favori. J'ai énormément appris auprès de vous pendant ces trois ans, du perfectionnement des méthodes scientifiques à la façon de présenter mes résultats comme si l'on racontait une histoire. Merci de m'avoir fait confiance, à moi, une géologue pure, et de m'avoir appris à pleinement apprécier la physique.

Je remercie également les membres de mon jury de thèse : Costanza Bonadonna, Tomaso Esposti Ongaro, Hélène Balcone-Boissard et Anne Le Friant pour avoir accepté de juger mon travail et pour notre discussion très enrichissante durant la soutenance de thèse. Merci de votre disponibilité, de votre bienveillance, et de vos compliments.

J'adresse mes remerciements les plus chaleureux aux membres de mon comité de thèse, Hélène Balcone-Boissard, Georges Boudon et Anne Mangeney, pour vos précieux conseils et avis prodigués tout au long de ma thèse.

Un grand merci à Steve Tait, Frédéric Girault, Guillaume Le Hir et Frédéric Fluteau pour nos collaborations fructueuses, et pour votre aide dans la rédaction de mes tous premiers articles scientifiques.

Je suis évidemment extrêmement reconnaissante à toute l'équipe (passée et présente) de l'Observatoire Volcanologique et Sismologique de la Martinique. Vous m'avez toujours accueillie à bras ouverts, tant en tant que stagiaire de master qu'en tant que thésarde. C'est en partie grâce à vous que j'ai eu le désir de revenir sur la Pelée, et de continuer à mieux la connaître. Un grand merci.

Un merci spécial à Ulrich Küppers, pour une super mission de terrain ensemble à la Martinique et pour m'avoir invitée à visiter le laboratoire de Munich et voir de jolies explosions de ponces ! Merci beaucoup à Olivier Roche, Julia Eychenne, et Maud Devès pour votre implication dans mon travail.

Un immense merci à toute l'équipe de Dynamique des Fluides Géologiques de l'IPGP, pour votre accueil et votre soutien durant ces trois années. Un merci spécial aux doctorants de l'équipe pour nos pauses cafés, thé, rhum, gâteaux et Mario Kart. Bien sûr, je remercie plus que tout ma super co-bureau, Alexandra Morand, sans qui ces trois ans n'auraient pas du tout été aussi agréables. Merci d'être une super amie (et cat-sitter !). Et tu feras attention, il y a kraken sous phytoplancton.

J'adresse un grand grand merci à toute l'équipe de Sciences de la Terre du Palais de la Découverte : Arnaud Lemaistre, Olivier Coulon, Vincent Pasquero, Emmanuelle Lambert, Monica Rotaru, et Nathalie Berthier. J'ai énormément appris auprès de vous pendant les deux ans de mission au Palais, je crois même que j'ai guéri ma phobie de parler en public ! J'étends ces remerciements aux super coachs des Jeunes Chercheurs, Aurélie Massaux, Véronique Polonovski, et Ludovic Fournier, ainsi qu'à mes compères doctorant.e.s/jeunes chercheur.e.s, Lucie Barbier, Alexis Dollion, Marine Martin-Lagarde, Pierre Trinh, et Laetitia Zaleski. Cette aventure des Jeunes Chercheurs a été fantastique et très gratifiante, et c'est grâce à vous tous. Les apéros que l'on continue de faire sont également un super bonus ;) Cela a été une vraie chance d'évoluer auprès de passionné.e.s de Sciences et de médiation tels que vous tous, un grand merci.

À mes wonderwomen, toutes exceptionnelles, Lorella, Caro, Alicia, Laurie, Aude, Hélène, Stéph, et encore une fois Alex ; et encore plus spécialement à mes soeurs de coeur, Orianne

viii

et Violaine, qui sont auprès de moi depuis plus de 25 ans : que vous dire à part un immense, profond, et ému MERCI. Vous toutes savez ce que représentait pour moi de devenir volcanologue, et votre soutien depuis toutes ces années a toujours été un vrai moteur pour aller dans cette direction. Plein de coeurs sur vous <3. Evidemment, je remercie aussi mes supermen, Brice (BroMo) et Nico, ainsi que Batman (aussi appelé Matthieu).

À toute ma famille, un grand grand merci pour votre soutien depuis toujours. J'ai une pensée spéciale pour Juliane, ma cousine chérie, Guillaume, et ma petite filleule Lena ainsi que son frère, passionné de volcans aussi, Loris. J'espère aller me balader sur un volcan avec vous bientôt ! Je remercie du fond du coeur Ghislaine et Didier Champion (ainsi que Guillaume, Violaine et Philippe bien sûr), pour m'avoir fait aimer les cailloux depuis mon tout jeune âge, pour m'avoir emmenée sur des volcans, pour m'avoir hébergée au début de ma thèse, pour votre soutien inconditionnel et vos cocottes en papier. Un merci spécial à Lucile et Emma, pour votre soutien, nos conversations Harry Potter et pour la tour Eiffeeell ! Et évidemment, plus que tout, et avec une grande émotion, un immense, immense, (...), immense merci à ma mamie Pierrette, mon papa et ma maman. Sans vous, rien de tout ça n'aurait été possible, vous m'avez portée depuis ma naissance, encouragée, supportée, et pour vous il a toujours été évident que je réussirai à réaliser mon rêve de volcans. Merci de votre soutien, de votre confiance, de votre amour, je vous dois tout. Je vous aime.

Je n'oublie pas mon petit chaton, merci à mon GGadji, pour la patachonnerie et la ronronthérapie. La maison est où tu es. Et merci aux autres petits loulous, Sok et Dew.

Je remercie enfin tous ceux qui m'ont encouragée, de près ou de loin, qu'ils soient encore là ou pas. Je dédie cette thèse à mes grands-parents : Daie, Papy Robert, et Mamie Emma. Je pense à vous chaque jour.

Résumé

Les panaches volcaniques produits par les éruptions explosives représentent un aléa majeur dans les zones à proximité de volcans. Les modèles physiques développés ces quarante dernières années ont eu pour but de mieux comprendre ces éruptions et de quantifier les aléas associés. Les tests de robustesse de ces modèles prédictifs doivent reposer sur des données de terrain précises et détaillées sur les éruptions passées des volcans actifs. Nous proposons dans cette thèse de revisiter l'histoire éruptive plinienne de la montagne Pelée en Martinique (Petites Antilles) sur les vingt-quatre derniers milliers d'années. Nos résultats combinant travaux de terrain et datations au ^{14}C nous permettent d'établir une nouvelle chronologie des éruptions passées en accord avec les observations réalisées sur un carottage des fonds sous-marins. Nous reconstruisons par la suite l'évolution dynamique des éruptions nouvellement découvertes de Bellefontaine (13 516 ans cal A.P.), Balisier (14 072 cal A.P.), Carbet (18 711 cal A.P.) et Étoile (21 450 cal A.P.) dont le grand intérêt réside dans leur axe de dispersion vers le sud, inhabituel et englobant des zones considérées comme sécurisées sur les cartes d'aléa actuelles. Les fortes similitudes observées entre toutes les éruptions pliniennes documentées de la montagne Pelée permettent de dresser un portrait du scénario éruptif le plus susceptible de se produire dans le futur. Ce scénario pouvant inclure un effondrement de la colonne éruptive et la production de coulées de densité pyroclastiques, nous modifions un modèle physique 1D de panache volcanique afin d'en améliorer les prédictions. Nous étudions dans un premier temps l'impact de la distribution de taille des fragments volcaniques sur la transition d'une colonne plinienne stable à une fontaine en effondrement. L'effet du vent est ensuite pris en compte grâce à des expériences en laboratoire inédites permettant de simuler des jets turbulents se formant dans un environnement soumis au vent. Nous proposons ainsi un nouveau modèle théorique validé par les expériences qui remet en cohérence les données de plusieurs éruptions pliniennes historiques majeures. Nous étudions ensuite la dispersion des cendres volcaniques lors des éruptions de Bellefontaine et Balisier à l'aide d'un modèle physique 2D pour comprendre l'origine de leur direction préférentielle vers le sud, et donc vers Fort-de-France, chef-lieu de la Martinique. Nos résultats permettent d'identifier des contextes atmosphériques particuliers durant lesquels le trajet du "jet-stream" subtropical est modifié, produisant alors des vents venant du nord sur la Martinique et pouvant disperser des cendres volcaniques sur les zones les plus peuplées. Cette approche intégrée, mêlant études de terrain, simulations numériques et expériences en laboratoire, nous permet alors de dresser une nouvelle carte d'aléa volcanique pour la Martinique considérant pour la première fois les éruptions pliniennes passées de la montagne Pelée depuis 24 000 ans, ainsi que la variabilité mensuelle des vents atmosphériques.

Mots-clés : montagne Pelée, éruption plinienne, dynamique éruptive, dispersion de cendres, aléa volcanique, tephrostratigraphie

Abstract

Volcanic plumes produced by explosive eruptions represent a major threat in areas located near volcanoes. Physical models have been developed over the past forty years with an aim of better understanding these eruptions and assessing associated hazards. To test these models, we need robust and detailed field data from past and historical eruptions at active volcanoes. In this PhD work, we revisit the Plinian eruptive history of the Mount Pelée volcano in Martinique (Lesser Antilles) for the last 24,000 years. Our results combining new extensive field studies and carbon-dating measurements allow us to establish a new chronology of past eruptions, consistent with volcanic deposits identified in a deep-sea sediment core. We then reconstruct the dynamical evolution of the newly discovered eruptions of Bellefontaine (13,516 years cal BP), Balisier (14,072 cal BP), Carbet (18,711 cal BP) and Étoile (21,450 cal BP), whose great interest stems from their unusual southward dispersal axis encompassing areas that are considered to be safe in current hazard maps. The strong similarities observed between all documented Plinian eruptions of Mount Pelée volcano allow us to draw an accurate picture of the Plinian eruptive scenario most likely to occur in the future. This scenario may include a column collapse and the production of deadly pyroclastic density currents; we thus upgrade a 1D physical model of volcanic plume in order to improve its predictions. We first study the impact of the total grain-size distribution on the transition from a stable Plinian plume to a collapsing fountain. The effect of wind is then taken into account using laboratory experiments simulating turbulent jets rising in a windy environment. This new theoretical model, validated by laboratory experiments, is consistent with field data from several major historical Plinian eruptions. We then study the southward dispersal axis of the Bellefontaine and Balisier eruptions using a 2D physical model, in order to better understand this unusual dispersion towards Fort-de-France, capital of Martinique. Our results allow identifying peculiar atmospheric circulations associated to a modification of the subtropical jet-stream path, thus producing northerly winds over Martinique and spreading tephra towards the most populated areas of the island. This integrated approach, combining field studies, theoretical predictions and laboratory experiments, allows us to build a new volcanic hazard map for Martinique by taking into account for the first time the Plinian eruptions of the Mount Pelée volcano of the last 24,000 years, together with monthly variability of atmospheric winds.

Keywords: Mount Pelée, Plinian eruption, eruptive dynamics, tephra dispersal, volcanic hazard assessment, tephrostratigraphy

Contents

Introduction générale

En mai 1902, la ville de Saint-Pierre, au nord de la Martinique, est la capitale intellectuelle et culturelle des Petites Antilles. Surnommée "le Petit Paris", elle accueille 28 000 habitants, au pied de la montagne Pelée. Depuis 1889, et de manière accrue depuis avril 1902, le volcan donne des signes de réveil (apparition de fumerolles, séismes, grondements, pluies de cendres, coulées de boue...). Le jeudi 8 mai 1902, à 7h52 heure locale, le dôme formé par de la lave très visqueuse au sommet du volcan explose et provoque une nuée ardente (également appelée coulée de densité pyroclastique), qui dévale les pentes du volcan à plus de 500 kilomètres par heure. Elle rase en quelques minutes la totalité de la ville de Saint-Pierre et détruit tous les navires de la rade (Figure 1). Seul un survivant est attesté, Louis-Auguste Cyparis (1875-1929) qui, emprisonné, a été protégé par les murs de sa cellule. L'activité éruptive se poursuivra de manière discontinue jusqu'en 1905, avec de nouvelles croissances et destructions de dômes entraînant 1 500 autres morts (principalement des habitants de Morne-Rouge, rasée par la nuée ardente du 30 août 1902).

Cette éruption catastrophique, la plus meurtrière du XXᵉ siècle, est à l'origine de la naissance de la volcanologie moderne, notamment grâce à Alfred Lacroix (1863-1948) qui observe et décrit largement cet événement dans son livre *La Montagne Pelée et ses éruptions* (Lacroix, 1904). C'est lui qui nomme "nuée ardente" le phénomène ayant ravagé la ville de Saint-Pierre et "**éruption péléenne**" ce type d'éruption à dômes.
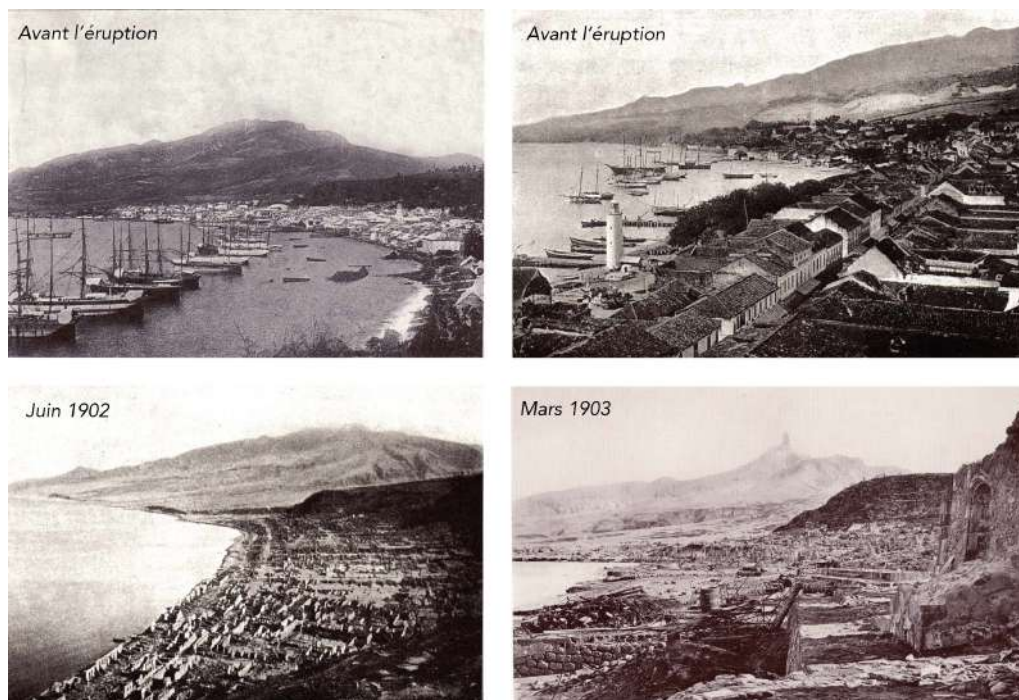
Figure 1: La baie et la ville de Saint-Pierre avant (première ligne) et après (deuxième ligne) l'éruption du 8 mai 1902 (Lacroix, 1904).

Les éruptions pliniennes, les plus puissantes des éruptions explosives

Aujourd'hui encore, quand la montagne Pelée, seul volcan actif de la Martinique, est évoquée, c'est souvent pour parler de la crise éruptive de 1902-1905 ayant entraîné la mort de presque 30 000 personnes. La Pelée a pourtant produit dans le passé des éruptions explosives bien plus puissantes : les **éruptions pliniennes**, tirant leur nom de la description par Pline le Jeune (61-113) de l'éruption du Vésuve (Italie) du 24 octobre 79, ayant causé la destruction de Pompéi, Herculanum, Stabiae et Oplontis. Ce sont les volcans explosifs situés dans des contextes de subduction (i.e. plongement d'une plaque tectonique -souvent océanique- sous

une autre plaque), tels que le Krakatoa (Indonésie), le Pinatubo (Philippines), le mont Saint-Helens (États-Unis), ou la montagne Pelée (France), qui produisent généralement des éruptions pliniennes.
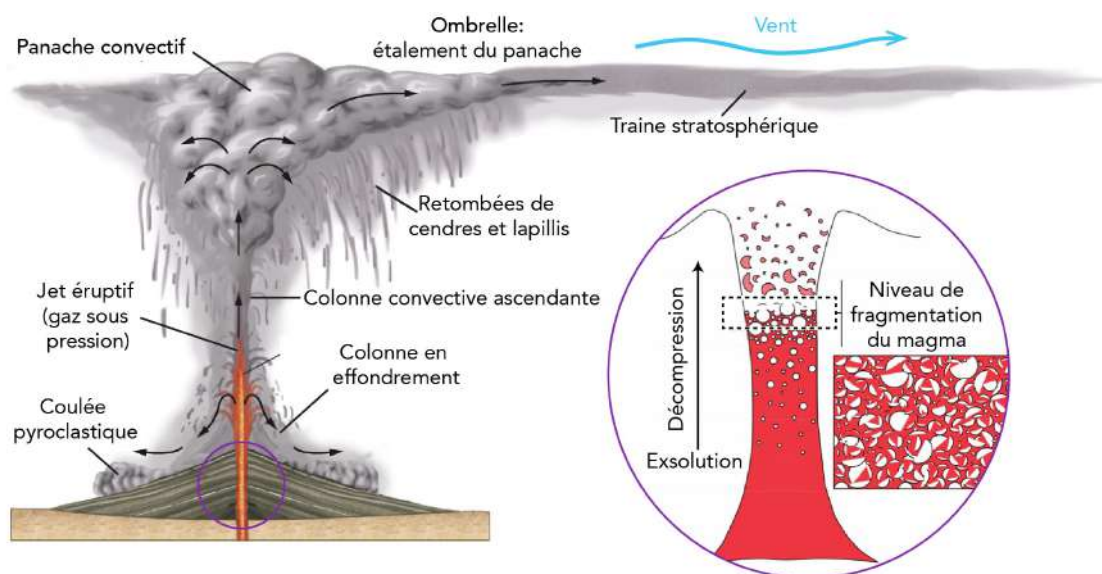
Figure 2: Phénomènes associés à une éruption explosive plinienne, *d'après Norton & Company*. L'encart (cercle violet, *modifié d'après Kaminski & Jaupart 1998*) illustre les phénomènes se produisant dans un conduit volcanique. À forte pression, les gaz sont dissous dans le magma (zone rouge). Lorsque le seuil de solubilité est atteint, des bulles de gaz se forment par exsolution, cette phase gazeuse occupe un volume de plus en plus important au fur et à mesure que le mélange magmatique remonte dans le conduit et se décomprime. Au niveau de fragmentation, le mélange magmatique passe d'un état de "mousse", tel que les bulles de gaz sont en suspension dans le liquide, à celui d'un jet de gaz turbulent portant des fragments de liquide.

Afin d'expliquer les phénomènes observés lors de ces éruptions (Figure 2), il faut comprendre ce qu'il se passe dans le conduit éruptif, à l'intérieur du volcan. Lorsque le magma remonte dans le conduit du volcan avant l'éruption, des bulles de gaz se forment par exsolution, mais ne peuvent s'échapper librement car ce magma est particulièrement visqueux. Alors que la pression diminue dans le conduit, le volume occupé par la phase gazeuse augmente jusqu'à atteindre un niveau dit de fragmentation, auquel le magma se pulvérise en fractions plus ou moins grossières (encart de la Figure 2). Ces fortes explosions projettent gaz, cendres volcaniques (fragments de roches volcaniques < 2 mm) et ponces (roches volcaniques très poreuses) dans l'atmosphère sous forme d'une colonne éruptive, dont l'ascension est au départ contrôlée uniquement par la quantité de mouvement ("gas-thrust region" ou jet éruptif avec gaz en surpression). Par la suite, durant son ascension, cette colonne turbulente ingère de l'air environnant. Le réchauffement de cet air froid par les matériaux contenus dans la colonne va la dilater et le cas échéant la faire devenir moins dense que l'atmosphère (inversion de flottabilité), ce qui favorisera l'ascension d'un panache convectif par poussée d'Archimède jusqu'à plusieurs dizaines de kilomètres de hauteur. Au niveau de flottabilité neutre, où la densité du panache devient égale à celle de l'atmosphère, la colonne va ensuite s'étaler sous la forme d'une ombrelle volcanique (Sparks, 1986). Au contraire, si la colonne est trop dense parce qu'elle n'ingère pas suffisamment d'air par rapport au flux de pyroclastes qu'elle transporte, elle aura tendance à s'effondrer sous son propre poids, entraînant la formation de coulées de densité pyroclastiques (Wilson *et al.*, 1980). Ces dernières, de par leurs vitesses et températures élevées, sont les phénomènes volcaniques les plus dangereux. Les deux régimes de panache stable et de colonne en effondrement peuvent se succéder

plusieurs fois au sein d'une même éruption, ce qui ne facilite pas la tâche de surveillance des volcanologues en observatoires.

Figure 3: Illustration des deux principaux régimes d'une éruption plinienne : panache plinien stable associé à des retombées de cendres (colonne de gauche) et colonne en effondrement associée à des coulées de densité pyroclastiques meurtrières (colonne de droite). *De haut en bas et de gauche à droite: éruptions de l'Etna (Italie) en décembre 2015 et du Santiaguito (Guatemala) en 2016, voitures et bâtiments recouverts de cendres après l'éruption du Rabaul (Papouasie-Nouvelle-Guinée) en 1984, et moulages de corps calcinés par les coulées de densité pyroclastiques du Vésuve (Italie) de 79. Crédits: Conred, USGS, A. Michaud-Dubuy.*

Si les volumes produits par les éruptions pliniennes stables ou avec colonnes en effondrement sont très similaires, leurs conséquences sur l'environnement sont très différentes (Figure 3). Dans le cas du régime plinien stable, le panache et son ombrelle vont injecter des cendres et des gaz volcaniques à très haute altitude, où les vents stratosphériques les dispersent sur de très grandes distances à l'échelle d'un hémisphère voire de l'ensemble du globe terrestre. L'interaction entre le dioxyde de soufre d'origine volcanique et les gaz atmosphériques vont entraîner la création d'acide sulfurique sous forme d'aérosols. Ces derniers peuvent rester en suspension dans l'atmosphère pendant plusieurs semaines, voire plusieurs mois, et faire plusieurs fois le tour de la Terre. Ce phénomène peut occasionner des refroidissements globaux pouvant aller de -0,5 °C (comme à la suite de l'éruption du Pinatubo, Philippines, en 1991, Self *et al.* 1996) à plus de -6 °C (comme estimé suite à l'éruption du supervolcan du Toba, Indonésie, il y a 73 000 ans, Williams 2012) et entraîner des pertes de récoltes, famines, épidémies, etc. À l'échelle plus locale, les éruptions pliniennes stables auront comme conséquences directes des retombées de cendres entraînant des difficultés respiratoires (Horwell & Baxter, 2006), des dommages matériels sur les habitations, les zones agricoles, et les routes, ainsi que des perturbations des voies de communication et du trafic aérien (Blake *et al.*, 2017) (Figure 3).

Dans le cas d'un régime plinien instable, les conséquences seront autrement plus dramatiques localement. Les coulées de densité pyroclastiques formées par l'effondrement de la colonne volcanique sont souvent très concentrées et canalisées dans les vallées, elles dévalent donc les pentes du volcan à grande vitesse (> 300 km/h). Ces caractéristiques, combinées à leur haute température (300 à 500 °C) et leur composition (gaz, cendres et roches volcaniques), en font le phénomène volcanique le plus dévastateur qui soit, ne laissant rien derrière son passage. Les moulages des corps calcinés des victimes de l'éruption du Vésuve en 79, retrouvés lors de fouilles archéologiques à Pompéi, donnent une idée de la brutalité du phénomène (Figure 3).

Les éruptions explosives (stromboliennes, vulcaniennes, péléennes, subpliniennes, pliniennes et ultrapliniennes) étant les plus dangereuses, les volcanologues américains G. Newhall and S. Self ont créé en 1982 l'indice d'explosivité volcanique (VEI, Newhall & Self 1982) pour faciliter la comparaison de ces éruptions entre elles (Figure 4). Généralement, cette échelle va de 0 à 8 (mais pourrait aller au-delà si nécessaire) ; chaque intervalle de l'échelle représente une augmentation du volume de dépôts par un facteur dix. Sur cette échelle, l'éruption de 1902 à la montagne Pelée possède un VEI de 4 (comme celle de l'Eyjafjöll en Islande en 2010). Cependant, afin d'anticiper les impacts des éruptions pliniennes sur les populations vivant au pied de volcans actifs, il est primordial d'aller au-delà de cette échelle de comparaison et d'étudier leur dynamique, c'est-à-dire les principes physiques régissant le déroulement d'une éruption plinienne : son déclenchement (stockage de magma et processus dans le conduit), sa stabilité (régime plinien ou d'effondrement), la dispersion de ses produits volcaniques, son impact potentiel sur l'environnement régional voire le climat global, etc.
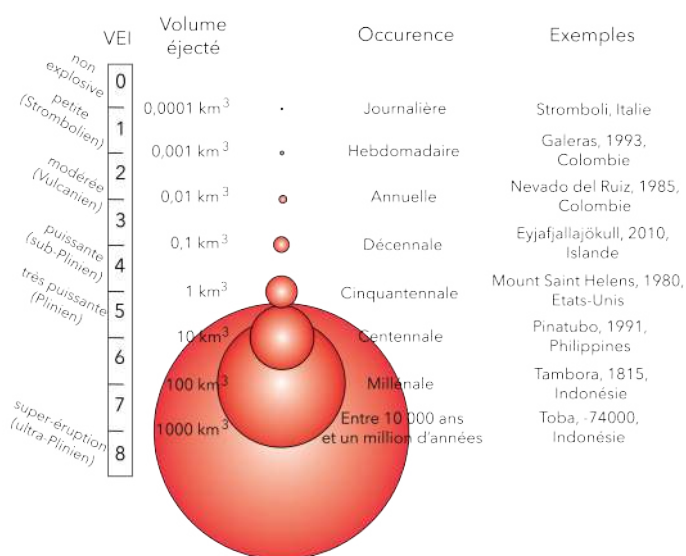
Figure 4: Échelle des intensités éruptives sur Terre ou VEI (*Volcanic Explosivity Index*, d'après Newhall & Self 1982).

Modélisation d'éruptions pliniennes

Les éruptions pliniennes sont parmi les événements volcaniques les moins fréquents, et sont donc difficiles à observer et analyser directement, en dépit des progrès sur la surveillance en temps réel. Une méthode robuste pour étudier, décrire et prévoir ces éruptions consiste à modéliser ces éruptions pliniennes, à partir d'approches théoriques, numériques et/ou analogiques. Les résultats de ces modèles peuvent ensuite être confrontés aux données récupérées sur le terrain.

Une première génération de modèles physiques 1D, a été conçue dans les années 1970 à 1990 (Wilson, 1976; Woods, 1988). Ces modèles, bien que simplifiés, ont permis d'expliquer les principes fondamentaux des grands processus volcaniques. La deuxième génération de modèles, qui a vu le jour après 1990, est plus sophistiquée. Elle voit le développement de modèles 1D améliorés, 2D, et la naissance des premiers modèles 3D permettant de mieux appréhender les processus volcaniques et leurs interactions entre eux. Trois grands "domaines" de processus volcaniques proches de la source sont reproduits par ces modèles : les processus liés à la dynamique des zones de stockage magmatique, ceux liés au conduit volcanique, et enfin les processus de surface. Mes travaux de thèse étant dédiés à l'étude de la dynamique des colonnes volcaniques issues d'éruptions pliniennes, je ne détaillerai que l'évolution de ce dernier type de modèles.
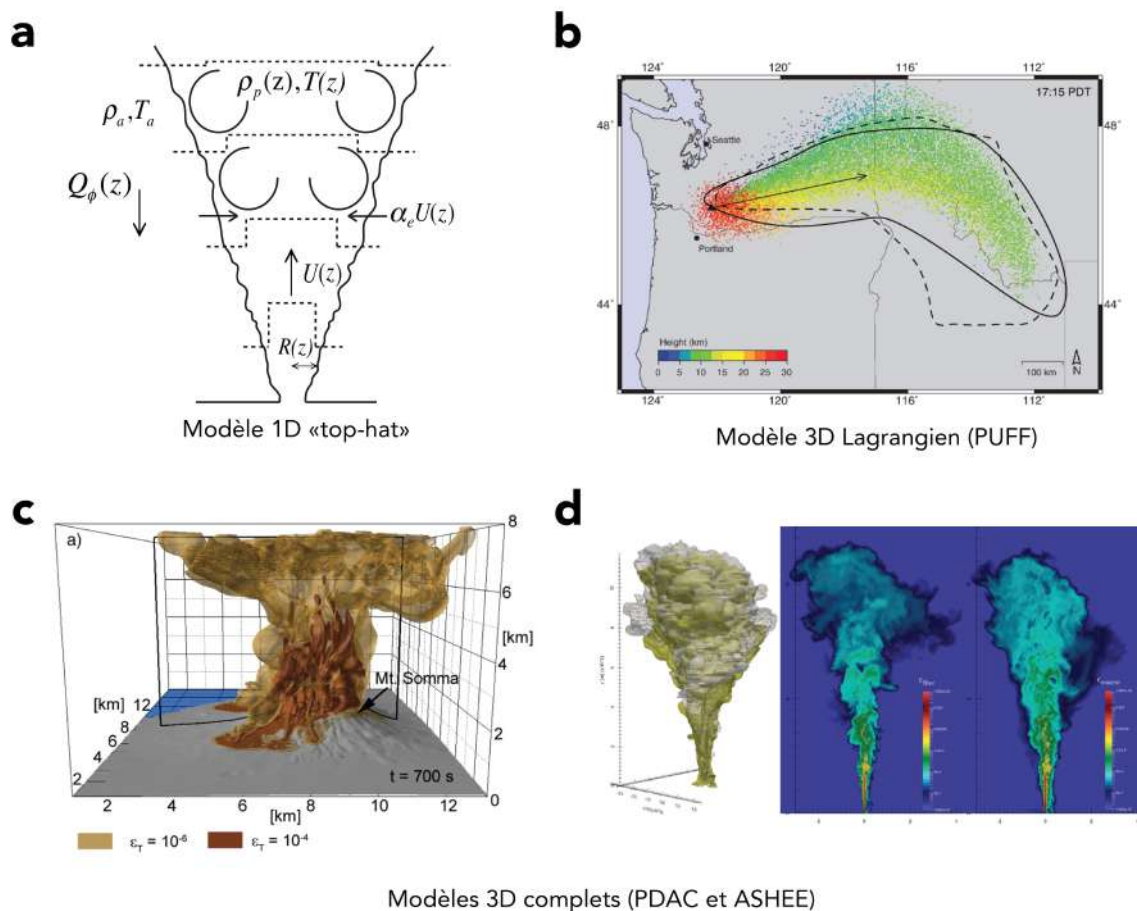
Figure 5: Illustrations de modélisation de colonnes volcaniques: **a** schéma conceptuel d'un jet turbulent contenant des particules, expliquant le fonctionnement d'un modèle 1D "top-hat" (Girault *et al.*, 2014); **b** extension aérienne du nuage de cendres prédit par le modèle 2D PUFF (Fero *et al.*, 2008) pour l'éruption du mont Saint-Helens (couleurs) comparée aux limites extérieures du nuage observées par satellite (trait et pointillés noirs); **c** simulation 3D d'une colonne en effondrement par le modèle PDAC (Esposti Ongaro *et al.*, 2008) pour le volcan du Vésuve montrant le matériel dense retombant au sol tandis que les particules plus fines s'élèvent; et **d** simulation 3D du modèle ASHEE (Cerminara *et al.*, 2016) d'un panache montrant les fractions volumiques de cendres (grossières en vert et fines en gris, à gauche), ainsi que deux coupes 2D montrant la distribution de concentration volumique de particules fines (au centre) et grossières (à droite).

Les modèles de première génération (antérieurs à 1990) dédiés à l'étude des processus volcaniques superficiels liés aux éruptions pliniennes, c'est-à-dire la dynamique des panaches éruptifs et les retombées de cendres, sont des modèles 1D en régime stationnaire (les variables ne dépendent pas du temps) et ne considérant que la variation des flux selon l'altitude. Ils

souvent issus d'une amélioration de la formulation globale (sur un volume de contrôle donné) dérivée de Morton *et al.* (1956) des principes de conservation de la masse, de la quantité de mouvement et de l'énergie. On considère dans ce formalisme "top-hat" que toutes les variables dynamiques sont constantes à une altitude donnée dans la colonne et nulles en dehors (Figure 5a). À une altitude z correspond ainsi une valeur de vitesse, et de densité valable depuis les bords jusqu'au coeur de la colonne : on suppose donc que le panache est parfaitement mélangé par un entraînement turbulent de fluide ambiant dont le coefficient est supposé constant.

Wilson (1976) analysa seulement la partie basale de la colonne ("gas-thrust region") en considérant son comportement similaire à celui d'un jet pur (se déplaçant uniquement grâce à sa quantité de mouvement). Les résultats de ce travail ont ensuite été appliqués aux premières études sur l'instabilité et l'effondrement d'une colonne, et sur la production des coulées de densité pyroclastiques (Sparks & Wilson, 1976; Sparks *et al.*, 1978). Les modèles analysant seulement la partie convective de la colonne (i.e. le panache ; Sparks 1986; Wilson & Walker 1987) ont permis de démontrer la relation entre la hauteur maximale atteinte par la colonne et son débit, d'étudier les variations de rayon, de densité et de vitesse en fonction de l'altitude, et de quantifier l'impact de la stratification atmosphérique sur la hauteur maximale de colonne. Sparks (1986) est le premier à prendre en compte le vent et l'ombrelle dans son modèle, ce qui permet de prédire la dispersion du matériel volcanique fin dans l'ombrelle. Sur cette base, Carey & Sparks (1986) ont développé un modèle inverse qui fournit la méthode la plus populaire actuellement pour déduire des dépôts retrouvés sur le terrain, la hauteur maximale de la colonne éruptive et les profils de vents. Enfin, les modèles analysant la colonne entière (jet + panache) prennent en compte l'entraînement d'air atmosphérique dans la colonne, et la conservation de l'énergie et son effet sur la densité du panache (Woods, 1988) ; ainsi que l'effet de la sédimentation et du déséquilibre thermique sur l'effondrement de colonne (Woods & Bursik, 1991).

Depuis 1990, les modèles eulériens (permettant de calculer l'évolution des grandeurs clefs de l'écoulement) 1D ont notamment été améliorés/développés pour l'étude de la sédimentation (Bursik *et al.*, 1992; Ernst *et al.*, 1996; Bonadonna *et al.*, 1998), de la fragmentation du magma dans le conduit et de la distribution de tailles de grains (PPM, Kaminski & Jaupart 1998, 2001; Girault *et al.* 2014), de la réduction de l'entraînement dans la partie basale de la colonne (PPM, Kaminski *et al.* 2005; Carazzo *et al.* 2006, 2008*a,b*), de la forme du cratère (Woods & Bower, 1995; Koyaguchi *et al.*, 2010), de la condensation ou de la formation de glace dans la colonne (PLUMERIA, Mastin 2007), et de l'effet du vent (PUFFIN, Bursik 2001; Degruyter & Bonadonna 2013; PLUMERISE, Woodhouse *et al.* 2013; PPM, Girault *et al.* 2016) sur la dynamique globale de la colonne volcanique. Ces modèles sont également communément utilisés pour reconstruire des éruptions passées (comme celui de Koyaguchi & Ohno 2001*a,b*) ou dans des buts opérationnels (gestion de crise par exemple). Le modèle PPM (Paris Plume Model), développé dans notre équipe de Dynamique des Fluides Géologiques à l'IPGP par les études successives citées plus haut, a permis d'explorer séparément les effets de la fragmentation du magma dans le conduit et de l'entraînement sur la stabilité des colonnes volcaniques, tandis que l'effet de la distribution de tailles de grains et du vent n'ont été testés que sur la hauteur maximale de colonne. L'effet combiné de tous ces phénomènes sur l'effondrement de colonne n'a pour l'instant jamais été étudié.

Des modèles 2D ont également permis de passer du calcul de valeurs moyennes le long de l'axe principal de la colonne à une distribution spatiale horizontale. Ces modèles sont dits transitoires multiphases et permettent de prendre en compte à la fois la partie ascendante et la partie descendante d'une colonne en effondrement (Neri & Dobran, 1994; Clarke *et al.*, 2002).
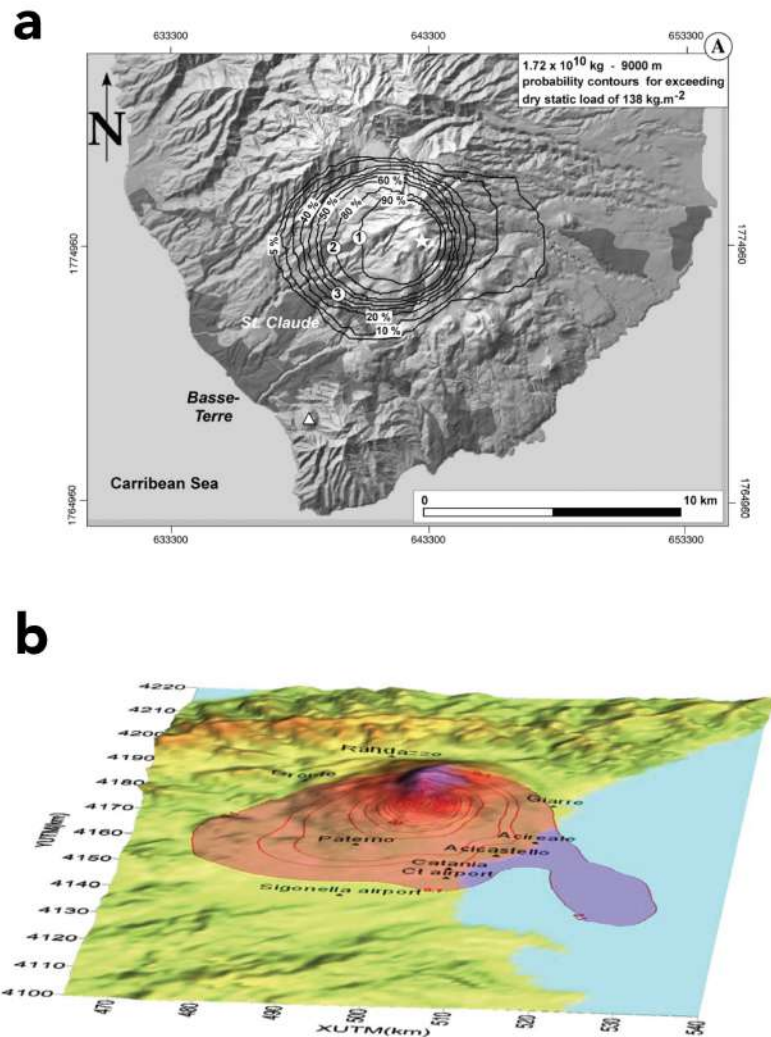
Figure 6: Illustrations de cartes générées par des modèles type advection-diffusion-sédimentation (ADS). **a** Carte probabiliste pour le volcan de la Soufrière (Guadeloupe) simulée par le modèle 2D HAZMAP (Komorowski *et al.*, 2008). Les contours en noirs indiquent les probabilités d'excéder 138 kg m^{-2} dans la zone concernée. **b** Carte de quantités de dépôts au sol en kg m^{-2} autour de l'Etna (Italie) générée par le modèle 3D VOL-CALPUFF (Barsotti *et al.*, 2008).

Enfin, les modèles 3D sont très diversifiés. Les modèles 3D lagrangiens (déterminant les trajectoires précises des particules en calculant leurs coordonnées grâce à un bilan de force) sont le plus souvent utilisés pour la prévision opérationnelle à court-terme de nuages de cendres volcaniques sur des distances > 100 km (HYSPLIT, Draxler & Hess 1998 ; PUFF, Fero *et al.* 2008, Figure 5b). Ces modèles ne traitent cependant pas la dynamique de la colonne, ils restent dépendant d'un terme source. Les modèles 3D complets (tels que PDAC, Esposti Ongaro *et al.* 2008 ; SK-3D, Suzuki *et al.* 2005 ; ou ASHEE, Cerminara *et al.* 2016) sont quant à eux basés sur la résolution dépendante du temps des équations de Navier-Stokes pour la conservation de la masse, de la quantité de mouvement et de l'énergie, décrivant à la fois la dynamique des fluides du mélange éruptif et l'atmosphère environnante. Ces modèles sont extrêmement utiles pour comprendre plus précisément les processus physiques (Figure 5c et d), prendre en compte des changements rapides de direction ou de vitesse d'un profil de vent ("wind shear") sur la dispersion des cendres, mais également l'effet de la topographie sur les coulées de densité pyroclastiques. Ils ne peuvent cependant pas être utilisés à des

fins prévisionnelles car souvent trop longs en temps de calcul.

Treize modèles 1D et 3D ont été comparés lors d'un récent exercice (Costa *et al.*, 2016) durant lequel deux cas ont été simulés par chacun des modèles : un cas de "strong plume" (c'est-à-dire une colonne "forte") soumis à peu de vent, et un cas de "weak plume" (une colonne "faible") soumis à un environnement très venteux. L'exercice a démontré que dans le cas du strong plume, les modèles 1D et 3D prédisent des hauteurs maximales de colonnes similaires, mais divergent sur les caractéristiques (température, fraction solide, etc) de la colonne. Dans le cas du weak plume et d'un environnement très venteux, les deux types de modèles divergent fortement dans leurs prédictions de hauteurs de colonnes. Ces conclusions mettent en avant la nécessité de mieux contraindre l'effet du vent dans les modèles 1D, et de paramétrer plus précisement l'entraînement d'air atmosphérique dans la colonne dû au vent (Costa *et al.*, 2016).

Tous ces modèles 1D, 2D et 3D précédemment décrits ont pour but de simuler le panache volcanique pour étudier les conditions contrôlant l'altitude maximale de la colonne (qui détermine la hauteur d'injection des cendres dans l'atmosphère) et l'effondrement de colonne (qui rend l'éruption bien plus dangereuse). La dispersion des cendres volcaniques dans l'atmosphère a également été étudiée numériquement à l'aide de modèles basés sur des équations d'advection-diffusion-sédimentation (ADS). Ces modèles eulériens peuvent être 2D (HAZMAP, Macedonio *et al.* 2005 ; ASHFALL, Hurst & Turner 1999 ; TEPHRA, Bonadonna *et al.* 2005) ou 3D (FALL3D, Costa *et al.* 2006 ; VOL-CALPUFF, Barsotti *et al.* 2008 ; ASH3D, Schwaiger *et al.* 2012). Les modèles 2D permettent de générer des cartes probabilistes basées sur des calculs de masses de particules déposées au sol (Figure 6a). Ils ne prennent pas en compte la dynamique de la colonne, mais seulement un point source. Les modèles 3D permettent de calculer des concentrations de téphra dans l'atmosphère ou des masses de dépôts au sol (Figure 6b) tout en incluant une description détaillée de la colonne volcanique. Ces deux types de modèles ont été comparés par Scollo *et al.* (2008), qui montrent que les résultats sont hautement sensibles aux incertitudes des paramètres d'entrée (hauteur maximale de colonne, débit de l'éruption...). Si les erreurs sur ces estimations sont réduites, les prédictions des modèles convergent entre elles. Ces modèles de type ADS sont souvent utilisés pour des prévisions en quasi temps réel à des fins opérationnelles, mais également pour la modélisation d'évènements passés ou pour la caractérisation de l'aléa.

L'aléa volcanique à la Martinique

Les modèles numériques sont couramment utilisés pour caractériser l'aléa volcanique explosif permettant dans un second temps d'évaluer les risques volcaniques. L'**aléa** représente la probabilité qu'un phénomène naturel (une coulée de lave par exemple) se produise à un certain endroit et moment, contrairement au **risque** qui lui représente la combinaison entre l'aléa et la vulnérabilité des enjeux (personnes, bâtiments, biens) présents dans la zone considérée (la destruction totale d'une maison par une coulée de lave par exemple). Le risque est donc évalué par la relation suivante (United Nations, 1992) :

$$\text{Risque} = \text{Aléa} \times \text{Vulnérabilité} \times \text{Enjeux}$$

En effet, pour qu'il y ait un risque lié au volcan, il faut qu'en plus du phénomène volcanique en lui-même, il y ait des enjeux menacés par ce phénomène (à ce titre, un volcan en éruption situé sur une île déserte représente un aléa, mais pas un risque). Pour mettre en oeuvre ces modèles numériques il faut bien sûr qu'ils soient basés sur une théorie physique solide, et que leurs résultats aient été dûment validés, soit par du benchmarking, soit par des expériences en laboratoire (comme évoqué dans la précédente section). Mais en complément, ils doivent également reposer sur des données de terrain qui permettent de proposer des scénarios

éruptifs. En effet, l'étude des magmas éruptés et des dépôts volcaniques est nécessaire pour étudier et comprendre les éruptions passées (Balcone-Boissard *et al.*, 2010).

Afin de produire une carte d'aléa volcanique, représentant uniquement les zones impactées par des phénomènes volcaniques en cas de future éruption, il faut donc tout d'abord connaître l'histoire passée du volcan. Actuellement, à la Martinique, la carte d'aléa utilisée dans le cadre du plan ORSEC (Organisation de la réponse de la sécurité civile) est celle élaborée par Stieltjes & Mirgon (1998) du BRGM (Bureau de recherches géologiques et minières) (Figure 7). Elle est basée sur l'histoire éruptive connue de la montagne Pelée établie par Westercamp & Traineau (1983) sur les 5 000 dernières années. Dans cette période de référence, 23 éruptions magmatiques (péléennes et pliniennes) ont été identifiées (Westercamp & Traineau, 1983), généralement associées à des éruptions phréatiques (ne mettant en jeu que le système hydrothermal du volcan, sans expulsion de magma frais - de façon analogue à la crise de 1976 en Guadeloupe). Ces trois types d'éruptions génèrent plusieurs aléas : des retombées de cendres, des intrusions (dômes)/coulées de lave, des coulées de densité pyroclastiques, et des émanations de gaz. Les études effectuées sur la montagne Pelée évoquent également des lahars (coulées de boue remobilisant des matériaux volcaniques, Aubaud *et al.* 2013), des mouvements de terrain (liés à des effondrements de flancs par exemple, Le Friant *et al.* 2003), et des tsunamis liés à ces lahars et mouvements de terrain.

Cependant, seules des informations datant des années 1980 et portant sur les seules éruptions récentes connues sont incluses dans cette carte : les éruptions pliniennes P1 ($\approx$ an 1300 de notre ère), P2 ($\approx$ an 280) et P3 ($\approx$ an 79) (Traineau *et al.*, 1989), et les éruptions péléennes récentes de 1929-1932, 1902-1905 (Lajoie & Boudon, 1989), Nuées de la rivière des Pères (NRP, entre 1310 et 1625), Nuées d'Ajoupa Bouillon (NAB, entre -550 et -850) et Nuées de Pointe la Mare (NPM, $\approx$ -2450). Les éruptions plus anciennes identifiées par Westercamp & Traineau (1983) n'ont en effet jamais été étudiées en détail. Stieltjes & Mirgon (1998) ont donc établi, en se basant sur ces huit scénarios, des matrices "intensité $\times$ fréquence" afin de quantifier pour chaque zone et chacun des aléas cités plus haut, un coefficient d'exposition à cet aléa. Ils ont ensuite pu construire des cartes pour chaque aléa, qu'ils ont combinées pour produire la carte intégrée d'aléa volcanique à la Martinique présentée en Figure 7. Cette carte synthétise donc l'extension spatiale probable des sept aléas considérés, dans l'hypothèse de l'éruption la plus puissante possible à la montagne Pelée. On observe que le nord de la Martinique est marqué par un aléa volcanique considérable, mais également que certaines zones (principalement côtières) au sud pourraient être menacées en cas de future éruption. La ville de Fort-de-France (zone la plus peuplée de l'île) et l'aéroport international Aimé Césaire sont quant à eux classés en zone d'exposition faible à nul.

Le risque volcanique peut être quantifié à partir de cette carte d'aléa en utilisant des fonctions de vulnérabilité qui permettent de moduler les risques d'endommagements/pertes potentiels selon les éléments exposés, et l'intensité des phénomènes les menaçant (Leone, 2004). En considérant 113 000 bâtiments présents sur l'île de la Martinique dont les taux d'endommagement ont été modulés par les mêmes niveaux d'intensité d'aléa volcanique fournis par Stieltjes & Mirgon (1998), il est possible de calculer un indice de risque de pertes absolues (encart de la Figure 7). La population est fortement réduite dans le nord de l'île (principalement à cause de la catastrophe de 1902 et du relief escarpé), pourtant cette carte de risque montre que les conséquences d'une éruption volcanique maximale seraient très importantes puisque près de 8 500 bâtiments et 308 km de routes et chemins sont situés en zone d'aléa majeur (délimitée par le perimètre potentiel d'évacuation en pointillé sur la carte). On peut noter que le risque volcanique est nul au-delà de la limite déterminée par la carte d'aléa, même si les enjeux (population et infrastructures) sont plus importants dans le sud de l'île.
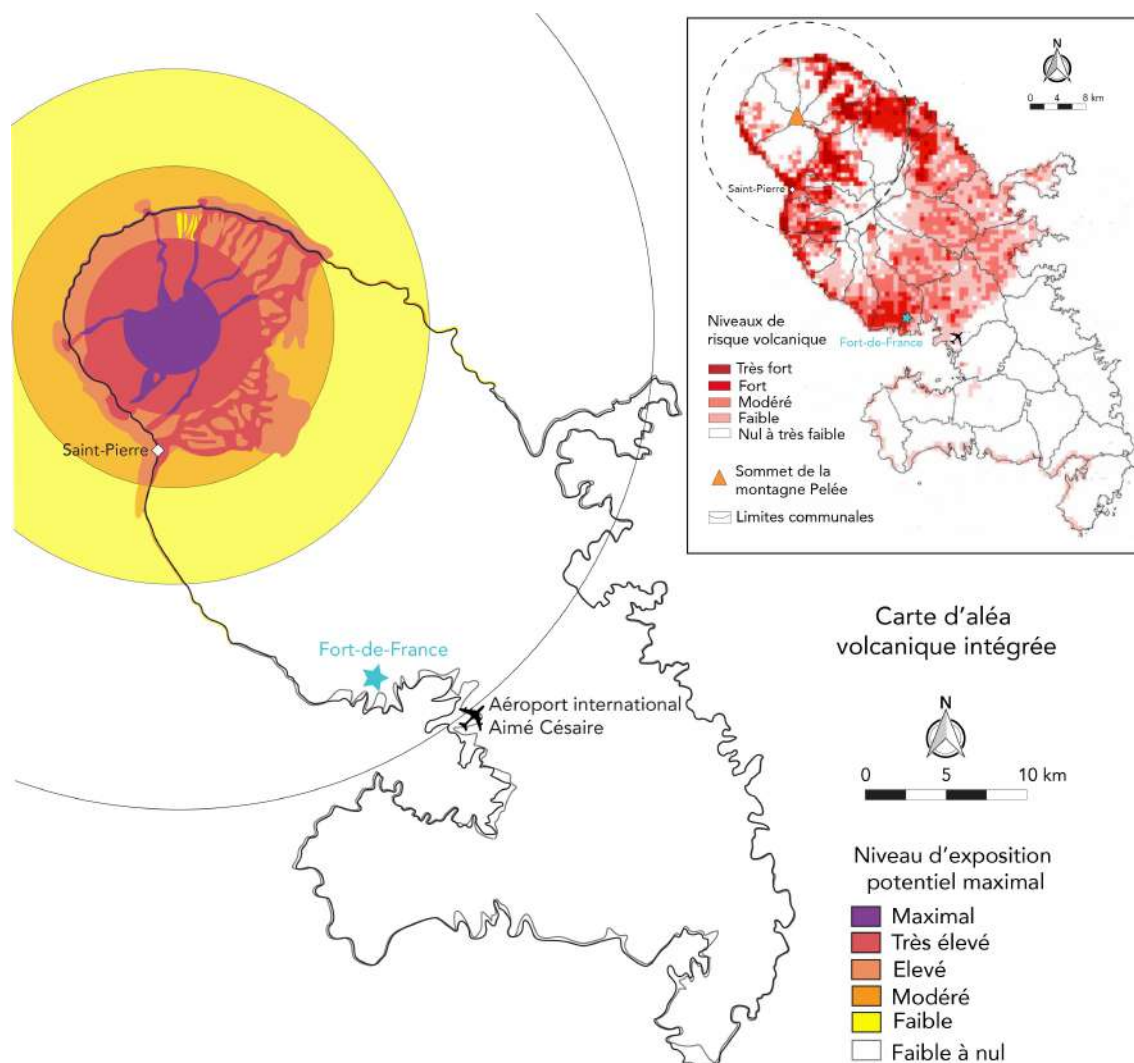
Figure 7: Carte d'aléa volcanique intégrée pour la Martinique montrant le niveau d'exposition potentiel maximal de chaque zone de l'île, *simplifiée d'après Stieltjes & Mirgon (1998)*. Les cercles correspondent aux zones concernées par les aléas de retombées aériennes de cendres, d'émanations de gaz et d'intrusions/coulées de lave ; les figurés autour de la montagne Pelée aux zones concernées par les aléas de coulées de densité pyroclastiques, de lahars et de mouvements de terrain ; et les figurés le long des côtes aux zones concernées par l'aléa tsunami d'origine volcanique. L'encart montre les niveaux de risque volcanique exprimés par un indice de pertes absolues liées à l'endommagement du bâti en cas d'éruption maximale crédible de la montagne Pelée, ainsi que le périmètre d'évacuation probable en cas d'éruption magmatique (ligne pointillée, Leone 2004).

Depuis la création de cette carte d'aléa, les trois éruptions pliniennes les plus récentes, P1, P2 et P3 ont été revisitées (Carazzo *et al.*, 2012, 2019, 2020). Ces études nous montrent que ces trois éruptions ont des VEI similaires (4−5) et qu'elles ont toutes les trois alterné entre des phases de panache stable et des phases d'effondrement de colonne avec production de coulées de densité pyroclastiques. Cependant, elles se différencient dans leurs axes de dispersion. Les éruptions P1 et P3 ont en effet projeté leurs cendres vers les flancs ouest-sud-ouest du volcan tandis que l'éruption P2 a envoyé son matériel en direction du nord-est, ce qui marque l'importance de l'orientation du vent pendant l'éruption. Il apparaît donc important de savoir si les éruptions pliniennes plus anciennes de la montagne Pelée reproduisent ce même schéma ou introduisent une variabilité supplémentaire dans la dispersion, ce qui modifierait fortement la carte d'aléa intégrée et augmenterait sensiblement le risque

dans le sud de l'île.

Une nouvelle étude des éruptions pliniennes de la montagne Pelée

Les travaux de thèse présentés dans ce manuscrit s'organisent en trois grands axes : la revisite de l'histoire éruptive de la montagne Pelée et l'identification de scénarii probables de futures éruptions (Partie 1), la modélisation physique de colonnes volcaniques en vue de préciser les conditions de stabilité ou d'effondrement de colonne (en présence d'un vent fort notamment, Partie 2), et enfin la caractérisation de l'aléa volcanique plinien à la Martinique (Partie 3). Chaque partie étant composée de deux chapitres, le manuscrit se décompose comme suit:

* Le chapitre 1 décrit le contexte de l'étude, les méthodes employées pour revisiter l'histoire éruptive, ainsi que les principaux résultats de deux nouvelles missions de terrain menées à la Martinique. Ces dernières nous ont permis d'identifier des éruptions pliniennes encore inconnues à la montagne Pelée.

* Le chapitre 2 présente la reconstruction de ces éruptions en déterminant leurs paramètres éruptifs (volume, hauteur de colonne, débit, durée, dispersion), afin de pouvoir comparer ces anciennes éruptions avec celles plus récentes et envisager un ensemble plus complet de scénarii probables.

* Le chapitre 3 détaille comment le modèle 1D PPM a été utilisé pour étudier les effets combinés de la distribution de tailles de grains et de la réduction d'entraînement à la base de la colonne sur les conditions de stabilité d'une colonne volcanique.

* Le chapitre 4 propose de nouvelles expériences analogiques permettant d'étudier des éruptions pliniennes en laboratoire, afin de caractériser plus précisément l'entraînement d'air atmosphérique dans la colonne dû au vent et d'étudier l'effet de ce dernier sur l'effondrement de colonne, grâce à PPM.

* Le chapitre 5 présente l'utilisation qui a été faite du modèle 2D HAZMAP (Macedonio *et al.*, 2005) pour simuler et étudier la dispersion des produits volcaniques issus des éruptions pliniennes connues de la montagne Pelée.

* Enfin, le chapitre 6 combine l'ensemble des résultats précédents afin d'aboutir à une nouvelle carte d'aléa volcanique plinien à la Martinique.

La conclusion synthétise les résultats de cette thèse et propose des éléments de réflexion pour établir de nouvelles pistes de recherche. Le chapitre 3, ainsi qu'une partie des chapitres 2 et 5 sont déjà publiés dans Michaud-Dubuy *et al.* (2018) et Michaud-Dubuy *et al.* (2019).

Bibliographie

AUBAUD, C., ATHANASE, J.-E., CLOUARD, V., BARRAS, A.-V. & SEDAN, O. 2013 A review of historical landslides, floods, and lahars in the Precheur river catchment, Montagne Pelée volcano (Martinique, Lesser Antilles). *Bull. Soc. Géol. Fr.* **184** (I), 137–154.

BALCONE-BOISSARD, H., BOUDON, G. & VILLEMANT, B. 2010 Textural and geochemical constraints on eruptive style of the 79 AD eruption at Vesuvius. *Bull. Volcanol.* **73**, 279–294.

BARSOTTI, S., NERI, A. & SCIRE, J.S. 2008 The VOL-CALPUFF model for atmospheric ash dispersal: 1. Approach and physical formulation. *J. Geophys. Res.* **113** (B03208).

Bibliographie

BLAKE, D.M., DELIGNE, N.I., WILSON, T.M. & WILSON, G. 2017 Improving volcanic ash fragility functions through laboratory studies: example of surface transportation networks. *J. Appl. Volcanol.* **6** (16).

BONADONNA, C., CONNOR, C.B., HOUGHTON, B.F., CONNOR, L., BYRNE, M., LAING, A. & HINCKS, T.K. 2005 Probabilistic modeling of tephra dispersal: Hazard assessment of a multiphase rhyolitic eruption at Tarawera, New Zealand. *J. Geophys. Res.* **110** (B03203).

BONADONNA, C., ERNST, G.G.J. & SPARKS, R.S.J. 1998 Thickness variations and volume estimates of tephra fall deposits: The importance of particle Reynolds number. *J. Volcanol. Geotherm. Res.* **81**, 173–187.

BURSIK, M. 2001 Effect of wind on the rise height of volcanic plumes. *Geophys. Res. Lett.* **28**, 3621–3624.

BURSIK, M.I., SPARKS, R.S.J., GILBERT, J.S. & CAREY, S.N. 1992 Sedimentation of tephra by volcanic plumes: I. Theory and its comparison with a study of the Fogo A plinian deposit, Sao Miguel (Azores). *Bull. Volcanol.* **54**, 329–344.

CARAZZO, G., KAMINSKI, E. & TAIT, S. 2006 The route to self-similarity in turbulent jets and plumes. *J. Fluid Mech.* **547**, 137–148.

CARAZZO, G., KAMINSKI, E. & TAIT, S. 2008*a* On the dynamics of volcanic columns: A comparison of field data with a new model of negatively buoyant jets. *J. Volcanol. Geotherm. Res.* **178**, 94–103.

CARAZZO, G., KAMINSKI, E. & TAIT, S. 2008*b* On the rise of turbulent plumes: Quantitative effects of variable entrainment for submarine hydrothermal vents, terrestrial and extra terrestrial explosive volcanism. *J. Geophys. Res. Solid Earth* **113**, 1–19.

CARAZZO, G., TAIT, S. & KAMINSKI, E. 2019 Marginally stable recent Plinian eruptions of Mt. Pelée volcano (Lesser Antilles): the P2 AD 280 eruption. *Bull. Volcanol.* **81**, 1–17.

CARAZZO, G., TAIT, S., KAMINSKI, E. & GARDNER, J. E. 2012 The recent Plinian explosive activity of Mt. Pelée volcano (Lesser Antilles): The P1 AD 1300 eruption. *Bull. Volcanol.* **74**, 2187–2203.

CARAZZO, G., TAIT, S., MICHAUD-DUBUY, A., FRIES, A. & KAMINSKI, E. 2020 Transition from stable column to partial collapse during the 79 cal CE P3 Plinian eruption of Mt Pelée volcano (Lesser Antilles). *J. Volcanol. Geotherm. Res. In press.* https://doi.org/10.1016/j.jvolgeores.2019.106764.

CAREY, S. & SPARKS, R.S.J. 1986 Quantitative models of the fallout and dispersal of tephra from volcanic eruption columns. *Bull. Volcanol.* **48**, 109–125.

CERMINARA, M., ESPOSTI ONGARO, T. & BERSELLI, L.C. 2016 ASHEE-1.0: A compressible, equilibrium-Eulerian model for volcanic ash plumes. *Geosci. Model Dev.* **9**, 697–730.

CLARKE, A.B., VOIGHT, B., NERI, A. & MACEDONIO, G. 2002 Transient dynamics of vulcanian explosions and column collapse. *Nature* **415**, 897–901.

COSTA, A., MACEDONIO, G. & FOLCH, A. 2006 A three-dimensional Eulerian model for transport and deposition of volcanic ashes. *Earth Planet. Sci. Lett.* **241** (3-4), 634–647.

COSTA, A., SUZUKI, Y. J., CERMINARA, M., DEVENISH, B. J., ESPOSTI ONGARO, T., HERZOG, M., VAN EATON, A. R., DENBY, L. C., BURSIK, M., DE' MICHIELI VITTURI, M., ENGWELL, S., NERI, A., BARSOTTI, S., FOLCH, A., MACEDONIO, G., GIRAULT, F., CARAZZO, G., TAIT, S., KAMINSKI, E., MASTIN, L. G., WOODHOUSE, M. J., PHILLIPS, J. C., HOGG, A. J., DEGRUYTER, W. & BONADONNA, C. 2016 Results of the eruptive column model inter-comparison study. *J. Volcanol. Geotherm. Res.* **326**, 2–25.

DEGRUYTER, W. & BONADONNA, C. 2013 Impact of wind on the condition for column collapse of volcanic plumes. *Earth Planet. Sci. Lett.* **377-378**, 218–226.

DRAXLER, R.R. & HESS, G.D. 1998 An overview of the HYSPLIT4 modelling system for trajectories, dispersion and deposition. *Aust. Met. Mag.* **47**, 295–308.

ERNST, G. J., STEPHEN, R., SPARKS, J., CAREY, N. & BURSIK, M. I. 1996 Sedimentation from turbulent jets and plumes. *J. Geophys. Res.* **101** (95), 5575–5589.

Esposti Ongaro, T., Neri, A., Menconi, G., de'Michieli Vitturi, M., Marianelli, P., Cavazzoni, C., Erbacci, G. & Baxter, P. J. 2008 Transient 3D numerical simulations of column collapse and pyroclastic density current scenarios at Vesuvius. *J. Volcanol. Geotherm. Res.* **178** (3), 378–396.

Fero, J., Carey, S.N. & Merrill, J.T. 2008 Simulation of the 1980 eruption of Mount St. Helens using the ash-tracking model PUFF. *J. Volcanol. Geotherm. Res.* **175**, 355–366.

Girault, F., Carazzo, G., Tait, S., Ferrucci, F. & Kaminski, E. 2014 The effect of total grain-size distribution on the dynamics of turbulent volcanic plumes. *Earth Planet. Sci. Lett.* **394**, 124–134.

Girault, F., Carazzo, G., Tait, S. & Kaminski, E. 2016 Combined effects of total grain-size distribution and crosswind on the rise of eruptive volcanic columns. *J. Volcanol. Geotherm. Res.* **326**, 103–113.

Horwell, C. J. & Baxter, P. J. 2006 The respiratory health hazards of volcanic ash: A review for volcanic risk mitigation. *Bull. Volcanol.* **69** (1), 1–24.

Hurst, A.W. & Turner, R. 1999 Performance of the program ashfall for forecasting ashfall during the 1995 and 1996 eruptions of Ruapehu volcano. *New Zealand J. Geol. Geophys.* **42** (4), 615–622.

Kaminski, E. & Jaupart, C. 1998 The size distribution of pyroclasts and the fragmentation sequence in explosive volcanic eruptions. *J. Geophys. Res.* **103**, 29759–29779.

Kaminski, E. & Jaupart, C. 2001 Marginal stability of atmospheric eruption columns and pyroclastic flow generation. *J. Geophys. Res.* **106** (B10), 21785–21798.

Kaminski, E., Tait, S. & Carazzo, G. 2005 Turbulent entrainment in jets with arbitrary buoyancy. *J. Fluid Mech.* **526**, 361–376.

Komorowski, J. C., Legendre, Y., Caron, B. & Boudon, G. 2008 Reconstruction and analysis of sub-plinian tephra dispersal during the 1530 A.D. Soufriere (Guadeloupe) eruption: Implications for scenario definition and hazards assessment. *J. Volcanol. Geotherm. Res.* **178**, 491–515.

Koyaguchi, T. & Ohno, M. 2001a Reconstruction of eruption column dynamics on the basis of grain size of tephra fall deposits. 1. Methods. *J. Geophys. Res.* **106**, 6499–6512.

Koyaguchi, T. & Ohno, M. 2001b Reconstruction of eruption column dynamics on the basis of grain size of tephra fall deposits. 2. Application to the Pinatubo 1991 eruption. *J. Geophys. Res.* **106**, 6513–6533.

Koyaguchi, T., Suzuki, Y. J. & Kozono, T. 2010 Effects of the crater on eruption column dynamics. *J. Geophys. Res.* **115** (7), 1–26.

Lacroix, A. 1904 *La Montagne Pelée et ses éruptions*. Masson, Paris.

Lajoie, J. & Boudon, G. 1989 The Peléan deposits in the Fort Cemetery of St. Pierre, Martinique: a model for the accumulation of turbulent nuées ardentes. *J. Volcanol. Geotherm. Res.* **38**, 113–130.

Le Friant, A., Boudon, G., Deplus, C. & Villemant, B. 2003 Large-scale flank collapse events during the activity of Montagne Pelée, Martinique, Lesser Antilles. *J. Geophys. Res.* **108** (B1), 1–15.

Leone, F. 2004 Une approche quantitative de la cartographie des risques naturels: application expérimentale au patrimoine bâti de la Martinique (Antilles Françaises). *Géomorphologie: Relief, Processus, Environnement* **3**, 209–222.

Macedonio, G., Costa, A. & Longo, A. 2005 A computer model for volcanic ash fallout and assessment of subsequent hazard. *Comput. Geosci.* **31**, 837–845.

Mastin, L. G. 2007 A user-friendly one-dimensional model for wet volcanic plumes. *Geochem. Geophys. Geosyst.* **8** (Q03014).

Michaud-Dubuy, A., Carazzo, G., Kaminski, E. & Girault, F. 2018 A revisit of the role of gas entrapment on the stability conditions of explosive volcanic columns. *J. Volcanol. Geotherm. Res.* **357**, 349–361.

Michaud-Dubuy, A., Carazzo, G., Tait, S., Le Hir, G., Fluteau, F. & Kaminski, E. 2019 Impact of wind direction variability on hazard assessment in Martinique (Lesser Antilles): The example of the 13.5 ka cal BP Bellefontaine Plinian eruption of Mount Pelée volcano. *J. Volcanol. Geotherm. Res.* **381**, 193–208.

MORTON, B.R., TAYLOR, G.I. & TURNER, J.S. 1956 Turbulent gravitational convection from maintained and instantaneous sources. *Philos. Trans. R. Soc. A* **234**, 1–23.

NERI, A. & DOBRAN, F. 1994 Influence of eruption parameters on the thermofluid dynamics of collapsing volcanic columns. *J. Geophys. Res.* **99** (B6), 11833–11857.

NEWHALL, CHRISTOPHER G. & SELF, STEPHEN 1982 The volcanic explosivity index (VEI) an estimate of explosive magnitude for historical volcanism. *J. Geophys. Res.* **87** (C2), 1231–1238.

SCHWAIGER, H.F., DENLINGER, R.P. & MASTIN, L.G. 2012 ASH3D: A finite-volume, conservative numerical model for ash transport and tephra deposition. *J. Geophys. Res.* **117** (B04204).

SCOLLO, S., FOLCH, A. & COSTA, A. 2008 A parametric and comparative study of different tephra fallout models. *J. Volcanol. Geotherm. Res.* **176**, 199–211.

SELF, S., ZHAO, J.-X., HOLASEK, R.E., TORRES, R.C. & KING, A.J. 1996 The atmospheric impact of the 1991 Mount Pinatubo eruption. In *Fire and Mud: Eruptions and Lahars of Mount Pinatubo, Philippines* (ed. C.G. Newhall & R.S. Punongbayan), pp. 1089–1115. Philippine Institute of Volcanology and Seismology, Queen City and University of Washington Press, Seattle.

SPARKS, R. S. J. 1986 The dimensions and dynamics of volcanic eruption columns. *Bull. Volcanol.* **48**, 3–15.

SPARKS, R. S. J. & WILSON, L. 1976 A model for the formation of ignimbrite by gravitational column collapse. *J. Geol. Soc. Lond.* **132**, 441–451.

SPARKS, R. S. J., WILSON, L. & HULME, G. 1978 Theoretical modelling of the generation, movement and emplacement of pyroclastic flows by column collapse. *J. Geophys. Res.* **83**, 1727–1739.

STIELTJES, L. & MIRGON, C. 1998 Approche méthodologique de la vulnérabilité aux phénomènes volcaniques : Test d'application sur les réseaux de la Martinique. In *Unpublished Internal Report No. R40098*. Bureau de Recherches Géologiques et Minières, Marseille.

SUZUKI, Y. J., KOYAGUCHI, T., OGAWA, M. & HACHISU, I. 2005 A numerical study of turbulent mixing in eruption clouds using a three-dimensional fluid dynamics model. *J. Geophys. Res.* **110**, B08201.

TRAINEAU, H., WESTERCAMP, D., BARDINTZEFF, J. M. & MISKOVSKY, J. C. 1989 The recent pumice eruptions of Mt. Pelée volcano, Martinique. Part I: Depositional sequences, description of pumiceous deposits. *J. Volcanol. Geotherm. Res.* **38**, 17–33.

UNITED NATIONS, ed. 1992 *Internationally agreed glossary of basic terms related to Disaster Management*. Department of Humanitarian Affairs.

WESTERCAMP, D. & TRAINEAU, H. 1983 The past 5,000 years of volcanic activity at Mt. Pelée Martinique (F.W.I.): Implications for assessment of volcanic hazards. *J. Volcanol. Geotherm. Res.* **17**, 159–185.

WILLIAMS, M. 2012 The $\sim$ 73 ka Toba super-eruption and its impact: History of a debate. *Quaternary International* **258**, 19–29.

WILSON, L. 1976 Explosive Volcanic Eruptions: III. Plinian Eruption Columns. *J. R. Astron. Soc.* **45**, 543–556.

WILSON, L., SPARKS, R. S. J. & WALKER, G. P. L. 1980 Explosive volcanic eruptions - IV. The control of magma properties and conduit geometry on eruption column behaviour. *Geophys. J. R. Astron. Soc.* **63**, 117–148.

WILSON, L. & WALKER, G.P.L. 1987 Explosive volcanic eruptions - VI. Ejecta dispersal in plinian eruptions: the control of eruption conditions and atmospheric properties. *Geophys. J. R. Astron. Soc.* **89**, 657–679.

WOODHOUSE, M. J., HOGG, A. J., PHILLIPS, J. C. & SPARKS, R. S. J. 2013 Interaction between volcanic plumes and wind during the 2010 Eyjafjallajökull eruption, Iceland. *J. Geophys. Res. Solid Earth* **118**, 92–109.

WOODS, A.W. 1988 The fluid dynamics and thermodynamics of eruption columns. *Bull. Volcanol.* **50**, 169–193.

WOODS, A. W. & BOWER, S. M. 1995 The decompression of volcanic jets in a crater during explosive eruptions. *Earth Planet. Sci. Lett.* **131**, 189–205.

WOODS, A. W. & BURSIK, M. I. 1991 Particle fallout, thermal disequilibrium and volcanic plumes. *Bull. Volcanol.* **53**, 559–570.

Part 1

Geological data and possible eruptive scenarii in Martinique

Chapter 1

A revisit of the eruptive history of Mount Pelée volcano

Table of contents

Résumé du chapitre 1

Les panaches volcaniques produits par les éruptions explosives représentent un aléa majeur dans les zones proches de stratovolcans. Les modèles physiques développés dans les quarante dernières années ont eu pour but de mieux comprendre ces phénomènes naturels et de quantifier les aléas volcaniques. Pour tester ces modèles, nous avons besoin de données de terrain précises et détaillées sur les éruptions passées des volcans actifs. La montagne Pelée sur l'île de la Martinique (Petites Antilles), ayant une histoire éruptive très riche, est une excellente candidate pour ces phases de validation. Ce volcan est particulièrement célèbre pour son éruption de 1902-1905, caractérisée par plusieurs cycles de croissance/destruction de dômes de lave et responsable du plus lourd bilan humain pour une éruption volcanique au vingtième siècle. Ce type d'éruption a d'ailleurs été nommé "péléenne" en référence à la montagne Pelée par Alfred Lacroix, qui a étudié cette crise éruptive (Lacroix, 1904). De précédentes études de terrain effectuées à la Martinique ont démontré que ce volcan n'a cependant pas seulement produit des éruptions péléennes dans le passé, mais également des éruptions pliniennes bien plus puissantes sur lesquelles nous avons peu d'informations (Westercamp & Traineau, 1983).

Dans cette première partie du manuscrit, nous nous proposons de revisiter l'histoire éruptive plinienne de la montagne Pelée sur les vingt-quatre derniers milliers d'années grâce à deux nouvelles campagnes de terrain effectuées à la Martinique, et de dégager de cette histoire éruptive les scénarii des potentielles futures éruptions du volcan. Dans ce chapitre, nous présentons tout d'abord le contexte géologique et météorologique de la Martinique, ainsi que la montagne Pelée et son histoire éruptive connue. Nous détaillons ensuite les méthodes utilisées sur le terrain pour reconnaître les dépôts d'éruption, les analyser et les dater. Nos résultats combinant travaux de terrain et datations au ^{14}C nous permettent d'établir une nouvelle chronologie des éruptions passées de la montagne Pelée. Celle-ci inclut six nouvelles éruptions dans les derniers vingt-quatre mille ans, dont quatre éruptions pliniennes et deux péléennes. En comparant les nouvelles éruptions pliniennes avec les dépôts volcaniques datés en mer, nous remarquons que trois sur quatre correspondent à des événements identifiés au large de la Martinique, ce qui renforce notre confiance dans cette nouvelle histoire éruptive.

L'histoire éruptive de la montagne Pelée est donc très riche avec au minimum 34 éruptions magmatiques au cours des derniers 24 000 ans. En se basant sur cette nouvelle histoire éruptive, nous pouvons estimer qu'une éruption plinienne se produit environ tous les 1 800 ans à la Martinique, et une éruption magmatique tous les 700 ans.

Parmi ces éruptions nouvellement découvertes, nous avons collecté assez de données (épaisseurs de dépôts et distribution des fragments lithiques à plusieurs affleurements, ainsi que des échantillons pour les analyses de tailles de grains) pour aller plus loin et reconstruire les paramètres éruptifs de quatre des nouvelles éruptions (celles nommées Bellefontaine, Balisier, Carbet et Etoile) en utilisant les méthodes décrites dans ce chapitre. Les résultats sont présentés dans le chapitre 2.

1   Introduction

Volcanic plumes produced by explosive eruptions represent a major hazard in areas located near volcanoes. Physical models have been developed over the past 40 years with an aim of better understanding these flows and assessing volcanic hazards. To test these models, we need robust and detailed field data from past and historical eruptions at active volcanoes. Mount Pelée in Martinique (Lesser Antilles) has a very rich eruptive history making it an excellent candidate to reach this goal. This volcano is particularly known for the 1902 dome-forming eruption, the deadliest eruption of the twentieth century. This eruption type was named "Pelean" eruption (in reference to the Mount Pelée) by Alfred Lacroix who studied the eruptive crisis of 1902-1905 (Lacroix, 1904). Previous fieldwork in Martinique showed that this volcano has however not only produced Pelean eruptions in the past, but also more powerful Plinian eruptions for which limited information exist (Westercamp & Traineau, 1983). Two new fieldwork campaigns performed during this PhD work have allowed us to improve our knowledge of the ancient eruptive history of Mount Pelée (up to 24,000 years ago), and thus to refine future possible eruptive scenarii.

This chapter is dedicated to a presentation of the Mount Pelée volcano and its currently known eruptive history, which I seek to update. First, I describe the geological and meteorological context of Martinique, both at a regional and local scale. Then, I describe the methods and results of the main observations made in the field allowing to establish a new chronology of the eruptive history of Mount Pelée. This refined chronology highlights four newly discovered eruptions including four Plinian ones, and one Pelean event in the past 24,000 years, that we describe in detail in the following chapter.

2   Geological and meteorological setting

2.1   The Lesser Antilles arc

The active Lesser Antilles arc, composed of about twenty main islands and countless smaller islands, delimits the Caribbean sea to the west and the Atlantic ocean to the east (Figure 1a). Most of the islands result from the subduction of the Atlantic oceanic lithosphere under the Caribbean plate, which takes place in the Lesser Antilles subduction zone since the Eocene ($\approx$ 55 Ma) at a current rate of about $1.3 - 4$ cm/yr (Macdonald *et al.*, 2000). This rate is rather low compared to other subduction zones (e.g., 8.1 cm/yr in Java; Jarrard 1986) and results in low volcanic production rate ($\approx 3 - 5$ km^3 Ma^{-1} km^{-1} calculated by Wadge 1984) and low seismic activity. This $\approx$ 800 km-long volcanic arc, extending from St Martin to Grenada islands, is generally subdivided into three branches.

The older external arc (in orange in Figure 1a) has been active from the Eocene to the Oligocene (Westercamp & Tazieff, 1980; Bouysse *et al.*, 1990; Macdonald *et al.*, 2000) leading to the formation of (from South to North) Grenada, Grenadines, St Lucia, Martinique, Amerique and Dien Bien Phu banks, Marie Galante, La Desirade, Grande-Terre (of Guadeloupe), Bertrand and Falmouth banks, Antigua, Animals banks, Barbuda, St Bartholomew, St Martin, Anguilla, Dog and Sombrero islands. The islands cited here and located to the north of Martinique are now partially or totally overlain by/composed of carbonate deposits, which make them the "Limestone Caribbees" (Bouysse *et al.*, 1990). The submarine banks can all be described as "guyots" (isolated underwater volcanic edifices with a flat top) now overlain by sediments (Bouysse & Martin, 1979; Bouysse & Guennoc, 1983).

The most recent internal arc (in red in Figure 1a) is not older than 7.7 Ma (Briden *et al.*,
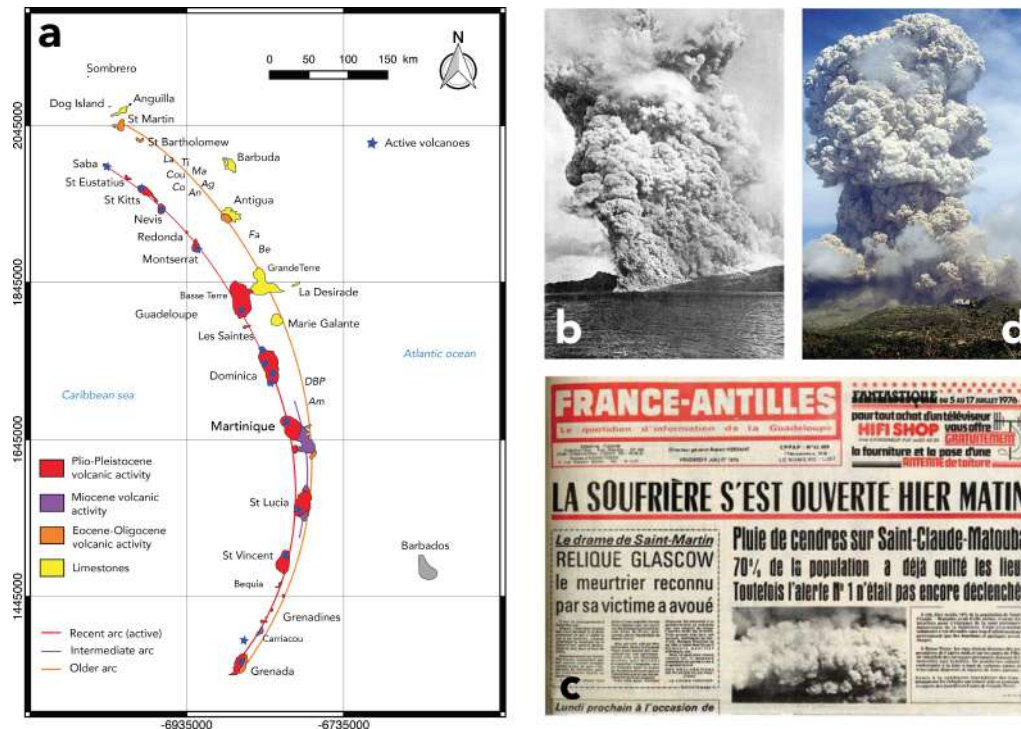
Figure 1: a Lesser Antilles volcanic arcs, *modified from Bouysse & Garrabé 1984*. Animal banks: Anoli (An), Agouti (Ag), Lambi (La), Coulirou (Cou), Titiri (Ti), Manicou (Ma), Colibri (Co); Falmouth bank (Fa), Bertrand bank (Be), Dien Ben Phu bank (DBP), Amerique bank (Am). All maps were generated using the open source QGIS software. Coordinates are in WGS 84 − UTM Zone 20 system. **b** "Nuée ardente" reaching the sea during the 1902 eruption of Mount Pelée volcano (Lacroix, 1904), **c** Newspaper cut (France Antilles) during the Soufrière (Guadeloupe) crisis in 1976, **d** Ash plume during the 1995 Soufriere Hills eruption in Montserrat, *photo by B. Voight.*

1979) and formed to the west of the ancient arc. The volcanic activity associated with this stage led to the formation of (from South to North) Grenada, Grenadines, St Vincent, St Lucia, Martinique, Dominica, Les Saintes, Basse-Terre (of Guadeloupe), Montserrat, Redonda, Nevis, St Kitts, St Eustatius and Saba (Bouysse *et al.*, 1990). The northern termination of this arc, extinct since the late Pliocene, corresponds to a 110-km long submarine segment including Luymes bank and Noroit seamount (Bouysse *et al.*, 1990).

The westward shift of the volcanic activity that occurred at the Miocene was interpreted by Bouysse & Westercamp (1990) as a consequence of the subduction of an aseismic ridge that locked both the Atlantic lithosphere subduction and part of the arc volcanism for a while, before the ridge was trapped underneath the Caribbean lithosphere. This geodynamical phenomenon marks the transition between the so-called "ancient arc" and "recent arc", the "intermediate arc" (in purple in Figure 1a) defining the volcanism that took place during the aseismic ridge subduction. The volcanic activity indeed pursued in Martinique, St Lucia and Carriacou (Grenada) during this stage (Westercamp & Tazieff, 1980). The location of Martinique island at the southern tip of the separation between the two main branches thus makes it a key location for the geodynamical study of this region as both the ancient and recent arc products are present on this island (Germa, 2008).

At least thirty volcanoes were active during the last 100 ka (Macdonald *et al.*, 2000). From South to North, some of these active volcanoes (represented by blue stars in Figure 1a) are: Mount Sainte Catherine (Grenada), Kick'em Jenny (Grenada), Soufriere (St Vincent), Soufriere (St Lucia), Mount Pelée (Martinique), Desolation Valley (Dominica), La Soufrière

(Guadeloupe), Soufriere Hills (Montserrat), Nevis Peak (Nevis), Mount Misery (St Kitt) and Mount Scenery (Saba) (Lindsay *et al.*, 2005). During the twentieth century, five of these volcanoes have erupted and produced rather minor explosive eruptions that however caused important damages and casualties: the Mount Pelée (1902−1905 and 1929−1932; Figure 1b), the Soufrière in Guadeloupe (1956, 1976−1977; Figure 1c), the Soufriere Hills in Montserrat (1933−1937, 1966−1967, 1996−1997, and 2010; Figure 1d) and the Kick'em Jenny (discovered in 1939 and which erupted in 1939, 1943, 1953, 1965, 1966, 1972, 1974, 1977, 1988, 1990 and 2015). A large number of explosive eruptions have occurred as recorded in the deposits on all these islands (Lindsay *et al.*, 2005). The strongest eruption recorded in the Lesser Antilles remains the Roseau event (Dominica) dated at 30,000 yr BP and estimated to be the only VEI 6 event in this region. The low eruptive frequency of these volcanoes makes them all the more dangerous as it gives time to the inhabitants to forget about the volcanic hazards that put them at risk.

2.2 Volcanic activity in Martinique

The island of Martinique has almost recorded the entire history of the Lesser Antilles from the Oligocene to the current time since the volcanic activity was continuous even during the intermediate arc formation (see Section 2.1). The geological map, published by Westercamp *et al.* (1990), gathers most of the geological, volcanological and geochemical results obtained by Grunevald (1965); Westercamp (1972); Andreieff *et al.* (1976); Nagle *et al.* (1976); Briden *et al.* (1979) and Westercamp & Andreieff (1983). In a simplified version of this map, given in Figure 2, we compiled this general information with the recent datations using K-Ar determinations on groundmass and plagioclase separates (Cassignol-Gillot technique) performed by Germa *et al.* (2011*a*,*b*), giving a whole picture of the volcanic activity of the island.

In Martinique, an effusive volcanic activity started about 24 Ma ago while the ancient arc of the Lesser Antilles was still active, and built up the east and southeast parts of the island (stage 1 in Figure 2), at the current locations of La Caravelle and Sainte-Anne peninsulas, respectively (Grunevald, 1965; Westercamp, 1972; Westercamp & Tazieff, 1980; Andreieff *et al.*, 1988; Westercamp *et al.*, 1990). K-Ar age determinations conducted on eight samples (basaltic-andesites to andesites) by Germa *et al.* (2011*a*) yield an age of about 24.8 ± 0.4 − 20.8 ± 0.4 Ma for these old arc lavas suggesting that the volcanic activity in Martinique was most probably continuous throughout this period with a peak activity around 23 Ma.

The active volcanic center then migrated slightly westwards and marked the beginning of the intermediate arc. NW-trending dikes emitting lava flows and hyaloclastites (with tholeiitic basalt to dacite compositions) developed on the western side of the ancient arc and built the NW-SE oriented Vauclin-Pitault submarine chain (stage 2 in Figure 2). This activity was probably alternating between high activity and background-level eruptive activity (Andreieff *et al.*, 1988; Westercamp *et al.*, 1989) before the volcanism became sub-aerial/aerial around 9 Ma (Labanieh, 2009). Germa *et al.* (2011*a*) obtained an age ranging from 16.1 ± 0.2 to 8.44 ± 0.12 Ma for this stage based on nine samples, showing an apparent gap in volcanism of about 4 Ma between the old arc end-of-activity and the beginning of the intermediate arc. Then, the aerial effusive Southwestern volcanism began and built the Trois Ilets peninsula, through the construction of the Morne Pavillon edifice, Gros Ilet lava dome and La Vatable lava flow (Westercamp *et al.* 1989, stage 3 in Figure 2). Three new datations on samples from these three structures (with a main andesitic composition to some exceptional garnet-bearing dacite composition) yield an age ranging from 9.18 ± 0.13 to 7.1 ± 0.1 Ma (Germa *et al.*, 2011*a*) for this stage 3. The intermediate arc was thus
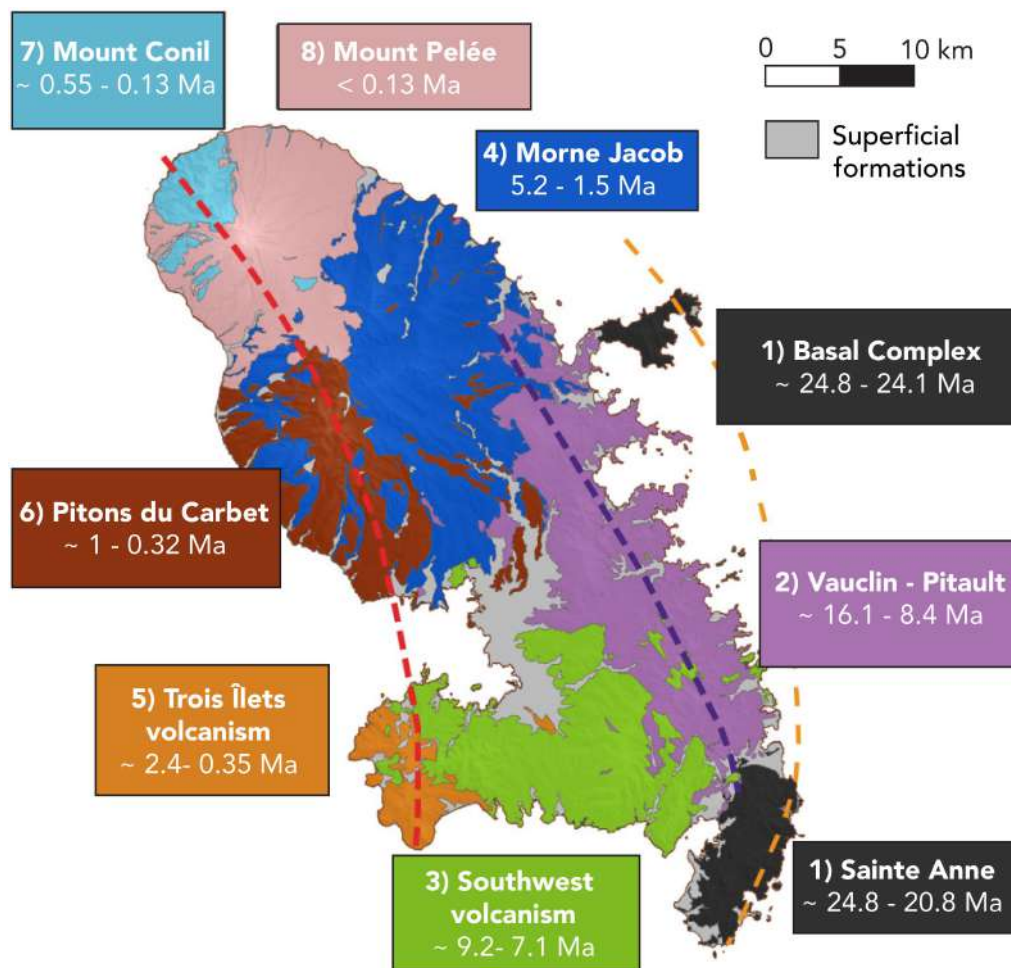
Figure 2: The different volcanic stages in Martinique (modified from the geological map of Westercamp *et al.* 1990) associated with their ages (Germa *et al.*, 2011*a*,*b*). The dashed lines represent the ancient (in orange), intermediate (in purple) and recent (in red) arcs.

active between 16 and 7 Ma, with an apparent peak activity around 12 Ma, a period during which the volcanic front migrated about 10 km westward from the ancient arc with a mean migration rate of 1.1 km/Myr (Germa *et al.*, 2011*a*). This rate is consistent with the rate of 1 km/Myr proposed by Wadge (1986) for the entire Lesser Antilles arc.

After a gap of about 1.6 Ma, the recent arc started to be active around 5.5 Ma with the construction of the sub-aerial Morne Jacob shield volcano 25 km to the north of the island (Westercamp *et al.* 1989, stage 4 in Figure 2). Lavas from this volcano are basaltic andesites to dacites and a dataset of twenty K-Ar datations yield a time range of activity of 5.14 ± 0.07 to 1.53 ± 0.03 Ma for this volcano (Germa *et al.*, 2010). The total volume emitted above the sea level during this stage was estimated to be 145 ± 32 km^3, meaning a time-averaged sub-aerial effusion rate of 0.04 ± 0.008 km^3/kyr (Germa *et al.*, 2010). The 14-km distance westward migration rate from the intermediate arc to the recent one is estimated to be 1.4 km/Myr, a value consistent with the subduction process (Germa *et al.*, 2011*a*). During the Morne Jacob last stage of activity, the Trois Ilets volcanism initiated in the southwest of the island completing the Trois Ilets peninsula (Westercamp *et al.* 1989, stage 5 in Figure 2). Its aerial eruptive activity alternated mainly between effusive and extrusive episodes (with short explosive episodes of low intensity) with compositions ranging from basaltic-andesite to dacite, and built several edifices from the Diamond islet in the south to

the Galocha pyroclastic flow in the north of the peninsula (Westercamp *et al.*, 1989; Germa *et al.*, 2011*b*). Five K-Ar datations yield an age of 2.358 ± 0.034 to 0.346 ± 0.027 Ma for this stage.

Simultaneously, the more explosive Carbet activity began north of the Trois Ilets peninsula, on the western flank of Morne Jacob volcano, and built first an old andesitic edifice around 1 Ma (Germa *et al.*, 2011*b*). Then, a flank collapse of about 30-40 km^3 (Boudon *et al.*, 2007) occurred at 337 ± 5 ka (Samper *et al.*, 2008), leaving a horseshoe-shaped structure opened to the west and characterized by massive debris avalanche deposits. Finally, the Pitons du Carbet, a group of seven voluminous lava domes plus five isolated smaller ones with an andesitic to dacitic compositions, were built inside the horseshoe structure produced by the flank collapse. Amongst those lava domes, five are still more than 1,000 meters-high. Five K-Ar datations yield an age of 998 ± 14 ka for the oldest stage (Morne Césaire) and 322 ± 6 ka for the youngest one (Plateau Courbaril, Pitons du Carbet s.s.) (Germa *et al.*, 2011*b*).

The active volcanic center then moved to the northern end of the island where it built the Mount Conil (Germa *et al.*, 2015), whose activity was also contemporary with the Trois Ilets and Carbet volcanisms and characterized by the formation of andesitic breccias, lava domes and lava flows. The beginning of Mount Conil activity was dated to 543 ± 8 ka, and was probably associated to subaerial lava flows and lava domes that built a cone-shape edifice, and then to lava domes and flows only until 189 ± 3 ka (Germa *et al.*, 2011*b*). Between this date and 127 ± 2 ka, a new cone was built on the southern flank of the first one, before a voluminous flank collapse destroyed the southwestern flank of the volcano (Le Prêcheur event). This collapse produced a 25 km^3 debris avalanche that reached the Caribbean Sea (Le Friant *et al.*, 2003; Germa *et al.*, 2011*b*; Boudon *et al.*, 2013; Germa *et al.*, 2015; Brunet *et al.*, 2016).

The Mount Pelée has been the only active volcano in Martinique for the last 127 ka (Boudon *et al.*, 2005; Germa *et al.*, 2015). The preserved northern rim of the flank-collapse structure formed a curved scarp in which the Paleo-Pelée cone (Vincent *et al.*, 1989) grew up during the 127-25 ka building stage (Le Friant *et al.*, 2003; Boudon *et al.*, 2005; Germa *et al.*, 2011*b*). Two flank collapses occurred during this time period: the St. Pierre event (between 127 and 45 ka, Brunet *et al.* 2017) destroyed the southwestern flank of the cone and produced a 13 km^3 debris avalanche into the Caribbean Sea (Le Friant *et al.*, 2015), before a third flank collapse (the Rivière Sèche event, Le Friant *et al.* 2003) happened. This last flank collapse, originally dated at 9 ka, occurred between 45-30 ka and produced a 1.8 km^3 debris avalanche into the Caribbean sea (Le Friant *et al.*, 2003; Le Friant *et al.*, 2015; Brunet *et al.*, 2017). During the St. Vincent period going from 27 to 19.5 ka (Traineau *et al.*, 1983), a new cone was built inside the horseshoe-shaped structure newly formed by the successive flank collapses. This activity was characterized by a series of open-vent eruptions producing scoria flows (Traineau *et al.*, 1983; Boudon, 1993), followed by a succession of Plinian and sub-Plinian events including the major eruptions SV1 and SV2, respectively dated at ≈ 25 and 22 ka (Traineau *et al.*, 1983). The volcano remained silent for at least 6 ka until the present stage of volcanic activity started at 13.5 ka. This "neo-Pelée" period is characterized by a series of successive dome-forming Pelean and open-vent Plinian eruptions (Roobol & Smith, 1976; Westercamp & Traineau, 1983; Vincent *et al.*, 1989; Boudon *et al.*, 2005). Such an alternation of eruptive style is commonly observed in the Lesser Antilles arc, as inferred from the analysis of past eruption deposits (Roobol & Smith, 1980, 2004; Lindsay *et al.*, 2005). In the following section, we describe more precisely the eruptive record of the neo-Pelée period.

2.3 Mount Pelée volcano

Mount Pelée (1,397 m *a.s.l.*) is a composite andesitic volcano almost entirely composed of pyroclastic deposits produced by two eruptive styles: Pelean (dome-forming eruptions), and Plinian (open-vent eruptions producing a sustained eruptive column) (Figure 3).

The recent eruptive history of Mount Pelée is well-documented thanks to several field-based studies (Roobol & Smith, 1976, 1980; Fisher *et al.*, 1980; Westercamp & Traineau, 1983; Bardintzeff *et al.*, 1989; Lajoie & Boudon, 1989; Bourdier *et al.*, 1989; Lajoie *et al.*, 1989; Traineau *et al.*, 1989; Boudon *et al.*, 2005; Carazzo *et al.*, 2012; Wright *et al.*, 2016; Carazzo *et al.*, 2019, 2020). On-land stratigraphic studies and measurements of ^{14}C indicate that at least 28 magmatic eruptions occurred during the last 13,500 years (Westercamp & Traineau, 1983; Boudon *et al.*, 2005), including the 1929-1932 Pelean eruption (Perret, 1937), the 1902-1904 Pelean (Lacroix, 1904; Fisher *et al.*, 1980; Lajoie & Boudon, 1989; Lajoie *et al.*, 1989), the 650 BP P1 Plinian (Westercamp & Traineau, 1983; Bardintzeff *et al.*, 1989; Traineau *et al.*, 1989; Carazzo *et al.*, 2012), the 1,670 BP P2 Plinian (Traineau *et al.*, 1989; Carazzo *et al.*, 2019), and the 2,010 BP P3 Plinian events (Westercamp & Traineau, 1983; Traineau *et al.*, 1989; Wright *et al.*, 2016; Carazzo *et al.*, 2020). At least ten Plinian eruptions occurred over the last 13.5 ka according to stratigraphic studies (Roobol & Smith, 1976; Traineau, 1982). Due to the lack of previous carbon-dating measurements in the literature, and because of the difficulty to recognize deposits that can be very similar to each other in an area often covered with vegetation, the most ancient Plinian eruptions remain poorly documented and/or require some revision.

During the past 5 ka, at least six Plinian eruptions (namely P1 to P6, from the most recent to the older one) and nine dome-forming eruptions occurred in Martinique (Westercamp & Traineau, 1983; Traineau *et al.*, 1989; Carazzo *et al.*, 2012). We detail here the powerful Plinian eruptions, which are characterized by the formation of a volcanic column that potentially collapsed at some stage during the course of the eruption. For details about the dome-forming eruptions, we refer to Westercamp & Traineau (1983).

The P1 eruption, dated at 650 ± 50 BP (Westercamp & Traineau, 1983; Traineau *et al.*, 1989), began with a dome-forming stage (Villemant & Boudon, 1999). The eruption then evolved towards a Plinian phase with the formation of a 19-22 km-high column that spread volcanic tephra over the southwestern flank of the volcano. After a phase of partial collapse, a total column collapse on ground occurred and formed a 1.3 km-high fountain with associated pyroclastic density currents (PDC) (Carazzo *et al.*, 2012).

The P2 eruption occurred at 1,670 ± 40 BP (Westercamp & Traineau, 1983) and started with a violent lateral blast directed to the northeast of the volcano. Shortly afterwards, an unstable Plinian column rose up to 23-26 km in the atmosphere, covering the northeastern slopes of Mount Pelée volcano with pumice fall deposits interbedded with low-concentration PDC deposits. Finally, the column collapsed and produced dense PDC feeding east and southwestern valleys (Carazzo *et al.*, 2019).

The P3 eruption, dated at 2,010 ± 140 BP, is probably the most powerful event at Mount Pelée volcano over the last 5 ka (Westercamp & Traineau, 1983; Traineau *et al.*, 1989; Carazzo *et al.*, 2020). The eruptive episode was originally divided into three events based on field observations, namely P3-1, P3-2 and P3-3 (Roobol & Smith, 1980; Westercamp & Traineau, 1983). Traineau *et al.* (1989) later reduced the P3 eruptive sequence to the P3-1 and P3-3 units only. Indeed, further fieldwork performed by the same authors led them to conclude that the P3-2 deposits were older than 2,010 BP, hence that the isopach map of P3-2 drawn by Westercamp & Traineau (1983) had to be revised (see Chapter 2, Michaud-
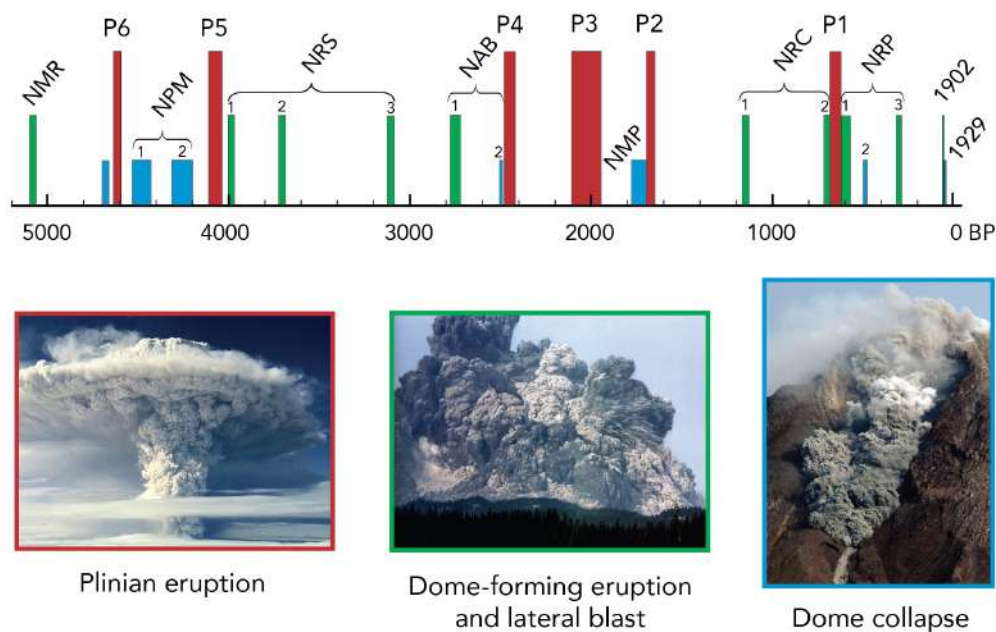
Figure 3: Eruptive history of Mount Pelée volcano for the past 5,000 years. For each eruption, the width of the bar corresponds to the uncertainty in eruption age, while the height and color indicate the eruption style (long red: Plinian, short blue: dome collapse, intermediate green: directed blast). The eruption names are as follows: *NMR*, Nuées ardentes Morne Rouge; *NPM*, Nuées ardentes Pointe la Mare; *NRS*, Nuées ardentes Rivière sèche; *NAB*, Nuées ardentes Ajoupa Bouillon; *NMP*, Nuées ardentes Morne Ponce; *NRC*, Nuées ardentes Rivière Claire; *NRP*, Nuées ardentes Rivière des Pères; *P*, Plinian. *Modified from Westercamp & Traineau (1983)*.

Dubuy *et al.* 2019). Eruptive parameters were unknown for the P3 eruption before our own measurements suggested that the Plinian column reached 28-30 km into the atmosphere and spread volcanic ash over the western slopes of the volcano during the P3-1 phase (Carazzo *et al.*, 2020). The eruption then evolved towards a more unstable regime with the formation of a column partially collapsing and generating PDC during the P3-3 phase (Carazzo *et al.*, 2020). The fall deposits can be found on both the western and eastern sides of the volcano whereas the PDC deposits are confined in western valleys (Westercamp & Traineau, 1983; Traineau *et al.*, 1989; Carazzo *et al.*, 2020).

The P4 eruption illustrates a different type of eruptive regime of the Mount Pelée volcano. This event is dated at 2,440 ± 50 BP, and is characterized by the formation of a small pyroclastic fountain. In this case, no sustained vertical eruptive column was produced and only PDC deposits can be found, filling several western valleys (Westercamp & Traineau, 1983).

The P5 eruption, 4,060 ± 90 BP, resembles the P1, P2 and P3 events. It started with a minor vent-opening phase covering the slopes of the volcano with a dark fine ash layer, and was immediately followed by a Plinian explosion leading to a uniform pumice fall deposit mostly to the east of the volcano. The volcanic column occasionally produced PDC feeding valleys on both the western and eastern flanks of the Mount Pelée (Westercamp & Traineau, 1983).

The P6 eruption, dated at 4,610 ± 50 BP, is similar to the P4 event, with the production of PDC first flowing eastward, and then feeding western valleys (Westercamp & Traineau, 1983), but no sustained Plinian column formed.

This recent Plinian eruptive history suggests that the Mount Pelée volcano reproduces

a rather similar scheme every time it erupts. A Plinian eruption usually starts with the formation of a volcanic plume causing ash falls, then the column eventually collapses producing PDC (P1, P2, P3, and P5 eruptions). Another type of eruptive regime is possible with the formation of a small fountain feeding PDC rushing down the volcano flanks (P4 and P6 eruptions). During the Plinian regime, the deposits can be spread in any direction, which highlights the importance of winds, a parameter of paramount importance when dealing with volcanic hazard assessment.

Our knowledge of the Plinian eruptions older than 5 ka (named P7 to P10) is currently very limited since only a few outcrops were identified and dated (Traineau, 1982), and thus further fieldwork is necessary to elaborate a full eruptive history.

2.4   Annual meteorological conditions over Martinique

Due to its central location in the Lesser Antilles arc, the island of Martinique (14°40" N, 61°00" W) is dominated by an oceanic tropical climate which can be splitted into two main seasons: the dry season (also named Lent season) extending from December to May, and the wet season extending from June to November during which the cyclonic hazard is higher (Figure 4). This dichotomy is directly caused by both the Azores high pressure zone (anticyclone) which controls the northeastern trade winds, and the equatorial low pressure zone called Intertropical Convergence Zone (ITCZ) where the northern hemisphere trade winds meet those of the southern hemisphere. During the dry season, the Azores anticyclone is shifted to the South, the pressure variations thus form regular easterly trade winds over Martinique scattering clouds and promoting a sunny and dry weather. During the wet season, the Azores anticyclone moves to the north, reducing the trade winds strength. The ITCZ comes closer to the Lesser Antilles yielding heavy rainfall over the island (Météo France, 2019).
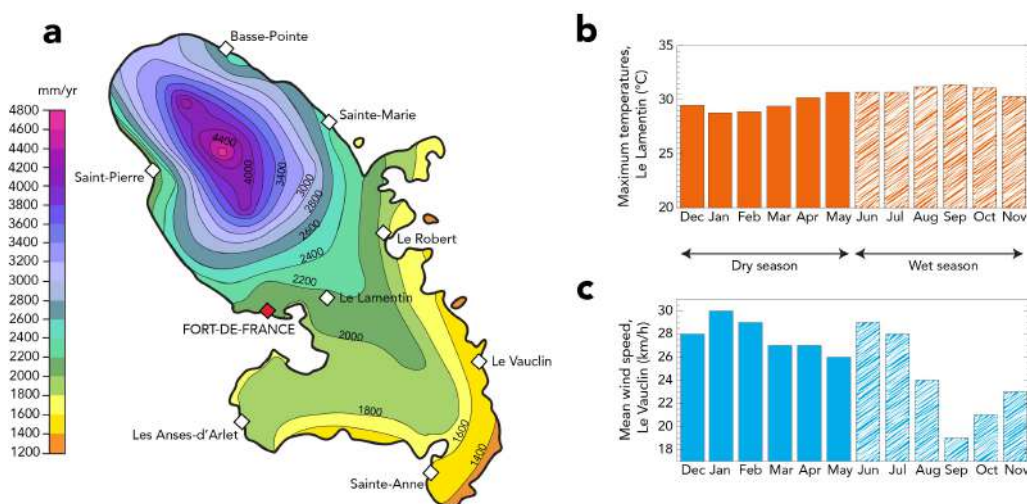
Figure 4: Overview of mean meteorological data in Martinique. **a** Mean rainfall during the 1981-2010 period (mm/yr), **b** mean surface temperatures measured at Le Lamentin (°C), **c** mean wind speed measured at the surface on the Atlantic coast (Le Vauclin) (km/h). *Data from Météo France.*

The island of Martinique is also subjected to strong local rainfall variations (Figure 4a). In the northern part of the island, the Atlantic coast and the hillsides exposed to easterly winds record the most important rainfall, while the northern Caribbean coast is protected by a mountainous topography ("Foehn" effect) and thus undergoes less rainfall and higher temperatures. In the southern part of Martinique, coastal edges are less subjected to rainfall,

but the temperatures remain higher on the Caribbean side than on the Atlantic one where stronger and more lasting winds occur. Throughout the island, the rainfall ranges from 2,000 mm/yr on the eastern coast to 1,400 mm/yr on the western coast, with a maximum value that can reach up to 10,000 mm/yr at the Mount Pelée summit.

The surface temperature is rather high and constant throughout the year in Martinique (Figure 4b), with a minimum reached both ashore and at sea in January-February and a maximum in September. The mean wind speed at the surface can however strongly vary (Figure 4c), with maximum values during the dry season influenced by strong E-NE trade winds, and minimum values during the wet season characterized by weaker E-SE trade winds.
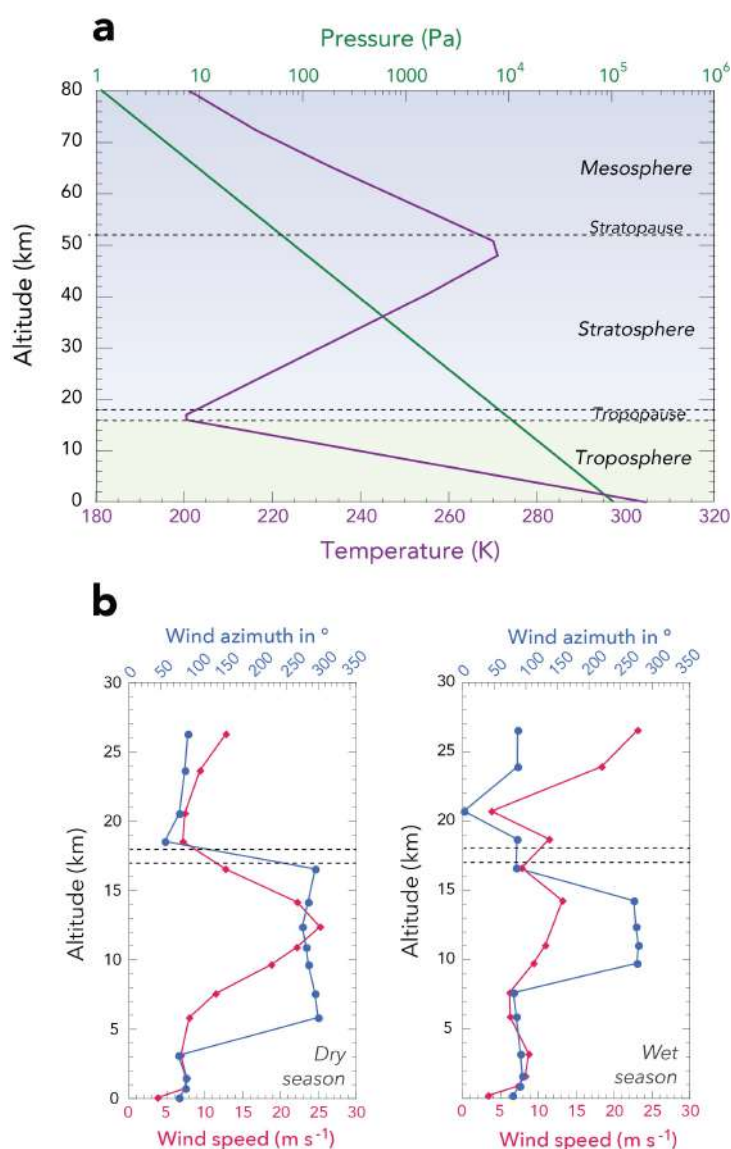
Figure 5: a Pressure (green) and temperature (purple) profiles in the atmosphere at tropical latitudes. The different layers of atmosphere are indicated, including the tropopause and stratopause (dotted lines), *modified from Carazzo* et al. *(2008)*. **b** Seasonal average wind speed (pink) and azimuth (blue) profiles for the dry (left) and wet (right) seasons based on monthly-averages of twice-daily radiosonde data for the Raizet (TFF5 98897) station from 1999 to 2005, *modified from Komorowski* et al. *(2008)*. The lower and upper boundaries of the tropopause are shown using dotted lines.

Figure 5a shows the variation of temperature (purple) and pressure (green) with the altitude at tropical latitudes (Carazzo *et al.*, 2008). This vertical thermal profile exhibits several layers in the atmosphere: the troposphere (about a dozen-kilometers thick), where most of the meteorological phenomena occur and characterized by a mean decrease of the temperature; the stratosphere (from $\approx$ 11 to 50 km-high), where the temperature strongly increases; the mesosphere (from 50 to 80 km-high), characterized by a rapid decrease of the temperature; and beyond 85 km high, the thermosphere where the temperature increases again (not shown in Figure 5a). Most of the volcanological phenomena occur in the troposphere and the stratosphere. The boundary between these two lowest layers of the atmosphere is called the tropopause whose altitude varies with the latitude: around 16-18 km-high in tropical regions, at 11 km-high at mid-latitudes, and even lower in polar regions (about 6 to 8 km-high). Woods (1995) demonstrated that the tropopause altitude has a strong effect of the volcanic plume maximum height. This effect can be explained by both the thermal gradient inversion, and abrupt changes in wind speed and direction at this altitude level.

Figure 5b shows the averaged wind speed (pink) and azimuth (blue) profiles in the atmosphere for both the dry (left) and wet (right) season (Komorowski *et al.*, 2008). As mentionned above, the tropical Caribbean climate is characterized by a strong influence of the northern hemisphere trade winds that blow from the east to the west in the low to mid-troposphere (up to $\approx$ 5 km-high during the dry season, and to $\approx$ 7 km-high during the wet season, Figure 5b). In the upper troposphere (between 7 and 18 km-high), the wind field is mostly characterized by westerlies (blowing from the west to the east) counter-trade winds of higher mean velocity compared to the trade winds (especially during the dry season). Beyond the tropopause, the stratospheric winds blow from the east to the west with a rather low speed during the dry season, while they have stronger variations both in speed and azimuth during the wet season. This high seasonal variability of winds has often a strong impact on tephra dispersal during an eruptive event (Chapters 5 and 6), as any sufficiently high volcanic column is affected by winds (Komorowski *et al.*, 2008).

The cyclonic season takes place in the Lesser Antilles during the wet season, mostly from August to October. In this region, a "cyclone" can either describe a tropical depression (mean wind speed < 63 km/h), a tropical storm (mean wind speed between 63 and 117 km/h), or a hurricane (mean wind speed > 117 km/h) (Météo France, 2019). These strong depression systems are related to eastern waves that form in northern Africa and then move in less than 3 or 5 days across the Atlantic ocean towards the Lesser Antilles. Since the 1980's, about twelve hurricanes form in the northern Atlantic ocean every year. In the last 50 years, twelve hurricanes and several tropical storms passed within less than 250 km from Martinique. Some of these events have caused important casualties on the island: a total of 60 people died during the hurricanes Dorothy in 1970, Allen in 1980, Klaus in 1990 and Emily in 2011. The hurricanes Dean in 2007 and Maria in 2017 resulted in severe damages on the crops and important economic losses. We will discuss the importance of these extreme meteorological events on tephra dispersal and hazard assessment in Chapter 5.

3 Methodology

3.1 Fieldwork

We identified pumice fallout deposits at 39 locations during two new extensive field studies performed in 2017 and 2019 in Martinique. Adding these 39 outcrops to the ones identified
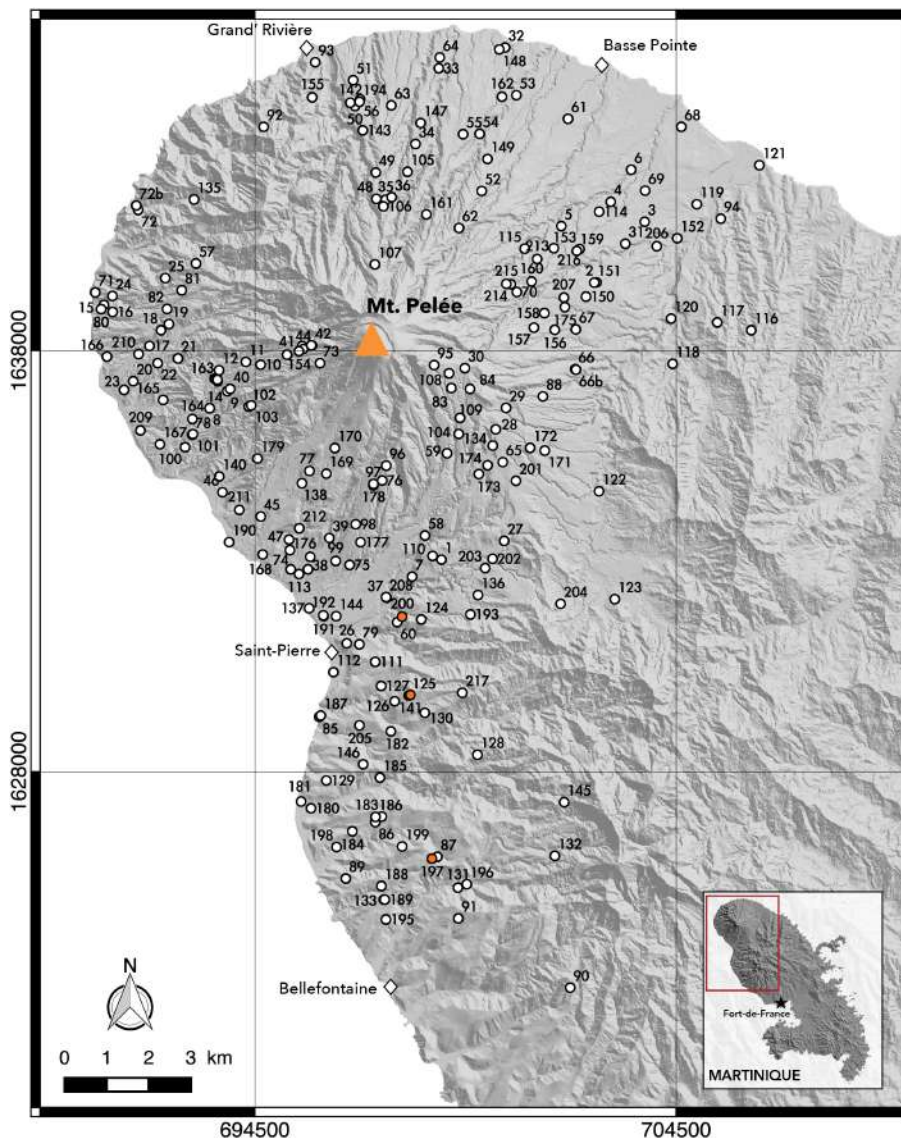
Figure 6: Overview of Martinique (inset). Numbers refer to studied outcrops where Plinian deposits from Mount Pelée are present. The orange triangle shows the location of the Mount Pelée summit. The orange outcrops are those discussed in Section 4.

during previous field campaigns by IPGP (Carazzo *et al.*, 2012, 2019, 2020), our complete field database now includes 217 locations (and about 1,000 depositional units) distributed all around the volcano except to the northwest where exposure is very limited due to dense tropical forest and difficult conditions of access (Figure 6).

At most outcrops, several deposits from different pumiceous eruptions were visible at the same location. These deposits are generally composed of coarse lapilli- to fine ash-sized pumices (porous volcanic rocks corresponding to viscous magma fragments expelled during an explosive eruption), lithic fragments (denser rocks coming from the erosion of the volcanic conduit during the eruption), and isolated crystals (Figure 7a). Deposits from two different eruptions are commonly separated by a dark or light brown palaeosol and exhibit an erosion surface at the top of the lower eruptive unit. An *eruptive sequence* is composed of several stages of the same eruption that we studied at several outcrops because the entire eruptive sequence is not always visible at a single location. As an example, deposits from

pyroclastic density currents are generally localized into valleys, while pumice fallout deposits from stable plumes are mostly distributed along a dispersal axis whose orientation depends on the wind blowing during the eruption.
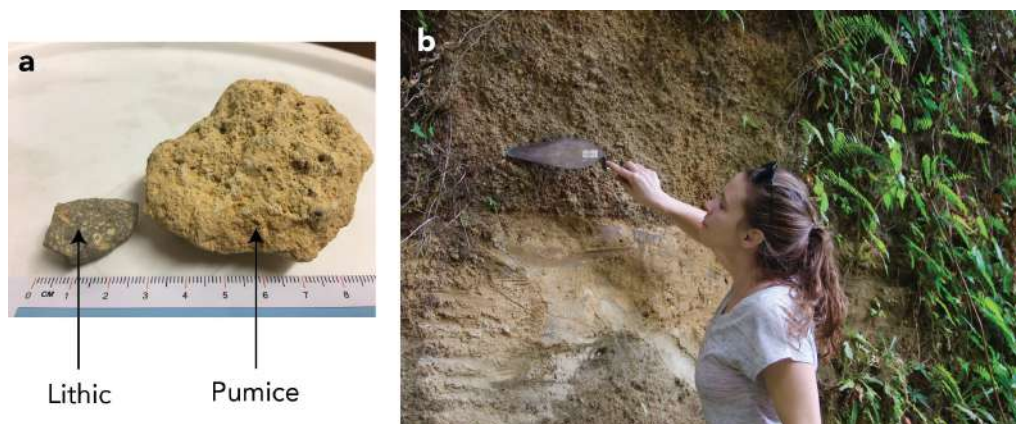
Figure 7: a Photograph of a lithic and a pumice, typical rocks found in Plinian deposits. **b** In the field, beginning to search for the five largest lithic fragments within the pumice fallout unit.

At every location, we first cleared the outcrop in order to take pictures. We then described every unit in terms of framework, fabric, grain-type and size characteristics, and measured the thickness of each layer of the sequence as well as the major axes of the five largest lithic fragments found in the deposits (Figure 7b). These measurements were made in order to later construct isopach and isopleth maps, which provide constraints on the volume of the deposits, the average column heights and exit velocities (see Section 3.4). Finally, when possible, we sampled palaeosols between eruptive units and/or charcoals within the pumice fallout deposits in order to refine the age of each eruptive sequence (Section 3.2), as well as bulk deposits in order to perform grain-size analyses in the laboratory (Section 3.3).

3.2 Radiocarbon dating

Nine palaeosol samples were used to provide new carbon-dating measurements for five eruptions. Ages were determined using an accelerator mass spectrometry at the LMC14 (Artemis, Laboratoire de Mesure du Carbone 14, CEA Saclay, France), and calibrated using the free software OxCal 4.3 (Bronk Ramsey, 2009) with the atmospheric IntCal13 calibration curve commonly used for the Northern hemisphere (Figure 8; Reimer 2013). The uncalibrated ages obtained for our stratigraphically-constrained samples were combined with those (when existing) of Traineau (1982) and Westercamp & Traineau (1983), and validated using the R_combine function of OxCal and χ^2 test prior to calibration (Ward & Wilson, 1978).

3.3 Grain-size analyses

The total grain-size distribution (TGSD) gives the mass percentage of the different particle classes at the source. It is an essential input for models of tephra transport and dispersion in the rising volcanic plume (see Chapter 3 and Michaud-Dubuy *et al.* 2018) and the spreading umbrella cloud (see Chapter 5 and Michaud-Dubuy *et al.* 2019). The TGSD of a given unit is calculated from the grain-size distribution of each individual sample collected in the field for this unit. The results are given in Chapter 2.
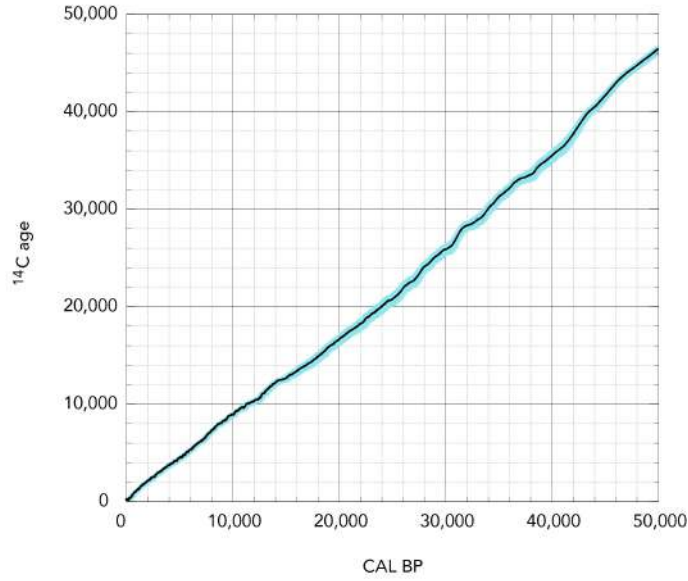
Figure 8: IntCal13 Northern Hemisphere atmospheric radiocarbon calibration curve (black line), modified from Reimer (2013). Uncertainties in the data are given by the blue envelope.

Fifty-eight samples from selected locations of eight eruptions were dried for 24h in an oven before being sieved by hand down to 6ϕ[1]. The crystals and lithic fragments were separated from pumices by hand in the size range -5ϕ (32 mm) to -2ϕ (4 mm). Laser diffraction data are not available for the smallest particles. Several techniques can be used to determine the TGSD of a tephra fall deposit, including weighting the individual analysis according to isopach mass (Rose & Durant, 2009), dividing the tephra fall deposit to calculate sectoral GSD (Carey & Sigurdsson, 1982), or using the Voronoi Tessellation statistical method (Bonadonna & Houghton, 2005). Here, we use volume calculations for isomass maps for each ϕ interval to determine the grain-size distributions of single sublayers. We calculated the cumulative frequency curves using the method of Kaminski & Jaupart (1998), which accounts for the power-law size distribution of the rock fragments (Hartmann, 1969; Turcotte, 1986; Alibidirov & Dingwell, 1996; Kueppers $et\ al.$, 2006):

$$N(R_p{\geq}r_p) = \lambda r_p^{-D}, \tag{1}$$

where $N(R_p{\geq}r_p)$ is the number of particles with a radius larger than or equal to r_p, λ is a normalization constant and D is the power-law exponent. This exponent fully characterizes the grain-size distribution of both fall and PDC deposits and generally ranges between 2.9 and 3.9 (Kaminski & Jaupart, 1998). The value of D quantifies the fraction of coarse ($D<3$, poorly efficient fragmentation), or fine ($D>3$, efficient fragmentation) particles in the deposit, hence reflects the fragmentation efficiency. Kaminski & Jaupart (1998) showed that D controls the total amount of gas available in the turbulent flow. It thus affects the maximum column height of sustained Plinian columns (Girault $et\ al.$, 2014) and collapsing fountains (see Chapter 3 and Michaud-Dubuy $et\ al.$ 2018). This parameter is thus important to characterize the eruption dynamics. Kaminski & Jaupart (1998) have shown that the exponent D can be accurately retrieved from field deposits by using any sufficiently large range of sizes because it would take gross changes/errors in the sieve data outside this range to affect its value. Thus, the lack of fine-grained particles lost at sea, or the uncertainties

---

[1]ϕ is a particle size notation with d_ϕ (mm) $= 2^{-\phi}$

in sieving analyses do not affect its estimation.

The total grain-size distribution of Plinian deposits is calculated here using the method of Kaminski & Jaupart (1998). We evaluated the total mass in sieve class ϕ, M_ϕ, by the volume integral:

$$M_\phi = \int_0^L h(l)C_\phi(l)A(l)\mathrm{d}l, \tag{2}$$

where $h(l)$ is the deposit thickness, $C_\phi(l)$ is the concentration of class ϕ at distance l from the vent, $A(l)\mathrm{d}l$ is the area bounded by isopachs at distances l and $l + \mathrm{d}l$, and L is the distance where h or C_ϕ drop to zero. We used linear interpolations for h and C_ϕ between localities.

3.4 Eruptive parameters

We retrieved the eruptive parameters of the newly identified eruptions from the field data using physical models of volcanic plumes. These eruptive parameters define an "identity card" of each eruption, containing the estimations of all the relevant data for risk management: the minimum erupted volume, the maximum height reached by the volcanic plume, the peak mass discharge rate (MDR) and the minimum duration of the eruption (Figure 9). The results are given in Chapter 2, and we detail here the reconstruction techniques.
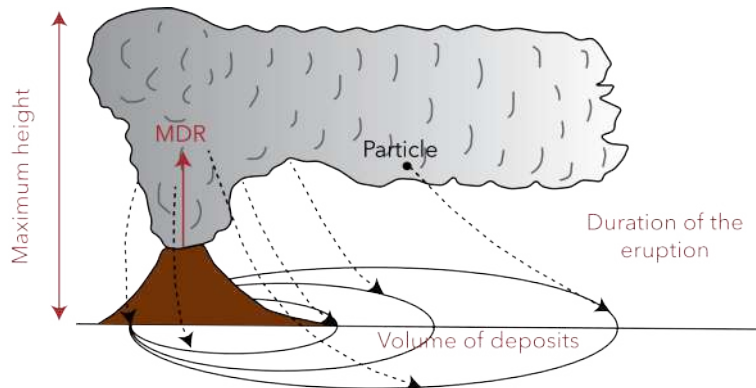
Figure 9: Eruptive parameters of a Plinian eruption estimated from physical models of volcanic plumes and data collected in the field: minimum erupted volume (in km^3), plume maximum height (in km), mass discharge rate (MDR, in $\mathrm{kg\,s^{-1}}$) and duration of the eruption (in h).

In Martinique, as in other tropical islands of small dimensions and subject to intense weathering, only proximal (and incompletely preserved) deposits are available, much being lost at sea. The volume calculations are thus bound to provide minimum estimates only. We inferred the volume of tephra fallout produced during an explosive eruption by using several methods based on the thinning trend of the deposit with distance from the source. We generated deposit thinning profiles from the isopach maps inferred from field data, and approximated them by exponential (Pyle, 1989), power-law (Bonadonna & Houghton, 2005) and Weibull (Bonadonna & Costa, 2012) fits computed using the AshCalc software (Daggit et al., 2014). From the final estimate of the minimum total volume, we estimated the total mass of tephra emitted during the eruption, the magnitude (Pyle, 2000) and the VEI (Newhall & Self, 1982) of the event.

We estimated the maximum column heights associated with the air fall deposits from the distribution of lithic fragments on our isopleth maps, using the model of Carey & Sparks

(1986) adapted to tropical atmospheric conditions in Central America (Carey & Sigurdsson, 1986). This model uses three isopleths (8, 16 and 32 mm) and their crosswind ranges to yield a maximum height and associated error bars (Figure 10). This method is independent of the wind speed as it uses crosswind ranges to estimate the maximum height. The alternative method of Bonadonna & Costa (2013) based on variations of lithic size with the distance from the source was also used to reinforce the confidence in the estimates. We also used these data to estimate the minimum exit velocity V of the volcanic plume at the vent. Extrapolating the exponential fit, we calculated a maximum lithic size at the vent. We then calculated the minimum velocity required to carry up this fragment up in the vertical plume, using (Bonadonna et al., 1998):

$$V \approx \sqrt{\frac{3.1 g \rho_p d_p}{\rho_a}}, \tag{3}$$

with $\rho_a = P/RT$, where P is the atmospheric pressure (Pa), R is the bulk constant of the column ($\mathrm{J\,K^{-1}\,kg^{-1}}$), and T is the magma temperature (K). ρ_p and d_p are the density and diameter of the maximum lithic clast, respectively.
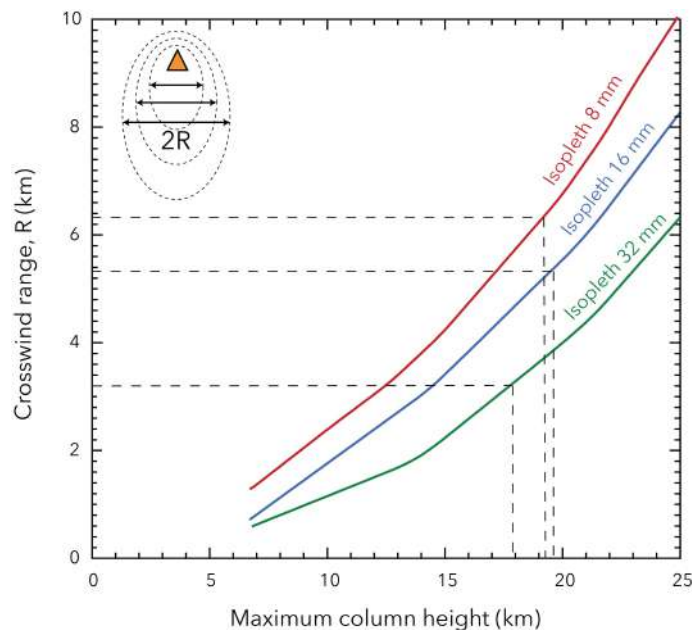
Figure 10: Crosswind range as a function of the maximum column height for three isopleths: lithics of 8 mm (red curve), 16 mm (blue curve) and 32 mm (green curve), *modified from Carey & Sigurdsson (1986)*.

We calculated the mass discharge rate (MDR) feeding the plume produced by the eruption based on the maximum height. We discarded the simplified formula linking the two parameters given by Carey & Sigurdsson (1986) in favor of the more recent empirical relationships from Carazzo et al. (2014) and Woodhouse et al. (2016), together with the model predictions of Girault et al. (2016) explicitly including the effect of TGSD on the plume dynamics (see Table 2 of Costa et al. 2016 for calculation details). Calculations were made for tropical atmospheric conditions. Finally, combining the MDR with the total mass of fallout deposits, we estimated a minimum duration for each eruptive event. Error bars on all eruptive parameters are calculated using error propagation.

4   Results

In this section, we present three key stratigraphic sections where the deposits of past eruptions of Mt Pelée volcano are clearly visible underneath those of the most recent eruptions (Section 4.1). We estimate the ages of these deposits based on new carbon-dating measurements (Section 4.2), and we discuss our results in the light of the current knowledge of the eruptive histoy of Mt Pelée volcano (Section 4.3). The three sections are presented from the closest to the farthest to the Mount Pelée summit (with a N-S axis).

4.1   Stratigraphic sections

4.1.1   The Mont Parnasse section

The Mont Parnasse section (outcrop 200 in Figure 6) is located at ≈ 6.5 km from the volcano summit, on the road D11 between St Pierre and Morne Étoile. Six units separated by brown soils can be distinguished on this outcrop (Figure 11a and b), which we describe from base to top.

Unit 0: The basal unit is a 60 cm-thick dark brown very poorly-sorted block-and-ash flow deposit containing bombs up to 150 mm made of porphyrite andesite. This deposit is unconsolidated, very altered, and overlain by a thick light brown silty well-sorted soil.

Unit 1: This layer is a ≈ 80 cm-thick blanket of clast-supported, white fine lapilli pumice bearing moderately coarse lithic fragments. This pumice fallout deposit is inversely graded and overlain by a brown ashy poorly-sorted soil.

Unit 2: This unit is a moderately coarse lithic-rich white pumice fall with a measured thickness of ≈ 60 cm. It is overlain by a light brown soil.

Unit 3: This unit is made of three sub-units not separated by any soil nor weathered surface. The first sub-unit (3_1) is a relatively well-sorted PDC deposit containing white coarse lapilli pumices and a few blocks of grey andesite floating in a matrix of ash particles. The total thickness could not be constrained precisely but it is certainly larger than 330 cm. The second subunit (3_2) consists of a thinner (≈ 150 cm) and much finer-grained PDC deposit. Finally, the third sub-unit (3_3) is a very characteristic yellowish sandy ash deposit of about 35 cm. The eruptive sequence is overlained by a relatively thin light brown soil.

Unit 4: This unit is also composed of two sub-units. The first one (4_1) is a very thin layer (≈ 8 cm) of dark grey lithic-rich pumice fallout, the second one (4_2) is a much thicker layer (≈ 180 cm) of coarse white pumice fallout bearing lithic fragments. This unit is overlain by a thin brown soil.

Unit 5: This final unit is a 200 cm-thick very poorly-sorted block-and-ash flow deposit containing mostly scoria bombs and a few white fine lapilli pumice. The top of the cliff could not be seen due to vegetation.

We summarize these observations in the stratigraphic log in Figure 11c.

4.1.2   The new OVSM section

The new OVSM section (outcrop 141 in Figure 6) was located at the construction site of the new Observatoire Volcanologique et Sismologique de la Martinique, ≈ 8.5 km from the Mount Pelée. At this outcrop, we identified nine units from different eruptions, three of
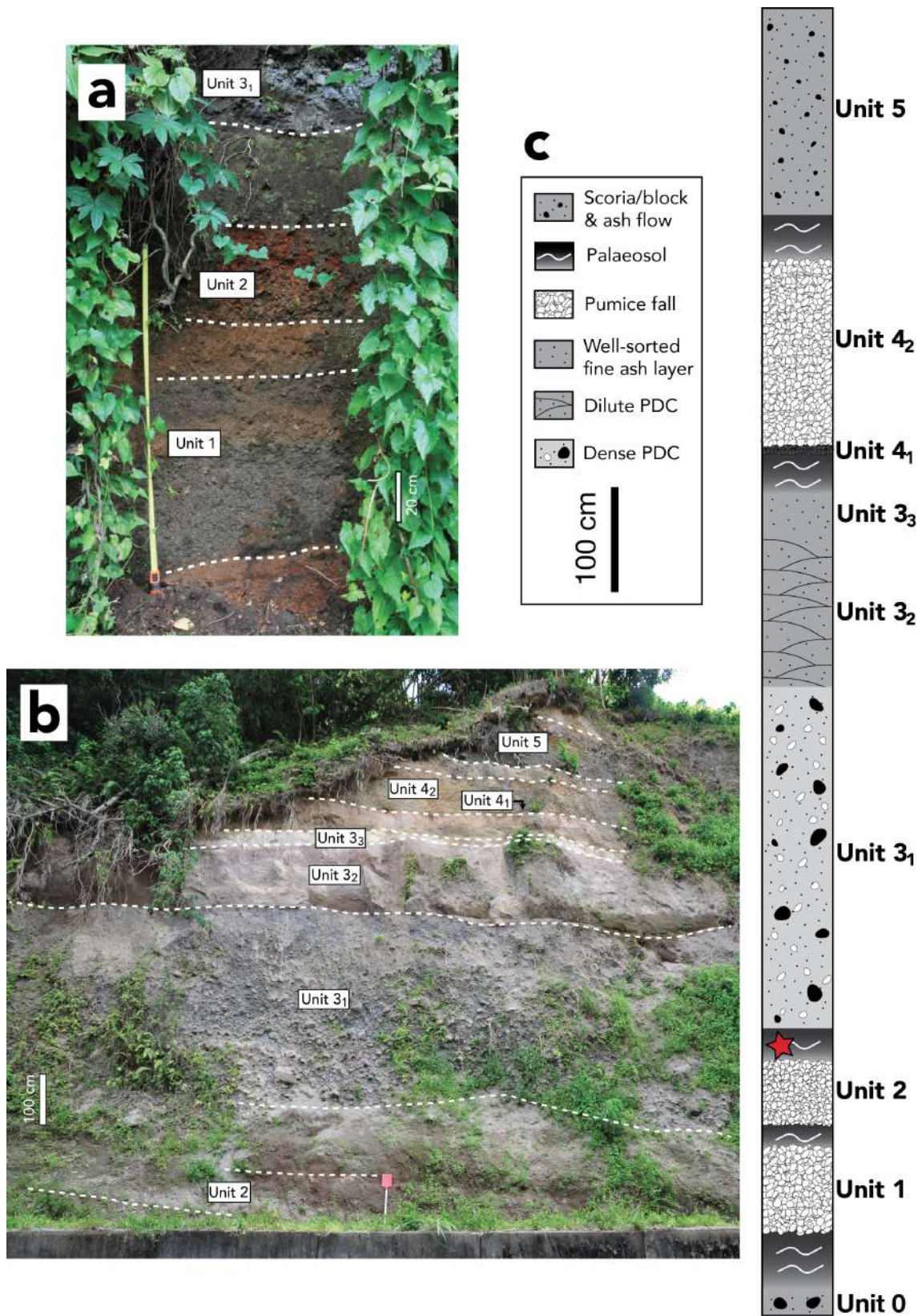
Figure 11: a and **b** Interpreted photographs of the Mont Parnasse section. The scale bar is either 20 cm or 1 m long. **c** Stratigraphic log of the section. The red star indicates the soil sampled for ^{14}C datation.

which were already observed at the Mont Parnasse section (Figure 12a). All units were separated from each other by a dark brown pumice-bearing soil.

From base to top:

Unit 3: Only the upper layer of the Unit 3 deposit (i.e., Unit 3_3) was present here. We described it as a yellowish sandy ash layer of about 40 cm.

Unit 4: We retrieved the two sub-units of the Unit 4 at this outcrop. Unit 4_1, a dark grey lithic-rich pumice fall, is 7-8 cm-thick; while Unit 4_2 has a thickness of 120 cm and can be described as a moderately coarse white pumice fallout.

Unit 5: This unit is a 33 cm-thick layer of fine-grained pumice-bearing scoria fallout, which was most likely elutriated from the top of the PDC described at the Mont Parnasse section.

Unit 6: This layer is a 35 cm-thick blanket of clast-supported, white fine lapilli pumice fallout with a grey sandy matrix of coarse ash.

Unit 7: This unit is a very thin ($\approx$ 6 cm) and fine-grained pumice fallout deposit with a grey sandy matrix of coarse ash particles.

Unit 8: This unit, of about 30 cm in thickness, resembled the Unit 7, and was described as a fine-grained pumice fall deposit with a grey sandy matrix becoming an ashy soil on top.

Unit 9: This unit is a poorly-sorted lithic-rich fine-grained pumice fallout deposit containing a few dark scoria; its measured thickness is $\approx$ 75 cm.

Unit 10: This unit has two sub-units, very similar to sub-units 4_1 and 4_2 at the Mont Parnasse section. Indeed, the sub-unit 10_1 is a very thin layer (about 7 cm) of dark grey fine-grained pumice fallout; whereas the sub-unit 10_2 is much thicker (about 40 cm) and consists of a reversely graded pumice fallout deposit. This layer is overlain by a relatively thick brown soil.

Unit 11: This final unit is a fine-grained pumice fall deposit with a grey sandy matrix whose precise thickness could not be measured as it is grading into a soil bearing vegetation.

We summarize these observations in the stratigraphic log in Figure 12b.

4.1.3   The Bellefontaine stadium section

Finally, the Bellefontaine stadium section (outcrop 197 in Figure 6), located at $\approx$ 12.3 km from the volcano, displayed the almost entire sequence from Unit 1 to Unit 10 (Figure 13a). All units are separated by a brown sandy pumice-bearing ashy soil. We describe this section from base to top and we summarize our observations in the stratigraphic log in Figure 13b.

Unit 1: At base, we retrieved a fine-grained pumice fall deposit with a grey sandy matrix measuring $\approx$ 20 cm corresponding to the Unit 1 found at the Mont Parnasse section.

Unit 2: The following unit was approximately 22 cm thick and could be described as a moderately coarse white pumice fall deposit with a grey sandy matrix corresponding to the Unit 2 identified at the Mont Parnasse section.

Unit 3: This very useful stratigraphic marker can be clearly seen in Figure 13, as a yellowish sandy well-sorted ash layer of about 26 cm. This layer corresponds to the sub-unit 3_3 identified at the Mont Parnasse and OVSM sections (Figures 11 and 12).

Unit 4: We identified the two sub-units of Unit 4 at this section. Unit 4_1 is $2.5-3$ cm thick and consists of a grey lithic-rich fine pumice fallout deposit, whereas Unit 4_2 ($\approx$ 80

Figure 12: a Interpreted photograph of the new OVSM section. The scale bar is 1 m long. **b** Stratigraphic log of the section.

cm) is a coarse white pumice fallout layer grading into a brown sandy pumice-bearing soil.

Unit 5: This unit is a thin layer ($\approx$ 11 cm) of very fine-grained pumice-bearing scoria fallout grading into soil, which corresponds to the Unit 5 identified at the OVSM section.

Unit 6: This layer is thinner than at the previous sections ($\approx$ 11 cm) but still could be described as a fine-grained pumice fallout deposit with a grey sandy matrix grading into a 15 cm-thick soil.

Unit 8: This unit is a 31 cm-thick moderately coarse white pumice fallout deposit. Because of the very low thickness of Unit 7 at the OVSM section (located 4 km north from the Bellefontaine stadium), we interpreted this deposit to belong to Unit 8.

Unit 10: The top of the section is made of a 5 cm-thick fine-grained pumice fallout deposit. Because the Unit 9 rather corresponds to a lithic-rich layer containing a few scoria at the OVSM section, we think it is missing here. We thus interpret this deposit as the Unit 10_2 of the OVSM section. Such a low thickness is consistent with a steady decrease in thickness with the distance from the source compared to the 40 cm found at the new OVSM section.

Several units detailed in this section were not identified in previous field studies, suggesting that we identified new major eruptions in Martinique. With an aim of dating these new events, we performed ^{14}C datations on soils sampled in the field (red stars in Figures
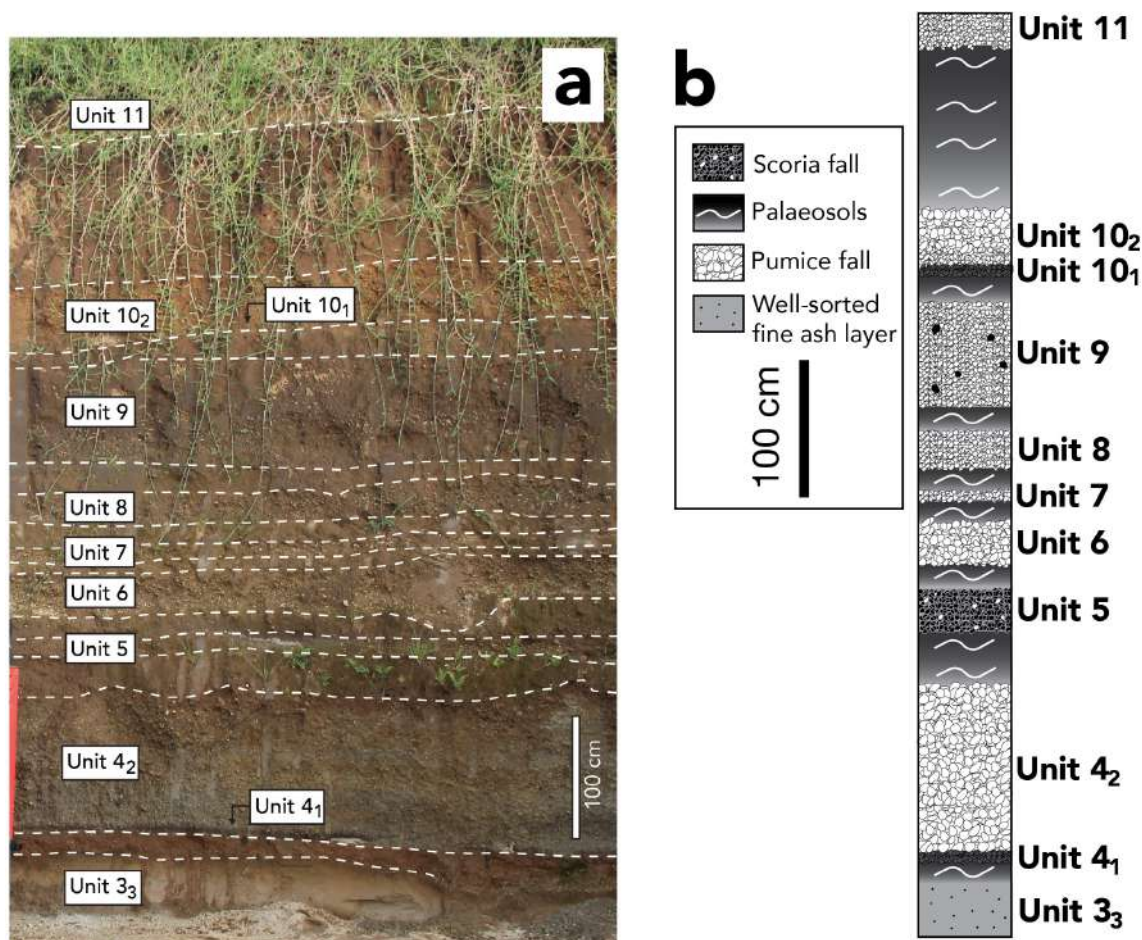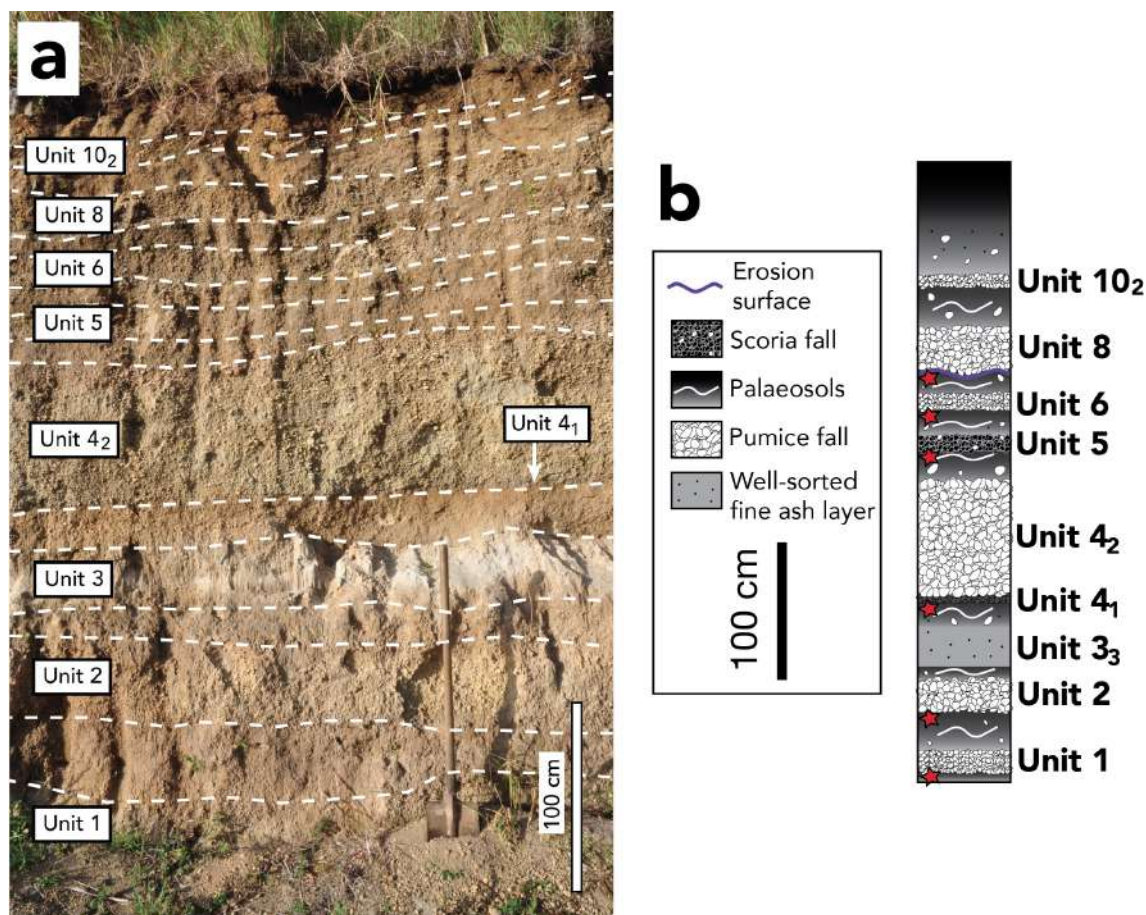
Figure 13: a Interpreted photograph of the Bellefontaine stadium section. The scale bar is 1 m long. **b** Stratigraphic log of the section. The red stars indicate the soils sampled for ^{14}C datation.

11c and 13c) using the method detailed in Section 3.2, to test the stratigraphic correlation made in the field and detailed in this section, and to identify and name every deposit.

4.2 ^{14}C ages: chronology of past eruptions

Nine palaeosols sampled at several locations in the field (either just below or just above a given deposit) were dated by radiocarbon measurements (see Section 3.2). Added to previous datations made by Traineau (1982) and Westercamp & Traineau (1983) (which we calibrated using the OxCal 4.3 online program), they provided precise constraints on the stratigraphic correlations made in the field, allowing us to discover and name four new pumiceous eruptions and to attribute the other deposits to six already-known eruptions of the Mount Pelée. Table 1 summarizes the results for the newly discovered/revisited eruptions.

Unit 0: We recognized this unit as the one described by Traineau *et al.* (1983) and Boudon (1993), and associated to the St Vincent stage of the Mount Pelée construction (see Section 2.2). We thus labelled it "SV".

Unit 1: Two soils sampled at the Bellefontaine stadium section yield an age of 21,450 ± 139 yr cal BP for this unit. This age does not correspond to any known event in Martinique, so we named it the **Etoile eruption**.

Table 1: Radiocarbon ages for newly discovered Plinian eruptions. Measurements were made by AMS at the LMC14 (Artemis, Laboratoire de Mesure du Carbone 14, CEA, Saclay, France). Ages were combined and calibrated using the OxCal 4.3 online program (Bronk Ramsey 2009; https://c14.arch.ox.ac.uk/embed.php?File=oxcal.html) together with the IntCal 13 curve Reimer (2013).

Eruption	Site	Sample material	$\delta^{13}C$ (%)	Ref.#	Radiocarbon age ($\pm 1\sigma$) year BP	Uncalibrated age ($\pm 1\sigma$) year BP	Calibrated age (95.4%, 2σ) year cal BP
Etoile (Unit 1)	197	soil	-20.4	A54008	17,750 ± 100	17,720 ± 71	**21,450 ± 139**
	197	soil	-22.0	A53009	17,690 ± 100		
Carbet (Unit 2)	203	soil	-27.2	A53018	14,530 ± 70	15,447 ± 47	**18,711 ± 60**
	200	soil	-23.9	A53015	15,210 ± 80		
	197	soil	-22.0	A53009	17,690 ± 100		
		Traineau (1982)		MPB208	12,130 ± 1,570		
		Traineau (1982)		MPB219	13,470 ± 260		
		Westercamp & Traineau (1983)		MPB161	18,940 ± 6,300		
Balisier (Unit 3)	200	soil	-23.9	A53015	15,210 ± 80	12,185 ± 52	**14,072 ± 84**
	203	soil	-27.2	A53018	14,530 ± 70		
	197	soil	-22.0	A53010	11,060 ± 60		
	182	soil	-26.0	A47845	10,540 ± 50		
Bellefontaine (Unit 4)	197	soil	-23.6	A53011	12,330 ± 60	11,695 ± 42	**13,516 ± 42**
	197	soil	-22.0	A53010	11,060 ± 60		
		Westercamp & Traineau (1983)		MPB97	10,280 ± 180		
P10 (Unit 6)	197	soil	-23.5	A53012	9,940 ± 60	9,920 ± 42	**11,334 ± 81**
	197	soil	-29.9	A53013	9,860 ± 60		

Unit 2: Three soils sampled at the Bellefontaine stadium section, the Mont Parnasse section and at an additional outcrop (numbered 203 in Figure 6) allowed us to date this unit at 18,711 ± 60 yr cal BP. We named this previously unknown event the **Carbet eruption**.

Unit 3: As this is a very unique deposit (see Chapter 2), we performed four new datations on four soils sampled at the Bellefontaine stadium and the Mont Parnasse sections, as well as at two other outcrops (numbered 182 and 203 on Figure 6). Based on the stratigraphic features of this unit, the thicknesses measured in the field, the outcrop locations, and the ages obtained by these new carbon-datations, we identified this unit as the NBC eruption (Nuée de Balisier-Calave) named by Traineau (1982). Because the NBC eruption is a very poorly known event, for which we found voluminous deposits in a new location beyond the current hazard map, we renamed this important event the **Balisier eruption**. Adding our datations to the previous ones made by Traineau (1982) and Westercamp & Traineau (1983), we dated this eruption at 14,072 ± 84 yr cal BP. We recognized the Unit 3_3 as the "ash hurricane deposit" described by Roobol & Smith (1976) and Traineau *et al.* (1989), and originally thought to be much younger than 14 ka cal BP.

Unit 4: Because of the presence of the yellowish ash layer (Unit 3_3) under the Unit 4, we recognized these deposits as the P3-2 deposits, originally thought to be part of the P3 eruption (see Section 2.3). We performed two datations on soils sampled at the Bellefontaine stadium section (at the base and top of the deposit). These two datations yield an age of 13,516 ± 42 yr cal BP, which do not correspond to any previously-known explosive eruption of the Mount Pelée. We thus named it the **Bellefontaine eruption** (Michaud-Dubuy *et al.*, 2019).

Unit 5: Based on the stratigraphic features of this unit, the thicknesses measured in the field and the outcrop locations, we identified this unit as the **NMC eruption** (Nuées ardentes de Morne Capot), described and named by Traineau (1982). Based on datations made by Traineau (1982) and Boudon *et al.* (2005), this event was dated at 13,132 ± 133 yr cal BP.

Unit 6: Two soils sampled at the Bellefontaine stadium section (at the base and top of the deposit) were dated. Based on the obtained ages, we identified this unit as a Plinian eruption briefly mentionned and dated by Traineau (1982) and Boudon *et al.* (2005). Adding our ^{14}C ages to a previous datation made by Westercamp & Traineau (1983) yields an age of 11,334 ± 81 yr cal BP. In agreement with the notation of Westercamp & Traineau (1983) for Plinian eruptions in Martinique, we named this event the **P10 eruption**.

Unit 7: We identified this unit as the **P9 eruption** (Traineau, 1982), based on the stratigraphic correlation made in the field. This eruption was previously dated by Traineau (1982) and Boudon *et al.* (2005) at 10,369 ± 131 yr cal BP.

Unit 8: We identified this unit as the **P8 eruption** (Traineau, 1982), based on the measured thicknesses in the field and the outcrop locations. This eruption was previously dated by Traineau (1982) and Boudon *et al.* (2005) at 8,587 ± 79 yr cal BP.

Unit 9: Based on the stratigraphic correlation, this unit corresponds to the **P7 eruption** named by Traineau (1982). This author dated this event at 7,515 ± 110 yr cal BP.

Unit 10: Considering the thicknesses measured in the field, the deposit characteristics and the stratigraphic correlation presented in this chapter, we identified this unit as the **P5 eruption**, a relatively well-known eruption dated by Traineau (1982); Boudon *et al.* (2005) and Smith & Roobol (1990) at 4,534 ± 98 yr cal BP.

Unit 11: Based on the same evidences as for the Unit 10, we identified this unit as the

P3 eruption, a well-known event dated at 1,871 ± 21 yr cal BP by Traineau (1982); Boudon *et al.* (2005); Smith & Roobol (1990), and recently revisited by Carazzo *et al.* (2020).

We note that the deposits of the P6, P4, P2 and P1 eruptions are absent from our stratigraphic sections that are all located to the south of the volcano. The P6, P4, and P1 products were dispersed to the west of the volcano (Westercamp & Traineau, 1983; Carazzo *et al.*, 2012), whereas those of the P2 eruption can be found to the northeast (Carazzo *et al.*, 2019).

4.3   A refined on-land eruptive history

Our stratigraphic correlations and both new and previous ^{14}C ages allow us to establish a new chronology of past eruptions of the Mount Pelée volcano summarized in Figure 14.
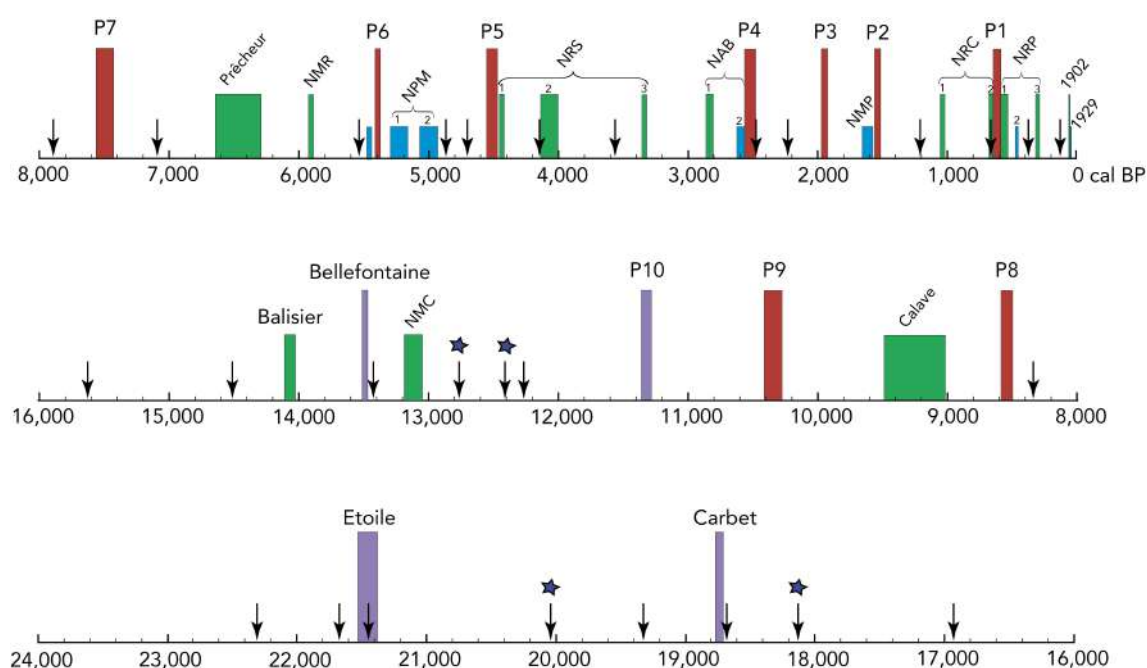
Figure 14: Refined eruptive history of Mount Pelée volcano for the past 24,000 years (in yr cal BP). For each eruption, the width of the bar corresponds to the uncertainty in eruption age, while the height and color indicate the eruption style (long red and purple: previously-known and newly-discovered Plinian eruptions, respectively, short blue: dome collapse, intermediate green: directed blast). The eruption names are as follows: *NMC*, Nuées ardentes de Morne Capot; *NMR*, Nuées ardentes Morne Rouge; *NPM*, Nuées ardentes Pointe la Mare; *NRS*, Nuées ardentes Rivière sèche; *NAB*, Nuées ardentes Ajoupa Bouillon; *NMP*, Nuées ardentes Morne Ponce; *NRC*, Nuées ardentes Rivière Claire; *NRP*, Nuées ardentes Rivière des Pères; *P*, Plinian. The black arrows correspond to the ages of volcanic deposits found at sea by an off-shore study (Boudon *et al.*, 2013), and the blue stars indicate event ages that could correspond to eruptions in Dominica (Boudon *et al.*, 2017).

As Martinique is a small island, the finest volcanic material from an eruption as well as flank-collapse products are generally lost at sea. Studying the marine sedimentary record preserved in marine cores collected offshore the island allows to access to this information. We compared the results presented in this section with those from the tephrochronological study of a deep-sea sediment core collected 50 km northwest of Martinique (Boudon *et al.*, 2013), which allowed identifying many marine tephra (black arrows in Figure 14). Three out of four of the new eruptions (Bellefontaine, Carbet and Etoile) that we identified in the field are retrieved in the deep-sea core, but many other events remained invisible at sea. As

the marine core was collected northwest of Martinique, Plinian events whose products went on the other side of the island could indeed have not reached the location of the drilling site. The marine tephra identified in the deep-sea sediment core, but not corresponding to any known eruptive event in Martinique could correspond either to small still-unknown Pelean events, or to volcanic deposits coming from another island. Four events (blue stars in Figure 14) could indeed correspond to pumiceous eruptions of Dominica (Boudon *et al.*, 2017).

This refined on-land eruptive history, now includes thirteen Plinian eruptions and twenty-one Pelean events (most of them characterized by lateral blasts of lava domes), which makes a total of thirty-four magmatic eruptions in the last 24,000 years cal BP. This is a minimum estimate as several Pelean events could remain unknown, and as we do not include the numerous phreatic eruptions that occurred at Mount Pelée volcano. The twenty-three eruptions that occurred in the last 6 ka cal BP are relatively well-known (Traineau, 1982; Westercamp & Traineau, 1983; Carazzo *et al.*, 2012, 2019, 2020) (Section 2.3). On the contrary, deposits from the six eruptions of the 6,000−12,000 cal BP period are poorly-preserved, making further interpretation impossible. We were however able to retrieve well-preserved deposits from the oldest (and newly discovered) events of this refined eruptive history (between 12,000 and 24,000 cal BP): the Bellefontaine, Balisier, Carbet and Etoile eruptions.

We can now interpret these events in terms of eruptive parameters (volume, column height,...) by using the methods described in Section 2, in order to better understand the global dynamics of Mount Pelée (Chapter 2), to obtain precise constraints for physical models of tephra dispersal (Chapter 5), and to move forward towards a better volcanic hazard assessment in Martinique (Chapter 6).

5   Conclusion

Combining new extensive field studies and carbon-dating measurements, we established a new chronology of recent past eruptions of the Mount Pelée volcano. We identified six new eruptions in the past 24 ka cal BP, including four Plinians eruptions and two Pelean events. When comparing our newly-discovered Plinian eruptions (in purple in Figure 14) with eruptive events dated on volcanic deposits found at sea (Boudon *et al.*, 2013) (black arrows in Figure 14), we find that three out of four correspond to an event spotted off-shore, which reinforces the reliability of this new eruptive history for the Mount Pelée.

This refined eruptive history is thus very rich with at least 34 magmatic eruptions in the last 24 ka cal BP. This is however only a minimum estimate as it is most probable that many Pelean eruptions that occurred between 10 ka and 24 ka cal BP could still remain unknown because of their small volumes which would have not been preserved due to intense weathering and/or flank collapses. Based on this new chronology, we calculated that a Plinian eruption occurs at least every ≈ 1.8 ka in Martinique.

Amongst these newly-discovered eruptions, we have collected enough data (thicknesses and distribution of lithics at several outcrops, together with samples for grain-size analyses) to go further and fully reconstruct the eruptive parameters of the four eruptions of Bellefontaine, Balisier, Carbet and Etoile by using the methods described in Section 3.3 and Section 3.4. The results are presented in the following Chapter 2.

References

ALIBIDIROV, M. & DINGWELL, D.B. 1996 Magma fragmentation by rapid decompression. *Nature* **380**, 146–148.

ANDREIEFF, P., BAUDRON, J.C. & WESTERCAMP, D. 1988 Histoire géologique de la Martinique (Petites Antilles): biostratigraphie (foraminifères), radiochronologie (potassium-argon), évolution volcano-structurale. *Géologie de la France* **2-3**, 39–70.

ANDREIEFF, P., BELLON, H. & WESTERCAMP, D. 1976 Chronométrie et stratigraphie comparée des édifices volcaniques et formations sédimentaires de la Martinique (Antilles Françaises). *Bulletin du BRGM* **Section IV**, 335–346, no 4.

BARDINTZEFF, J.M., MISKOVSKY, J.C., TRAINEAU, H. & WESTERCAMP, D. 1989 The recent pumice eruptions of Mt. Pelée, Martinique. Part II: Grain-size studies and modelling the last Plinian phase P1. *J. Volcanol. Geotherm. Res.* **38**, 35–48.

BONADONNA, C. & COSTA, A. 2012 Estimating the volume of tephra deposits: A new simple strategy. *Geology* **40**, 415–418.

BONADONNA, C. & COSTA, A. 2013 Plume height, volume, and classification of explosive volcanic eruptions based on the Weibull function. *Bull. Volcanol.* **75**, 1–19.

BONADONNA, C., ERNST, G.G.J. & SPARKS, R.S.J. 1998 Thickness variations and volume estimates of tephra fall deposits: The importance of particle Reynolds number. *J. Volcanol. Geotherm. Res.* **81**, 173–187.

BONADONNA, C. & HOUGHTON, B.F. 2005 Total grain-size distribution and volume of tephra-fall deposits. *Bull. Volcanol.* **67**, 441–456.

BOUDON, G. 1993 La montagne Pelée, Martinique : évolution volcanologique. *Mem. Soc. geol. France* **163**, 231–238.

BOUDON, G., BALCONE-BOISSARD, H., SOLARO, C. & MARTEL, C. 2017 Revised chronostratigraphy of recurrent ignimbritic eruptions in Dominica (Lesser Antilles arc): Implications on the behavior of the magma plumbing system. *J. Volcanol. Geotherm. Res.* **343**, 135–154.

BOUDON, G., LE FRIANT, A., KOMOROWSKI, J.C. & DEPLUS, C. 2007 Volcano flank instability in the Lesser Antilles Arc: Diversity of scale, processes, and temporal recurrence. *J. Geophys. Res.* **112**, B0825.

BOUDON, G., LE FRIANT, A., VILLEMANT, B. & VIODE, J.P. 2005 Martinique. In *Volcanic Hazard Atlas of the Lesser Antilles* (ed. J.M. Lindsay, R.E.A. Robertson, J.B. Sheperd & S. Ali), pp. 127–146. Seismic Research Unit, The University of the West Indies, Trinidad and Tobago, W.I.

BOUDON, G., VILLEMANT, B., LE FRIANT, A., PATERNE, M. & CORTIJO, E. 2013 Role of large flank-collapse events on magma evolution of volcanoes: Insights from the Lesser Antilles Arc. *J. Volcanol. Geotherm. Res.* **263**, 224–237.

BOURDIER, J.L., BOUDON, G. & GOURGAUD, A. 1989 Stratigraphy of the 1902 and 1929 nuée-ardente deposits, Mt. Pelée, Martinique. *J. Volcanol. Geotherm. Res.* **38**, 77–96.

BOUYSSE, P. & GARRABÉ, F. 1984 Neogene tectonic Evolution of the Limestone Caribees in the Guadeloupe Archipelago. *C.R. Acad. Sc. Paris Serie I* **298**, 763–766.

BOUYSSE, P. & GUENNOC, P. 1983 Données sur la structure de l'arc insulaire des Petites Antilles, entre Ste-Lucie et Anguilla. *Marine Geology* **53**, 131–166.

BOUYSSE, P. & MARTIN, P. 1979 Caractères morphostructuraux et évolution géodynamique de l'arc insulaire des Petites Antilles (Campagne ARCANTE 1). *Bulletin du BRGM* **section IV (3/4)**, 185–210.

BOUYSSE, P. & WESTERCAMP, D. 1990 Subduction of Atlantic aseismic ridges and Late Cenozoic evolution of the Lesser Antilles island arc. *Tectonophysics* **175**, 349–380.

BOUYSSE, P., WESTERCAMP, D. & ANDREIEFF, P. 1990 The Lesser Antilles Island arc. *Proc. Ocean Drill Program Sci Results* **110**, 29–44.

BRIDEN, J.C., REX, D.C., FALLER, A.M. & TOMBLIN, J.F. 1979 K-Ar geochronology and paleomagnetism of volcanic rocks in the Lesser Antilles island arc. *Phil. Transac. Roy. Soc. Lon.* **291** (1383), 485–528.

BRONK RAMSEY, C. 2009 Bayesian analysis of radiocarbon dates. *Radiocarbon* **51**, 337–360.

BRUNET, M., LE FRIANT, A., BOUDON, G., LAFUERZA, S., TALLING, P., HORNBACH, M., ISHIZUKA, O., LEBAS, E., GUYARD, H. & PARTY, IODP EXPEDITION 340 SCIENCE 2016 Composition, geometry, and emplacement dynamics of a large volcanic island landslide offshore martinique: From volcano flank-collapse to seafloor sediment failure. *Geochem. Geophys. Geosyst.* **17**, 699–724.

BRUNET, M., MORETTI, L., LE FRIANT, A., MANGENEY, A., FERNÁNDEZ NIETO, E.D. & BOUCHUT, F. 2017 Numerical simulation of the 30-45 ka debris avalanche flow of Montagne Pelée volcano, Martinique: From volcano flank collapse to submarine emplacement. *Nat. Hazards* **87**, 1189–1222.

CARAZZO, G., GIRAULT, F., AUBRY, T., BOUQUEREL, H. & KAMINSKI, E. 2014 Laboratory experiments of forced plumes in a density-stratified crossflow and implications for volcanic plumes. *Geophys. Res. Lett.* **41**, 8759–8766.

CARAZZO, G., KAMINSKI, E. & TAIT, S. 2008 On the rise of turbulent plumes: Quantitative effects of variable entrainment for submarine hydrothermal vents, terrestrial and extra terrestrial explosive volcanism. *J. Geophys. Res. Solid Earth* **113**, 1–19.

CARAZZO, G., TAIT, S. & KAMINSKI, E. 2019 Marginally stable recent Plinian eruptions of Mt. Pelée volcano (Lesser Antilles): The P2 AD 280 eruption. *Bull. Volcanol.* **81**, 1–17.

CARAZZO, G., TAIT, S., KAMINSKI, E. & GARDNER, J. E. 2012 The recent Plinian explosive activity of Mt. Pelée volcano (Lesser Antilles): The P1 AD 1300 eruption. *Bull. Volcanol.* **74**, 2187–2203.

CARAZZO, G., TAIT, S., MICHAUD-DUBUY, A., FRIES, A. & KAMINSKI, E. 2020 Transition from stable column to partial collapse during the 79 cal CE P3 Plinian eruption of Mt Pelée volcano (Lesser Antilles). *J. Volcanol. Geotherm. Res. In press.* https://doi.org/10.1016/j.jvolgeores.2019.106764.

CAREY, STEVEN & SIGURDSSON, HARALDUR 1982 Influence of particle aggregation on deposition of distal tephra from the May 18, 1980, eruption of Mount St. Helens volcano. *J. Geophys. Res.* **87**, 7061–7072.

CAREY, STEVEN & SIGURDSSON, HARALDUR 1986 The 1982 eruptions of El Chichon volcano, Mexico (2): Observations and numerical modelling of tephra-fall distribution. *Bull. Volcanol.* **48**, 127–141.

CAREY, S. & SPARKS, R.S.J. 1986 Quantitative models of the fallout and dispersal of tephra from volcanic eruption columns. *Bull. Volcanol.* **48**, 109–125.

COSTA, A., SUZUKI, Y. J., CERMINARA, M., DEVENISH, B. J., ESPOSTI ONGARO, T., HERZOG, M., VAN EATON, A. R., DENBY, L. C., BURSIK, M., DE' MICHIELI VITTURI, M., ENGWELL, S., NERI, A., BARSOTTI, S., FOLCH, A., MACEDONIO, G., GIRAULT, F., CARAZZO, G., TAIT, S., KAMINSKI, E., MASTIN, L. G., WOODHOUSE, M. J., PHILLIPS, J. C., HOGG, A. J., DEGRUYTER, W. & BONADONNA, C. 2016 Results of the eruptive column model inter-comparison study. *J. Volcanol. Geotherm. Res.* **326**, 2–25.

DAGGIT, M.L., MATHER, T.A., PYLE, D.M. & PAGE, S. 2014 AshCalc-a new tool for the comparison of the exponential, power-law and Weibull models of tephra deposition. *J. Appl. Volcanol.* **3:7**.

FISHER, R.V., SMITH, A.L. & ROOBOL, M.J. 1980 Destruction of St. Pierre, Martinique by ash cloud surges, May 8 and 20, 1902. *Geology* **8**, 472–476.

GERMA, A. 2008 Evolution volcano-tectonique de l'île de la Martinique (arc insulaire des Petites Antilles): nouvelles contraintes géochronologiques et géomorphologiques. PhD thesis, Université Paris XI Orsay.

GERMA, A., LAHITTE, P. & QUIDELLEUR, X. 2015 Construction and destruction of Mont Pelée volcano: Volumes and rates constrained from a geomorphological model of evolution. *J. Geophys. Res. Earth Surf.* **120**, 1206–1226.

GERMA, A., QUIDELLEUR, X., LABANIEH, S., CHAUVEL, C. & LAHITTE, P. 2011*a* The volcanic evolution of Martinique island: Insights from K-Ar dating into the Lesser Antilles arc migration since the Oligocene. *J. Volcanol. Geotherm. Res.* **208**, 122–135.

Germa, A., Quidelleur, X., Labanieh, S., Lahitte, P. & Chauvel, C. 2010 The eruptive history of Morne Jacob volcano (Martinique Island, French West Indies): Geochronology, geomorphology and geochemistry of the earliest volcanism in the recent Lesser Antilles arc. *J. Volcanol. Geotherm. Res.* **198**, 297–310.

Germa, A., Quidelleur, X., Lahitte, P., Labanieh, S. & Chauvel, C. 2011*b* The K-Ar Cassignol-Gillot technique applied to western Martinique lavas: A record of Lesser Antilles arc activity from 2 Ma to Mount Pelée volcanism. *Quat. Geochronol.* **6**, 341–355.

Girault, F., Carazzo, G., Tait, S., Ferrucci, F. & Kaminski, E. 2014 The effect of total grain-size distribution on the dynamics of turbulent volcanic plumes. *Earth Planet. Sci. Lett.* **394**, 124–134.

Girault, F., Carazzo, G., Tait, S. & Kaminski, E. 2016 Combined effects of total grain-size distribution and crosswind on the rise of eruptive volcanic columns. *J. Volcanol. Geotherm. Res.* **326**, 103–113.

Grunevald, H. 1965 *Géologie de la Martinique. Mémoires pour servir à l'explication de la carte géologique détaillée de la France*. Paris.

Hartmann, W.K. 1969 Terrestrial, lunar and interplanetary rock fragmentation. *Icarus* **10**, 201–213.

Jarrard, R.D. 1986 Relations among subduction parameters. *Rev. Geophys.* **24**, 217–284.

Kaminski, E. & Jaupart, C. 1998 The size distribution of pyroclasts and the fragmentation sequence in explosive volcanic eruptions. *J. Geophys. Res.* **103**, 29759–29779.

Komorowski, J. C., Legendre, Y., Caron, B. & Boudon, G. 2008 Reconstruction and analysis of sub-plinian tephra dispersal during the 1530 A.D. Soufriere (Guadeloupe) eruption: Implications for scenario definition and hazards assessment. *J. Volcanol. Geotherm. Res.* **178**, 491–515.

Kueppers, U., Perugini, D. & Dingwell, D. B. 2006 "Explosive energy" during volcanic eruptions from fractal analysis of pyroclasts. *Earth Planet. Sci. Lett.* **248** (3-4), 800–807.

Labanieh, S. 2009 Géochimie de l'île de la Martinique aux Petites Antilles. PhD thesis, Université Joseph Fourier, Grenoble (France).

Lacroix, A. 1904 *La Montagne Pelée et ses éruptions*. Masson, Paris.

Lajoie, J. & Boudon, G. 1989 The Peléan deposits in the Fort Cemetery of St. Pierre, Martinique: A model for the accumulation of turbulent nuées ardentes. *J. Volcanol. Geotherm. Res.* **38**, 113–130.

Lajoie, J., Boudon, G. & Bourdier, J-L. 1989 Depositional mechanics of the 1902 pyroclastic nuée-ardente deposits of Mt. Pelée, Martinique. *J. Volcanol. Geotherm. Res.* **38**, 131–142.

Le Friant, A., Boudon, G., Deplus, C. & Villemant, B. 2003 Large-scale flank collapse events during the activity of Montagne Pelée, Martinique, Lesser Antilles. *J. Geophys. Res.* **108** (B1), 1–15.

Le Friant, A., Ishizuka, O., Boudon, G., Palmer, M. R., Talling, P. J., Villemant, B., Adachi, T., Aljahdali, M., Breitkreuz, C., Brunet, M., Caron, B., Coussens, M., Deplus, C., Endo, D., Feuillet, N., Fraas, A. J., Fujinawa, A., Hart, M. B., Hatfield, R. G., Hornbach, M., Jutzeler, M., Kataoka, K. S., Komorowski, J.-C., Lebas, E., Lafuerza, S., Maeno, F., Manga, M., Martínez-Colón, M., McCanta, M., Morgan, S., Saito, T., Slagle, A., Sparks, S., Stinton, A., Stroncik, N., Subramanyam, K. S. V., Tamura, Y., Trofimovs, J., Voight, B., Wall-Palmer, D., Wang, F. & Watt, S. F. L. 2015 Submarine record of volcanic island construction and collapse in the Lesser Antilles arc: First scientific drilling of submarine volcanic island landslides by IODP Expedition 340. *Geochem. Geophys. Geosyst.* **16** (2), 420–442.

Lindsay, J.M., Robertson, R.E.A., Shepherd, J.B. & Ali, S. 2005 *Volcanic Hazard Atlas of the Lesser Antilles*. Seismic Research Unit, The University of the West Indies, Trinidad and Tobago, W.I.

Macdonald, R., Hawkesworth, C.J. & Heath, E. 2000 The Lesser Antilles volcanic chain: a study in arc magmatism. *Earth Sci. Rev.* **49**, 1–76.

Michaud-Dubuy, A., Carazzo, G., Kaminski, E. & Girault, F. 2018 A revisit of the role of gas entrapment on the stability conditions of explosive volcanic columns. *J. Volcanol. Geotherm. Res.* **357**, 349–361.

Michaud-Dubuy, A., Carazzo, G., Tait, S., Le Hir, G., Fluteau, F. & Kaminski, E. 2019 Impact of wind direction variability on hazard assessment in Martinique (Lesser Antilles): the example of the 13.5 ka cal BP Bellefontaine Plinian eruption of Mount Pelée volcano. *J. Volcanol. Geotherm. Res.* **381**, 193–208.

Météo France 2019 Le climat en martinique. *Tech. Rep.*. Météo France, available at http://www.meteofrance.gp/documents/3714888/5579049/climat972_2pages.pdf/1bb26ab1-630b-4fd4-9757-9adb5da948a6.

Nagle, F., Stipp, J.J. & Fisher, D.E. 1976 K–Ar geochronology of the Limestone Caribbees and Martinique, Lesser Antilles, West Indies. *Earth Planet. Sci. Lett* **29**, 401–412.

Newhall, Christopher G. & Self, Stephen 1982 The volcanic explosivity index (VEI) an estimate of explosive magnitude for historical volcanism. *J. Geophys. Res.* **87** (C2), 1231–1238.

Perret, F.A. 1937 *The Eruption of Mt. Pelée 1929-1932*. Carnegie Institution of Washington.

Pyle, D.M. 1989 The thickness, volume and grainsize of tephra fall deposits. *Bull. Volcanol.* **51** (1), 1–15.

Pyle, D.M. 2000 Sizes of volcanic eruptions. In *Encyclopedia of Volcanoes* (ed. H.E. Sigurdsson, B. Houghton, H. Reimer, Stiw J. & S. McNutt), pp. 263–269. Academic Press, San Diego.

Reimer, P. 2013 Selection and treatment of data for radiocarbon calibration: an update to the international calibration (IntCal) criteria. *Radiocarbon* **55**, 1923–1945.

Roobol, M.J. & Smith, A.L. 1976 Mount Pelée, Martinique: A pattern of alternating eruptive styles. *Geology* **4**, 521–524.

Roobol, M.J. & Smith, A.L. 1980 Pumice Eruptions of the Lesser Antilles. *Bull. Volcanol.* **43** (2), 277–286.

Roobol, M.J. & Smith, A.L. 2004 *Volcanology of Saba and St. Eustatius, Northern Lesser Antilles*. Koninklijke Nederlandse Akademie Van Wetenschappen.

Rose, W.I. & Durant, A.J. 2009 El Chichon volcano, April 4, 1982: volcanic cloud history and fine ash fallout. *Nat. Hazards* **51** (363).

Samper, A., Quidelleur, X., Boudon, G., Le Friant, A. & Komorowski, J.C. 2008 Radiometric dating of three large volume flank collapses in the Lesser Antilles arc. *J. Volcanol. Geotherm. Res.* **176** (4), 485–492.

Smith, A.L. & Roobol, M.J. 1990 Mount Pelée, Martinique: A study of an Active Island Arc Volcano. *Geol. Soc. Am. Memoir* **175**.

Traineau, H. 1982 Contribution à l'étude géologique de la Montagne Pelée (Martinique): Evolution de l'activité éruptive au cours de la période récente. PhD thesis, Université Paris XI.

Traineau, H., Westercamp, D., Bardintzeff, J. M. & Miskovsky, J. C. 1989 The recent pumice eruptions of Mt. Pelée volcano, Martinique. Part I: Depositional sequences, description of pumiceous deposits. *J. Volcanol. Geotherm. Res.* **38**, 17–33.

Traineau, H., Westercamp, D. & Coulon, C. 1983 Mélanges magmatiques à la Montagne Pelée (Martinique). Origine des éruptions de type Saint-Vincent. *Bull. Volcanol.* **46** (3), 243–269.

Turcotte, D.L. 1986 Fractals and fragmentation. *J. Geophys. Res.* **91**, 1921–1926.

Villemant, B. & Boudon, G. 1999 H_2O and halogen (F, Cl, Br) behaviour during shallow magma degassing processes. *Earth Planet. Sci. Lett.* **168**, 271–286.

Vincent, P.M., Bourdier, J.L. & Boudon, G. 1989 The primitive volcano of Mount Pelée: Its construction and partial destruction by flank collapse. *J. Volcanol. Geotherm. Res.* **38**, 1–15.

Wadge, G. 1984 Comparison of volcanic production rates and subduction rates in the Lesser Antilles and Central America. *Geology* **12**, 555–558.

References

WADGE, G. 1986 The dykes and structural setting of the volcanic front in the Lesser Antilles island arc. *Bull. Volcanol.* **48**, 349–372.

WARD, G.K. & WILSON, S.R. 1978 Procedures for comparing and combining radiocarbon age determinations: A critique. *Archaeometry* **20**, 19–31.

WESTERCAMP, D. 1972 Contribution à l'étude du volcanisme en Martinique. PhD thesis, Université de Paris-Sud.

WESTERCAMP, D. & ANDREIEFF, P. 1983 Saint Barthélémy et ses îlets, Antilles françaises: stratigraphie et évolution magmato-structurale. *Bulletin de la Société Géologique de France* **XXV** (6), 873–883.

WESTERCAMP, D., ANDREIEFF, P., BOUYSSE, P., COTTEZ, S. & BATTISTINI, R. 1989 *Notice explicative, Carte géol. France (1/50 000), feuille MARTINIQUE*. Orléans : Bureau de recherches géologiques et minières, 246 pp. Carte géologique par Westercamp D., Pelletier B., Thibaut P.M., and Traineau, H.

WESTERCAMP, D., PELLETIER, B., THIBAUT, P.M. & TRAINEAU, H. 1990 *Carte géol. France (1/50 000), feuille MARTINIQUE*. Orléans : Bureau de recherches géologiques et minières, notice explicative par Westercamp D., Andreieff P., Bouysse P., Cottez S., Battistini R. (1989), 246 pp.

WESTERCAMP, D. & TAZIEFF, H. 1980 *Martinique, Guadeloupe, Saint-Martin, La Désirade*. Masson, Paris, 135 pp.

WESTERCAMP, D. & TRAINEAU, H. 1983 The past 5,000 years of volcanic activity at Mt. Pelée Martinique (F.W.I.): Implications for assessment of volcanic hazards. *J. Volcanol. Geotherm. Res.* **17**, 159–185.

WOODHOUSE, M.J., HOGG, A.J. & PHILLIPS, J.C. 2016 A global sensitivity analysis of the PlumeRise model of volcanic plumes. *J. Volcanol. Geotherm. Res.* **326**, 54–76.

WOODS, A. W. 1995 The dynamics of explosive volcanic eruptions. *Rev. Geophys.* **33**, 495–530.

WRIGHT, J.V., SMITH, A.L., ROOBOL, M. J., MATTIOLI, G. S. & FRYXELL, J.E. 2016 Distal ash hurricane (pyroclastic density current) deposits from a ca. 2000 yr B.P. Plinian-style eruption of Mount Pelée, Martinique: Distribution, grain-size characteristics, and implications for future hazard. *Geol. Soc. Am. Bull.* **128** (5/6), 777–791.

Chapter 2

Reconstruction of the newly discovered eruptions

Table of contents

Résumé du chapitre 2

Ce chapitre est dédié à la reconstruction des éruptions nouvellement découvertes de Belle-fontaine (13 516 ans cal A.P.[1]), Balisier (14 072 ans cal A.P.), Carbet (18 711 ans cal A.P.) et Etoile (21 450 ans cal A.P.) pour lesquelles nous avons assez de données de terrain de bonne qualité, en utilisant les méthodes décrites dans le chapitre 1. Le grand intérêt de ces éruptions réside dans leur axe de dispersion inhabituel englobant des zones considérées comme sécurisées sur les cartes d'aléa actuelles.

Nous détaillons tout d'abord dans ce chapitre les principaux résultats de nos études de terrain avec une description de la stratigraphie de chacune des quatre éruptions et de la distribution spatiale de leurs dépôts, ainsi que les résultats des analyses de tailles de grains faites sur les dépôts prélevés sur le terrain. Les datations effectuées nous apprennent que l'éruption plinienne que nous avons nommé Bellefontaine, dont les dépôts avaient été précédemment identifiés et attribués par Westercamp & Traineau (1983) à l'éruption P3, est en fait bien plus ancienne. Les deux autres dépôts pliniens étudiés dans ce chapitre étaient par contre jusqu'ici inconnus, et nous les nommons les éruptions Carbet et Etoile. Enfin, nous avons découvert et étudié un dépôt de retombées de cendres tout à fait exceptionnel puisqu'il résulte d'une colonne éruptive secondaire qui s'est formée au-dessus de la coulée de densité pyroclastique créée par l'éruption péléenne NBC (Nuées de Balisier Calave, nommée par Traineau 1982). En conséquence, nous avons nommé "Balisier" la séquence éruptive entière (coulée de densité pyroclastique et panache secondaire).

Grâce à ces études de terrain, à nos échantillons de dépôts, et à nos mesures d'épaisseurs et de tailles de lithiques, nous avons reconstruit dans ce chapitre les paramètres éruptifs (volume de dépôts, hauteur maximale de colonne, flux de masse, durée...) de chacune des quatre nouvelles éruptions. Nous avons ensuite comparé ces paramètres à ceux des éruptions plus récentes de la montagne Pelée (P1, en l'an 1300 de notre ère; P2, en l'an 280 de notre ère; et P3, en l'an 79 de notre ère) et montré que la montagne Pelée produit depuis 24 000 ans des éruptions très similaires les unes aux autres. Les éruptions P3 et Balisier se distinguent par leur forte puissance, comparées respectivement aux autres éruptions pliniennes et péléennes de la Martinique. Les fortes similitudes entre tous ces événements éruptifs nous permettent de dresser un portrait du scénario éruptif le plus susceptible de se produire dans le futur. L'éruption la plus probable durerait quelques heures, produirait une colonne d'environ 20 km de haut alimentée par un flux de masse entre 10^7 et 10^8 $\mathrm{kg\,s^{-1}}$. Ses dépôts auraient un volume compris entre 0.1 et 1 km^3 DRE, avec une majorité de particules fines (exposant de loi puissance $D > 3.3$). Comme le vent peut provenir de n'importe quelle direction, les produits volcaniques de cette future éruption pourraient être dispersés vers n'importe quelle zone de la Martinique (incluant Fort-de-France, la zone la plus peuplée de l'île), ou même atteindre une autre île des Caraïbes (comme la Dominique ou Sainte-Lucie). Le scénario d'une éruption plus puissante plinienne (VEI 5) ou péléenne (impliquant un panache secondaire menaçant des zones normalement sécurisées lors de ce type d'éruption) est également probable.

---

[1]A.P. est l'abréviation de "avant le présent" et désigne les âges exprimés en nombre d'années comptées vers le passé à partir de l'année 1950 du calendrier grégorien. Ici, ces âges sont calibrés à partir d'une courbe d'étalonnage prenant en compte les fluctuations du taux de radiocarbone dans l'atmosphère au cours du temps.

1   Introduction

This chapter is dedicated to the reconstruction of the newly discovered/revisited Belle-fontaine (13,516 ± 42 yr cal BP), Balisier (14,072 ± 84 yr cal BP), Carbet (18,711 ± 60 yr cal BP) and Etoile (21,450 ± 139 yr cal BP) eruptions, for which we have enough high-quality field data, by using the methods presented in Chapter 1, Section 3. The great interest of these eruptions stems from their unusual southward dispersal (see Section 2.2), which encompasses areas that are considered to be safe in current hazard maps (see Intro-duction, Figure 7). Comparing the eruptive parameters of these new eruptions with those of the most recent Plinian eruptions of the Mount Pelée volcano (P1, P2 and P3; Carazzo *et al.* 2012, 2019, 2020) leads to a more precise and more robust characterization of the eruptive dynamics of the volcano, and thus gives us an insight of its possible future eruptions.

First, we present the main results of our field study, with a description of both the stratigraphy of each eruptive sequence and the spatial distribution of the deposits, as well as the results of the grain-size analyses performed on deposits sampled in the field. We then interpret these results in terms of eruptive dynamics, and quantify the minimum erupted volumes, maximum column heights, and peak mass discharge rates of each eruption. In the last section, we finally summarize these eruptive parameters and discuss a possible future eruptive scenario at the Mount Pelée volcano.

2   Field study

2.1   Stratigraphy of the units

2.1.1   The Bellefontaine sequence

The Bellefontaine deposits are easily recognizable by the presence of a strong stratigraphic marker: a yellowish very well-sorted fine ash layer, referred to by Roobol & Smith (1976) and Traineau *et al.* (1989) as an "ash hurricane deposit", underlying the Bellefontaine sequence and separated from it by a dark brown soil. The nature and origin of this deposit that belongs to the Balisier sequence are detailed in the following Section 2.1.2. As detailed in Chapter 1, the Bellefontaine deposits were originally thought to be part of the P3-2 phase of the P3 eruption (Chapter 1, Section 2.3, Westercamp & Traineau 1983) before our new carbon-dating measurements revealed that this event was much older (Chapter 1, Section 4.2). Based on diagnostic sedimentary, stratigraphic and physical features of its deposits, we divide the Bellefontaine eruption into two main phases, called Unit A and Unit B.

Unit A: the opening phase of the eruption spread a thin (1-8 cm) dark grey lithic-rich pumice fall layer over ≈ 130 km^2 to the south of the vent. This pumice fall layer, referred as Unit A, is unstratified, unconsolidated and contains ≈ 30 wt% of lithic fragments. The contact with the overlying layer is always sharp, without erosion or weathering of the top of the unit, which shows that Unit A and the overlying unit are part of the same event (Figure 1).

Unit A's thickness regularly decreases with distance from the source to the south, which thus corresponds to the downwind direction. The deposit can be found up to 14 km to the south but is missing on the west and east flanks of the volcano. The relatively widespread nature of this deposit, its uniformly decreasing thickness with distance from the source, its framework (clast-supported), and its grain type characteristics (pumice and juvenile lithic fragments) show that Unit A is a fall deposit resulting from a violent explosion associ-

ated with a vent-opening phase producing a short-duration, lithic-rich, and small plume, consistent with the low thickness of this unit.
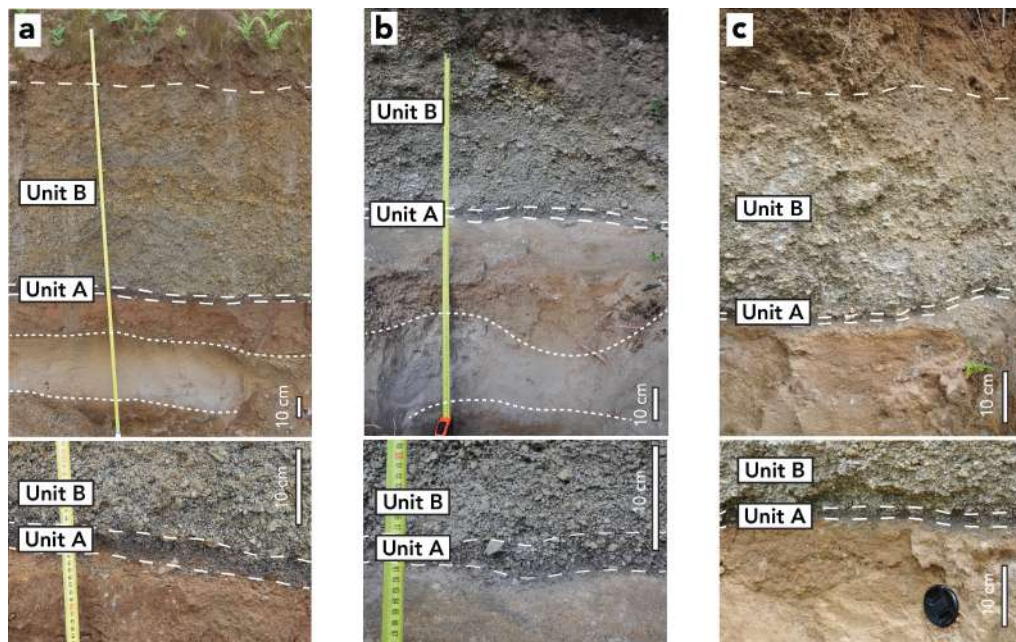
Figure 1: Representative photographs of the Bellefontaine deposits in Martinique at sites **a** 141, **b** 185 and **c** 184 (see Figure 4 for outcrop location). The layer within the dotted lines corresponds to the stratigraphic marker (so-called "ash hurricane") discussed in the main text and belonging to the Balisier sequence. The small photographs give a closer look at the deposits from the opening phase. All scale bars are 10 cm long.

Unit B: the main layer of the Bellefontaine sequence overlies Unit A and is referred as Unit B. It is a blanket of clast-supported, coarse white pumice with a grey sandy matrix (Figure 1) bearing a few grey pumices. Unit B contains dark juvenile and red altered accidental lithic fragments in a total amount of ≈ 7 wt% at the base. At most sites, both pumice and maximum lithic size increase slightly in the uppermost part of the unit.

In the downwind direction (to the south), Unit B has a maximum thickness of 180 cm at 6.5 km from the crater, and steadily thins to 30 cm within 16 km of the vent. In the crosswind direction (East-West), Unit B is 180 cm thick in the most proximal sections (within 6.5 km from the vent), and thins to 45 cm within 8.4 km of the crater. Based on its characteristics, we identify Unit B as the main fall deposit of the eruption.

2.1.2   The Balisier sequence

We divide the Balisier deposits into three major units based on diagnostic sedimentary, stratigraphic and physical features. The sequence starts with a thick poorly-sorted pyroclastic density current (PDC) deposit (Unit A) immediately overlain by a thinner layer of fine-grained PDC deposit (Unit B), and the yellowish well-sorted ash layer mentionned in Section 2.1.1 as a strong stratigraphic marker (Unit C). We now describe in more detail these three units.

Unit A: this thick layer is a greyish white relatively well-sorted deposit containing large angular to sub-rounded coarse lapilli pumices and a few blocks of andesite floating in a matrix of ash particles (Figure 2a and b). Unit A is about 3.3 meters-thick at the center of the valley, ≈ 6.5 km from the source (location 200), while its thickness decreases on the hills (locations 202 and 203) where it reaches a maximum of 77 cm. The relatively limited

dispersal of this unit, its irregular thickness, the type of grain and matrix indicate that Unit A is a dense pyroclastic density current deposit. As mentionned in Chapter 1, the Unit A description and thicknesses at locations 200, 202 and 203, as well as our ^{14}C datations of this deposit, are consistent with the NBC (Nuées ardentes de Balisier Calave) eruption described and dated by Traineau (1982) and identified in this area by Westercamp *et al.* (1990). The NBC eruption is described by Traineau (1982) as highly volumetric pyroclastic density current resulting from a Pelean event covering the southern flank of the volcano.
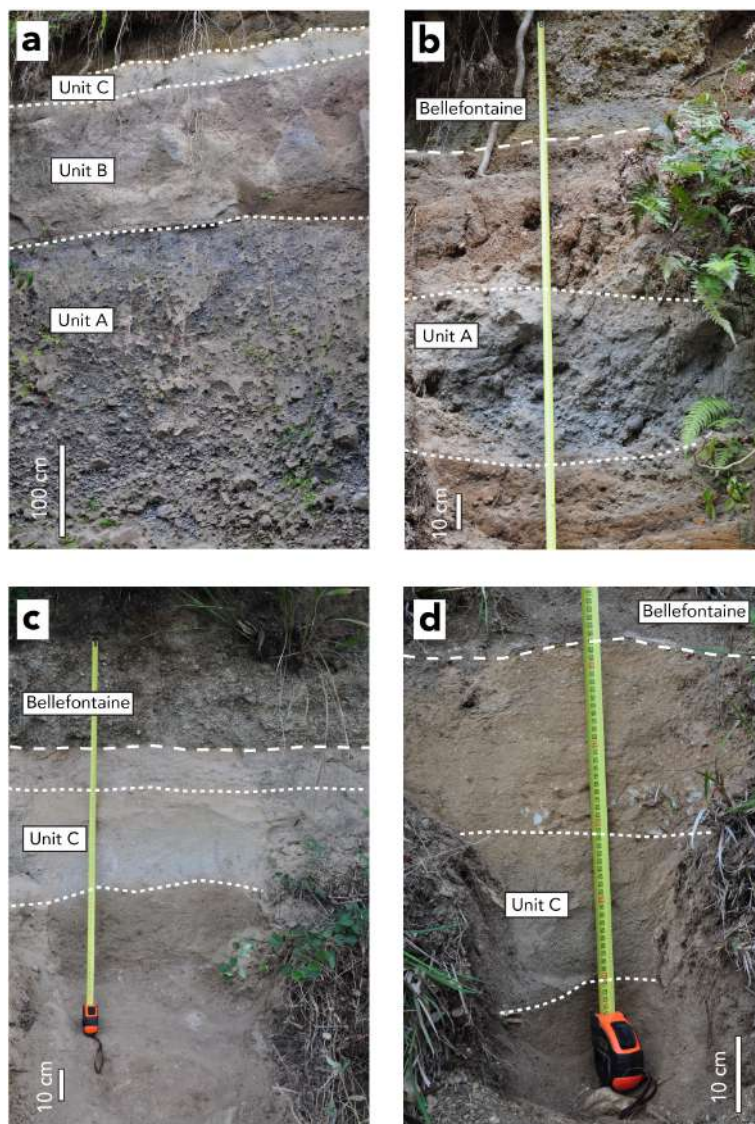
Figure 2: Representative photographs of the Balisier deposits in Martinique at sites **a** 200, **b** 202, **c** 198, and **d** 91 (see Figure 7 for outcrop location). The layer above the white dashed line corresponds to the Bellefontaine deposits described in Section 2.1.1. Scale bars are either 100 or 10 cm long.

Unit B: this unit consists of a thinner grey laminated well-sorted fine-grained material containing pumice, lithic fragments and crystals dispersed into a matrix of dense angular glass fragments (Figure 2a). This unit is only visible at location 200 where it is $\approx$ 150 cm thick; and where the contact with the underlying Unit A and the overlying Unit C is sharp, suggesting that there was no time break between the deposition of the three units. Its characteristics indicate that Unit B is a low-concentration pyroclastic density current deposit that most likely detached from the top of the PDC that produced Unit A.

Unit C: the top unit of the Balisier sequence is a yellowish very well-sorted ash layer spread over $\approx$ 49 km^2 between the cities of St Pierre and Bellefontaine. This unit exhibits no stratification, no lamination and is very uniform at all outcrops. The contact with the underlying Unit B (when present) is always sharp, without erosion or weathering of the bottom of the unit, which shows that Units A, B, and C are part of the same event (Figure 2a).

Unit C's thickness does not regularly decrease with distance from the volcano, as most pumice fallout deposits would do. The maximum thickness is instead found near the Le Carbet city center at $\approx$ 11.6 km from the Mount Pelée summit (location 184), while the minimum thickness is $\approx$ 14 km away from the volcano (location 91). This peculiar dispersal (see Section 2.2.2), as well as its grain characteristics (see Section 2.3.2) indicate that Unit C is likely to be a co-PDC deposit resulting from an ash plume that rose above the PDC generated by the Pelean event.

2.1.3   The Carbet sequence

The Carbet eruption produced only one deposit unit, often overlying the Etoile eruption deposits in the field, but always separated from it by a brown ashy poorly-sorted soil (Figure 3). This eruption spread a clast-supported, lithic-rich, moderately coarse white pumice fall containing juvenile and accidental lithic fragments in a total amount of $\approx$ 15 % at the base. No grading is observed within the deposits that cover $\approx$ 146 km^2.

In the southward downwind direction, the Carbet deposits have a maximum thickness of 70 cm at 6.5 km from the vent, and thins to 15 cm within 14 km of the source. Few outcrops are available in the crosswind direction (East-West), but the deposits are 50 cm thick in the most proximal and eastern section (6 km away from the Mount Pelée). Based on its characteristics, the single unit of the Carbet eruption is a fall deposit.
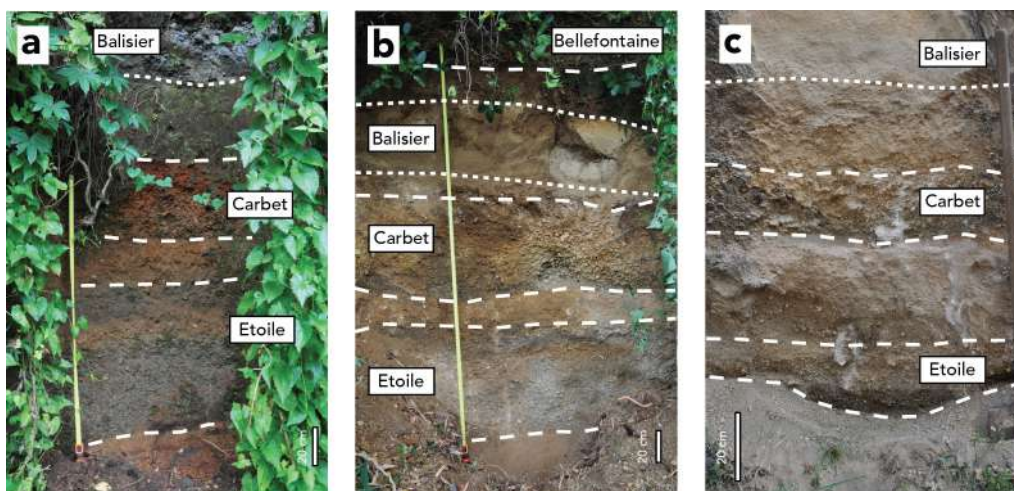
Figure 3: Representative photographs of the Carbet and Etoile deposits in Martinique at sites **a** 200, **b** 127, and **c** 188 (see Figure 9 for outcrop location). The layer between the white dotted line corresponds to the Balisier deposits described in Section 2.1.2. All scale bars are 20 cm long.

2.1.4   The Etoile sequence

The Etoile sequence is also composed of a single unit described as a blanket of clast-supported, lithic-rich, moderately coarse white pumice covering a $\approx$ 102 km^2 area on the

southern flank of the volcano (Figure 3). These deposits contain juvenile and accidental lithic fragments in a total amount of $\approx 7\ \%$ at the base.

In the downwind direction (to the south), the Etoile deposits have a maximum thickness of 79 cm at 6.5 km from the vent, and thins to 20 cm within 13 km of the source. In the crosswind direction (East-West), the deposits are 51 cm thick in the most proximal and eastern section (6 km away from the Mount Pelée). Based on its characteristics, the single unit of the Etoile eruption is a fall deposit.


2.2   Spatial distributions of the deposits

2.2.1   The Bellefontaine sequence

We identified the Bellefontaine eruption deposits at 29 locations over 217 outcrops studied in northern Martinique (Figure 4a). Figure 4b shows a stratigraphic correlation of Bellefontaine outcrops along two different dispersal axes (North-South and West-East, see Figure 4a for localization). The complete sequence can be found up to 13.9 km from the crater (sites 200, 185, 197, and 91 in Figure 4b).

Thickness measurements at each location are reported on isopach maps for the two phases of the Bellefontaine eruption (Figure 5a and b) later used to calculate the volume of deposits (see Section 3.1). Unit A deposits are widespread on the south flank of the volcano, and vary between 8 cm at 6.5 km from the crater to 1 cm further south (Figure 5a). Unit B deposits are much thicker (Figure 5b), which allows a better-constrained volume. We thus use the crosswind distance found for Unit B as a maximum extent for the isopachs of both units. Because Unit A is not very thick, the error on the contribution of this phase to the total volume estimation can be expected to be low. The thicknesses of both units show ellipsoidal contour patterns indicating fallout dispersion towards the south (Figure 5a and b). This direction of dispersal is in good agreement with the P3-2 isopach map of Westercamp & Traineau (1983) (Figure 6).

The lack of Bellefontaine deposits between the vent and our most northern location (202) is most likely due to the last major flank collapse that occurred at ≈ 9 ka and removed most of the old volcanic material into the sea as a debris avalanche (Le Friant *et al.*, 2003). Voluminous PDC deposits of recent eruptions (P3, P2, P1, 1902, 1929) indeed filled up the large depression created by the flank collapse, and neither Roobol & Smith (1976), nor Westercamp & Traineau (1983) report outcrops of Bellefontaine deposits in this area. In order to obtain some field data in this key area, we studied the stratigraphic sections given by Smith & Roobol (1990) who performed 30 deep core drillings around Mt Pelée volcano (Figure 6). We have identified Bellefontaine eruption deposits at two boreholes located to the south and to the east of the volcano with thicknesses consistent with our own measurements in these areas (Figure 5b). Bellefontaine pumice fallout deposits might also be present in three additional boreholes to the west of the volcano, where several pumice fallout deposits older than 2,447 BP but younger than 36,095 BP are present. The lack of precise dating (or presence of a stratigraphic marker) prevents us from positively identifying the Bellefontaine eruption deposits in these three boreholes, but their potential thicknesses are always comprised between 10 and 40 cm.

We measured the major axis of the five largest lithic fragments at each outcrop to build an isopleth map for the Bellefontaine eruption later used to estimate the maximum column height and minimum exit velocity (see Section 3.2). Because of the Unit A deposit's thinness, it was too difficult to sample lithics belonging to this unit, so we constructed only a maximum

Figure 4: a Overview of our field area in Martinique. White circles and numbers refer to localities where Bellefontaine deposits are present. Black dots show outcrop locations where Bellefontaine deposits are absent (due to erosion) and/or too deeply buried under recent eruption deposits. The dotted line links the locations used in **b**, stratigraphic logs of representative sections of the Bellefontaine deposits. The red stars in section 197 (Bellefontaine stadium section in Chapter 1) indicate the soils sampled for ^{14}C dating. All maps were generated using the open source QGIS software. Coordinates are in WGS 84 – UTM Zone 20 system.

lithic isopleth map for Unit B (Figure 5c). The isopleth map of the base of Unit B is well-constrained thanks to the good preservation of the deposit. We note that the southern direction of the dispersal axis is consistent with that inferred from the isopach map.

2.2.2   The Balisier sequence

We identified the Balisier deposits at 26 locations over 217 outcrops studied (Figure 7a). Figure 7b shows a stratigraphic correlation of Balisier outcrops along two different dispersal axes (North-South and West-East, see Figure 7a for localization). The deposits from the co-PDC plume (Unit C) can be found up to 16.1 km from the crater (site 90 in Figure 7a).
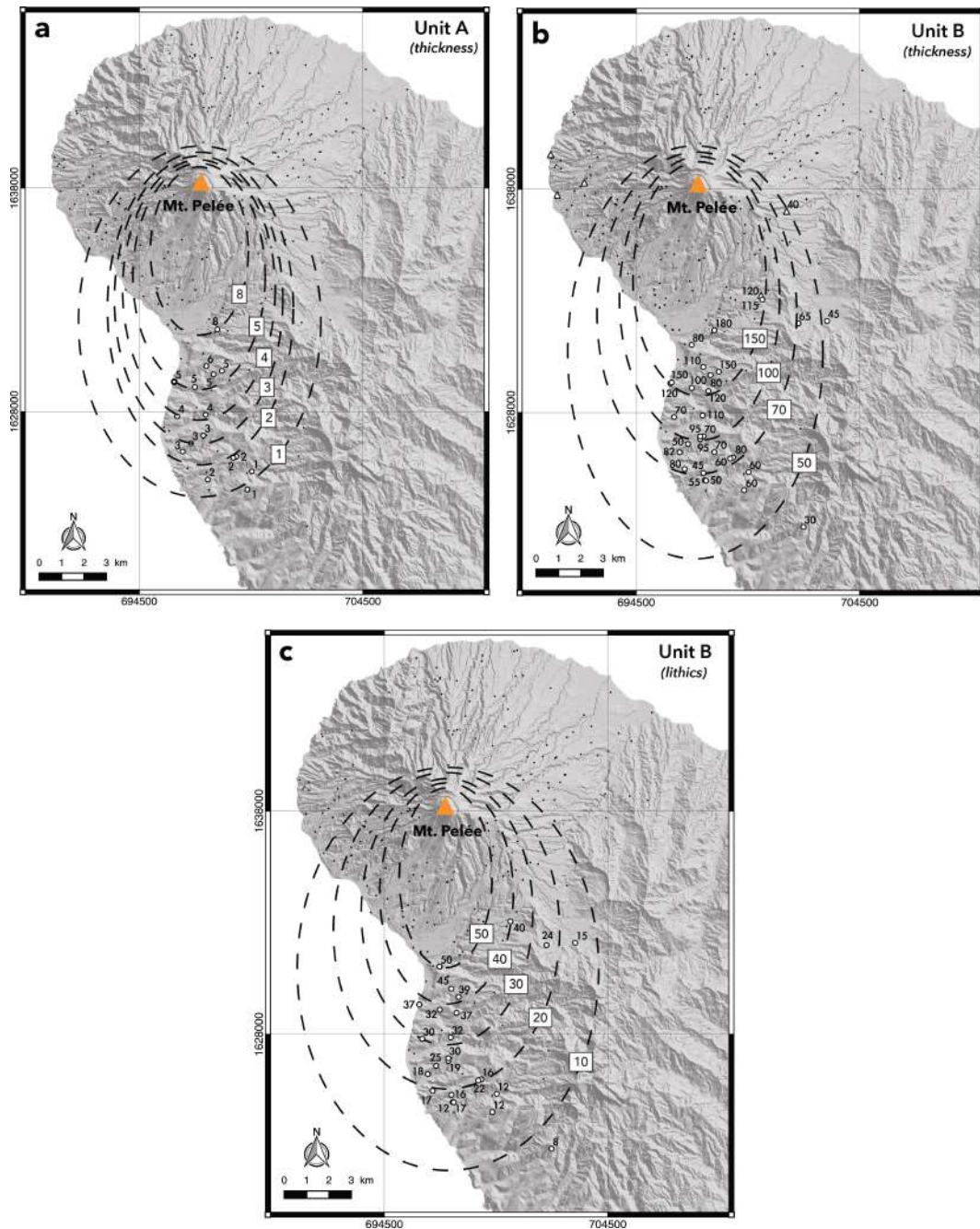
Figure 5: Isopach maps (in centimeters) for **a** Unit A and **b** Unit B, and **c** isopleth map (in millimeters) for lithic fragments sampled at the base of Unit B (Bellefontaine eruption). Open circles indicate measured sample locations; triangles indicate drilling locations from Smith & Roobol (1990) where we have identified Bellefontaine deposits (see Section 2.2.1 for details). Directions of dispersal axes inferred from isopach and isopleth maps are consistent with each other.

Thickness measurements at each location are reported in the isopach map shown in Figure 8, later used to calculate the volume of deposits (see Section 3.1). The Unit A deposits are only retrieved at three locations, and their maximum thicknesses (blue numbers in Figure 8) are measured at location 200, which seems to mark the maximum extent of the PDC. Unit C deposits (red numbers in Figure 8) are spread on the southern flank of the volcano, between the towns of Saint-Pierre and Bellefontaine, and vary between 35 cm at 6.5 km from the crater to 3 cm at 16.1 km from the vent. The maximum thicknesses (45−55
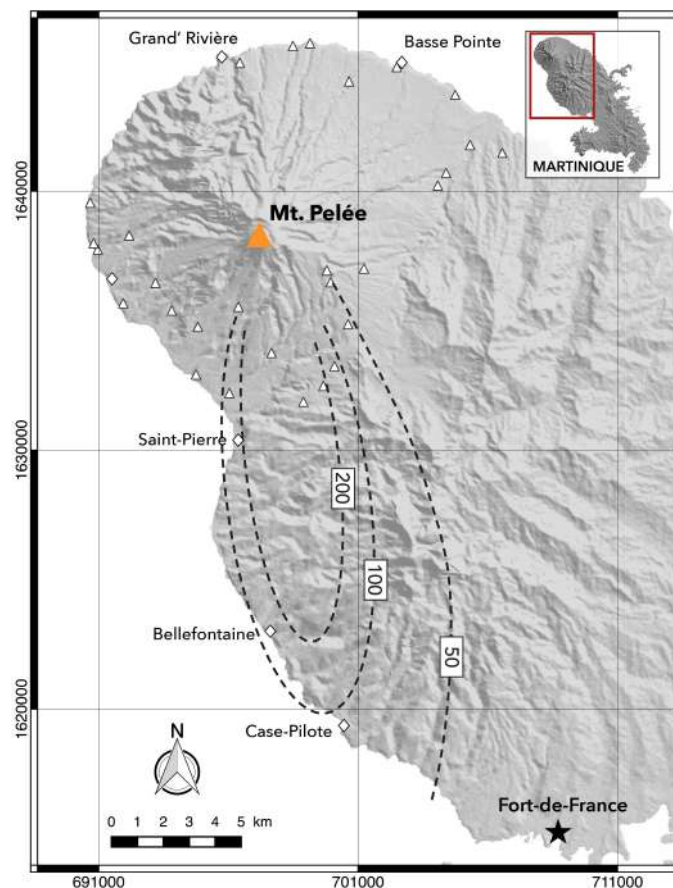
Figure 6: Isopach map (in centimeters) of the P3-2 sequence (here renamed the Bellefontaine eruption) as drawn by Westercamp & Traineau (1983). Triangles indicate all drilling locations from Smith & Roobol (1990).

cm) are however not located at the most proximal locations but at $\approx 8{-}12$ km away from the Mount Pelée, which suggests that the source of the Unit C is shifted from the volcanic vent. In addition, the Unit C's most proximal location coincides with the maximum extent of the PDC deposits from Units A and B (Figure 8). These two peculiar characteristics confirm that the Unit C results from one or several co-PDC plumes that rose above the PDC at a distance of about 6.5 km from the vent.

Such a phenomenon was often observed and studied, both in the field and using laboratory experiments. As a PDC is rushing down the volcano flanks, particles sediment from the base of the current, and air is entrained at the top (Andrews & Manga, 2011; Bursik & Woods, 1996). The entrained air, heated by the particles, expands and causes the density of the upper portions of the PDC to decrease below that of the surrounding atmospheric air. As for a plume rising above the volcano vent during a Plinian eruption, this density decrease thus allows a buoyancy reversal and the formation of a co-PDC plume (Bursik & Woods, 1996). Three mechanisms enhance this buoyancy reversal and can explain the formation of a co-PDC plume: a strong elutriation by mechanical fracturation of the largest clasts into fine ash particles (e.g., 1991 Unzen eruption, Watanabe *et al.* 1999); an interaction with a body water such as the entrance into the sea (e.g., 1815 Tambora eruption, Sigurdsson & Carey 1989); or the encounter with a topographical barrier that traps the largest basal clasts on the ground and favors the rise of the upper finest particles as a buoyant co-PDC plume (e.g., 2006 Tungurahua eruption, Engwell & Eychenne 2016).
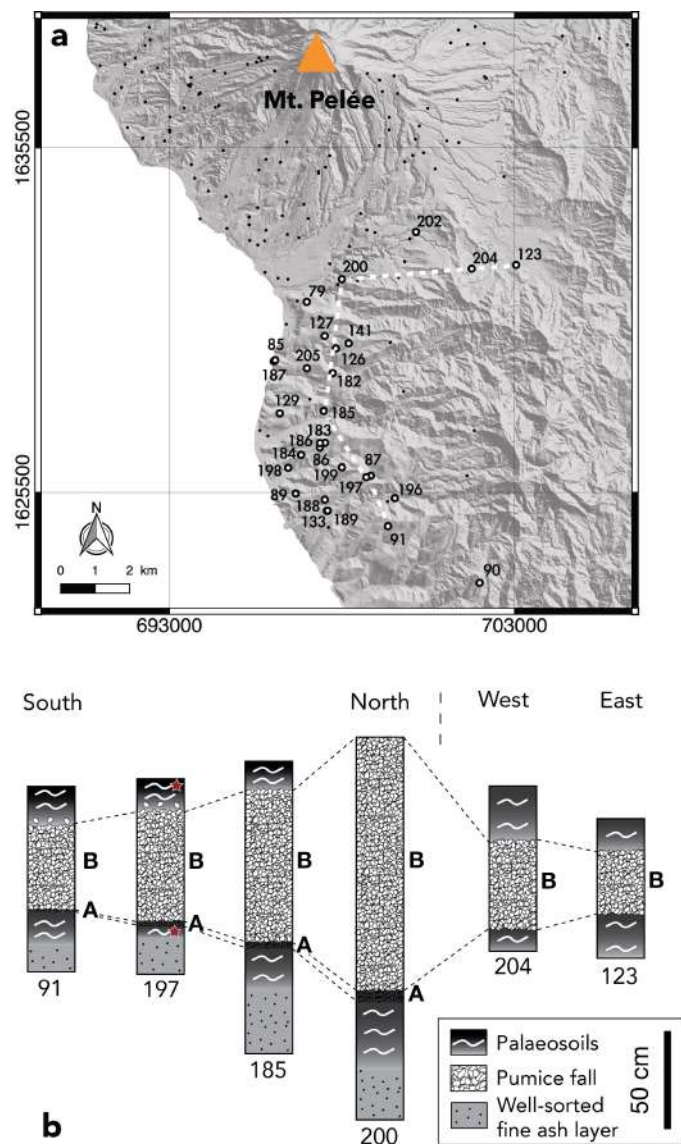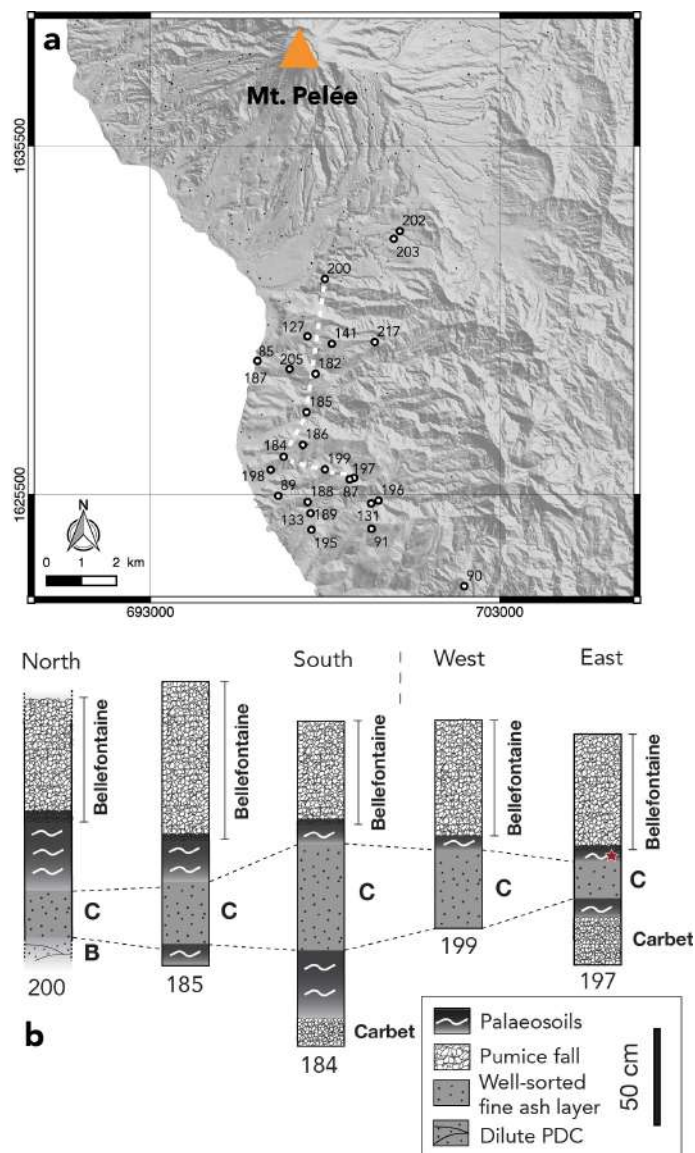
Figure 7: a Overview of our field area in Martinique. White circles and numbers refer to localities where Balisier deposits are present. Black dots show outcrop locations where Balisier deposits are absent (due to erosion) and/or too deeply buried under recent eruption deposits. The dotted line links the locations used in **b**, stratigraphic logs of representative sections of the Balisier deposits. The red stars in section 197 (Bellefontaine stadium section in Chapter 1) indicate the soils sampled for ^{14}C dating.

Elutriation by mechanical fracturation of the largest clasts requires them to collide and break off for a long time within the flowing PDC to become fine ash particles, implying that the co-PDC liftoff generally occurs near the maximum runout distance (Andrews & Manga, 2011; Engwell & Eychenne, 2016). In Martinique, the distance between the Mount Pelée summit and the sea is relatively small (< 10 km), hence this mechanism alone is not very likely to produce co-PDC plumes. The interaction with a body water may thus be a good candidate to explain the formation of the Balisier deposits. However, this type of interaction generally results in the formation of gas-pipes (Sigurdsson & Carey, 1989), and/or accretionary lapillis (Watanabe *et al.*, 1999), and/or the presence of shell and coral fragments in the deposits, which we never observed in the field. Moreover, we found no evidence that the basal part of the PDC reached the sea (Figure 8). The maximum extent of the PDC corresponds instead to the inner edge of the horseshoe-shaped structure created

by the second flank collapse that occurred between 127 and 25 ka (Le Friant *et al.*, 2003; Boudon *et al.*, 2005; Brunet *et al.*, 2017), suggesting that the hypothesis of the interaction with a topographical barrier is the most realistic scenario for this eruption.
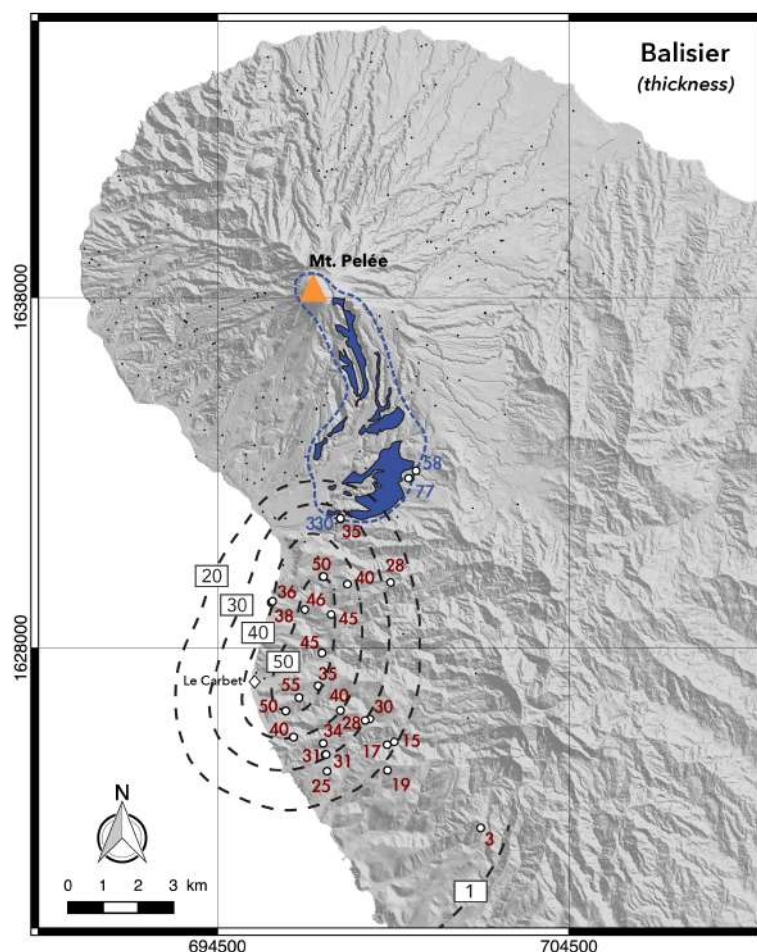
Figure 8: Isopach map (dashed lines, in centimeters) of the Balisier eruption. Open circles indicate measured sample locations with thicknesses measured for the Unit A deposits (in blue) and for the Unit C deposits (in red). The blue patches represent areas where Unit A deposits were identified by Westercamp *et al.* (1990), and the dotted blue line stands for the extrapolated global extent of the PDC deposits.

As the Balisier deposits are very fine-grained, it was too difficult to sample lithics belonging to this unit, and we thus could not construct a maximum lithic isopleth map for this eruption.

Due to the very few locations where Unit A and B deposits are present, we focus on the Unit C in the following sections. The deposits from the Unit C are indeed of special interest as they result from the formation of one or several substantial co-PDC plumes, and as they were found in areas considered to be safe in the current hazard map (see Introduction, Figure 7). For simplicity, we refer to the Unit C deposits as the Balisier deposits/eruption in the following sections, and we consider that only one co-PDC plume was produced.

2.2.3   The Carbet sequence

We identified the Carbet eruption deposits at 14 locations over 217 outcrops studied in northern Martinique (Figure 9a). Figure 9c shows a stratigraphic correlation of Carbet

outcrops along two different dispersal axes (North-South and West-East, see Figure 9a for localization). The deposits can be found up to 13.9 km from the vent (site 91 in Figure 9a).
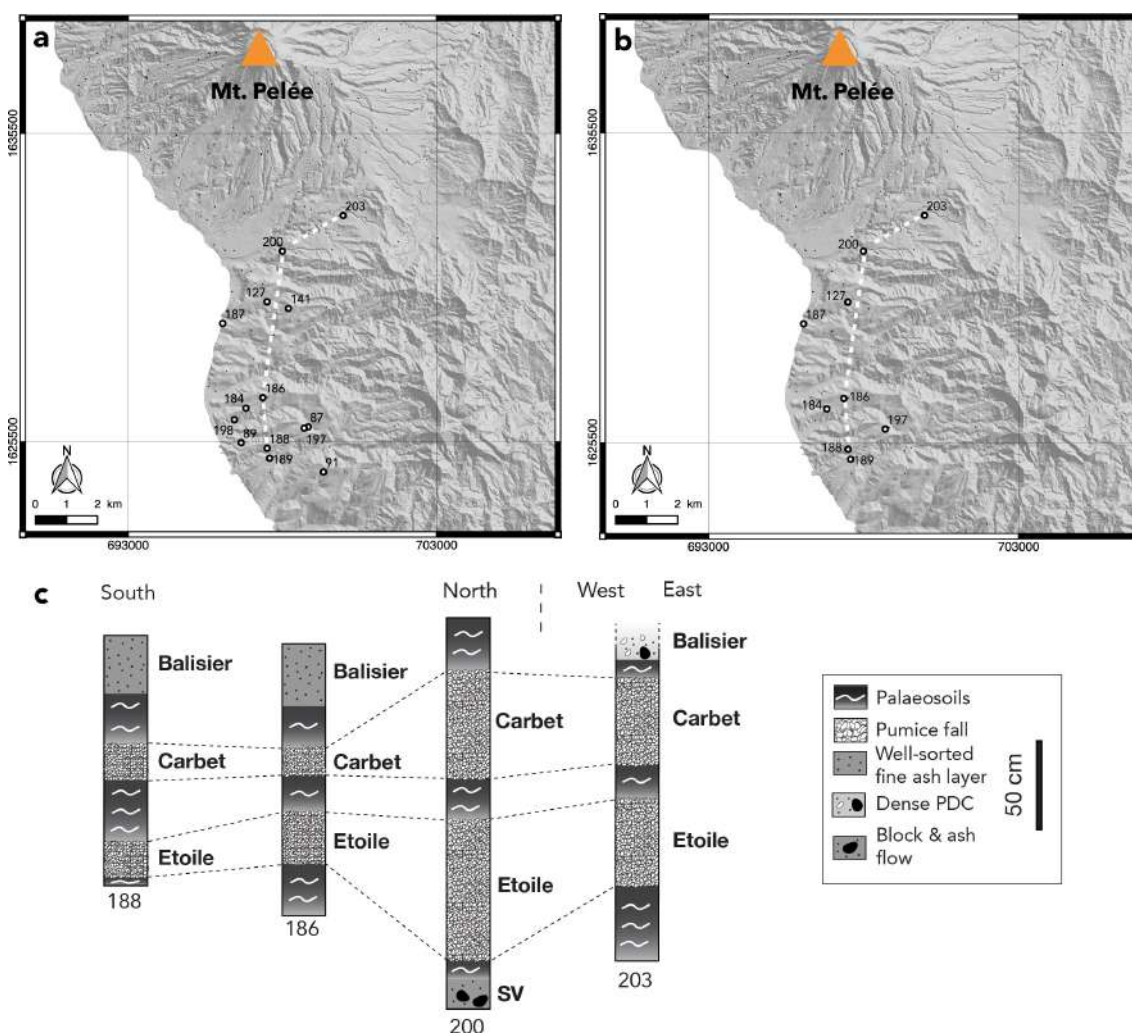
Figure 9: Overviews of our field area in Martinique, where white circles and numbers refer to localities where **a** Carbet deposits and **b** Etoile deposits are present. Black dots show outcrop locations where **a** Carbet and **b** Etoile deposits are absent (due to erosion) and/or too deeply buried under recent eruption deposits. The dotted lines link the locations used in **c**, stratigraphic logs of representative sections of the Carbet and Etoile deposits.

Thickness measurements at each location are reported in the isopach map shown in Figure 10a, later used to calculate the volume of deposits (see Section 3.1). The Carbet deposits can only be found on the southern flank of the Mount Pelée volcano, and vary between 70 cm at 6.5 km from the vent to 15 cm further south (Figure 10a). These thickness measurements show ellipsoidal contour patterns indicating a fallout dispersion towards the south-southwest, a slightly different dispersal axis than for the Bellefontaine eruption.

As the Carbet deposits are not very well-preserved, we were able to measure the major axis of the five largest lithic fragments at only a few outcrops in order to build an isopleth map for the Carbet eruption (Figure 10b). The resulting map, later used to estimate the maximum height and minimum exit velocity (see Section 3.2), is yet rather well-constrained and shows a direction of dispersal consistent with the one inferred from the isopach map.

2.2.4   The Etoile sequence

We identified the Etoile eruption deposits at 9 locations over 217 outcrops studied in northern Martinique (see Figure 9b). Figure 9c shows a stratigraphic correlation of Etoile outcrops along two different dispersal axes (North-South and West-East, see Figure 9b for localization). The deposits can be found up to 13.2 km from the volcano summit (site 189 in Figure 9b).
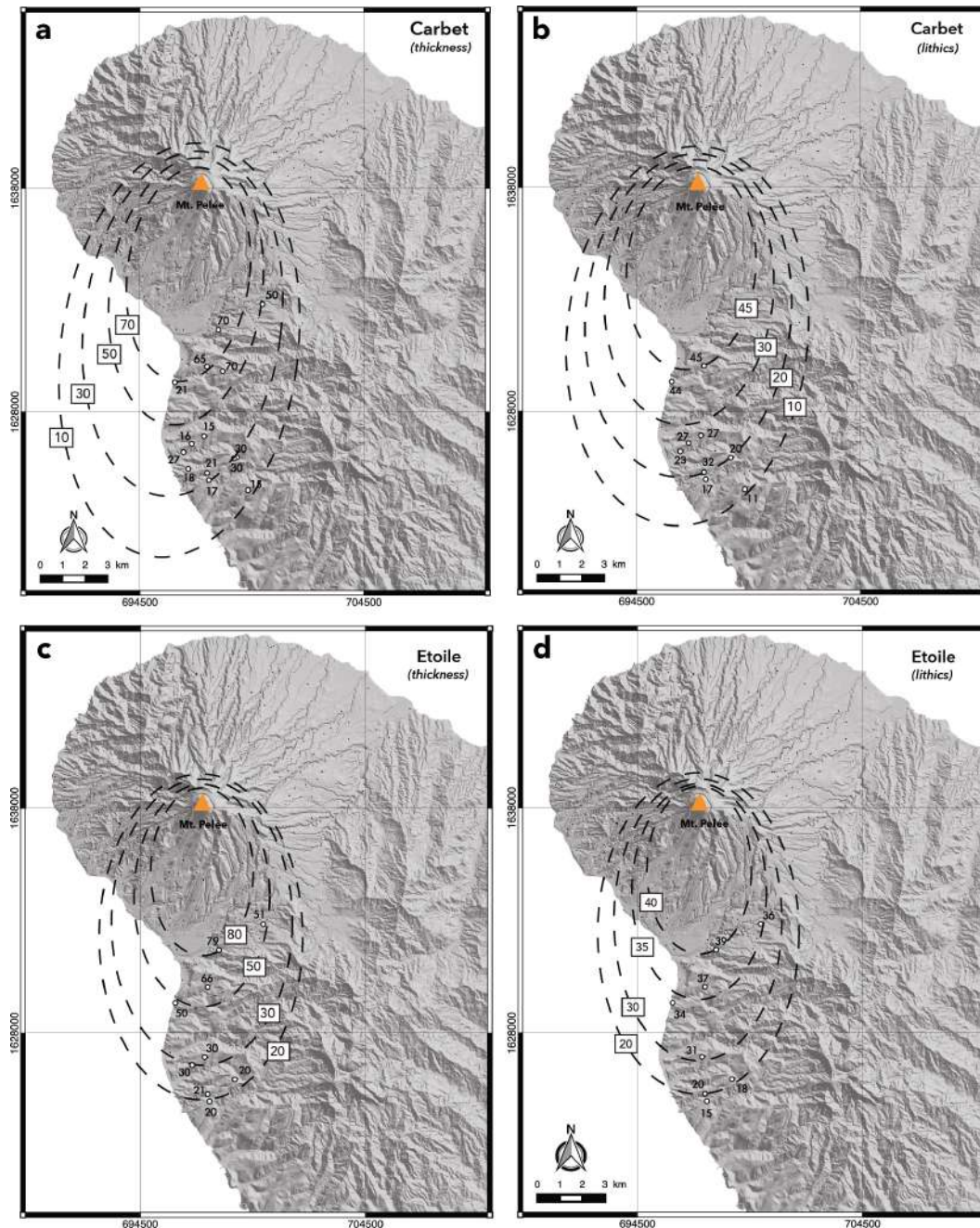
Figure 10: Isopach maps (in centimeters) for **a** Carbet eruption and **c** Etoile eruption, and isopleth map (in millimeters) for lithic fragments sampled at the base of **b** Carbet eruption and **d** Etoile eruption. Open circles indicate measured sample locations where we have identified Carbet and/or Etoile deposits (see Section 2.2 for details). The directions of dispersal axes inferred from isopach and isopleth maps are consistent with each other.

Thickness measurements at each location are reported in the isopach map shown in Figure 10c, later used to calculate the volume of deposits (see Section 3.1). The Etoile deposits can only be found on the southern flanks of the Mount Pelée volcano, and vary between 79 cm at 6.5 km from the vent to 20 cm further south (Figure 10c). These thickness measurements show ellipsoidal contour patterns indicating a fallout dispersion towards the south.

We measured the major axis of the five largest lithic fragments at each outcrop to build an isopleth map for the Etoile eruption later used to estimate the maximum height and minimum exit velocity (see Section 3.2). The isopleth map in Figure 10d is rather well-constrained thanks to the good preservation of the deposit, and shows a southern direction of the dispersal axis consistent with the one inferred from the isopach map.

2.3   Grain-size analyses

2.3.1   The Bellefontaine eruption

Sixteen samples from selected locations of Unit A and Unit B deposits were sampled and analyzed in order to determine the grain-size distribution of single sub-layers (Table 1) using the method described in Chapter 1, section 3.3. Individual grain-size distributions are shown in Appendix A.

Table 1: Sampling of the Bellefontaine deposits for grain-size analysis.

Sample	Site	Unit	Subunit	Altitude (m)	Distance from the vent (km)	Thickness (cm)
1	85	A	Bulk	37	9.0	5
2	126	A	Bulk	266	8.6	5
3	133	A	Bulk	188	13.3	2
4	141	A	Bulk	364	8.5	5
5	184	A	Bulk	154	11.6	3
6	185	A	Bulk	113	10.3	4
7	197	A	Bulk	335	12.3	2
8	89	B	Bulk	118	12.8	80
9	91	B	Bulk	380	13.9	60
10	127	B	Bulk	161	8.2	75
11	184	B	Bulk	154	11.6	50
12	185	B	Bulk	113	10.3	110
13	188	B	Bulk	171	12.9	45
14	189	B	Bulk	196	13.2	50
15	196	B	Bulk	173	13.0	60
16	197	B	Bulk	335	12.3	80

Unit A is fine-grained and poorly sorted with a relatively broad unimodal distribution (Figure A1a and b). At the different sites, the median diameter (Md ranging from -1.45ϕ to -0.10ϕ) and sorting (σ ranging from 1.17 to 1.56) have the typical values of fall deposits, but the amount of ash particles (< 2 mm) reaches relatively high values (up to 94 wt%). Unit B shows typical fallout characteristics with median diameter ranging from -2.93ϕ to -0.24ϕ and sorting ranging from 1.62 to 2.10. The grain-size distribution of individual samples is generally bimodal and shows variations in minimum, maximum, and modal grain-size

depending on distance from the vent (Figure A1c and d). The top of Unit B is always slightly coarser grained than its base, and the amount of ash particles (< 2 mm) increases regularly from proximal to distal locations (i.e., from 31 to 73 wt%).

We calculated the total grain-size distribution of both units using the method of Kaminski & Jaupart (1998) (see section 3.3 in Chapter 1). The ash fraction (< 2 mm) reaches 78 wt% for Unit A and 61 wt% for Unit B. We infer that the power-law exponent D that fully characterizes the TGSD decreases from $D = 3.6 \pm 0.1$ for Unit A (i.e., the population of fragments is dominated by fine ash particles) to $D = 3.0 \pm 0.1$ for Unit B (i.e., the population of fragments is evenly balanced between coarse and fine ash particles). These values are fully consistent with measurements made for various pumice fallout deposits (Kaminski & Jaupart, 1998), in particular those emplaced during small (i.e., $\approx$ 20 km-high) Plinian eruptions (Costa *et al.*, 2016). The total grain-size distribution of Unit A is unimodal and centered around 0ϕ (Figure 11a). Unit B is bimodal with peaks at -2.5ϕ and 1ϕ (Figure 11b). The median diameter is -0.44ϕ for Unit A and -0.91ϕ for Unit B, and the sorting is 1.36 for Unit A and 1.94 for Unit B.
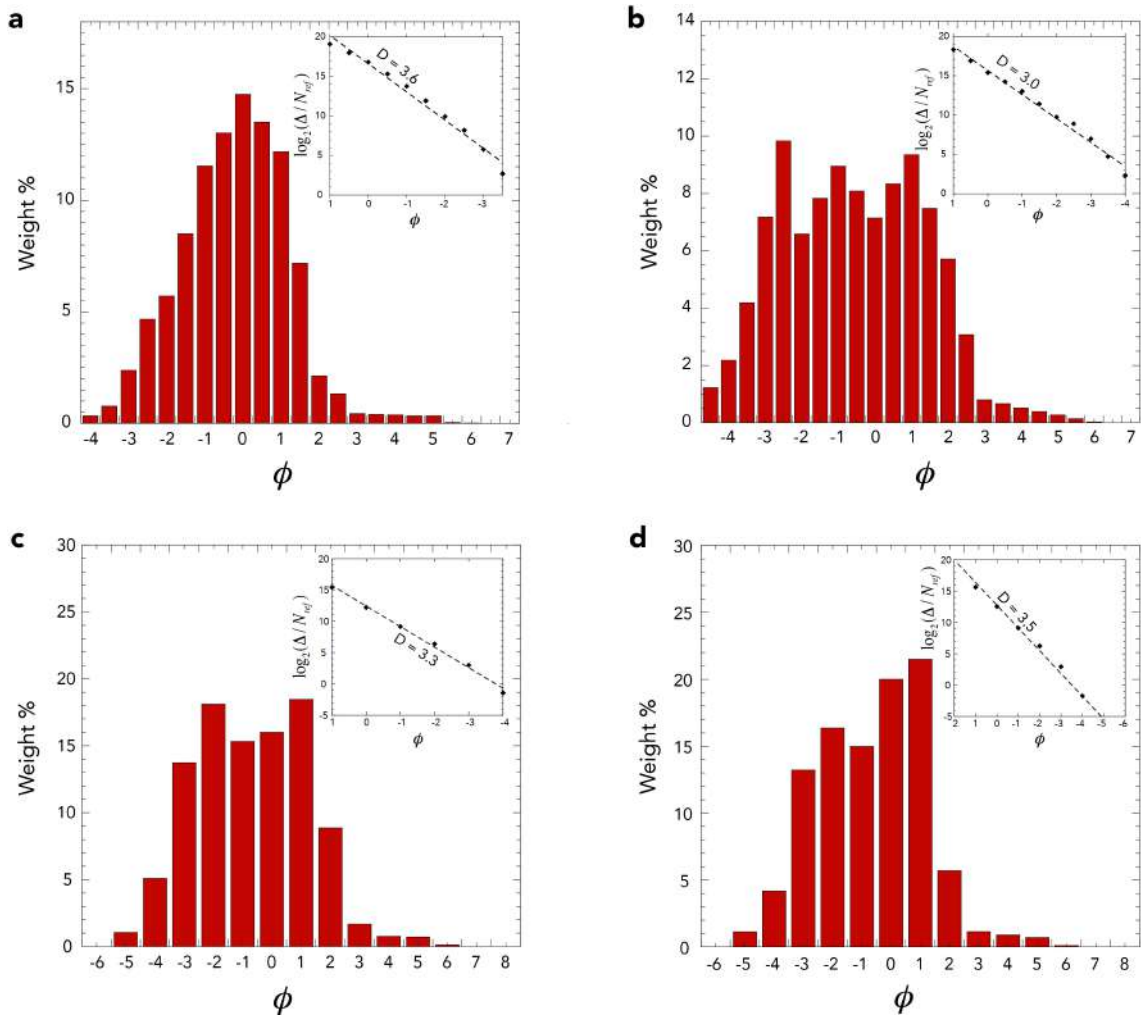
Figure 11: Reconstructed total grain-size distribution for **a** Unit A and **b** Unit B of the Bellefontaine eruption, **c** the Carbet eruption, and **d** the Etoile eruption. The insets show the same grain-size distributions reported as the number of fragments in each sieve class Δ normalized by an arbitrary constant N_{ref}, as a function of size. The size bounds used to estimate the power-law exponent D are $-4\ \phi$ to $1\ \phi$ (16 mm to 0.5 mm).

2.3.2   The Balisier eruption

Four samples collected at locations 182, 184, 187 and 189 (see Figure 7a for localization) were analyzed using secondary electrons SEM. We observed only two classes of particles in the Balisier deposits: crystals and pumices (Figure 12), which confirms that these deposits are volcanic material. We noted during the observations that the population of particles was very homogeneous in size, and that the particles seemed well-preserved. Some particles show a local variability in bubble shapes (tubular elongation), which can be interpreted as evidence for shear along the volcanic conduit margins.
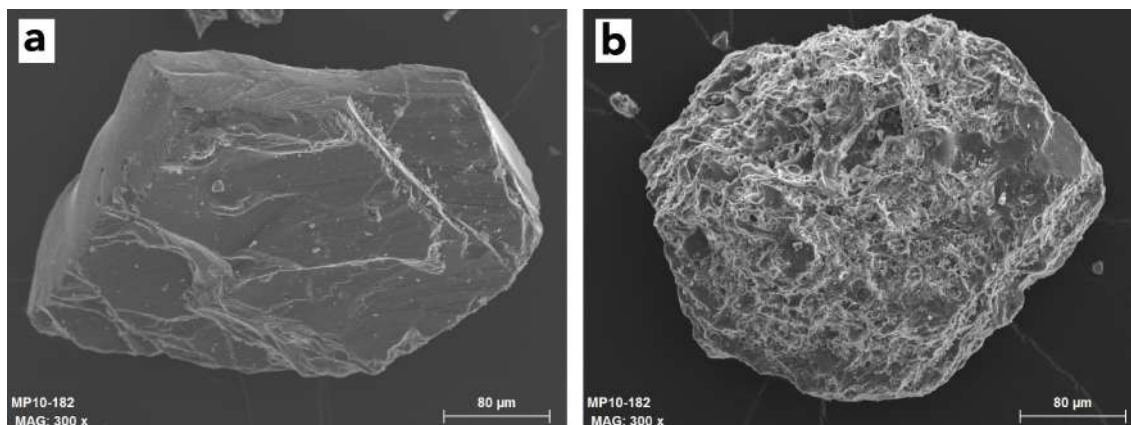
Figure 12: Secondary electrons SEM images of particles identified in the Balisier deposits: **a** an isolated crystal and **b** a highly vesiculated pumice. All scale bars are 80 μm long. *Courtesy of O. Roche.*

Fifteen samples from selected locations of Balisier deposits were sampled and analyzed in order to determine the grain-size distribution of single sub-layers (Table 2) using the method described in Chapter 1, section 3.3.

The Balisier deposits are very fine-grained and well-sorted with a strong unimodal distribution (Figure A1e and f). The grain-size distribution of individual samples shows small variations in minimum and maximum depending on the distance from the possible source (i.e., the topographical barrier). At the different sites, the median diameter (Md ranging from 1.3ϕ to 1.7ϕ) and sorting (σ ranging from 0.71 to 1.47) have the typical values of fall deposits (Figure 13a), but the amount of ash particles (< 2 mm) is always very high (from 93 wt% to 100 wt%).

We calculated the total grain-size distribution of these deposits using the method of Kaminski & Jaupart (1998) (see section 3.3 in Chapter 1). The ash fraction (< 2 mm) reaches 99.4 wt%. From these results, we calculated a power-law exponent D (fully characterizing the TGSD) of 4.6, which confirms that the population of fragments is strongly dominated by fine ash particles (inset in Figure 13b). The total grain-size distribution of the Balisier eruption is unimodal and centered around 2ϕ (Figure 13b). The median diameter is 1.62ϕ, while the sorting is 0.91. These values are slightly more important than those generally expected from co-PDC deposits but remain close to the values found for the co-PDC deposits originating from dome collapses at the Unzen or Montserrat volcanoes (between 3 and 5.5ϕ, Figure 6 in Engwell & Eychenne 2016).

2.3.3   The Carbet eruption

Eight samples from selected locations of Carbet deposits were sampled and analyzed in order to determine the grain-size distribution of single sub-layers (Table 2) using the method

described in Chapter 1, section 3.3.
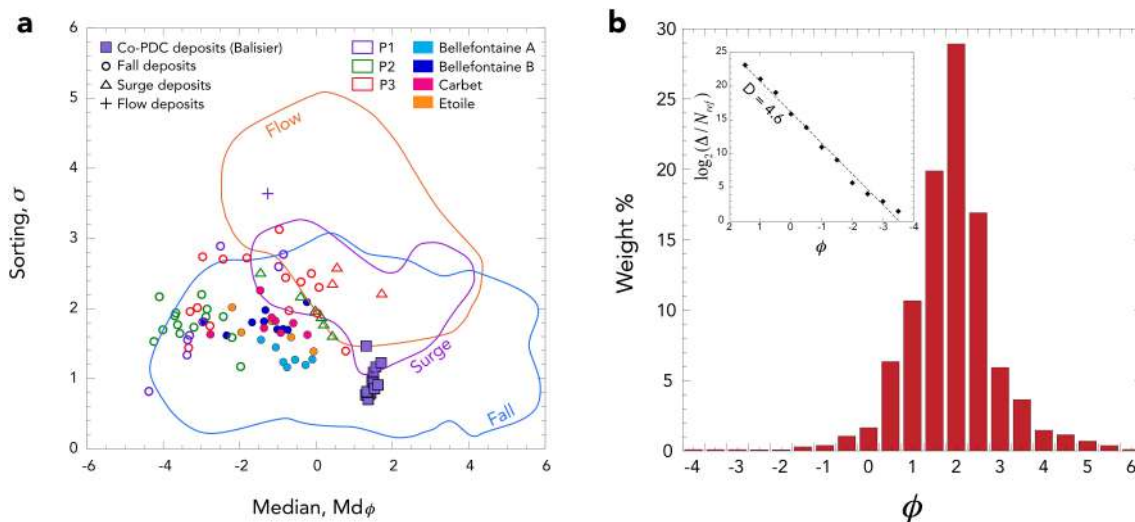
Figure 13: Grain-size analyses of the Balisier deposits. **a** Plot of median diameter vs. sorting of individual samples from several Mount Pelée eruptions compared to typical fields given by Walker (1971). Data for the P1, P2 and P3 eruptions are from Carazzo *et al.* (2012, 2019, 2020). **b** Reconstructed total grain-size distribution for the Balisier eruption (Unit C). The inset shows the same grain-size distribution reported as the number of fragments in each sieve class Δ normalized by an arbitrary constant N_{ref}, as a function of size. The size bounds used to estimate the power-law exponent D are -4 ϕ to 1 ϕ (16 mm to 0.5 mm).

The Carbet deposits show typical fallout characteristics with median diameter ranging from -2.77ϕ to -0.23ϕ and sorting ranging from 1.63 to 2.26. The grain-size distribution of individual samples is generally bimodal and shows variations in minimum, maximum, and modal grain-size depending on distance from the vent (Figure A2a and b). The amount of ash particles (< 2 mm) increases regularly from proximal to distal locations (i.e., from 30.4 to 80.7 wt%).

We calculated the total grain-size distribution of these deposits using the method of Kaminski & Jaupart (1998) (see Chapter 1, section 3.3). The ash fraction (< 2 mm) reaches 62 wt%. From these results, we calculated a power-law exponent D of 3.3, which shows that the population of fragments is dominated by fine particles (inset in Figure 11c). The total grain-size distribution of the Carbet eruption is bimodal with peaks at -2ϕ and 1ϕ (Figure 11c). The median diameter is -1.27ϕ, while the sorting is 1.93. These values are fully consistent with measurements made for various pumice fallout deposits (Kaminski & Jaupart, 1998) in particular those emplaced during small (i.e., $\approx$ 20 km-high) Plinian eruptions (Costa *et al.*, 2016).

2.3.4   The Etoile eruption

Five samples from selected locations of Etoile deposits were sampled and analyzed in order to determine the grain-size distribution of single sub-layers (Table 2) using the method described in Chapter 1, section 3.3.

The Etoile deposits show typical fallout characteristics with median diameter ranging from -2.2ϕ to -0.07ϕ and sorting ranging from 1.39 to 2.02. The grain-size distribution of individual samples is generally bimodal and shows variations in minimum, maximum, and modal grain-size depending on distance from the vent (Figure A2c and d). The amount of ash particles (< 2 mm) increases regularly from proximal to distal locations (i.e., from 46.9 to 86.2 wt%).

Table 2: Sampling of the Balisier (Unit C), Carbet, and Etoile deposits for grain-size analysis.

Sample	Site	Unit	Subunit	Altitude (m)	Distance from the vent (km)	Thickness (cm)
1	85	Balisier	Bulk	37	9.0	38
2	87	Balisier	Bulk	312	12.4	30
3	89	Balisier	Bulk	118	12.8	40
4	91	Balisier	Bulk	380	13.9	19
5	127	Balisier	Bulk	161	8.2	50
6	133	Balisier	Bulk	188	13.3	31
7	182	Balisier	Bulk	239	9.2	45
8	184	Balisier	Bulk	154	11.6	55
9	185	Balisier	Bulk	113	10.3	45
10	186	Balisier	Bulk	211	11.2	35
11	187	Balisier	Bulk	30	8.9	36
12	188	Balisier	Bulk	171	12.9	34
13	189	Balisier	Bulk	196	13.2	31
14	196	Balisier	Bulk	173	13.0	15
15	197	Balisier	Bulk	335	12.3	28
1	89	Carbet	Bulk	118	12.8	130
2	127	Carbet	Bulk	161	8.2	50
3	184	Carbet	Bulk	154	11.6	20
4	186	Carbet	Bulk	211	11.2	15
5	187	Carbet	Bulk	30	8.9	21
6	188	Carbet	Bulk	171	12.9	21
7	197	Carbet	Bulk	335	12.3	22
8	198	Carbet	Bulk	30	12.0	27
1	127	Etoile	Bulk	161	8.2	66
2	186	Etoile	Bulk	211	11.2	30
3	187	Etoile	Bulk	30	8.9	50
4	197	Etoile	Bulk	335	12.3	20
5	200	Etoile	Bulk	216	6.5	79

We calculated the total grain-size distribution of these deposits using the method of Kaminski & Jaupart (1998) (see Chapter 1, section 3.3). The ash fraction (< 2 mm) reaches 65.1 wt%. From these results, we calculated a power-law exponent D of 3.5, which shows that the population of fragments is dominated by rather fine particles (inset in Figure 11d). The total grain-size distribution of the Etoile eruption is bimodal with peaks at -2ϕ and 1ϕ (Figure 11d). The median diameter is -1.03ϕ, while the sorting is 1.83. These values are really similar to the ones found for the Bellefontaine and the Carbet eruptions (Figure 13a).

3   Eruptive dynamics

We now calculate the eruption parameters of the four newly discovered/revisited eruptions using the methods described in Chapter 1, section 3.4. All eruptive parameters are summarized in Table 3.

3.1   Erupted volumes

Figure 14a and b gives the thinning trend of Units A and B deposits of the Bellefontaine sequence based on proximal isopach contours (Figure 5a and b). Integration of the two-segment exponential fit (Fierstein & Nathenson, 1992), the power-law fit (Bonadonna & Houghton, 2005), and the Weibull fit (Bonadonna & Costa, 2012) computed using the AshCalc software (Daggit *et al.*, 2014) all yield a volume of 0.41 km^3. We thus retain a minimal volume of 0.41 km^3 for the Unit B fallout. The corresponding DRE volume is 0.175
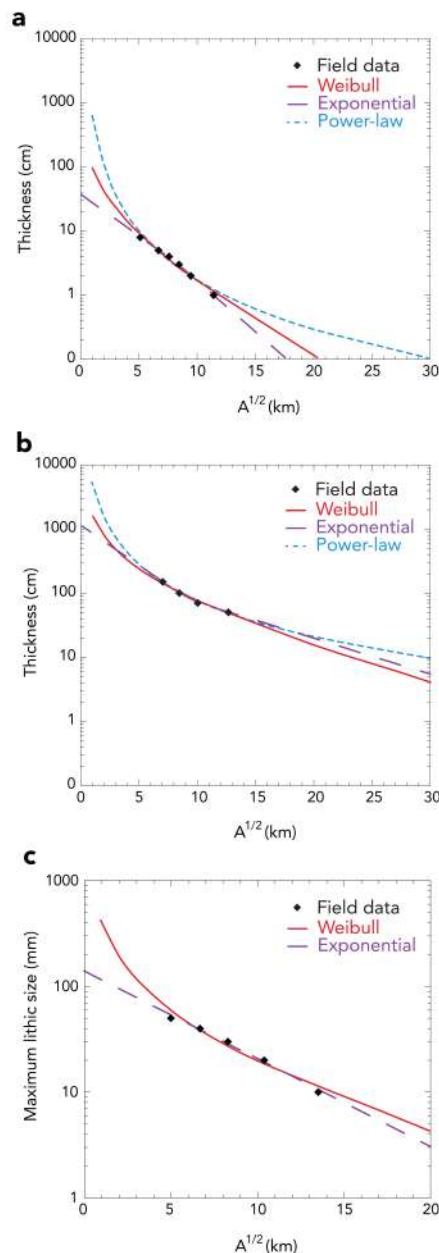
Figure 14: Deposit thinning profiles generated from the isopach maps for **a** Unit A and **b** Unit B of the Bellefontaine eruption, represented by semi-log plots of square root of isopach area (in kilometers) versus thickness (in centimeters). Thinning trends are approximated by exponential (purple dashed line), power-law (blue dotted line) and Weibull (red solid line) fits. **c** Semi-log plot of square root of isopleth area (in kilometers) versus lithic clast size (in millimeters), showing the Weibull and exponential best fits for the base of Unit B. All fitting parameters are given in Appendix B.

km^3 based on deposit and magma densities of 1070 kg m^{-3} and 2500 kg m^{-3}, respectively (Traineau *et al.*, 1989). The same methods used for Unit A yield a volume of 0.01 km^3, 0.02 km^3, and 0.01 km^3 for the exponential fit, the power-law fit, and the Weibull fit, respectively. We thus retain a minimal volume of 0.01 − 0.02 km^3 for Unit A, corresponding to a DRE volume of 0.004 − 0.009 km^3.

The final estimate of the total volume of the **Bellefontaine eruption** (Unit A + Unit B) is thus 0.180 − 0.184 km^3 DRE, and the total mass of tephra emitted is estimated to be 4.5 − 4.6 × 10^{11} kg, which corresponds to a magnitude 4.6 (Pyle, 2000) and a VEI 4 event (Newhall & Self, 1982).

Figure 15 gives the thinning trend of Unit C deposits of the Balisier sequence based on proximal isopach contours (Figure 8). Integration of the two-segment exponential fit (Fierstein & Nathenson, 1992), the power-law fit (Bonadonna & Houghton, 2005), and the Weibull fit (Bonadonna & Costa, 2012) computed using the AshCalc software (Daggit *et al.*, 2014) yield a volume of 0.036, 0.045 and 0.029 km^3, respectively. We thus retain a minimal volume of 0.036 ± 0.008 km^3 for the Unit C. The corresponding DRE volume is 0.016 ± 0.003 km^3 based on deposit and magma densities of 1070 kg m^{-3} and 2500 kg m^{-3}, respectively (Traineau *et al.*, 1989). Here, we use the area covered by the dense PDC deposits to assess their volume. The cumulative dense PDC (Unit A) covers 14 km^2, with an average thickness of 3 ± 1 meters (Figure 8). This yields a minimum volume of 0.042 ± 0.014 km^3 DRE. As we have only one thickness measurement for the surge deposits (Unit B), we cannot assess its volume. Comparing the volumes of Unit A and Unit C, we estimate an elutriation factor of 25%, a value in good agreement with those measured for the 1997 Montserrat (10%), 1980 Mt St Helens (23%), 75,000 yr BP Toba (30%), and 1815 Tambora (40%) eruptions (Woods & Wohletz, 1991; Bonadonna *et al.*, 2002).
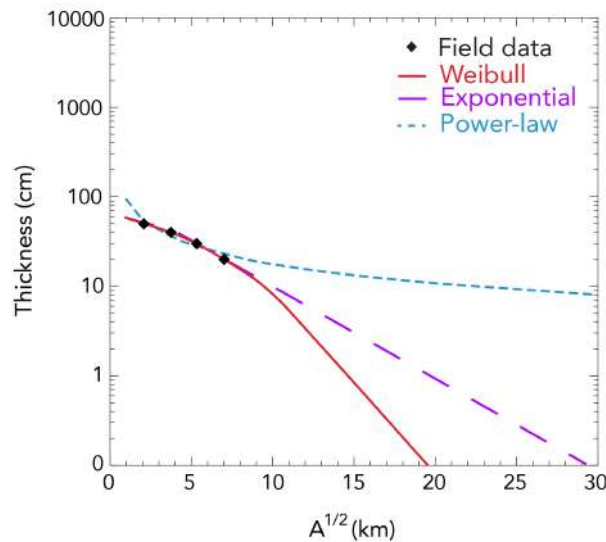
Figure 15: Deposit thinning profiles generated from the isopach map for the Balisier eruption, represented by a semi-log plot of square root of isopach area (in kilometers) versus thickness (in centimeters). Thinning trends are approximated by exponential (purple dashed line), power-law (blue dotted line) and Weibull (red solid line) fits. All fitting parameters are given in Appendix B.

These results yield a minimum total volume of 0.058 ± 0.017 km^3 DRE for the **Balisier eruption** (Unit A + Unit C), and the total mass of tephra emitted is estimated to be 1 − 2 × 10^{11} kg, which corresponds to a magnitude 4.1 (Pyle, 2000) and a VEI 4 event (Newhall & Self, 1982).

Figure 16a and c gives the thinning trend of the Carbet and Etoile eruptions, respectively, based on proximal isopach contours (Figure 10a and c).

Integration of the one-segment exponential fit (Pyle, 1989), the power-law fit (Bonadonna & Houghton, 2005), and the Weibull fit (Bonadonna & Costa, 2012) computed using the AshCalc software (Daggit *et al.*, 2014) for the Carbet eruption yield a volume of 0.114, 0.197 and 0.118 km^3, respectively. We thus retain a minimal volume of 0.143 ± 0.047 km^3. The corresponding total DRE volume of the **Carbet eruption** is 0.061 ± 0.02 km^3 based on deposit and magma densities of 1070 kg m^{-3} and 2500 kg m^{-3}, respectively (Traineau *et al.*, 1989). The total mass of tephra emitted is estimated to be $1 - 2 \times 10^{11}$ kg, which corresponds to a magnitude 4.1 (Pyle, 2000) and a VEI 4 event (Newhall & Self, 1982).
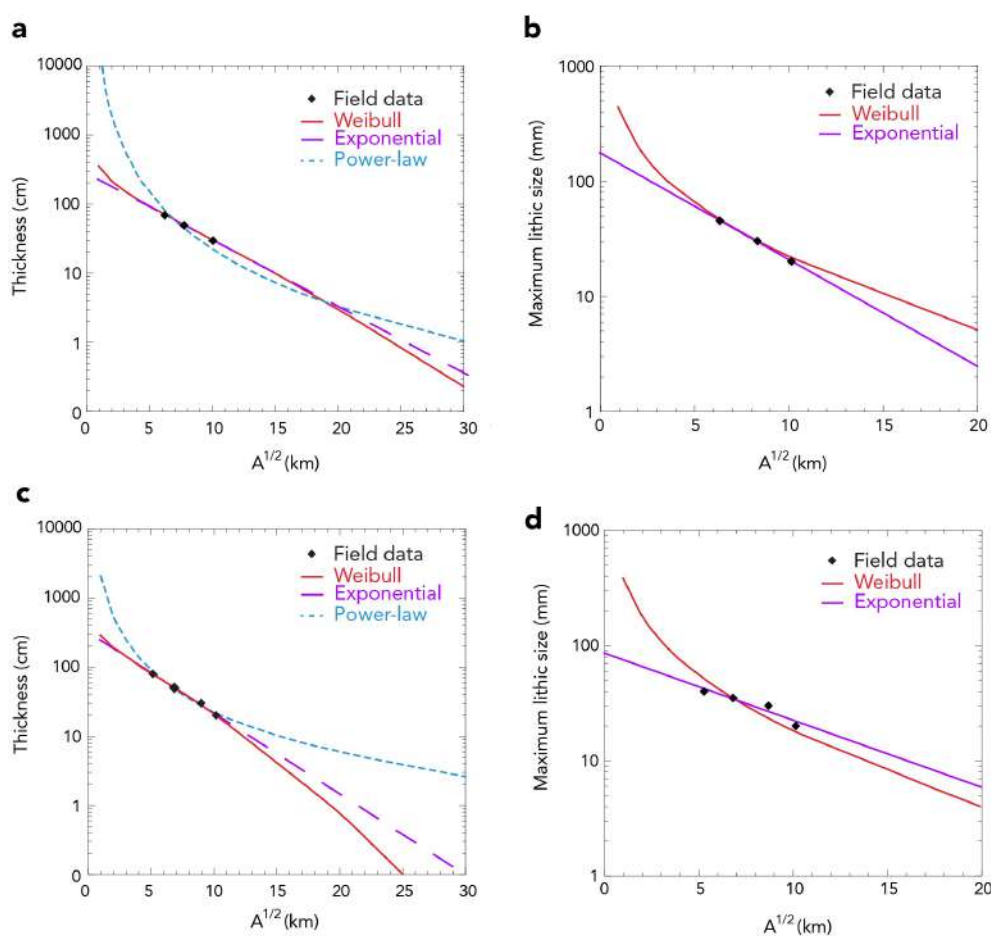
Figure 16: Deposit thinning profiles generated from the isopach maps for the **a** Carbet and **c** Etoile eruptions, represented by semi-log plots of square root of isopach area (in kilometers) versus thickness (in centimeters). Thinning trends are approximated by exponential (purple dashed line), power-law (blue dotted line) and Weibull (red solid line) fits. Semi-log plot of square root of isopleth area (in kilometers) versus lithic clast size (in millimeters), showing the Weibull and exponential best fits for **b** Carbet and **d** Etoile eruptions. All fitting parameters are given in Appendix B.

The same methods used for the Etoile eruption yield a volume of 0.088 km^3, 0.120 km^3, and 0.085 km^3 for the exponential fit, the power-law fit, and the Weibull fit, respectively. We thus retain a minimal volume of 0.1 ± 0.02 km^3 for the **Etoile eruption**, corresponding to a DRE volume of 0.042 ± 0.01 km^3. The total mass of tephra emitted is estimated to be $0.8 - 1.3 \times 10^{11}$ kg, which corresponds to a magnitude 4 (Pyle, 2000) and a VEI 4 event (Newhall & Self, 1982).

3.2 Column heights and exit velocities

Bellefontaine eruption: we use the model of Carey & Sparks (1986) adapted to tropical atmospheric conditions in Central America (Carey & Sigurdsson, 1986) to infer the maximum height reached by the Bellefontaine eruptive column (see Chapter 1, section 3.4). Within this framework, our isopleth map (Figure 5c) yields a maximum height of 20.1 ± 0.4 km for the plume that produced the base of Unit B. Figure 14c gives the decreasing trend of maximum lithic size as a function of the square root of isopleth contours for fragments collected at the base of Unit B. Following the approach of Bonadonna & Costa (2013), a Weibull fit gives a maximum height of 19.7 ± 0.1 km for the volcanic plume at the beginning of the Unit B, which is equivalent to the estimation made using the method of Carey & Sigurdsson (1986). We thus retain an average value of 20 ± 0.5 km for the maximum height reached by the volcanic plume that produced Unit B.

We also use data of Figure 14c to estimate the minimum exit velocity of the volcanic plume at the vent (see Chapter 1, section 3.4). Extrapolating the exponential curve in Figure 14c down to $A^{1/2} = 0$, we can calculate a maximum lithic size at the vent that, using Equation (3) in Chapter 1, gives a minimum velocity required to carry up this fragment up in the vertical plume of 232 ± 10 m s^{-1}. Using the same method on a decreasing trend of the maximum lithic size as a function of half the crosswind range, we infer a minimum exit velocity of 214 ± 10 m s^{-1}. We thus retain an average minimum exit velocity at the vent of 223 ± 20 m s^{-1} for the beginning of Unit B.

Balisier eruption: As we have no isopleth map for the Balisier eruption, we estimate the maximum height of the co-PDC plume by using the PDC run-out and the mass discharge rate associated with it. Alternatively, we could estimate the maximum height using the mass of deposits (as in Bonadonna *et al.* 2002) but this method would increase the error in our estimation as we consider for simplicity that only one co-PDC produced the deposits found in the field. Our results are detailed in the following subsection.

Carbet eruption: As for the Bellefontaine eruption, we infer a maximum column height of 18.7 ± 0.6 km from our isopleth map (Figure 10b) and using the model of Carey & Sigurdsson (1986). Figure 16b gives the decreasing trend of maximum lithic size as a function of the square root of isopleth contours for fragments collected at the base of Carbet deposits. Following the approach of Bonadonna & Costa (2013), a Weibull fit gives a maximum height of 20.5 ± 0.1 km for the volcanic plume at the beginning of the eruption. We thus retain an average value of 19.6 ± 0.7 km for the maximum height reached by the volcanic plume.

Extrapolating the exponential curve in Figure 16b down to $A^{1/2} = 0$, we can calculate a maximum lithic size at the vent that, using Equation (3) in Chapter 1, gives a minimum velocity required to carry up this fragment up in the vertical plume of 260 ± 10 m s^{-1}. Using the same method on a decreasing trend of the maximum lithic size as a function of half the crosswind range, we infer a minimum exit velocity of 257 ± 10 m s^{-1}, which is very close to the first estimate. We thus retain an average minimum exit velocity at the vent of 258 ± 20 m s^{-1} for the beginning of the Carbet eruption.

Etoile eruption: We infer a maximum column height of 18.4 ± 0.3 km from our isopleth map (Figure 10d) and using the model of Carey & Sigurdsson (1986). Figure 16d gives the decreasing trend of maximum lithic size as a function of the square root of isopleth contours for fragments collected at the base of Etoile deposits. Following the approach of Bonadonna & Costa (2013), a Weibull fit gives a maximum height of 19.7 ± 0.1 km for the volcanic plume at the beginning of the eruption. We thus retain an average value of 19 ± 0.4 km for

the plume maximum height.

Extrapolating the exponential curve in Figure 16d down to $A^{1/2} = 0$, we can calculate a maximum lithic size at the vent that, using Equation (3) in Chapter 1, gives a minimum velocity required to carry up this fragment up in the vertical plume of 182 ± 10 m s^{-1}. Using the same method on a decreasing trend of the maximum lithic size as a function of half the crosswind range, we infer a minimum exit velocity of 184 ± 10 m s^{-1}, which is very close to the first estimate. We thus retain an average minimum exit velocity at the vent of 183 ± 20 m s^{-1} for the beginning of the Etoile eruption.

3.3   Mass discharge rates and durations

Bellefontaine eruption: We calculate the mass discharge rate (MDR) feeding the plume produced by Bellefontaine eruption based on the maximum height and using empirical scaling relationships from Carazzo *et al.* (2014) and Woodhouse *et al.* (2016), which explicitly include the effect of wind (see Chapter 1, section 3.4). A first estimate is given by considering a linear wind profile increasing from 0 m s^{-1} at the ground to 20-30 m s^{-1} at the tropopause. Within this framework, a maximum column height of 20 km, and tropical atmospheric conditions, yield a maximum MDR of $(2 - 4.8) \times 10^7$ kg s^{-1} for the Carazzo *et al.* (2014) relationship and a maximum MDR of 5×10^7 kg s^{-1} for the Woodhouse *et al.* (2016) one. A third estimate can be obtained by considering a more realistic and complex wind profile as in Girault *et al.* (2016) who calculated the maximum height reached by a volcanic column as a function of the total grain-size distribution at the vent. Taking their complex wind profile, which is closer to the average wind profiles in the Lesser Antilles as it shows a wind shear in speed and a reversal in direction (Dunion, 2011), we infer a maximum MDR of 6×10^7 kg s^{-1}.

Based on these three estimates, we retain a peak MDR for the beginning of Unit B of $(5 \pm 1) \times 10^7$ kg s^{-1}, a value corresponding to an eruption intensity of 10.7 (Pyle, 2000). Combined with the total mass of fallout deposits (Section 3.1), this MDR provides a minimum duration of about 2.5 ± 0.5 hours for the Bellefontaine eruption.

Balisier eruption: We calculate the MDR required to produce the Unit A PDC run-out of 7.1 km using the method of Bursik & Woods (1996), and found $\approx 10^8$ kg s^{-1}. Taking an elutriation factor of 25% (Section 3.1) yields a source MDR for the Unit C of $\approx 2.5 \times 10^7$ kg s^{-1}. Such a MDR corresponds to a ≈ 13 km-high co-PDC plume (Woods & Wohletz, 1991). The uncertainties of these estimates are not straightforward to quantify, as all the calculations mostly rely on the estimated MDR for Unit A (and as several co-PDC plumes could have been produced). Our preliminary estimate of the co-PDC plume height will be tested using a tephra dispersion model in Chapter 5. Combining the total MDR of $\approx 10^8$ kg s^{-1} for the Balisier eruption with the total mass of deposits calculated earlier (Section 3.1), we obtain an intensity of 11 for this eruption and a minimum duration for the PDC of ≈ 25 minutes.

Carbet eruption: Using a maximum column height of 19.6 km, tropical atmospheric conditions, together with the same methods than for the Bellefontaine eruption, we obtain a maximum MDR of $(2 - 2.7) \times 10^7$ kg s^{-1} for the Carazzo *et al.* (2014) relationship, 3.8 $\times 10^7$ kg s^{-1} for the Woodhouse *et al.* (2016) one, and 1.2×10^7 kg s^{-1} with the complex wind profile of Girault *et al.* (2016). We thus retain a peak MDR of $(3 \pm 2) \times 10^7$ kg s^{-1} for the Carbet eruption, a value corresponding to an eruption intensity of 10.5. Combined with the total mass of fallout deposits (Section 3.1), this MDR provides a minimum duration of ≈ 85 minutes for the Carbet eruption.

Table 3: Summary of the estimated eruptive parameters for the Plinian Bellefontaine, Carbet and Etoile eruptions (this study), the Pelean Balisier eruption (this study), and comparison with the recent Plinian eruptions P1 (Carazzo *et al.*, 2012), P2 (Carazzo *et al.*, 2019) and P3 (Carazzo *et al.*, 2020). * Value given for the co-PDC plume.

Parameters	Bellefontaine (13,516 cal BP)	Balisier (14,072 cal BP)	Carbet (18,711 cal BP)	Etoile (21,450 cal BP)	P1 (650 BP)	P2 (1,670 BP)	P3 (2,010 BP)
Volume (km³ bulk/DRE)	0.42/0.18	0.13/0.06	0.14/0.06	0.1/0.04	0.37/0.16	1.8/0.77	2.38/1.02
Erupted mass (kg)	4.55×10^{11}	1.5×10^{11}	1.5×10^{11}	1.05×10^{11}	4×10^{11}	1.7×10^{12}	2.4×10^{12}
VEI	4	4	4	4	4	4	5
Magnitude	4.6	4.1	4.1	4	4.6	5.2	5.4
Max. height (km)	20	$\approx 13^*$	19.6	19	22	26	30
Exit velocity (m s⁻¹)	214–232	–	257–260	182–184	150–165	180–200	210–220
Max. PDC runout (km)	–	7.1	–	–	4.5–8	7–11.5	7–10.3
Max. MDR (fall, kg s⁻¹)	5×10^7	$\approx 10^8$ (PDC)	3×10^7	2.6×10^7	3.6×10^7	1.1×10^8	1.4×10^8
Duration	>2h30	>25 min (PDC)	>1h30	>1h	>5h	>7h	>11h
Max. intensity	10.7	11	10.5	10.4	11	11.5	11.4
TGSD	$D = 3.0\text{--}3.6$ Md=-0.91--0.44ϕ $\sigma = 1.94\text{--}1.36$	$D = 4.6$ Md=1.62ϕ $\sigma = 0.91$	$D = 3.3$ Md=-1.27ϕ $\sigma = 1.93$	$D = 3.5$ Md=-1.03ϕ $\sigma = 1.83$	$D = 3.2\text{--}3.3$ Md=-3.7ϕ $\sigma = 2.32$	$D = 3.4\text{--}3.5$ Md=-2.8--3.1ϕ $\sigma = 1.8\text{--}2$	$D = 3.3$ Md=-0.2ϕ $\sigma = 2.3$
Dispersal axis	S	S	SSW	S	SW	NNE	WSW

Etoile eruption: Accounting for a maximum column height of 19 km, tropical atmospheric conditions, together with the same methods than for the Bellefontaine eruption, we obtain a maximum MDR of $(2.3 - 3.1) \times 10^7$ kg s^{-1} for the Carazzo *et al.* (2014) relationship, 4.1×10^7 kg s^{-1} for the Woodhouse *et al.* (2016) one, and 1×10^7 kg s^{-1} with the complex wind profile of Girault *et al.* (2016). We thus retain a peak MDR of $(2.6 \pm 1.5) \times 10^7$ kg s^{-1} for the Etoile eruption, a value corresponding to an eruption intensity of 10.4. This MDR provides a minimum duration of ≈ 66 minutes for the Etoile eruption when combined with the total mass of fallout deposits (Section 3.1).

4   Discussion

4.1   Summary of eruptive parameters

First and foremost, the Bellefontaine, Carbet and Etoile events contrast with the three most recent Plinian eruptions at Mount Pelée volcano (P1, P2, and P3, see Table 3) by their unusual southward dispersal. But one can note some other differences between these six eruptions. The minimum eruption durations are estimated to be 2h30, 1h30 and 1h for the Bellefontaine, Carbet and Etoile eruptions, respectively, compared to 11h for P3, 7h for P2, and 5h for P1, making these older Plinian eruptions relatively short-duration events in Martinique. Grain-size analyses reveal that the eruptive products of the Bellefontaine eruption are coarser ($D = 3.0$ for main Unit B) than those of the Carbet ($D = 3.3$), Etoile ($D = 3.5$), P3 ($D = 3.3$), P2 ($D = 3.4$) and P1 eruptions ($D = 3.2$). Moreover, the Bellefontaine, Carbet and Etoile eruptions seem to have produced rather stable columns as no PDC deposits were identified (which would mean that no column collapse occurred), while the most recent Plinian eruption at Mount Pelée all experienced column collapse phases.

The minimum exit velocities inferred for the Bellefontaine ($214-232$ m s^{-1}) and P3 ($210-220$ m s^{-1}) eruptions are similar to each other and larger than those of the Etoile ($182-184$ m s^{-1}), P1 ($150-165$ m s^{-1}), and P2 ($180-200$ m s^{-1}) events. The minimum exit velocity estimated for the Carbet eruption is even higher ($257-260$ m s^{-1}), which could mean that the Bellefontaine, Carbet and P3 eruptions would have exsolved gas contents higher than those of the Etoile, P1 and P2 events. We do not have any estimate of exsolved gas contents for the oldest Plinian eruptions, but Carazzo *et al.* (2020) indeed showed that P3 has higher exsolved gas contents ($2-2.9$ wt%) than P1 ($1.6-2.1$ wt%) and P2 ($1.7-2.1$ wt%).

Apart from these points, the eruptive parameters retrieved from field data for the Bellefontaine, Carbet, and Etoile eruptions are close to those estimated for the P1, and P2 eruptions (Table 3). All five eruptions are VEI 4 events during which the Plinian column reached a similar maximum height (i.e., $19-21$ km for the Bellefontaine event, 19.6 km for the Carbet event, and 19 km for the Etoile eruption, compared to $22-26$ km for P2, and $19-22$ km for P1). Their mass discharge rates are also very similar to each other ($\approx 10^7$ kg s^{-1}). The P3 eruption steps out from the usual pattern, as this is the only VEI 5 event recorded at Mount Pelée volcano, with a maximum column height reaching 30 km and a MDR larger than 1.4×10^8 kg s^{-1}.

The Balisier eruption is a rather unique Pelean event in the eruptive history of Mount Pelée, which first produced a PDC of similar runout distance (7.1 km) than those of P1 ($4.5-8$ km), P2 ($7-11.5$ km) and P3 ($7-10.3$ km). As this PDC encountered a topographical barrier (i.e., the inner edge of the structure created by the flank collapse that occurred

between 127 and 25 ka, Le Friant *et al.* 2003; Brunet *et al.* 2017), a $\approx$ 13 km-high co-PDC plume rose and spread volcanic ash over the St-Pierre/Bellefontaine area. This column height estimate bears large uncertainties (see Section 3.3) but is very similar to the maximum column heights reached by the co-PDC plumes produced by the 1997 Soufriere Hills eruption in Montserrat (few hundred meters to 15 km, Bonadonna *et al.* 2002; Engwell & Eychenne 2016), and the 1990 Mount Redoubt eruption in Alaska (12 km, Woods & Kienle 1994; Engwell & Eychenne 2016), also originating from dome-forming events. The elutriation factor calculated using our estimated volumes of Unit A and C reaches 25%. Similar calculations made during the 1997 Montserrat, 1980 Mount St. Helens, 75,000 yr BP Toba, and 1815 Tambora eruptions provide similar estimates (between 10 and 40%), which reinforces the confidence that our estimated elutriation factor is relevant. Although the TGSD of the Unit C deposits is much finer ($D = 4.6$, because of the strong elutriation producing the co-PDC plume) compared to other eruptions studied here, the Pelean Balisier eruption is very similar to the stronger Plinian eruptions of Mount Pelée volcano in terms of other eruptive parameters. Its volume and erupted mass are even equal to those of the Carbet eruption. Moreover, the Balisier eruption spread volcanic ash towards the south beyond the town of St-Pierre, which is very unusual for a Pelean event.

These six Plinian eruptions and the Pelean event named Balisier, rather similar in terms of eruptive parameters, show the importance of wind variability in setting the main dispersal axis because they spread tephra in different directions (Table 3). Taken together, they impacted the totality of the northern part of Martinique (up to Fort-de-France), and thus constitute a strong basis to include Plinian eruptions in volcanic hazard assessment in Martinique. The Balisier eruption also demonstrates that even the volcanic hazards characterizing Pelean events should be considered beyond the towns of St-Pierre and Le Carbet towards south, as a co-PDC plume rising from a pyroclastic density current generated by a dome-forming eruption can also spread volcanic material beyond the safe area limits of the current hazard map (see Introduction, Figure 7).

4.2   Possible scenario for hazard assessment

We have now a more precise knowledge of the dynamics of six Plinian eruptions that occurred at the Mount Pelée volcano in the past 24,000 years. Comparing the eruptive parameters of these eruptions, together with the Balisier event ones, allows us to forecast what is the most probable eruptive scenario in the future at Mount Pelée volcano.

Figure 17 shows the main eruptive parameters (MDR and volume ranges) of the seven reconstructed eruptions (fall phases only) from the Mount Pelée volcano. The MDR vs. volume plot is divided into nine squares standing for nine eruptive scenarii, with a volume increasing from 0.01 to 10 km^3 DRE and a MDR ranging from 10^6 to 10^9 kg s^{-1}. These conditions cover the entire range of eruptive parameters calculated for the Mount Pelée eruptions. One can note that we find at this volcano the positive correlation between MDR and the total volume ejected during the Plinian phases already demonstrated for 45 eruptions by Carey & Sigurdsson (1989).

From Figure 17, we determine that the most likely future eruptive scenario in Martinique would be an eruption with a MDR ranging between 10^7 and 10^8 kg s^{-1}, and a volume between 0.1 and 1 km^3 DRE. Three out of seven eruptions are indeed in these eruptive parameters ranges. The Carbet and Etoile eruptions define the second most likely eruptive scenario with the same range of MDR, but with lower volume (between 0.01 and 0.1 km^3 DRE). The P2 and P3 eruptions, both reaching a MDR $> 10^8$ kg s^{-1}, define two less likely,
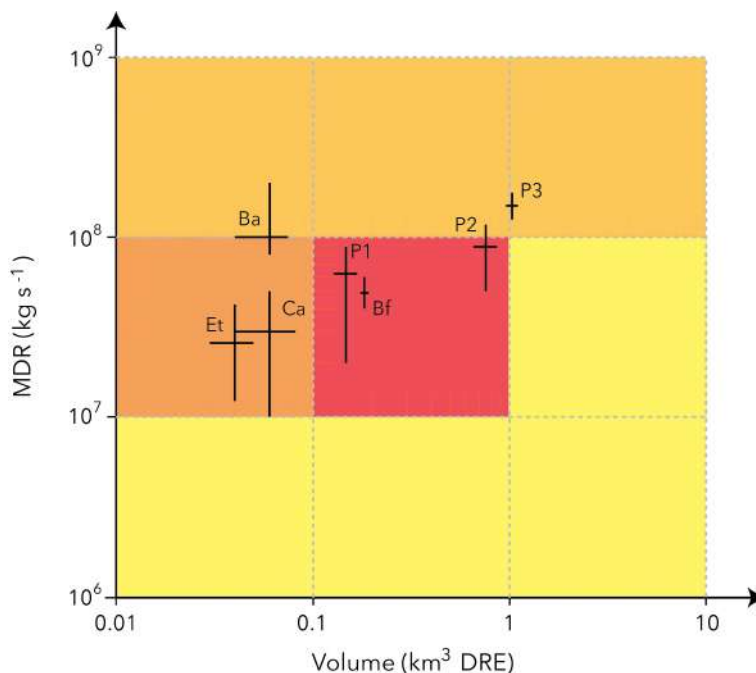
Figure 17: Mass discharge rates of fall phases from the seven reconstructed eruptions of the Mount Pelée volcano as a function of their total volumes: *Ba: Balisier; Ca: Carbet; Et: Etoile; Bf: Bellefontaine.* The space is divided into nine squares each corresponding to a range of MDR and volume (i.e., an eruptive scenario) and showing the likelihood of these eruptive scenarii from red (most likely) to yellow (less likely).

but still probable, eruptive scenarii. The P3 eruption, the most powerful event that occurred in the recent eruptive history of the Mount Pelée volcano, shows that an eruption producing a > 1 km^3 DRE volume can indeed occur once again in the future. The Balisier event, a remarkably powerful Pelean event that produced a substantial co-PDC plume, also increases the likelihood of a small volume eruption (between 0.01 and 0.1 km^3 DRE) associated with a strong MDR $> 10^8$ kg s^{-1}. But one must bear in mind that this kind of eruption, even likely to happen again in the future, remains highly exceptional. Finally, even if the eruptive record in the field does not show any Mount Pelée eruption in the four remaining fields (in yellow in Figure 17), we still have to consider them likely to happen, especially as we are not considering the Pelean and phreatic events in this study, which remain the most probable scenarii in the future (Boudon *et al.*, 2005).

As for the other eruptive parameters, our study showed that the total grain-size distribution of a future eruption should be characterized by a power-law exponent $D > 3$ and most probably > 3.3. Given the dispersal axes of each Plinian eruptions, we have to consider that the wind could come from any direction during a future eruption, and thus we shall reconsider the areas under volcanic threat in Martinique.

This overall interpretation of what could be a future likely eruptive scenario in Martinique remains subjective. We will go further into details in Chapter 6, where we use a more thorough correlation matrix together with ash dispersal simulations to investigate more precisely the volcanic hazard in Martinique.

5   Conclusion

In this first part of the manuscript, we detailed how we discovered/revisited four new eruptions in Martinique thanks to two new field campaigns. We dated each of these new events, and reconstructed the eruptive history of the Mount Pelée volcano for the last 24 ka (Chapter 1). One of the three Plinian eruptions newly discovered was originally thought to be part of the P3 eruption. We demonstrated in Chapter 1, that it is in fact a much older event, and we named it the Bellefontaine eruption. The two other Plinian deposits found in the field were completely unknown and we named them the Carbet and Etoile eruptions. Apart from these, we also discovered and studied an exceptional fall deposit resulting from a co-PDC plume that rose above the pyroclastic flow formed by a Pelean eruption originally identified and named NBC by Traineau (1982). We decided to name the entire eruptive sequence (dense PDC, dilute PDC and co-PDC deposits) the Balisier eruption.

Thanks to our field studies, our deposit samples, and our thickness and lithic size measurements, we reconstructed in this chapter the eruptive parameters of each of these new four eruptions. We then compared these parameters to those of the most recent Plinian eruptions in Martinique: the P1 (Carazzo *et al.*, 2012), P2 (Carazzo *et al.*, 2019), and P3 (Carazzo *et al.*, 2020) events. We showed that the Mount Pelée volcano produced rather similar eruptions in its recent past (less than 24,000 years). The P3 and Balisier eruptions remarkably step out of this pattern as they are respectively powerful Plinian and Pelean events, when compared to the other recent eruptions in Martinique. Thanks to the similarities between these eruptions, we drew an accurate picture of the Plinian eruptive scenario most likely to happen in the future. This most probable eruption would produce a ≈ 20 km-high column and reach a peak MDR between 10^7 and 10^8 kg s^{-1}. Its deposits would have a volume comprised between 0.1 and 1 km^3 DRE, with a dominant population of rather fine particles ($D > 3.3$). As the wind could come from any direction, the volcanic products of this future eruption could spread to any area in Martinique (including the most populated area at Fort-de-France), or even reach another Caribbean island (such as Dominica or St Lucia). The scenario of a more powerful Plinian (VEI 5 type) or Pelean (involving a co-PDC plume threatening areas not usually endangered by a dome-forming eruption) event remains probable.

Before investigating further the Plinian volcanic hazard in Martinique (Part 3) by simulating the ash dispersal of two eruptions of the Mount Pelée volcano (Chapter 5) and by constructing a new hazard map (Chapter 6), we detail in the following Part 2 our studies on the impact of grain-size distribution (Chapter 3) and wind (Chapter 4) on the dynamics of Plinian eruptions. These two parameters indeed varied in the past eruptive history of the Mount Pelée volcano.

Appendix A
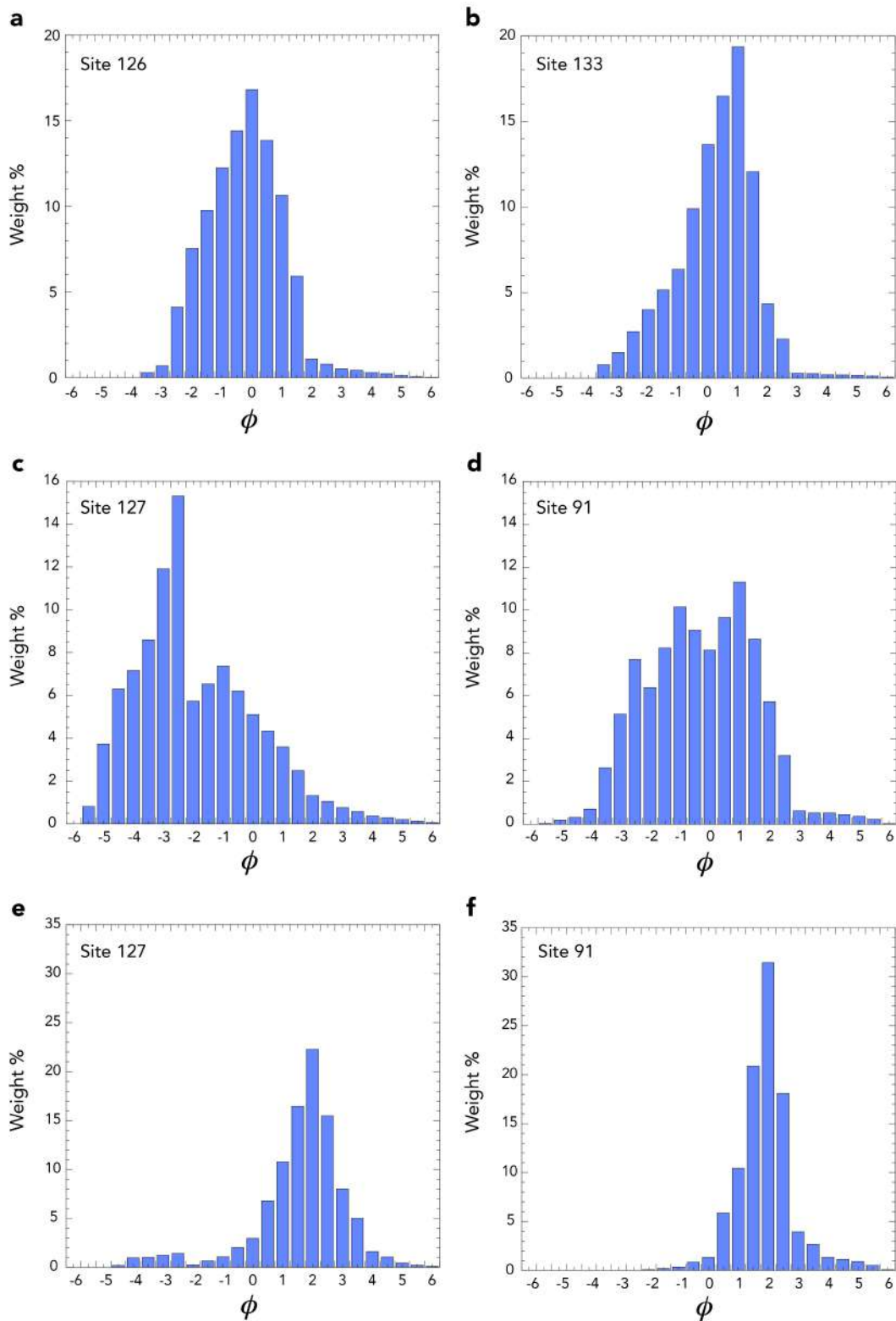
Figure A1: Grain-size distribution of selected samples representing **a** and **b** the Unit A of the Bellefontaine eruption, **c** and **d** the Unit B of the Bellefontaine eruption, and **e** and **f** the Unit C of the Balisier eruption. The left-hand and right-hand columns stand for proximal and distal samples from the source, respectively (see Figure 4 for outcrop location).
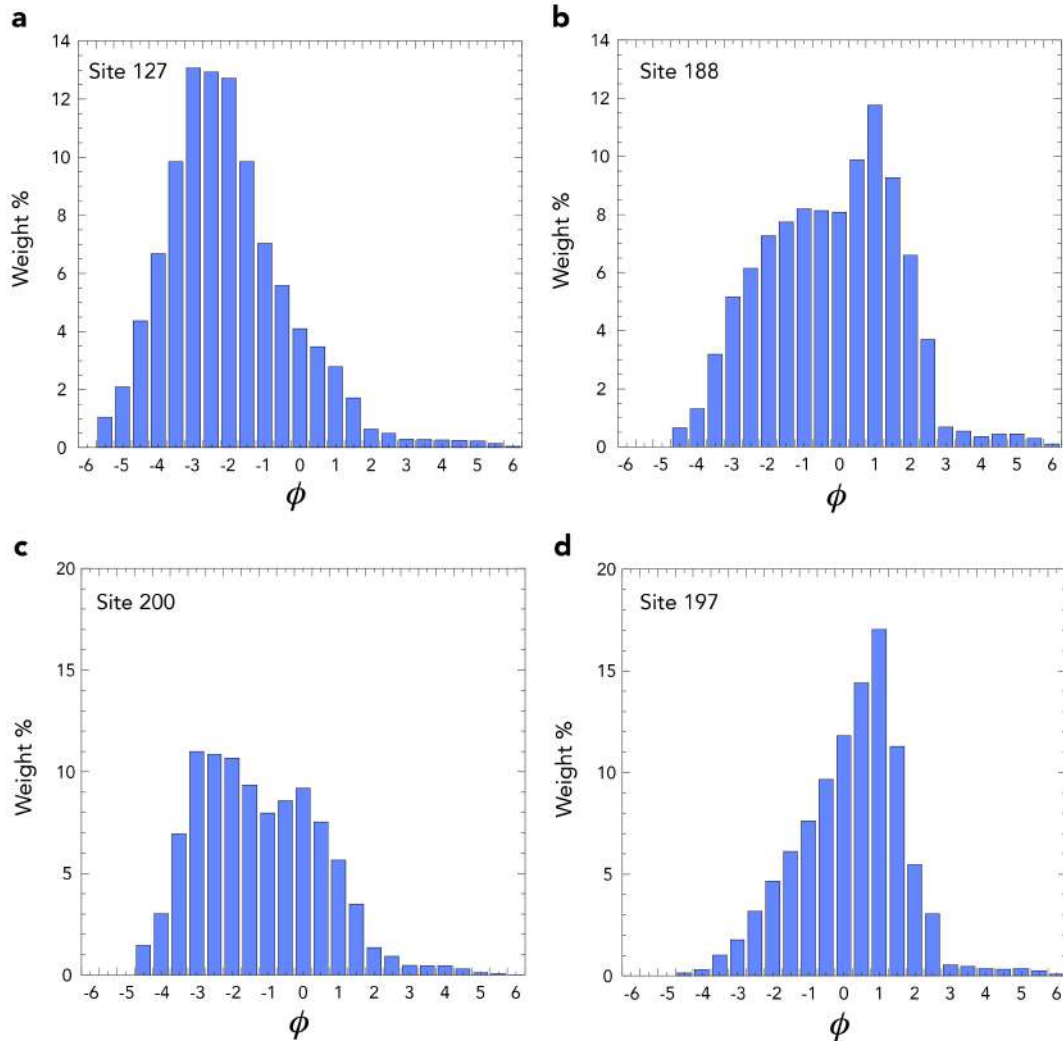
Figure A2: Grain-size distribution of selected samples representing **a** and **b** the Carbet unit, and **c** and **d** the Etoile unit. The left-hand and right-hand columns stand for proximal and distal samples from the source, respectively (see Figure 9 for outcrop location).

Appendix B

Table B1: Fitting parameters used for the erupted volume calculations in Section 3.1.

Fitting method	Bellefontaine	Balisier	Carbet	Etoile
Exponential	Two segments	Two segments	One segment	One segment
Power-law	Prox. limit (PL) = 1 km Dist. limit (DL) = 20 km	PL = 1 km DL = 15 km	PL = 2 km DL = 600 km	PL = 2 km DL = 30 km
Weibull	5 runs, 1000 iterations per run λ: 0−100 k: 0−2			

References

ANDREWS, B.J. & MANGA, M. 2011 Effects of topography on pyroclastic density current runout and formation of coignimbrites. *Geology* **39** (12), 1099–1102.

BONADONNA, C. & COSTA, A. 2012 Estimating the volume of tephra deposits: A new simple strategy. *Geology* **40**, 415–418.

BONADONNA, C. & COSTA, A. 2013 Plume height, volume, and classification of explosive volcanic eruptions based on the Weibull function. *Bull. Volcanol.* **75**, 1–19.

BONADONNA, C., ERNST, G.G.J. & SPARKS, R.S.J. 1998 Thickness variations and volume estimates of tephra fall deposits: The importance of particle Reynolds number. *J. Volcanol. Geotherm. Res.* **81**, 173–187.

BONADONNA, C. & HOUGHTON, B.F. 2005 Total grain-size distribution and volume of tephra-fall deposits. *Bull. Volcanol.* **67**, 441–456.

BONADONNA, C., MAYBERRY, G.C., CALDER, E.S., SPARKS, R.S.J., CHOUX, C., JACKSON, P., LEJEUNE, A.M., LOUGHLIN, S.C., NORTON, G.E., ROSE, W.I., RYAN, G. & YOUNG, S.R. 2002 Tephra fallout in the eruption of Soufriere Hills Volcano, Montserrat. In *The Eruption of Soufriere Hills Volcano, Montserrat from 1995 to 1999* (ed. T.H. Druitt & B.P. Kokelaar), pp. 483–516. Geological Society, London, Memoirs.

BOUDON, G., LE FRIANT, A., VILLEMANT, B. & VIODE, J.P. 2005 Martinique. In *Volcanic Hazard Atlas of the Lesser Antilles* (ed. J.M. Lindsay, R.E.A. Robertson, J.B. Sheperd & S. Ali), pp. 127–146. Seismic Research Unit, The University of the West Indies, Trinidad and Tobago, W.I.

BRUNET, M., MORETTI, L., LE FRIANT, A., MANGENEY, A., FERNÁNDEZ NIETO, E.D. & BOUCHUT, F. 2017 Numerical simulation of the 30-45 ka debris avalanche flow of Montagne Pelée volcano, Martinique: from volcano flank collapse to submarine emplacement. *Nat. Hazards* **87**, 1189–1222.

BURSIK, M.I. & WOODS, A.W. 1996 The dynamics and thermodynamics of large ash flows. *Bull. Volcanol.* **58**, 175–193.

CARAZZO, G., GIRAULT, F., AUBRY, T., BOUQUEREL, H. & KAMINSKI, E. 2014 Laboratory experiments of forced plumes in a density-stratified crossflow and implications for volcanic plumes. *Geophys. Res. Lett.* **41**, 8759–8766.

CARAZZO, G., TAIT, S. & KAMINSKI, E. 2019 Marginally stable recent Plinian eruptions of Mt. Pelée volcano (Lesser Antilles): The P2 AD 280 eruption. *Bull. Volcanol.* **81**, 1–17.

CARAZZO, G., TAIT, S., KAMINSKI, E. & GARDNER, J. E. 2012 The recent Plinian explosive activity of Mt. Pelée volcano (Lesser Antilles): The P1 AD 1300 eruption. *Bull. Volcanol.* **74**, 2187–2203.

CARAZZO, G., TAIT, S., MICHAUD-DUBUY, A., FRIES, A. & KAMINSKI, E. 2020 Transition from stable column to partial collapse during the 79 cal CE P3 Plinian eruption of Mt Pelée volcano (Lesser Antilles). *J. Volcanol. Geotherm. Res. In press.* https://doi.org/10.1016/j.jvolgeores.2019.106764.

CAREY, STEVEN & SIGURDSSON, HARALDUR 1986 The 1982 eruptions of El Chichon volcano, Mexico (2): Observations and numerical modelling of tephra-fall distribution. *Bull. Volcanol.* **48**, 127–141.

CAREY, S. & SIGURDSSON, H. 1989 The intensity of Plinian eruptions. *Bull. Volcanol.* **51**, 28–40.

CAREY, S. & SPARKS, R.S.J. 1986 Quantitative models of the fallout and dispersal of tephra from volcanic eruption columns. *Bull. Volcanol.* **48**, 109–125.

COSTA, A., PIOLI, L. & BONADONNA, C. 2016 Assessing tephra total grain-size distribution: Insights from field data analysis. *Earth Planet. Sci. Lett.* **443**, 90–107.

DAGGIT, M.L., MATHER, T.A., PYLE, D.M. & PAGE, S. 2014 AshCalc-a new tool for the comparison of the exponential, power-law and Weibull models of tephra deposition. *J. Appl. Volcanol.* **3:7**.

DUNION, J.P. 2011 Rewriting the climatology of the tropical North Atlantic and Caribbean Sea atmosphere. *J. Clim.* **24**, 893–908.

References

Engwell, S. & Eychenne, J. 2016 Contribution of Fine Ash to the Atmosphere From Plumes Associated With Pyroclastic Density Currents. In *Volcanic Ash: Hazard Observation*. Elsevier.

Fierstein, J. & Nathenson, M. 1992 Another look at the calculation of fallout tephra volumes. *Bull. Volc.* **54**, 156–167.

Girault, F., Carazzo, G., Tait, S. & Kaminski, E. 2016 Combined effects of total grain-size distribution and crosswind on the rise of eruptive volcanic columns. *J. Volcanol. Geotherm. Res.* **326**, 103–113.

Kaminski, E. & Jaupart, C. 1998 The size distribution of pyroclasts and the fragmentation sequence in explosive volcanic eruptions. *J. Geophys. Res.* **103**, 29759–29779.

Le Friant, A., Boudon, G., Deplus, C. & Villemant, B. 2003 Large-scale flank collapse events during the activity of Montagne Pelée, Martinique, Lesser Antilles. *J. Geophys. Res.* **108** (B1), 1–15.

Michaud-Dubuy, A., Carazzo, G., Tait, S., Le Hir, G., Fluteau, F. & Kaminski, E. 2019 Impact of wind direction variability on hazard assessment in Martinique (Lesser Antilles): The example of the 13.5 ka cal BP Bellefontaine Plinian eruption of Mount Pelée volcano. *J. Volcanol. Geotherm. Res.* **381**, 193–208.

Newhall, Christopher G. & Self, Stephen 1982 The volcanic explosivity index (VEI) an estimate of explosive magnitude for historical volcanism. *J. Geophys. Res.* **87** (C2), 1231–1238.

Pyle, D.M. 1989 The thickness, volume and grainsize of tephra fall deposits. *Bull. Volcanol.* **51** (1), 1–15.

Pyle, D.M. 2000 Sizes of volcanic eruptions. In *Encyclopedia of Volcanoes* (ed. H.E. Sigurdsson, B. Houghton, H. Reimer, Stiw J. & S. McNutt), pp. 263–269. Academic Press, San Diego.

Roobol, M.J. & Smith, A.L. 1976 Mount Pelée, Martinique: A pattern of alternating eruptive styles. *Geology* **4**, 521–524.

Sigurdsson, H. & Carey, S. 1989 Plinian and co-ignimbrite tephra fall from the 1815 eruption of Tambora volcano. *Bull. Volcanol.* **51**, 243–270.

Smith, A.L. & Roobol, M.J. 1990 Mount Pelée, Martinique: A study of an Active Island Arc Volcano. *Geol. Soc. Am. Memoir* **175**.

Traineau, H. 1982 Contribution à l'étude géologique de la Montagne Pelée (Martinique) : Evolution de l'activité éruptive au cours de la période récente. PhD thesis, Université Paris XI.

Traineau, H., Westercamp, D., Bardintzeff, J. M. & Miskovsky, J. C. 1989 The recent pumice eruptions of Mt. Pelée volcano, Martinique. Part I: Depositional sequences, description of pumiceous deposits. *J. Volcanol. Geotherm. Res.* **38**, 17–33.

Walker, G.P.L. 1971 Grain-size characteristics of pyroclastic deposits. *J. Geology* **79**, 696–714.

Watanabe, K., Ono, K., Sakaguchi, K., Takada, A. & Hoshizumi, H. 1999 Co-ignimbrite ash-fall deposits of the 1991 eruptions of Fugen-dale, Unzen Volcano, Japan. *J. Volcanol. Geotherm. Res.* **89**, 95–112.

Westercamp, D., Pelletier, B., Thibaut, P.M. & Traineau, H. 1990 *Carte géol. France (1/50 000), feuille MARTINIQUE*. Orléans : Bureau de recherches géologiques et minières, notice explicative par Westercamp D., Andreieff P., Bouysse P., Cottez S., Battistini R. (1989), 246 pp.

Westercamp, D. & Traineau, H. 1983 The past 5,000 years of volcanic activity at Mt. Pelée Martinique (F.W.I.): Implications for assessment of volcanic hazards. *J. Volcanol. Geotherm. Res.* **17**, 159–185.

Woodhouse, M.J., Hogg, A.J. & Phillips, J.C. 2016 A global sensitivity analysis of the PlumeRise model of volcanic plumes. *J. Volcanol. Geotherm. Res.* **326**, 54–76.

Woods, A. W. & Kienle, J. 1994 The dynamics and thermodynamics of volcanic clouds: Theory and observations from the April 15 and April 21, 1990 eruptions of Redoubt volcano, Alaska. *J. Volcanol. Geotherm. Res.* **62** (1-4), 273–299.

Woods, A. W. & Wohletz, K. 1991 Dimensions and dynamics of co-ignimbrite eruption columns. *Nature* **350**, 225–227.

Part 2

Physical model of explosive volcanic plumes

Chapter 3

A revisit of the role of gas entrapment on the stability conditions of explosive volcanic columns

Table of contents

Résumé du chapitre 3

Ce chapitre est dédié à l'amélioration d'un modèle physique de panache volcanique afin de mieux cerner le comportement de ces écoulements. Les éruptions volcaniques explosives produisent des jets turbulents à hautes vitesses qui peuvent former soit une colonne plinienne stable (par flottabilité positive) ou une fontaine en effondrement produisant des coulées de densité pyroclastiques. Déterminer les conditions à la source menant à ces deux régimes extrêmes est un enjeu majeur de la volcanologie physique. Classiquement, la limite entre les deux régimes est définie par un flux de masse critique avant effondrement pour une quantité donnée de gaz libre dans le mélange éruptif (gaz libre + pyroclastes) à l'évent. Des études précédentes ont montré qu'une concordance entre théorie et données de terrain peut être atteinte dans deux cas différents: (i) par la prise en compte de l'effet de piégeage de gaz dans les fragments grossiers de ponces, qui abaisse la quantité de gaz effective, en fonction de la distribution totale de tailles de grains des fragments pyroclastiques, ou (ii) par la prise en compte de la réduction d'entraînement turbulent à la base de la colonne volcanique due à sa flottabilité négative.

Dans ce chapitre, nous cherchons à combiner ces deux effets en utilisant un modèle 1D de colonne volcanique incluant la sédimentation pour suivre l'évolution de la distribution totale de tailles de grains. Dans les éruptions pliniennes puissantes ($> 10^7 \, \mathrm{kg \, s^{-1}}$), la perte de particules par sédimentation diminue la charge en particules durant l'ascension du panache, ce qui favorise la formation d'une colonne stable. Dans ce cas, nous obtenons qu'une distribution totale de tailles de grains grossière favorise la formation de panaches stables, un résultat contre-intuitif et contredisant les prédictions de modèles considérant le piégeage de gaz dans les fragments pyroclastiques grossiers. Pour interpréter cette conclusion, nous reconsidérons l'effet de piégeage de gaz et montrons qu'en général, il a un rôle dominant sur l'effondrement de colonne comparé à la sédimentation, et empêche la formation de colonnes stables. Cet effet radical est réduit si la porosité ouverte est incorporée dans le modèle, par exemple en considérant que certaines bulles contenues dans un fragment volcanique sont connectées à l'extérieur. Les caractéristiques des coulées de densité pyroclastiques produites par effondrement de colonne sont ensuite prédites en fonction de la distribution totale de tailles de grains et du flux de masse à la source.

Enfin, nous testons le modèle théorique en utilisant deux éruptions historiques bien documentées: les éruptions du Taupo (s'étant produite autour de l'an 186 de notre ère) et du Vésuve (en 79 de notre ère). Les prédictions de notre modèle sont cohérentes avec les données de l'éruption du Taupo, mais pas avec celles du Vésuve. Pour ce dernier cas, nous suggérons que les caractéristiques de la distribution totale de tailles de grains impliquent de prendre en compte le déséquilibre thermique entre le gaz et les pyroclastes au sein du panache.

Abstract

Explosive volcanic eruptions produce high-velocity turbulent jets that can form either a stable buoyant Plinian column or a collapsing fountain producing pyroclastic density currents (PDC). Determining the source conditions leading to these extreme regimes is a major goal in physical volcanology. Classically, the regime boundary is defined as the critical eruptive mass discharge rate (MDR) before collapse for a given amount of free gas in the eruptive mixture (free gas + pyroclasts) at the vent. Previous studies have shown that an agreement between theory and field data can be achieved in two different frameworks: (i) by accounting for the effect of gas entrapment in large pumice fragments, which lowers the effective gas content, depending on the total grain-size distribution (TGSD) of pyroclastic fragments, or (ii) by accounting for the reduction of turbulent entrainment at the base of the volcanic column due to its negative buoyancy.

Here, we aim at combining these two using a 1D model of volcanic column that includes sedimentation to follow the evolution of the TGSD. In powerful ($\geq 10^7 \ \mathrm{kg \, s^{-1}}$) Plinian eruptions, the loss of particles by sedimentation acts as to decrease the load of particles during the plume rise, which favors the formation of a stable column. In this case, we obtain that coarse TGSD promote the formation of stable plumes, a result at odds with the predictions of models considering gas entrapment in large pyroclastic fragments. To interpret this conclusion, we reconsider the effect of gas entrapment and show that in general, it has a dominant role on column collapse compared to particle sedimentation, and hinders the formation of buoyant columns. This drastic effect is reduced when incorporating open porosity, e.g. by considering that some bubbles inside a fragment are connected to the exterior. The characteristics of the PDC produced by column collapse are then predicted as a function of the TGSD and MDR at the source.

We further test the model using two well-documented historical events, the $\approx$186 CE Taupo and 79 CE Vesuvius eruptions. Our model predictions are consistent with the Taupo eruption record, but not with the Vesuvius one. In this latter case, we suggest that the characteristics of the TGSD imply to take into account the thermal disequilibrium between gas and pyroclasts.

1   Introduction

Explosive volcanic eruptions stand as one of the most powerful and dangerous natural phenomena on Earth. During these extreme events, the magma ascending from depth is fragmented in the conduit and expelled at the vent as a dense turbulent mixture of hot gas and pyroclasts. The mass discharge rate of these high-velocity turbulent jets usually ranges between 10^6 and 10^9 kg s^{-1} (Carey & Sigurdsson, 1989). Depending on its mass discharge rate, a volcanic jet can follow remarkably different dynamical evolutions during its rise in the atmosphere. In the buoyant regime (also called "Plinian" regime), the volcanic mixture forms a vertical column that rises up to tens of kilometers before spreading out laterally to form an horizontal umbrella cloud (Sparks, 1986). In the fountain regime (or "collapse" regime), the turbulent jet collapses to the ground and produces pyroclastic density currents (PDC) rushing down the volcano flanks. When eruption conditions are close to those of column collapse, the regime is transitional: an unstable buoyant column still rises to high altitudes but occasionally generates PDC. The two eruptive regimes, which can occur one after another and even alternate during the same eruption, mainly determine the associated hazards. Whereas a rain of ash and pumices produced during the Plinian regime may cause infrastructure damages (e.g., Wilson *et al.* 2014), major perturbations of air traffic (e.g., Miller & Casadevall 2000; Schmidt *et al.* 2014) and breathing difficulties (e.g., Horwell & Baxter 2006; Horwell 2007; Horwell *et al.* 2013), PDC most commonly lead to massive human and material losses (e.g., Spence *et al.* 2004; Wilson *et al.* 2014). The prediction of column behavior is therefore fundamental to assess the impact of explosive volcanic eruptions. The understanding and prediction of the source (and environmental) conditions leading to either a buoyant plume or a collapsing fountain remains a major goal in physical volcanology.

The dual behavior described above rises from the evolution of the volcanic column bulk density during its ascent in the atmosphere. At the vent, the hot mixture of gas and pyroclasts has a bulk density greater than the ambient air, and its initial momentum drives the plume ascent. Thereafter, owing to turbulent mixing, cold atmospheric air is entrained into the flow and heated by the hot pyroclasts, leading to a rapid expansion of the gas and an associated decrease of the bulk density of the jet (Sparks & Wilson 1976; Woods 1988, 1995). In the meantime, the jet momentum decreases with altitude due to its negative buoyancy. A stable Plinian column forms when the bulk density of the volcanic mixture becomes lower than that of the atmospheric air before complete exhaustion of its initial momentum. Then, the volcanic plume rises by natural convection until it reaches a neutral buoyancy level and spreads out laterally. In the fountain regime, the jet consumes its initial momentum before becoming buoyant and thus collapses to the ground producing PDC.

Since the 1970's, various methods have been used to study the stability of volcanic columns produced by explosive eruptions (or equivalently the conditions leading to PDC production). A first generation of theoretical models was developed based on a simplified 1D approach (Wilson, 1976; Sparks, 1986; Woods, 1988) stemming from the widely used "top-hat" formalism of Morton *et al.* (1956). These models rely on the "dusty-gas" hypothesis where particles are considered small enough to remain in thermal and mechanical equilibrium with the gas. In that case, the volcanic mixture can be represented as a single "equivalent" gaseous phase. This convenient formalism has been used to quantitatively study the relationship between the maximum height of the plume and the source mass discharge rate (Settle, 1978; Wilson *et al.*, 1980; Carey & Sigurdsson, 1989) and to determine the conditions leading to column collapse.

Wilson *et al.* (1980) showed that the mass fraction of free gas in the eruptive mixture at the vent (gas + pyroclastic fragments) and mass discharge rate (MDR) strongly control the transition between the stable Plinian plume and the collapsing fountain regimes, a conclusion later confirmed by laboratory experiments (Woods & Caulfield, 1992). Other effects have been considered in order to determine quantitatively this regime boundary. Woods & Bursik (1991) demonstrated that particle sedimentation has a minor effect on the column dynamics, but thermal disequilibrium significantly changes the column behavior and can induce a column collapse. Woods & Bower (1995) and Koyaguchi *et al.* (2010) calculated the conditions for which jet decompression in a crater can yield subsonic velocities and column collapse. Degruyter & Bonadonna (2013) showed that high velocity atmospheric winds can significantly increase the amount of air engulfed in the volcanic column hence making it more stable.

More sophisticated 2D axisymetric and 3D models, based on the time-dependent solution of the Navier-Stokes and energy conservation equations, have been developed to describe the fluid dynamics of the eruptive mixture and the surrounding atmosphere (Valentine & Wohletz, 1989; Neri & Dobran, 1994; Suzuki *et al.*, 2005; Esposti Ongaro *et al.*, 2008). These models improved our understanding of the dynamics of explosive volcanic columns by exploring ranges of parameters that are beyond the limitations imposed by 1D models. However, a recent intercomparison exercise revealed that the results of 2D and 3D models diverge in some of their predictions depending on the assumptions made to solve the governing equations (Costa *et al.*, 2016*b*). On the other hand, 1D models predictions show similarities with those of 3D models, suggesting that 1D models can be used to adequately describe the general behavior of volcanic columns.

Among the different studies on the stability of volcanic plumes, two - Kaminski & Jaupart (2001) and Carazzo *et al.* (2008*a*) - have compared the model predictions of collapse with field constraints in a systematic way, and have shown that previous models tended to significantly favor the buoyant regime in comparison to the natural cases. Kaminski & Jaupart (1998, 2001) demonstrated that gas entrapment in large pumice during the fragmentation process significantly reduces the effective amount of free gas available at the base of the column and promote column collapse. Carazzo *et al.* (2008*a*) studied the effects of reduced turbulent entrainment due to negative buoyancy at the base of the column and showed that it also promotes column collapse. Gas entrapment and reduced entrainment act in the same direction and, when taken independently, yield model predictions consistent with field data. However, these two phenomena have not been considered together yet, and it can be argued that their combined effect could be to favor too much the collapse regime compared to the natural cases, hence reducing their performances in determining accurately the conditions of collapse. Here we propose to combine the two effects, which requires to take into account the evolution of the total grain size distribution (TGSD) due to sedimentation (Girault *et al.*, 2014).

Our paper is organized as follows. In Section 2, we describe our physical 1D model of explosive volcanic columns. In Section 3, we analyze the results of the model taking into account variable entrainment as a function of buoyancy, sedimentation, gas entrapment, and open porosity, and we investigate the control of these parameters and phenomena on the conditions leading to column collapse. We further quantify the fountain height and characterize the PDC produced in the collapse regime. In Section 4, we compare our theoretical predictions with field data from two well-known historical eruptions ($\approx$186 CE Taupo and 79 CE Vesuvius). In Section 5, we discuss additional effects that may influence the transition between stable and collapsing eruptive columns, and we conclude in Section 6.

2   Physical model of explosive volcanic columns

2.1   Conservation equations and constitutive laws

Our model relies on a 1D steady-state "top-hat" formalism for a conical jet in which all the dynamical variables are considered constant inside the jet and zero outside (Morton *et al.*, 1956). The horizontal rate of entrainment of the surrounding fluid is assumed to be proportional to the local vertical ascension rate of the plume, through a constant entrainment coefficient α_e. Our work is based on the improved version of the Woods (1988) model, that explicitly considers the conservation of energy and its effect on the evolution of the bulk density of the flow. As in Woods (1988), we consider thermal and mechanical equilibrium between the volcanic gas and the particles. For a particle-laden volcanic jet and a calm stratified atmosphere, the three macroscopic conservation equations of mass, momentum and energy flow rates in steady-state are written as (Woods, 1988; Woods & Bursik, 1991; Bursik, 2001; Costa *et al.*, 2006; Girault *et al.*, 2014):

$$\frac{d}{dz}(\rho U R^2) \;=\; 2\rho_a U_e R + \sum_{\phi=1}^{N_\phi} \frac{dQ_\phi}{dz}, \tag{1}$$

$$\frac{d}{dz}(\rho U^2 R^2) \;=\; g(\rho_a - \rho)R^2 + U\sum_{\phi=1}^{N_\phi} \frac{dQ_\phi}{dz}, \tag{2}$$

$$\frac{d}{dz}(\rho U R^2 c_p T) \;=\; 2\rho_a U_e R c_a T_a - \rho_a g U R^2 + c_p T\sum_{\phi=1}^{N_\phi} \frac{dQ_\phi}{dz}, \tag{3}$$

where $R(z)$ is the column radius, $U(z)$ is the vertical velocity, g is the acceleration of gravity, ρ, c_p and T are the density, the specific heat and the temperature at constant pressure of the bulk mixture, respectively, ρ_a, c_a and T_a are those of the atmosphere (all variables are defined in the Notation section). $Q_\phi = x_\phi \rho U R^2$, where x_ϕ is the mass proportion of ϕ-sized particles in the GSD, is the discharge rate of ϕ-sized particles (kg s^{-1}) distributed within 20 classes of grain sizes ranging from $d_{min} = 10\phi$ (1 μm) to $d_{max} = -9\phi$ (0.5 m) with one ϕ intervals. Magma temperature is taken as the average of andesitic magma ($T_0 = 1200$ K). As illustrated in Figure 1, U_e is the entrainment rate at the edge of the plume, defined as $U_e = \alpha_e U$ (Morton *et al.*, 1956), which is here function of the column buoyancy relative to the ambient air, and is expressed as (Kaminski *et al.*, 2005):

$$\alpha_e \;=\; \frac{C}{2} + \left(1 - \frac{1}{A}\right)\mathrm{Ri}, \tag{4}$$

where $\mathrm{Ri} = g(\rho_a - \rho)R/\rho_a U^2$ is the Richardson number in the plume, and A and C are dimensionless parameters depending on the flow structure. C is taken as a constant ($\approx$ 0.135) whereas A evolves as a function of the downstream distance from the source and buoyancy (see Appendix A).

To follow the evolution of the density in the plume as a function of entrainment and temperature variations with height, we use the same constitutive equations as in Woods (1988):
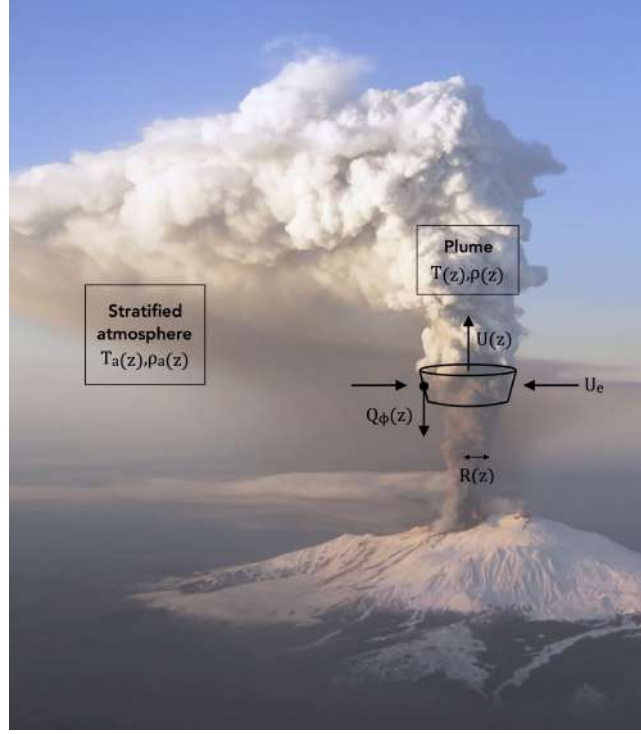
Figure 1: Photograph of Mt. Etna (December 2014) illustrating some physical parameters used in this study (see text and Notation section for symbol description).

$$\frac{1}{\rho} = \frac{(1 - x_g)}{\rho_p} + \frac{x_g R_g T}{P_a}, \tag{5}$$

$$x_g = 1 + (x_{g_0} - 1)\frac{\rho_0 U_0 R_0^2}{\rho U R^2}, \tag{6}$$

$$R_g = R_a + (R_{g_0} - R_a)\left(\frac{1 - x_g}{x_g}\right)\left(\frac{x_{g_0}}{1 - x_{g_0}}\right), \tag{7}$$

$$c_p = c_a + (c_{p_0} - c_a)\left(\frac{1 - x_g}{1 - x_{g_0}}\right), \tag{8}$$

where $\rho_p = 2000$ kg m^{-3} is the average density of the particles, $x_g(z)$ is the effective gas mass fraction, $R_{g_0} = 461$ J K^{-1} kg^{-1} and $R_a = 287$ J K^{-1} kg^{-1} are the bulk column and the air gas constants, respectively, $P_a(z)$ is the atmospheric pressure, and the subscript $_0$ denotes a value at the vent. $P_a(z)$, $T_a(z)$ and $\rho_a(z)$ depend on the atmospheric conditions which we take as typical polar, mid-latitude or tropical (Glaze & Baloga, 1996; Carazzo *et al.*, 2008*b*).

2.2   Particle sedimentation

To account for the mass loss of ϕ-sized particles from the edges of the column, we consider it to be proportional to the mass discharge rate of particles Q_ϕ and to the terminal fall velocity V_ϕ, such as (Woods & Bursik, 1991; Ernst *et al.*, 1996; Girault *et al.*, 2014):

$$\frac{dQ_\phi}{dz} = -p_s \frac{Q_\phi}{R}\frac{V_\phi}{U}, \tag{9}$$

where p_s is a probability of sedimentation experimentally determined and taken equal to 0.27 ± 0.01 (Ernst *et al.*, 1996; Girault *et al.*, 2014, 2016). For a given particle size, the fallout velocity V_ϕ is calculated using the formulae of Bonadonna *et al.* (1998):

$$V_\phi = \begin{cases} \sqrt{\frac{3.1 d_\phi g (\rho_p - \rho)}{\rho_a}} & \text{for } \mathrm{Re}_\phi \geq 500, \\[2mm] d_\phi \left(\frac{4 g^2 (\rho_p - \rho)^2}{225 \mu \rho_a} \right)^{1/3} & \text{for } 0.4 \leq \mathrm{Re}_\phi \leq 500, \\[2mm] \frac{d_\phi^2 g (\rho_p - \rho)}{18 \mu} & \text{for } \mathrm{Re}_\phi \leq 0.4, \end{cases} \tag{10}$$

where d_ϕ is the particle diameter of a ϕ-sized particle, $\mu(z)$ is the dynamic viscosity of air (Sutherland, 1893), and $\mathrm{Re}_\phi = \rho d_\phi V_\phi / \mu$ is the particle Reynolds number.

2.3   Grain-size distribution and amount of gas at the vent

In explosive eruptions, GSD of pyroclasts results from a fragmentation sequence in the conduit before the eruption. The rapid decompression of magma during its ascent causes a "primary" fragmentation (Alibidirov & Dingwell, 1996), which disintegrates bubbly magma into fragments, then followed by a "secondary" fragmentation of larger fragments into finer ash (Kaminski & Jaupart, 1998). During this sequence, magmatic gas separates into two phases: an entrapped one contained in bubbles within the clasts, and a continuous one carrying fragments and ashes. This latter phase corresponds to the effective amount of "free" gas that has to be considered for the modeling of the turbulent flow. Within this framework, clast size plays a key role in setting the amount of gas released at fragmentation: large fragments (pumices) retain a larger amount of gas than small fragments (ashes) do. Field data (Kaminski & Jaupart, 1998) and fragmentation experiments (e.g., Kueppers *et al.* 2006) have shown that volcanic rocks fragment according to a power-law distribution:

$$N(R \geq r) = \lambda r^{-D}, \tag{11}$$

where $N(R \geq r)$ is the number of fragments of size R larger than or equal to r, λ is a normalization constant and D is the power-law exponent.

The two main parameters that control the stability of a volcanic plume are the mass discharge rate and the momentum flow rate at the vent, or, equivalently, the mass discharge rate and exit velocity (Wilson *et al.*, 1978; Woods, 1988; Sparks *et al.*, 1997). Because the exit velocity is mainly controlled by the amount of gas in the volcanic mixture, x_{g0}, (e.g., Wilson *et al.* 1980; Koyaguchi *et al.* 2010; see Appendix B) the transition between the Plinian and Fountain regimes is often given as a threshold mass discharge rate for a given gas mass fraction. Here, we calculate x_{g0} as the total fraction of exsolved gas minus the amount of exsolved gas trapped in large particles, using the model of Kaminski & Jaupart (1998, 2001).

If bubbles inside a fragment are not connected to the exterior, the fraction of gas released by each fragment is given by $\frac{V_{out}}{V_{gas}} = \frac{3b}{r}$ for particle with a radius r larger than $3b$, and $\frac{V_{out}}{V_{gas}} = 1$ for particles smaller than $3b$, where b is the mean bubble radius in the magma. These relationships can then be used to calculate the total gas released at fragmentation (Figure 2a) provided that the TGSD - hence D - is known, as well as the smallest and largest particle sizes r_{min} and r_{max}, and the mean bubble size. As discussed by Kaminski &
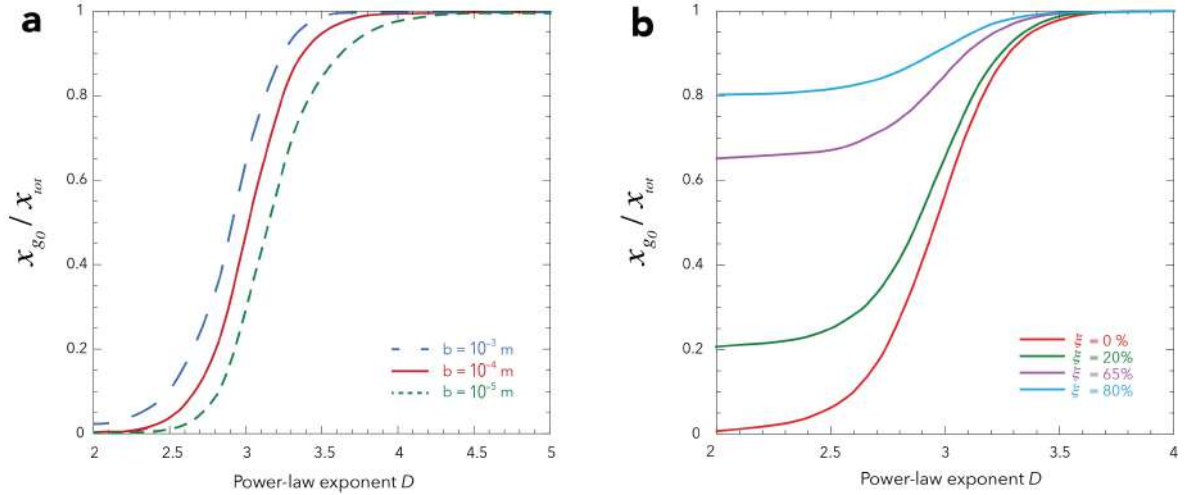
Figure 2: a Fraction of gas released at fragmentation as a function of the power-law exponent D (modified from Kaminski & Jaupart 1998). The dashed blue, solid red and dotted green lines correspond to the calculated fraction of gas released when considering a bubble size of 10^{-3}, 10^{-4}, and 10^{-5} m, respectively. **b** Fraction of effective gas released after fragmentation and the development of an open porosity ξ as a function of D. The red, green, purple, and blue lines correspond to calculations made with $\xi = 0$, 20, 65, and 80%, respectively.

Jaupart (1998), the exact values of r_{min} and r_{max} do not significantly affect the calculations, and uncertainties on their determination change the result by $\pm$ 5% only. Indeed, where fine particles dominate (i.e., $D > 3$), the fragments do not significantly entrap gas since all their bubbles are connected to the exterior. The exact value of r_{min} is therefore not critical as long as it is much smaller than $3b$. On the other hand, where large particles dominate (i.e., $D < 3$) the average fragment size is much larger than the bubble size, hence fragments do not significantly release gas. The results are also weakly sensitive to the exact value of b or to more complex bubble size distribution in the magma. Figure 2a gives the fraction of gas released at fragmentation as a function of D for three different values of the mean bubble size (from 10 μm to 1 mm) and shows that this does not change the results by more than 5%. The main parameter controlling the mass fraction released at fragmentation is therefore the power-law exponent D. For the rest of the paper we set $r_{min} = 0.5$ μm, $r_{max} = 0.25$ m (see Section 2.1), and $b = 100$ μm, and we take a power-law exponent D ranging from 2.5 (coarsest distribution) to 3.3 (finest distribution), a value beyond which the results are no longer affected by the precise value of D.

Several studies have shown that inside pumices, some of the bubbles are connected to the exterior (e.g., Toramaru 1988; Klug & Cashman 1996) and contribute to an additional release of gas through this "open porosity". Measurements made on trachytic pumices from the Vesuvius 79 CE (Shea *et al.*, 2012), on dacitic pumices from the Novarupta 1912 (Nguyen *et al.*, 2014), on andesitic pumices from Soufriere Hills 1997 (Formenti & Druitt, 2003), Taranaki 1655 CE (Platz *et al.*, 2007), and Lascar 1993 (Formenti & Druitt, 2003), and on rhyolitic pumice from Kos Plateau Tuff 161,000 BP (Bouvet de Maisonneuve *et al.*, 2009), and Mount Mazama 7700 BP eruptions (Klug *et al.*, 2002), lead to open porosity between 60 to 70% for explosive eruptions regardless of the magma composition.

To take into account open porosity in our model, we relax the gas entrapment hypothesis of Kaminski & Jaupart (1998) by introducing a new parameter $\xi = \frac{V_{outgassed}}{V_{trapped}}$ where $V_{outgassed}$ is the volume of gas initially entraped in the fragment but now released through the connected open porosity, and $V_{trapped}$ is the volume of gas initially trapped into the

fragments at fragmentation. For particles with a radius larger than $3b$, the definition of ξ leads to $\frac{V_{out}}{V_{gas}} = \frac{3b(1-\xi)+\xi r}{r}$, and we keep $\frac{V_{out}}{V_{gas}} = 1$ for particles smaller than $3b$. Thus, in the extreme case where no open porosity develops, the volume of gas initially entraped but released is null ($\xi = 0$) and $\frac{V_{out}}{V_{gas}} = \frac{3b}{r}$. On the other hand, if the open porosity reaches 100%, all the gas initially entraped is released ($\xi = 1$) and $\frac{V_{out}}{V_{gas}} = 1$ for all particles. Figure 2b gives the effective fraction of gas released after fragmentation and the development of an open porosity as a function of D for four different values of ξ (0, 20, 65 and 80%).

2.4   Exit velocity at the base of the eruptive column

In explosive eruptions, the volcanic mixture generally exits the vent at a sonic velocity (U_v) and with a pressure (P_v) larger than the atmospheric pressure (P_a). After its rapid decompression to the atmospheric pressure, the velocity of the mixture U_0 is supersonic and can be expressed as (Woods & Bower, 1995):

$$U_0 = U_v + \frac{S}{Q}(P_v - P_a), \tag{12}$$

where S is the cross-sectional area of the conduit, and Q is the mass discharge rate feeding the eruption. In the case of a free decompression (i.e., not controlled by the shape of the crater) and for a cylindrical conduit, it is possible to obtain U_0 as a function of the amount of gas in the mixture for a given mass discharge rate (see Appendix B). We will use these conditions in the next parts of the article and we will discuss in Section 5.1 the consequences of the presence of a crater.

For a given set of source conditions, the dynamical parameters of the plume, i.e. its velocity, radius, density and temperature are then calculated at each step of altitude z in a mid-latitude atmosphere using Eqs. (1)-(12).

3   Results

3.1   Prediction of column collapse

To compare the model predictions with the previous studies of Kaminski & Jaupart (2001) and Carazzo *et al.* (2008a), we define the column regimes as a function of source mass discharge rate and total gas content, which can both be retrieved from field data.

Figure 3 shows the predictions of the model for column collapse when accounting for reduced entrainment and particle sedimentation without gas entrapment (i.e., $x_{g0} = x_{tot}$). The transition curve is highly influenced by the value of D: the critical mass discharge rate before collapse is shifted by about one order of magnitude between the coarsest ($D = 2.5$) and finest ($D = 3.3$) population. For mass discharge rates larger than 10^7 kg s^{-1}, low values of D tend to increase the critical mass discharge rate at which collapse occurs. In this case, the loss of particles by sedimentation decreases significantly the column mass discharge rate during its rise, but is not large enough to drain out the thermal reservoir available to heat up the entrained cold atmospheric air, which helps the generation of a buoyant plume. We thus obtain that when sedimentation only is taken into account, coarse distributions (i.e. low values of D) promote the formation of stable plumes, a result apparently at odds with the conclusions of Kaminski & Jaupart (2001). To settle these conflicting results, we study the net effect of sedimentation when gas entrapment is also considered.
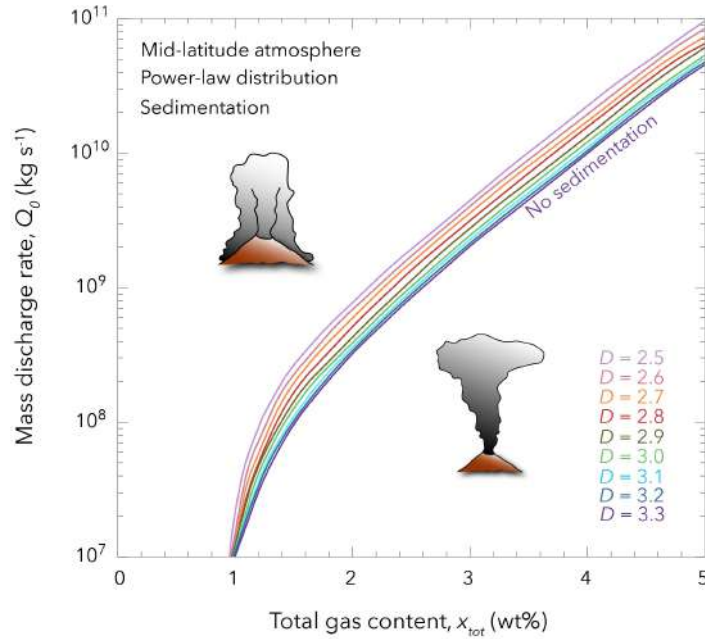
Figure 3: Threshold mass discharge rate (in $kg\,s^{-1}$) at the transition between buoyant and collapse regimes as a function of the total gas content in the volcanic mixture (in wt%). Each curve represents the theoretical threshold for a different value of the power-law exponent D. The curve calculated without sedimentation displayed in Figure 4 of Carazzo *et al.* (2008a) is the same as the one calculated here with $D = 3.3$. We consider a mid-latitude atmosphere, the magma temperature is taken as the average of andesitic magma ($T_0 = 1200$ K), and only sedimentation is introduced in the model compared to Carazzo *et al.* (2008a).

Figure 4 shows the combined effect of particle sedimentation and gas entrapment compared to the case considering gas entrapment but no sedimentation. We consider here that the exponent D controls the effective "free" gas content (Figure 2a) and that there is no open porosity (ξ=0). We find that gas entrapment, hence the characteristics of the population of particles produced by fragmentation, has in general a dominant role on column collapse compared to particle sedimentation. However, for D values smaller than 2.8, sedimentation and gas entrapment are of equal importance and act together to hamper and even make impossible the formation of stable plumes. This result is consistent with the observations of Kaminski & Jaupart (1998) who compiled values of D systematically larger than 3.0 in all the pumice fallout deposits they considered. The shift between the two transition curves calculated at $D = 2.8$ (Figure 4) suggests that, for small values of D, gas entrapment results in the decrease of the vertical velocity near the vent, which further enhances the effect of particle sedimentation.

The model accounting for gas entrapment and a constant entrainment presented by Kaminski & Jaupart (1998), and the model described by Carazzo *et al.* (2008a) accounting for a variable entrainment but no gas entrapment, both make the formation of a buoyant column less likely. The combined effects of sedimentation, gas entrapment and reduced entrainment lead to the drastic effect on the transition described here (Figure 4) and casts some doubt on their ability to reproduce natural data previously explained by each model considered separately. These two models are however end-members and the introduction of open porosity may yield a more balanced conclusion.

Figure 5 shows the combined effect of particle sedimentation, gas entrapment and post-fragmentation outgassing due to open porosity for three values of open porosity: 20%, 65% (average value from natural samples) and 80%. As expected, it appears that for low values
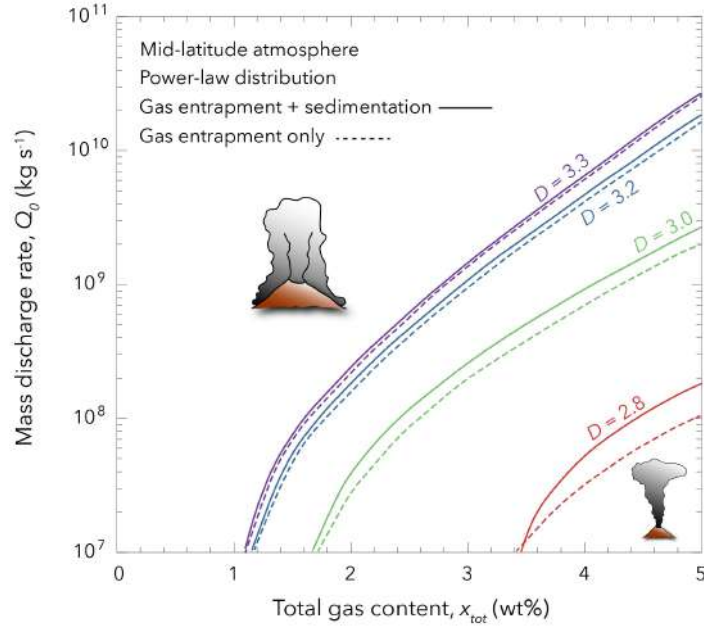
Figure 4: Threshold mass discharge rate (in kg s^{-1}) at the transition between buoyant and collapse regimes as a function of the total gas content in the volcanic mixture (in wt%). Each color corresponds to a different value of the power-law exponent D. Solid curves represent the theoretical threshold from our model considering both gas entrapment and sedimentation, and dashed curves represent that from our model considering gas entrapment only (as in Kaminski & Jaupart 2001). We consider a mid-latitude atmosphere, and the magma temperature is taken as the average of andesitic magma ($T_0 = 1200$ K).

of D, the larger the open porosity, the easier it becomes to generate a buoyant plume. This illustrates how post-fragmentation outgassing reduces the impact of gas entrapment shown in Figure 4. When accounting for an open porosity of 65%, the critical mass discharge rate at which collapse occurs is increased by up to two orders of magnitude for $D < 3$, and by up to a factor of 2 for $D > 3$, compared with predictions made without open porosity (Figure 4). For $D > 3$, the critical mass discharge rate is also increased by up to a factor of 3 compared with predictions made without sedimentation and gas entrapment (i.e., Figure 4 in Carazzo *et al.* 2008a).

3.2   Predictions for the dynamics of collapsing fountains

Girault *et al.* (2014) showed that the power-law exponent of the TGSD at the vent reduces the maximum height reached by a stable plume by 30% for mass discharge rates larger than 10^7 kg s^{-1}. To investigate a similar effect in the case of collapsing volcanic fountains, we performed calculations for a power-law exponent D ranging from 2.5 to 3.3 and for two different values of total exsolved gas content of 2 and 4 wt% (Figure 6). For each value of gas content, we tested two different initial MDR corresponding to conditions near the plume/fountain transition (i.e., 3.10^8 kg s^{-1} for $x_{g0} = 2$ wt%, and 10^{10} kg s^{-1} for $x_{g0} = 4$ wt%) and far from it (i.e., 10^{10} kg s^{-1} for $x_{g0} = 2$ wt%, and 10^{11} kg s^{-1} for $x_{g0} = 4$ wt%). We further consider an open porosity of 65%. We compare the maximum height reached by the fountain when accounting for particle sedimentation (Sed) and/or gas entrapment (GE) and/or open porosity (OP) or none of these effects. Figure 6 shows that particle sedimentation alone has a negligible (yet positive) effect on the maximum fountain height. When gas entrapment alone or gas entrapment plus sedimentation are taken into account, the maximum fountain height strongly decreases when D decreases, in agreement with the
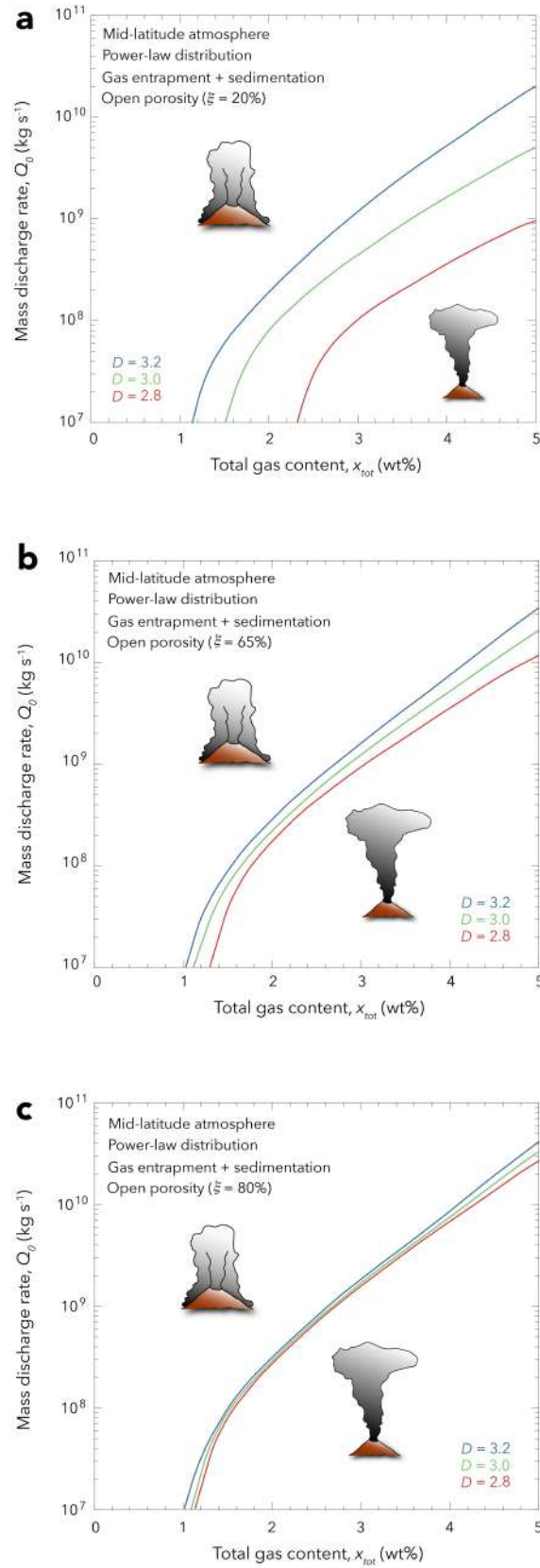
Figure 5: Threshold mass discharge rate (in kg s^{-1}) at the transition between buoyant and collapse regimes as a function of the total gas content in the volcanic mixture (in wt%). Each color represents a different value of the power-law exponent D when taking into account sedimentation, gas entrapment and an open porosity of **a** $\xi = 20\%$, **b** $\xi = 65\%$, and **c** $\xi = 80\%$. We consider a mid-latitude atmosphere, and the magma temperature is taken as the average of andesitic magma ($T_0 = 1200$ K).
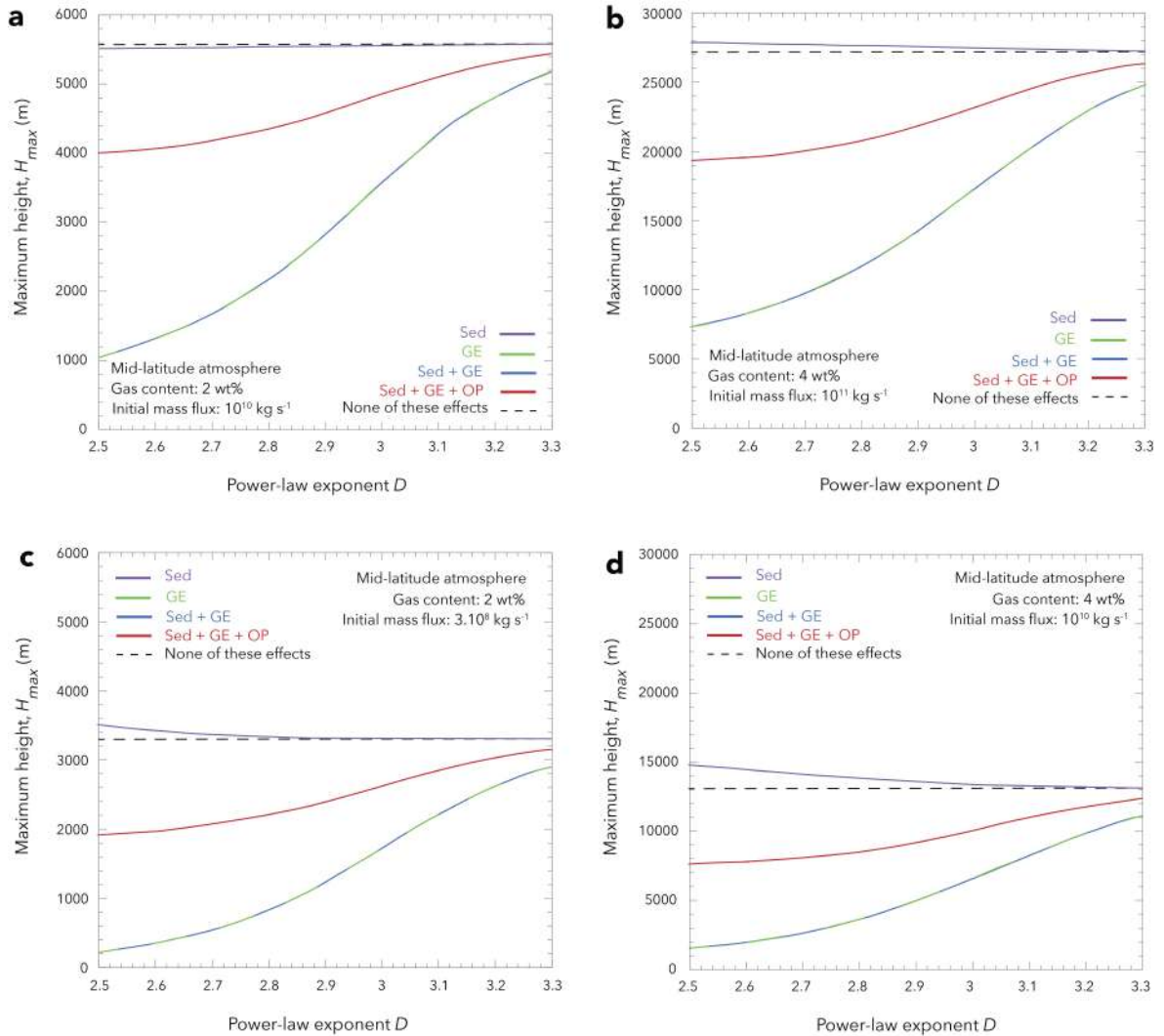
Figure 6: Theoretical predictions of maximum height reached by a volcanic fountain as a function of power-law exponent D when accounting for different effects: Sed = sedimentation, GE = gas entrapment, OP = open porosity ($\xi = 65\%$), or for none of these effects. The green curve corresponds to the model of Kaminski & Jaupart (1998, 2001), the dashed curve to the model of Carazzo *et al.* (2008*a*) and the blue curve to the model of Girault *et al.* (2014). Calculations are made at conditions far above the transition curves with an initial exsolved gas content and an initial mass discharge rate of **a** 2 wt% and 10^{10} kg s^{-1}, and **b** 4 wt% and 10^{11} kg s^{-1}, and just above the transition curves for initial values of **c** 2 wt% and 3.10^8 kg s^{-1}, and **d** 4 wt% and 10^{10} kg s^{-1}. We consider a mid-latitude atmosphere, and the magma temperature is taken as the average of andesitic magma ($T_0 = 1200$ K) in all calculations.

results of Girault *et al.* (2014), which emphasizes the dominant role of gas entrapment. The change in fountain height can reach up to a factor of 5 for conditions far from the transition (Figures 6a, b), to a factor of 15 for conditions near the transition (Figures 6c, d). Finally, when an open porosity of 65% is taken into account (Sed+GE+OP), the effect of gas entrapment is largely reduced and intermediate fountain heights are obtained (red curves in Figure 6).

Figure 6 shows that when mainly composed of fine particles (i.e., high D value), the fountain will reach a relatively high altitude allowing the resulting PDC to cover larger distances on ground. On the other hand, when the fountain has a coarser distribution of fragments (i.e., low D value), it will reach a lower maximum height, and one can expect the
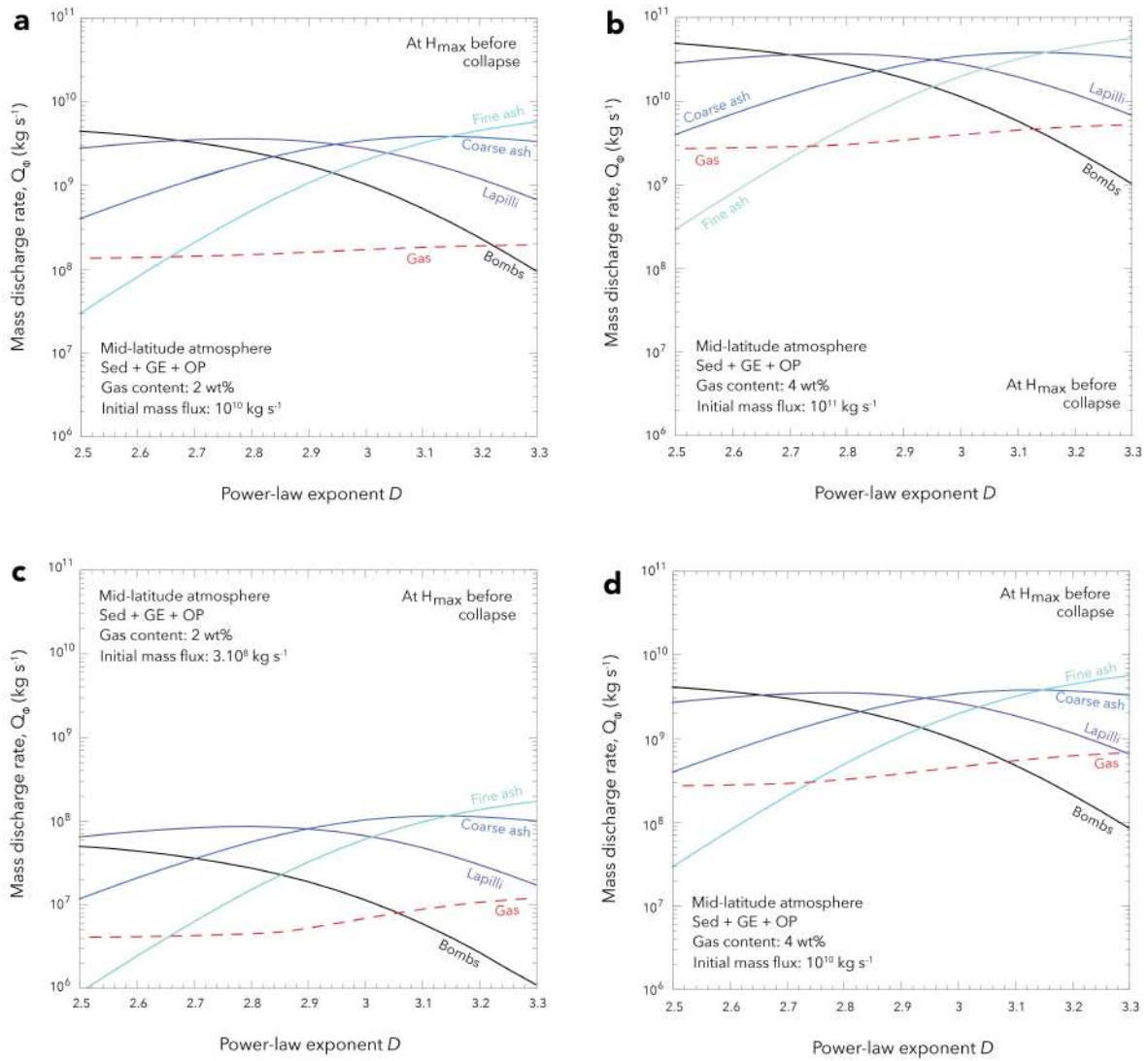
Figure 7: Theoretical predictions of particles and gas mass discharge rates as a function of the power-law exponent D at the maximum height of a collapsing fountain when accounting for sedimentation, gas entrapment and an open porosity of 65%. Calculations are made at the same conditions as in Figure 6. Particle ranges are provided in the text.

resulting PDC to be restricted to closer distances from the vent due to the smaller potential energy available. Bursik & Woods (1996) showed that varying the MDR by an order of magnitude changed the run-out distance reached by the PDC by a factor of ≈ 2.4 (Figure 12a of Bursik & Woods 1996), an increase that can be explained by doubling the height of the column in the plume model (Woods, 1988). In our model, a change in fountain height of a factor 1.5 is obtained when varying D from 2.5 to 3.3 (red curves in Figures 6a, b, c, d), suggesting in turn that the run-out distance will increase by a factor of ≈ 2 for this change of D.

Our model can also be used to infer the grain size distribution in the PDC generated by a collapsing column. The results are presented in Figure 7 based on four particle classes: bombs (-9 to -7 ϕ), lapilli (-6 to -1 ϕ), coarse ash (0 to 6 ϕ), and fine ash (7 to 10 ϕ). For low values of D, the collapsing fountain is more concentrated and enriched in coarse fragments (bombs and lapilli) at its maximum height. These large fragments shall form dense PDC loaded with bombs and lapilli. Conversely, for high values of D, the collapsing

fountain is mainly made of fine ash particles at its maximum height, which will produce dilute PDC mostly made of coarse and fine ash particles. Varying the initial gas content and the MDR feeding the fountain does not affect these conclusions (Figure 7), suggesting that D has a major control on the population of particles in the PDC produced during column collapse.

4   Comparison with natural cases

We now compare our model predictions with historical eruptions providing well-constrained values of gas contents, MDR and power-law exponent D. There are however only a few examples of such well-documented events, and here we choose two famous historical ones: the $\approx$186 CE Taupo and the 79 CE Vesuvius eruptions. All the available geological data are summarized in Table 1.

4.1   The $\approx$186 CE Taupo eruption

The Taupo eruptive episode consists of a series of Plinian and phreato-Plinian eruptions (Walker, 1980; Froggatt, 1981; Talbot *et al.*, 1994; Wilson, 1985, 1993; Wilson & Walker, 1985; Houghton *et al.*, 2014). The stratigraphic sequence starts with a phreato-Plinian ash layer (Y1) overlain by a Plinian fallout (Y2 or Hatepe), and two phreato-Plinian ash layers (Y3 and Y4 or Rotongaio). The main sequence corresponds to a Plinian fallout deposit (Y5 or Taupo Plinian pumice) interbedded with intraplinian ignimbrites (Y6 or early ignimbrite flow units) and covered by PDC deposits (Y7 or Taupo ignimbrite). Here, we focus on the Y2, Y5-6 and Y7 phases as they represent the transition between Plinian, transitional, and collapse regimes, respectively. During these phases, the MDR increases from 1.8×10^8 kg s^{-1} during Y2 (Carey & Sigurdsson, 1989) to 2×10^9 kg s^{-1} during Y5/6 (Carey & Sigurdsson, 1989; Houghton *et al.*, 2014; Carazzo *et al.*, 2015), and to 1.4×10^{10} kg s^{-1} during Y7 (Carey & Sigurdsson, 1989; Bursik & Woods, 1996). These values have been debated in the literature. Here we retain average values for Y2, Y5/6 and Y7, and we use the minimum and maximum MDR proposed in the literature to estimate an error bar in Figure 8 (see Table 1).

Dunbar & Kyle (1993) estimated the dissolved water content to 4.3 ± 0.5 wt% for the Y2 and Y5-6 phases and to 3.6 ± 0.5 wt% for the last collapsing phase Y7. We correct these values for the presence of crystals and lithic fragments, which do not contain volatiles (Kaminski & Jaupart, 2001). Considering a proportion of crystals and lithics contents of 20% (Dunbar *et al.*, 1989) and assuming complete degassing, we deduce a total gas mass fraction in the mixture of 3.44 ± 0.4 wt% for both the Y2 and Y5-6 phases and 2.88 ± 0.4 wt% for the Y7 phase. The power-law exponent D is taken to be 3.2, as calculated by Kaminski & Jaupart (1998), the magma temperature is set to 1133 K, as measured by Shane (1998), and the exit velocity is set to 306 ± 10 m s^{-1}, as determined from the isopleth maps of the transitional phase Y5-6 (Walker, 1980). We note that using the power-law exponent $D = 3.2$ and an open porosity of 60-70% gives $\frac{x_{g0}}{x_{tot}} \approx 0.94$ (Figure 2b) hence a small net effect of gas entrapment. Together with the total gas mass fraction of 3.44 wt%, this value gives a calculated exit velocity of 275 ± 5 m s^{-1} for the Y5-6 phase (Appendix B), which is consistent with the exit velocity constrained from the distribution of lithic fragments.

Figure 8 compares the eruptive parameters inferred for the Taupo eruption (i.e., mass discharge rate and total gas content) and the transition between the stable plumes and the collapsing fountains predicted when considering particle sedimentation, gas entrapment and

Table 1: Eruption conditions of the 79 CE Vesuvius and ≈186 CE Taupo events.

Eruption (deposit)	Dissolved gas content, n_0 (wt%)	Total gas content, x_{tot} (corrected for phenocrysts and lithics, wt%)	Total crystal content and lithics content (%)	Mass discharge rate, MDR (minimum and maximum values, kg s^{-1})	Power-law exponent D	Magma temperature, T_0 (K)	Plume maximum height (km)	Estimated minimal vent velocity (m s^{-1})	References
Vesuvius 79 CE (0.25 W/EU2)	6.0 ± 0.44 (1)	4.08 ± 0.3	20% (2); 12% (3)	3.1×10^6 - 1.2×10^7 (4)	3.0 (5)	1123 (6)	26.3 (4)	195 ± 10 (4)	(1) Cioni 2000; (2) Shea et al. 2009; (3) Sigurdsson et al. 1982; (4) Carey & Sigurdsson 1987; (5) Costa et al. 2016a; (6) Gurioli et al. 2005
Vesuvius 79 CE (0.5 W/EU2)				4.6×10^6 - 1.8×10^7 (4)					
Vesuvius 79 CE (0.75 W/EU2)				8.5×10^6 - 3.4×10^7 (4)					
Vesuvius 79 CE (1 W/EU2)				3.6×10^7 - 1.4×10^8 (4)					
Vesuvius 79 CE (W/G-S1/EU3)	4.95 ± 0.2 (1)	2.57 ± 0.1	28% (2); 20% (3)	7.5×10^7 - 3×10^8 (4)		1323 (6)	32.0 (4)	260 ± 10 (4)	
Taupo ≈186 CE (Y2)	4.3 ± 0.5 (7)	3.4 ± 0.4	20% (8)	9×10^7 - 3.6×10^8 (9)	3.2 (13)	1133 (14)	33 (9)	288 ± 10 (16)	(7) Dunbar & Kyle 1993; (8) Dunbar et al. 1989; (9) Carey & Sigurdsson 1989; (10) Houghton et al. 2014; (11) Carazzo et al. 2015; (12) Bursik & Woods 1996; (13) Kaminski & Jaupart 2001; (14) Shane 1998; (15) Walker 1980; (16) Walker 1981
Taupo ≈186 CE (Y5)				3.3×10^8 - 1.1×10^9 (9, 10)*			31-37 (10); 50 (15)	140 ± 10 (10); 306 ± 10 (15)	
Taupo ≈186 CE (Y6)				5.8×10^8 - 1.9×10^9 (9, 10, 11)*			/	/	
Taupo ≈186 CE (Y5-6)				9×10^8 - 3×10^9 (9, 10, 11)*			/	/	
Taupo ≈186 CE (Y7)	3.6 ± 0.5 (7)	2.9 ± 0.4		7.7×10^9 - 2×10^{10} (9, 12)**			/	/	

* The MDR feeding the Y5 phase is an average value from MDR proposed by Carey & Sigurdsson (1989) and MDR calculated from the maximum height proposed by Houghton et al. (2014); the MDR feeding the Y6 phase is calculated from the MDR of Y5 and from masses of deposits for Y5 and Y6 given in Carazzo et al. (2015); the MDR feeding the Y5-6 phase is the addition of the two precedent values.
** Average value from MDR proposed by Carey & Sigurdsson (1989) and MDR proposed by Bursik & Woods (1996).
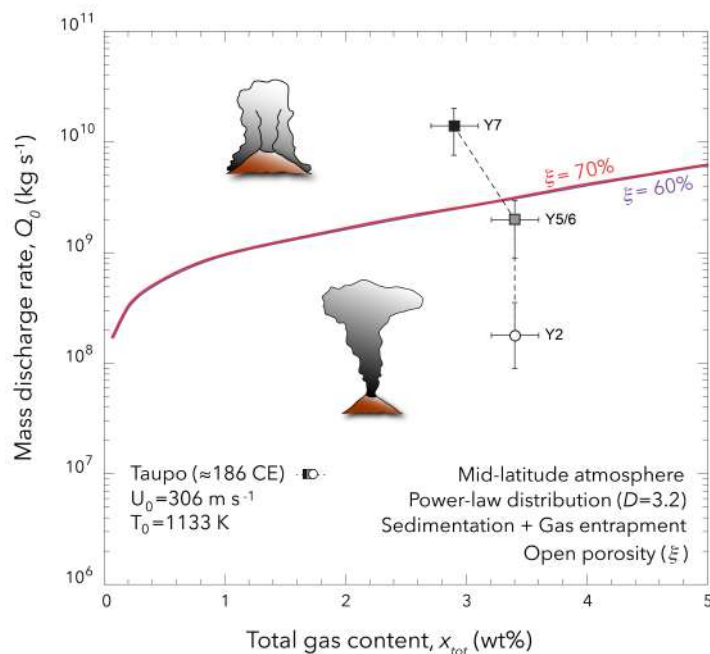
Figure 8: Eruptive conditions of the ≈186 CE Taupo eruption in terms of source mass discharge rate (in $kg\,s^{-1}$) and total gas content (in wt%). The curves give the threshold mass discharge rate for column collapse when accounting for sedimentation and gas entrapment. Calculations are made for a power-law exponent $D = 3.2$ calculated from field deposits (Kaminski & Jaupart, 1998), an initial magma temperature of 1133 K (Shane, 1998), and an exit velocity of 306 $m\,s^{-1}$ (Walker, 1980). The open circle stands for the stable Plinian phase Y2, the grey square for the two stages of transitional regime Y5-Y6, and the black square for the final total collapse Y7 (Table 1).

an open porosity of 60-70%. The good agreement between the model predictions and the field data illustrates the global consistency of the model.

4.2   The 79 CE Vesuvius eruption

The 79 CE Vesuvius eruption is one of the most well-documented historical Plinian event (Lirer *et al.* 1973; Sigurdsson *et al.* 1982, 1985, 1990; Carey & Sigurdsson 1987; Cioni 2000; Cioni *et al.* 1995, 2008; Balcone-Boissard *et al.* 2010; Shea *et al.* 2012 and references therein) and allows a thorough comparison with our theoretical predictions. The eruption started with a short phreatomagmatic phase and then pursued with a paroxysmal Plinian phase for about 17 h. First, a buoyant stable column rose up to ≈ 27 km high and produced a massive layer of white pumice (WP) fallout deposits that can be decomposed in 4 chronostratigraphic levels (levels 0.25W, 0.5W, 0.75W and 1W of the white fallout sequence; Carey & Sigurdsson 1987). This phase is also called EU2 in the literature (Cioni *et al.*, 1995, 2008; Balcone-Boissard *et al.*, 2010; Shea *et al.*, 2012). After a first partial collapse, the magma composition changed and yielded more unstable conditions. The column reached a maximum height of ≈ 33 km and generated several grey pumice (GP) fallout deposits interbedded with surges (levels W/G-S1, S1-S2, S2-S3, S3-S4 of the grey fallout sequence; Carey & Sigurdsson 1987). This transitional phase is also called EU3 in the literature (Cioni *et al.*, 1995, 2008; Balcone-Boissard *et al.*, 2010; Shea *et al.*, 2012). A first total collapse ended this magmatic phase. The eruption pursued for another few hours with a last short-lived plume before a second total collapse marking the end of the eruption (Balcone-Boissard *et al.*, 2010).

The mass eruption rates of successive phases were calculated, from the column heights

inferred from the isopleth maps and the temperate discharge curves of Sparks (1986): the MDR increased from 6.1×10^6 to 7.1×10^7 kg s^{-1} for the WP fall sequence and then up to 1.5×10^8 kg s^{-1} for the first partial collapse involving GP (Carey & Sigurdsson, 1987; Kaminski & Jaupart, 2001). We retain an uncertainty of a factor of 2 for the MDR, which corresponds to the change in MDR required to reach the same column height when using the model of Sparks (1986) or a more recent one (Girault et al., 2014). The total dissolved gas content of the melt is estimated to 6.00 ± 0.44 wt% at the beginning of the Plinian stable phase, and then decreased to 4.95 ± 0.20 wt% at the WP/GP boundary (Cioni, 2000). Using the same method as for the Taupo eruption, we correct these values for the presence of crystals and lithic fragments. The crystals content increased from 20% during the WP phase to 28% during the GP phase (Shea et al., 2009), and the lithics content increased from 12% during the WP phase to 20% during the GP phase (Sigurdsson et al., 1982). Assuming complete degassing, we find that the total gas mass fraction in the magma decreased from 4.08 ± 0.30 wt% during the WP phase to 2.57 ± 0.10 wt% during the GP phase. The power-law exponent D is taken to be 3.0 as measured by Costa et al. (2016a), the magma temperature is set to 1323 K, as measured by Gurioli et al. (2005) for the GP phase, and the exit velocity is set to 260 ± 10 m s^{-1} for the GP phase from the isopleth maps of Carey & Sigurdsson (1987). We note that using the power-law exponent $D = 3.0$ and an open porosity of 60-70% gives $\frac{x_{g_0}}{x_{tot}} \approx 0.84$ (Figure 2b). Together with the total gas mass fraction of 2.57 wt%, this value gives a calculated exit velocity of 230 ± 5 m s^{-1} for the W/G-S1 phase (Appendix B), which is consistent with the exit velocity constrained from the distribution of lithic fragments.
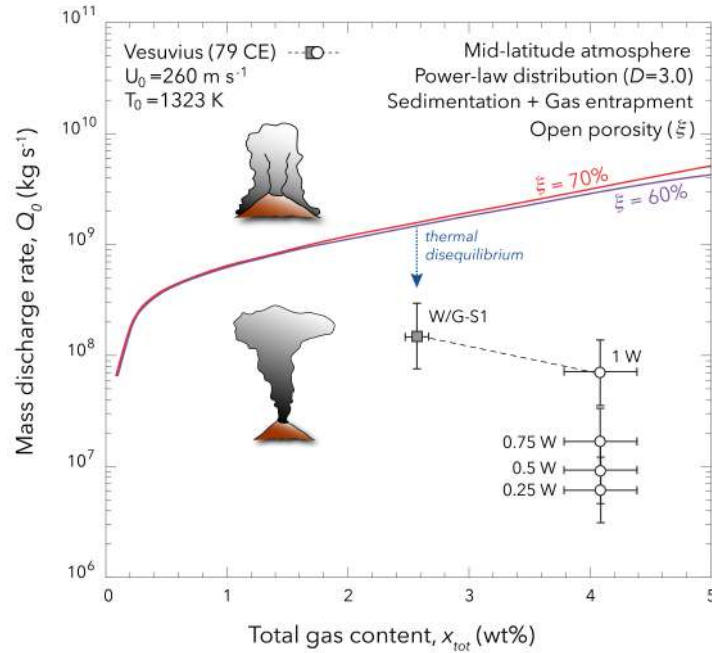
Figure 9: Eruptive conditions of the 79 CE Vesuvius eruption in terms of source mass discharge rate (in kg s^{-1}) and gas content (in wt%). The curves give the threshold mass discharge rate for column collapse when accounting for sedimentation and gas entrapment. Calculations are made for a power-law exponent D = 3.0 calculated from field deposits (Costa et al., 2016a), an initial magma temperature of 1323 K (Gurioli et al., 2005), and an exit velocity of 260 m s^{-1} (Carey & Sigurdsson, 1987). The open circles stand for stable Plinian phases (white pumices, WP or EU2) and the grey square for the first stage of transitional regime (grey pumice, GP or EU3) (Table 1).

Figure 9 compares the eruptive parameters inferred for the Vesuvius eruption (i.e., mass discharge rate and total gas content) and the transition between the stable plumes and the collapsing fountains predicted when considering particle sedimentation, gas entrapment and an open porosity of 60-70%. The model fails to reproduce the conditions of the transition between the Plinian stable regime of the WP fallout sequence and the collapse regime at the beginning of the GP fallout sequence. As all the model parameters are set by the field constraints, they cannot be tuned to improve the model predictions. However, we note that field deposits from this eruption are characterized by a power-law exponent D = 3.0, a D value that defines the transition between a population dominated by coarser fragments (i.e., $D < 3$) and a population dominated by ash (i.e., $D > 3$). We suggest that the hypothesis of thermal equilibrium has to be reconsidered for $D = 3.0$. For $D > 3$, the ash particles dominating the population are small enough to remain in thermal equilibrium (Woods & Bursik, 1991). For $D < 3$, coarse pumices rapidly settle to the ground leaving fine and coarse ash particles in thermal equilibrium in the column. For $D = 3.0$, there is no dominant population: the average size of the fragments is intermediate between fine ash and lapilli fragments, and is too large to ensure perfect thermal equilibrium. In that case column collapse is favored and the critical mass discharge rate before collapse can be reduced by up to an order of magnitude (Figure 5 of Woods & Bursik 1991), which would shift the theoretical predictions towards a better agreement with field data from the 79 CE Vesuvius eruption.

5   Discussion

5.1   The effect of crater shape on exit velocity

Gas entrapment – more or less modulated by the open porosity - reduces the amount of gas in the mixture and, in turn, the vertical velocity at the base of the plume. The presence of a crater with a specific shape can similarly reduce the velocity at the base of the plume (Woods & Bower, 1995; Koyaguchi et al., 2010), and it is always possible to define a crater shape that will perfectly mimic the effect of gas entrapment. As field data provide only constraints on the exit velocity, it is not possible to decide which model should be chosen. Overall, both decompression in a crater and gas entrapment can occur during an eruption and act together to set the conditions for collapse. In the case of the Taupo eruption, the global consistency between our model predictions with gas entrapment and open porosity and field data can be taken as a strong argument in favor of this framework. Adding a crater constraining decompression in the case of Taupo will actually decrease the agreement between model predictions and the data. In the case of Vesuvius, our model does not predict correctly the transition, but the predictions would not be changed if a crater is added as the exit velocity will remain constrained by the lithics.

5.2   Effect of wind on column collapse

The presence of wind can affect the plume dynamics and stability (Bursik, 2001; Degruyter & Bonadonna, 2013; Woodhouse et al., 2013; Suzuki & Koyaguchi, 2013, 2015; Mastin, 2014; Girault et al., 2016). Thereotical and numerical studies show that for high MDR and/or low wind velocity, the volcanic column forms a strong plume not affected by the wind field (Bonadonna & Phillips, 2003). For low MDR and/or high wind velocity, the volcanic plume trajectory is strongly controlled by the wind strength and direction, and the volcanic

column forms a weak bended plume (Bursik, 2001). The critical MDR before collapse is also strongly increased by a crosswind relative to no wind conditions, thus promoting the formation of a stable plume (Degruyter & Bonadonna, 2013; Girault *et al.*, 2016). Girault *et al.* (2016) showed that this effect is more pronounced for small MDR when $D < 3$ than for large MDR when $D > 3$, and that it strongly depends on the shape of the wind profile. The incorporation of crosswind in our model would thus requires to exactly know the shape of the wind profile, a parameter that is unknown for historical eruptions, and to parameterize the turbulent entrainment coefficient due to wind (commonly named β). The latter is currently unconstrained from laboratory experiments (Costa *et al.*, 2016*b*), and its relation with the turbulent entrainment coefficient α still remains unclear (Aubry *et al.*, 2017*b*,*a*). We therefore consider that a systematic study of this effect remains outside the scope of the present study.

We however check the validity of our no wind model when applied to the two historical eruptions considered here, using the method of Carazzo *et al.* (2014) to estimate the impact of wind on the plume dynamics. According to the isopleths maps determined from field data, the maximum wind velocity reached about 28 m s^{-1} during the WP phase of the 79 CE Vesuvius eruption, 31 m s^{-1} during the GP phase (Carey & Sigurdsson, 1987), and 27 m s^{-1} during the $\approx$186 CE Taupo eruption (Carey & Sparks, 1986). Together with the source conditions given in Table 1, we calculate the ratio of the dimensionless wind velocity to the dimensionless plume velocity W^*/U^* which is used as a proxy to infer the plume regime (Carazzo *et al.*, 2014). The 79 CE Vesuvius column is found to be a slightly distorted plume at the beginning of the eruption ($W^*/U^* \approx 0.2$) and a strong plume before the column collapses ($W^*/U^* \approx 0.1$). The $\approx$186 CE Taupo column is found to be a strong plume during the entire eruption ($W^*/U^* \approx 0.06$). For these two historical eruptions, atmospheric winds did not affect significantly the plume dynamics, and can thus be neglected when investigating the mechanisms leading to column collapse.

6 Conclusions

We have tested the combined effects of gas entrapment and reduced entrainment using a 1D turbulent plume model accounting for particle sedimentation. Compared with the predictions of previous studies accounting for gas entrapment or reduced entrainment only, this model favors too much column collapse compared with natural cases. We thus take into account open porosity, i.e. the fraction of bubbles preserved inside a fragment after fragmentation but connected to the exterior, which helps to generate stable plumes. We then predict various grain-size distributions in PDC depending on the TGSD (hence D value) at the volcanic vent. Low D values tend to promote the formation of relatively small fountains producing concentrated PDC with large particles, and reaching relatively low run-out distances. High D values tend to promote the formation of higher fountains producing dilute PDC containing mostly fine particles and covering larger distances. Finally, we compare the model predictions to the two well-known eruptions of Taupo ($\approx$186 CE) and Vesuvius (79 CE). We find a good agreement between theoretical predictions and field data for the Taupo eruption. For the Vesuvius eruption characterized by a power-law exponent $D = 3.0$, we suggest that thermal disequilibrium could explain the discrepancy between our predictions and field data.

Notation

a radius of the conduit, m

A buoyancy parameter, dimensionless

b bubble diameter, m

C shear stress parameter, 0.135, dimensionless

c_a specific heat at constant pressure of the atmosphere, 998 $\mathrm{J\,K^{-1}}$

c_p specific heat at constant pressure of the particles, 1100 $\mathrm{J\,K^{-1}}$

D exponent of the power-law distribution of particles, dimensionless

d_ϕ particle diameter, m

f frictional forces per unit of volume acting on the flow, $\mathrm{N\,m^{-3}}$

g gravitational acceleration, 9.81 $\mathrm{m\,s^{-2}}$

n total volatile content of the melt, wt%

N_ϕ number of classes of particle size, 20

P flow pressure in the conduit, Pa

P_a atmospheric pressure, Pa

P_v flow pressure at the vent, Pa

p_s probability of sedimentation, 0.27 ± 0.01, dimensionless

Q mass discharge rate feeding the eruption, $\mathrm{kg\,s^{-1}}$

Q_ϕ mass discharge rate of particles, $\mathrm{kg\,s^{-1}}$

r particle radius, m

r_{max} maximum particle size considered in this study, m

r_{min} minimum particle size considered in this study, m

R column radius, m

R_0 column radius at the vent, m

R_a gas constant of the atmospheric air, 287 $\mathrm{J\,K^{-1}\,kg^{-1}}$

Re_ϕ Reynolds number of the particles, dimensionless

R_g bulk constant of the mixture in the column, $R_{g0} = 461\ \mathrm{J\,K^{-1}\,kg^{-1}}$

Ri local Richardson number, dimensionless

S cross-sectional area of the conduit, $\mathrm{m^2}$

T flow temperature, K

T_a ambient atmospheric temperature for a mid-latitude atmosphere, 273 K

T_0 average andesitic magma temperature, 1200 K

u velocity of the magma-volatiles mixture, $\mathrm{m\,s^{-1}}$

U average vertical velocity in the column, $\mathrm{m\,s^{-1}}$

U_0 column average vertical velocity after decompression, $\mathrm{s^{-1}}$

U_e entrainment rate at the edge of the plume, $\mathrm{m\,s^{-1}}$

U_v average vertical velocity at the vent, $\mathrm{m\,s^{-1}}$

$V_{outgassed}$, volume of gas released due to the development of open porosity, $\mathrm{m^3}$

$V_{trapped}$, volume of gas initially trapped at fragmentation, $\mathrm{m^3}$

V_ϕ particle fallout velocity, $\mathrm{m\,s^{-1}}$

x_g effective gas mass fraction, dimensionless

x_{tot} total gas content, dimensionless

z vertical axis, m

z^* dimensionless height, $z^* = z/(2R_0)$

α_e variable entrainment coefficient, dimensionless

λ normalization constant of the power-law distribution, dimensionless

μ_0 dynamic viscosity of air at the vent, $\mu_0 = 1.832 \times 10^{-5}$ Pa s

μ_l liquid viscosity, 10^5 Pa s

ϕ particle size notation, $d_\phi = 2^{-\phi}$

ρ bulk density of the volcanic mixture, $\mathrm{kg\,m^{-3}}$

ρ_a atmospheric density, $\mathrm{kg\,m^{-3}}$

ρ_l liquid density, 2500 $\mathrm{kg\,m^{-3}}$

ρ_p particle density, 2000 $\mathrm{kg\,m^{-3}}$

ρ_v flow density at the vent, $\mathrm{kg\,m^{-3}}$

$\Delta\rho$ density difference between the liquid and the country rock, 100 $\mathrm{kg\,m^{-3}}$

ξ fraction of gas initially trapped and released by open porosity, dimensionless

$_0$ values at the vent

Appendix A

The model of turbulent entrainment of Kaminski *et al.* (2005) introduced two dimensionless variables: C, which gives the fraction of kinetic energy available for turbulent entrainment, and A which depends on the half width of velocity and density profiles in the jet. Carazzo *et al.* (2006, 2008*a*,*b*) further showed that A is not a constant but evolves as a function of the distance from the source and buoyancy. They propose the following empirical formula:

$$A = A_j + \frac{(A_p - A_j)}{4}\left(\frac{z}{L_m} - 1\right), \tag{A 1}$$

where A_j and A_p are the values of A for a pure jet (Ri $= 0$), and a pure plume (no mass discharge rate at the source), respectively. L_m is the Fisher length scale, defined as:

$$L_m = \frac{M_0^{3/4}}{F_0^{1/2}}, \tag{A 2}$$

where M_0 and F_0 are the momentum and buoyancy flow rates at the source, respectively. These parameters were estimated from laboratory measurements (Carazzo *et al.*, 2006) and can be fitted as a function of the dimensionless height $z^* = z/(2R_0)$ by:

$$\left.\begin{aligned}A_j &= 1.1 + 4.6.10^{-3} \times (z^*)^2 - 2.10^{-4} \times (z^*)^3 \\ A_p &= 1.3 + 3.4.10^{-3} \times (z^*)^2 + 2.1.10^{-4} \times (z^*)^3\end{aligned}\right\} \text{ for } z^* < 15, \tag{A 3}$$

and

$$\left.\begin{aligned}A_j &= 2.45 - 1.05\exp(-4.65.10^{-3} \times z^*) \\ A_p &= 1.42 - 4.42\exp(-2.188.10^{-1} \times z^*)\end{aligned}\right\} \text{ for } z^* > 15, \tag{A 4}$$

This set of equations is injected into Eq. (4) to calculate the entrainment coefficient α_e at each altitude step z.

Appendix B

We derive an expression for the exit velocity after decompression following Woods & Bower (1995). For an impermeable conduit, the mass discharge rate Q remains constant with depth, so that the mass conservation equation gives

$$Q = \rho u S = \text{cst}, \tag{B 1}$$

where ρ and u are the density and the velocity of the magma-volatiles mixture, respectively, and $S = \pi a^2$ is the cross-sectional area of the conduit with a its radius. For simplicity, we assume that the conduit has a constant cross-section.

The momentum conservation equation in the conduit can be written as (Wilson *et al.*, 1980; Woods & Bower, 1995; Koyaguchi, 2005)

$$\rho u \frac{du}{dz} + \frac{dP}{dz} = -\rho g - f, \tag{B 2}$$

where f is the frictional forces acting on the flow, P the flow pressure in the conduit, and g the gravitational acceleration.

Before exsolution, we consider that the liquid can be modelled as a Poiseuille flow, where the mass discharge rate Q is linked to the conduit radius a by

$$Q = \frac{\rho_l \pi a^4 \Delta \rho g}{8 \mu_l}, \tag{B 3}$$

where ρ_l and μ_l are the liquid density and viscosity taken as $2500 \ \text{kg m}^{-3}$ and $10^5 \ \text{Pa s}$, respectively, and $\Delta \rho$ is the density difference between the liquid and the country rock, which we set at $100 \ \text{kg m}^{-3}$. Combining Eqs. (B1) and (B3) gives

$$\frac{S}{Q} = \left(\frac{8 \pi \mu_l}{Q \rho_l \Delta \rho g} \right)^{1/2}, \tag{B 4}$$

which can be replaced in Eq. (12).

We now seek for an expression for U_v and P_v in Eq. (12). Above the fragmentation level, the particle-gas mixture density depends on the effective amount of free gas x_g in the volcanic mixture, such as

$$\rho = \left(\frac{1 - x_g}{\rho_p} + \frac{x_g R_g T}{P} \right)^{-1}, \tag{B 5}$$

where we assume that ρ_p and T remain constant in the conduit (Woods & Bower, 1995).

By replacing Eqs. (B1) and (B5) into Eq. (B2), one can write

$$\frac{dP}{dz} \left(1 - u^2 x_g R_g T \frac{\rho^2}{P^2} \right) = -\rho g - f, \tag{B 6}$$

which can be used to find the velocity at the vent U_v by setting the coefficient on the left-hand side to zero, which yields

$$U_v = \frac{P_v}{\rho_v}(x_g R_g T)^{-1/2}, \qquad (B\ 7)$$

where ρ_v is given by Eq. (B5) for $P = P_v$. The pressure at the vent P_v can be calculated by combining Eqs. (B1) and (B7) to get:

$$P_v = \frac{Q}{S}(x_g R_g T)^{1/2}, \qquad (B\ 8)$$

which can be rewritten by using Eq. (B4) as:

$$P_v = \left(\frac{Q x_g R_g T \rho_l \Delta \rho g}{8\pi \mu_l}\right). \qquad (B\ 9)$$

From Eqs. (B4), (B5), (B7), (B9) together with Eq. (12) one can then calculate U_0, the vertical velocity of the volcanic column after decompression.

References

ALIBIDIROV, M. & DINGWELL, D.B. 1996 Magma fragmentation by rapid decompression. *Nature* **380**, 146–148.

AUBRY, T.J., CARAZZO, G. & JELLINEK, A.M. 2017*a* Turbulent Entrainment Into Volcanic Plumes: New Constraints From Laboratory Experiments on Buoyant Jets Rising in a Stratified Crossflow. *Geophys. Res. Lett.* **44**, 10,198–10,207.

AUBRY, T.J., JELLINEK, A.M., CARAZZO, G., GALLO, R., HATCHER, K. & DUNNING, J. 2017*b* A new analytical scaling for turbulent wind-bent plumes: Comparison of scaling laws with analog experiments and a new database of eruptive conditions for predicting the height of volcanic plumes. *J. Volcanol. Geotherm. Res.* **343**, 233–251.

BALCONE-BOISSARD, H., BOUDON, G. & VILLEMANT, B. 2010 Textural and geochemical constraints on eruptive style of the 79 AD eruption at Vesuvius. *Bull. Volcanol.* **73**, 279–294.

BONADONNA, C., ERNST, G.G.J. & SPARKS, R.S.J. 1998 Thickness variations and volume estimates of tephra fall deposits: The importance of particle Reynolds number. *J. Volcanol. Geotherm. Res.* **81**, 173–187.

BONADONNA, C. & PHILLIPS, J.C. 2003 Sedimentation from strong volcanic plumes. *J. Geophys. Res. Solid Earth* **108**, 1–28.

BOUVET DE MAISONNEUVE, C., BACHMANN, O. & BURGISSER, A. 2009 Characterization of juvenile pyroclasts from the Kos Plateau Tuff (Aegean Arc): Insights into the eruptive dynamics of a large rhyolitic eruption. *Bull. Volcanol.* **71**, 643–658.

BURSIK, M. 2001 Effect of wind on the rise height of volcanic plumes. *Geophys. Res. Lett.* **28**, 3621–3624.

BURSIK, M.I. & WOODS, A.W. 1996 The dynamics and thermodynamics of large ash flows. *Bull. Volcanol.* **58**, 175–193.

CARAZZO, G., GIRAULT, F., AUBRY, T., BOUQUEREL, H. & KAMINSKI, E. 2014 Laboratory experiments of forced plumes in a density-stratified crossflow and implications for volcanic plumes. *Geophys. Res. Lett.* **41**, 8759–8766.

CARAZZO, G., KAMINSKI, E. & TAIT, S. 2006 The route to self-similarity in turbulent jets and plumes. *J. Fluid Mech.* **547**, 137–148.

CARAZZO, G., KAMINSKI, E. & TAIT, S. 2008*a* On the dynamics of volcanic columns: A comparison of field data with a new model of negatively buoyant jets. *J. Volcanol. Geotherm. Res.* **178**, 94–103.

CARAZZO, G., KAMINSKI, E. & TAIT, S. 2008*b* On the rise of turbulent plumes: Quantitative effects of variable entrainment for submarine hydrothermal vents, terrestrial and extra terrestrial explosive volcanism. *J. Geophys. Res. Solid Earth* **113**, 1–19.

CARAZZO, G., KAMINSKI, E. & TAIT, S. 2015 The timing and intensity of column collapse during explosive volcanic eruptions. *Earth Planet. Sci. Lett.* **411**, 208–217.

CAREY, S. & SIGURDSSON, H. 1987 Temporal variations in column height and magma discharge rate during the 79 A.D. eruption of Vesuvius. *Geol. Soc. Am. Bull.* **99**, 303–314.

CAREY, S. & SIGURDSSON, H. 1989 The intensity of Plinian eruptions. *Bull. Volcanol.* **51**, 28–40.

CAREY, S. & SPARKS, R.S.J. 1986 Quantitative models of the fallout and dispersal of tephra from volcanic eruption columns. *Bull. Volcanol.* **48**, 109–125.

CIONI, R. 2000 Volatile content and degassing processes in the AD 79 magma chamber at Vesuvius (Italy). *Contrib. Mineral. Petrol.* **140** (1), 40–54.

CIONI, R., BERTAGNINI, A., SANTACROCE, R. & ANDRONICO, D. 2008 Explosive activity and eruption scenarios at Somma-Vesuvius (Italy): Towards a new classification scheme. *J. Volcanol. Geotherm. Res.* **178** (3), 331–346.

CIONI, R., CIVETTA, L., MARIANELLI, P., METRICH, N., SANTACROCE, R. & SBRANA, A. 1995 Compositional layering and syn-eruptive mixing of a periodically refilled shallow magma chamber: The AD 79 plinian eruption of Vesuvius. *J. Petrol.* **36** (3), 739–776.

COSTA, A., MACEDONIO, G. & FOLCH, A. 2006 A three-dimensional Eulerian model for transport and deposition of volcanic ashes. *Earth Planet. Sci. Lett.* **241** (3-4), 634–647.

COSTA, A., PIOLI, L. & BONADONNA, C. 2016*a* Assessing tephra total grain-size distribution: Insights from field data analysis. *Earth Planet. Sci. Lett.* **443**, 90–107.

COSTA, A., SUZUKI, Y. J., CERMINARA, M., DEVENISH, B. J., ESPOSTI ONGARO, T., HERZOG, M., VAN EATON, A. R., DENBY, L. C., BURSIK, M., DE' MICHIELI VITTURI, M., ENGWELL, S., NERI, A., BARSOTTI, S., FOLCH, A., MACEDONIO, G., GIRAULT, F., CARAZZO, G., TAIT, S., KAMINSKI, E., MASTIN, L. G., WOODHOUSE, M. J., PHILLIPS, J. C., HOGG, A. J., DEGRUYTER, W. & BONADONNA, C. 2016*b* Results of the eruptive column model inter-comparison study. *J. Volcanol. Geotherm. Res.* **326**, 2–25.

DEGRUYTER, W. & BONADONNA, C. 2013 Impact of wind on the condition for column collapse of volcanic plumes. *Earth Planet. Sci. Lett.* **377-378**, 218–226.

DUNBAR, N.W., KYLE, P.R. & WILSON, C.J.N. 1989 Evidence for limited zonation in silicic magma systems, Taupo Volcanic Zone, New Zealand. *Geology* **17** (3).

DUNBAR, N. W. & KYLE, P. R. 1993 Lack of volatile gradient in the Taupo plinian-ignimbrite transition: Evidence from melt inclusion analysis. *Am. Mineral.* **78** (5-6), 612–618.

ERNST, G. J., STEPHEN, R., SPARKS, J., CAREY, N. & BURSIK, M. I. 1996 Sedimentation from turbulent jets and plumes. *J. Geophys. Res.* **101** (95), 5575–5589.

ESPOSTI ONGARO, T., NERI, A., MENCONI, G., DE'MICHIELI VITTURI, M., MARIANELLI, P., CAVAZZONI, C., ERBACCI, G. & BAXTER, P. J. 2008 Transient 3D numerical simulations of column collapse and pyroclastic density current scenarios at Vesuvius. *J. Volcanol. Geotherm. Res.* **178** (3), 378–396.

FORMENTI, Y. & DRUITT, T. H. 2003 Vesicle connectivity in pyroclasts and implications for the fluidisation of fountain-collapse pyroclastic flows, Montserrat (West Indies). *Earth Planet. Sci. Lett.* **214** (3-4), 561–574.

FROGGATT, P. C. 1981 Stratigraphy and nature of Taupo pumice formation. *N. Z. J. Geol. Geophys.* **24** (2), 231–248.

GIRAULT, F., CARAZZO, G., TAIT, S., FERRUCCI, F. & KAMINSKI, E. 2014 The effect of total grain-size distribution on the dynamics of turbulent volcanic plumes. *Earth Planet. Sci. Lett.* **394**, 124–134.

GIRAULT, F., CARAZZO, G., TAIT, S. & KAMINSKI, E. 2016 Combined effects of total grain-size distribution and crosswind on the rise of eruptive volcanic columns. *J. Volcanol. Geotherm. Res.* **326**, 103–113.

GLAZE, S. & BALOGA, S. M. 1996 Sensitivity of buoyant plume heights to ambient atmospheric conditions: Implications for volcanic eruption columns. *J. Geophys. Res.* **101**, 1529–1540.

GURIOLI, L., HOUGHTON, B. F., CASHMAN, K. V. & CIONI, R. 2005 Complex changes in eruption dynamics during the 79 AD eruption of Vesuvius. *Bull. Volcanol.* **67** (2), 144–159.

HORWELL, C. J. 2007 Grain-size analysis of volcanic ash for the rapid assessment of respiratory health hazard. *J. Environ. Monit.* **9** (10), 1107–1115.

HORWELL, C. J. & BAXTER, P. J. 2006 The respiratory health hazards of volcanic ash: A review for volcanic risk mitigation. *Bull. Volcanol.* **69** (1), 1–24.

HORWELL, C. J., BAXTER, P. J., HILLMAN, S. E., CALKINS, J. A., DAMBY, D. E., DELMELLE, P., DONALDSON, K., DUNSTER, C., FUBINI, B., KELLY, F. J., LE BLOND, J. S., LIVI, K. J.T., MURPHY, F., NATTRASS, C., SWEENEY, S., TETLEY, T. D., THORDARSON, T. & TOMATIS, M. 2013 Physicochemical and toxicological profiling of ash from the 2010 and 2011 eruptions of Eyjafjallajökull and Grímsvötn volcanoes, Iceland using a rapid respiratory hazard assessment protocol. *Environ. Res.* **127**, 63–73.

HOUGHTON, B. F., CAREY, R. J. & ROSENBERG, M. D. 2014 The 1800a Taupo eruption:" Ill wind" blows the ultraplinian type event down to Plinian. *Geology* **42** (5), 459–461.

KAMINSKI, E. & JAUPART, C. 1998 The size distribution of pyroclasts and the fragmentation sequence in explosive volcanic eruptions. *J. Geophys. Res.* **103**, 29759–29779.

KAMINSKI, E. & JAUPART, C. 2001 Marginal stability of atmospheric eruption columns and pyroclastic flow generation. *J. Geophys. Res.* **106** (B10), 21785–21798.

KAMINSKI, E., TAIT, S. & CARAZZO, G. 2005 Turbulent entrainment in jets with arbitrary buoyancy. *J. Fluid Mech.* **526**, 361–376.

KLUG, C., CASHMAN, K. & BACON, C. 2002 Structure and physical characteristics of pumice from the climactic eruption of Mount Mazama (Crater Lake), Oregon. *Bull. Volcanol.* **64** (7), 486–501.

KLUG, C. & CASHMAN, K. V. 1996 Permeability development in vesiculating magmas: Implications for fragmentation. *Bull. Volcanol.* **58** (2-3), 87–100.

KOYAGUCHI, TAKEHIRO 2005 An analytical study for 1-dimensional steady flow in volcanic conduits. *J. Volcanol. Geotherm. Res.* **143** (1-3), 29–52.

KOYAGUCHI, T., SUZUKI, Y. J. & KOZONO, T. 2010 Effects of the crater on eruption column dynamics. *J. Geophys. Res.* **115** (7), 1–26.

KUEPPERS, U., PERUGINI, D. & DINGWELL, D. B. 2006 "Explosive energy" during volcanic eruptions from fractal analysis of pyroclasts. *Earth and Planetary Science Letters* **248** (3-4), 800–807.

LIRER, L., PESCATORE, T., BOOTH, B. & WALKER, G. P. L. 1973 Two Plinian pumice-fall deposits from Somma-Vesuvius, Italy. *Geol. Soc. Am. Bull.* **84** (3), 759–772.

MASTIN, L. G. 2014 Testing the accuracy of a 1-D volcanic plume model in estimating mass eruption rate. *J. Geophys. Res.* **119**, 2474–2495.

MILLER, T. P. & CASADEVALL, T. J. 2000 Volcanic ash hazards to aviation. In *Encyclopedia of Volcanoes* (ed. H.E. Sigurdsson), pp. 915–930. Academic Press, San Diego.

MORTON, B.R., TAYLOR, G.I. & TURNER, J.S. 1956 Turbulent gravitational convection from maintained and instantaneous sources. *Philos. Trans. R. Soc. A* **234**, 1–23.

References

NERI, A. & DOBRAN, F. 1994 Influence of eruption parameters on the thermofluid dynamics of collapsing volcanic columns. *J. Geophys. Res.* **99** (B6), 11833–11857.

NGUYEN, C. T., GONNERMANN, H. M. & HOUGHTON, B. F. 2014 Explosive to effusive transition during the largest volcanic eruption of the 20th century (Novarupta 1912, Alaska). *Geology* **42** (8), 703–706.

PLATZ, T., CRONIN, S. J., CASHMAN, K. V., STEWART, R. B. & SMITH, I. E. M. 2007 Transition from effusive to explosive phases in andesite eruptions - A case-study from the AD1655 eruption of Mt. Taranaki, New Zealand. *J. Volcanol. Geotherm. Res.* **161** (1-2), 15–34.

SCHMIDT, A., WITHAM, C. S., THEYS, N., RICHARDS, N. A. D., THORDARSON, T., REDINGTON, A. L., JOHNSON, B. T., HAYWARD, C. L. & CARSLAW, K. S. 2014 Assessing hazards to aviation from sulfur dioxide emitted by explosive Icelandic eruptions. *J. Geophys. Res.* **119**, 14180–14196.

SETTLE, M. 1978 Volcanic eruption clouds and the thermal power output of explosive eruptions. *J. Volcanol. Geotherm. Res.* **3** (3-4), 309–324.

SHANE, P. 1998 Correlation of rhyolitic pyroclastic eruptive units from the Taupo volcanic zone by Fe-Ti oxide compositional data. *Bull. Volcanol.* **60** (3), 224–238.

SHEA, T., GURIOLI, L. & HOUGHTON, B. F. 2012 Transitions between fall phases and pyroclastic density currents during the AD 79 eruption at Vesuvius: Building a transient conduit model from the textural and volatile record. *Bull. Volcanol.* **74** (10), 2363–2381.

SHEA, T., LARSEN, J. F., GURIOLI, L., HAMMER, J. E., HOUGHTON, B. F. & CIONI, R. 2009 Leucite crystals: Surviving witnesses of magmatic processes preceding the 79AD eruption at Vesuvius, Italy. *Earth Planet. Sci. Lett.* **281** (1-2), 88–98.

SIGURDSSON, H., CAREY, S., CORNELL, W. & PESCATORE, T. 1985 The eruption of Vesuvius in AD 79. *Natl. Geogr. Res.* **1**, 332–387.

SIGURDSSON, H., CASHDOLLAR, S. & SPARKS, R. S. J. 1982 The eruption of Vesuvius in AD 79: Reconstruction from historical and volcanological evidence. *Am. J. Archaeol.* **86**, 39–51.

SIGURDSSON, H., CORNELL, W. & CAREY, S. 1990 Influence of magma withdrawal on compositional gradients during the AD 79 Vesuvius eruption. *Nature* **345**, 519–521.

SPARKS, R. S. J. 1986 The dimensions and dynamics of volcanic eruption columns. *Bull. Volcanol.* **48**, 3–15.

SPARKS, R. S. J., BURSIK, M., CAREY, S., GILBERT, J. S., GLAZE, L. S., SIGURDSSON, H. & WOODS, A. W. 1997 *Volcanic Plumes*. John Wiley, New York.

SPARKS, R. S. J. & WILSON, L. 1976 A model for the formation of ignimbrite by gravitational column collapse. *J. Geol. Soc. Lond.* **132**, 441–451.

SPENCE, R. J. S., BAXTER, P. J. & ZUCCARO, G. 2004 Building vulnerability and human casualty estimation for a pyroclastic flow: A model and its application to Vesuvius. *J. Volcanol. Geotherm. Res.* **133** (1-4), 321–343.

SUTHERLAND, W. 1893 The viscosity of gases and molecular forces. *Philos. Mag.* **39** (5), 507–531.

SUZUKI, Y. & KOYAGUCHI, T. 2015 Effects of wind on entrainment in volcanic plumes. *J. Geophys. Res. B.* **120**, 6122–6140.

SUZUKI, Y. J. & KOYAGUCHI, T. 2013 3D numerical simulation of volcanic eruption clouds during the 2011 Shinmoe-dake eruptions. *Earth Planets Space* **65**, 581–589.

SUZUKI, Y. J., KOYAGUCHI, T., OGAWA, M. & HACHISU, I. 2005 A numerical study of turbulent mixing in eruption clouds using a three-dimensional fluid dynamics model. *J. Geophys. Res.* **110**, B08201.

TALBOT, J. P., SELF, S. & WILSON, C. J. N. 1994 Dilute gravity current and rain-flushed ash deposits in the 1.8 ka Hatepe Plinian deposit, Taupo, New Zealand. *Bull. Volcanol.* **56**, 538–551.

TORAMARU, A. 1988 Formation of propagation pattern in two-phase flow systems with application to volcanic eruptions. *Geophys. J.* **95**, 613–623.

VALENTINE, G. A. & WOHLETZ, K. H. 1989 Numerical Models of Plinian Eruption Columns and Pyro-clastic Flows. *J. Geophys. Res.* **94** (B2), 1867–1887.

WALKER, G. P. L. 1980 The Taupo pumice: Product of the most powerful known (ultraplinian) eruption? *J. Volcanol. Geotherm. Res.* **8**, 69–94.

WALKER, G. P. L. 1981 Plinian eruptions and their products. *Bull. Volcanol.* **44-2**, 223–240.

WILSON, C. J. N. 1985 The Taupo eruption, New Zealand II. The Taupo Ignimbrite. *Philos. Trans. R. Soc. Lond.* **314** (1529), 199–310.

WILSON, C. J. N. 1993 Stratigraphy, chronology, styles and dynamics of late quaternary eruptions from Taupo volcano, New Zealand. *Philos. Trans. R. Soc. Lond.* **343**, 205–306.

WILSON, C. J. N. & WALKER, G. P. L. 1985 The Taupo eruption, New Zealand. I general aspects. *Philos. Trans. R. Soc. Lond.* **314**, 199–228.

WILSON, G., WILSON, T. W., DELIGNE, N. I. & COLE, J. W. 2014 Volcanic hazard impacts to critical infrastructure: A review. *J. Volcanol. Geotherm. Res.* **286**, 148–182.

WILSON, L. 1976 Explosive Volcanic Eruptions: III. Plinian Eruption Columns. *J. R. Astron. Soc.* **45**, 543–556.

WILSON, L., SPARKS, R. S. J., HUANG, T. C. & WATKINS, N. D. 1978 The Control of Volcanic Column Heights by Eruption Energetics and Dynamics. *J. Geophys. Res.* **83** (B4), 1829–1836.

WILSON, L., SPARKS, R. S. J. & WALKER, G. P. L. 1980 Explosive volcanic eruptions - IV. The control of magma properties and conduit geometry on eruption column behaviour. *Geophys. J. R. Astron. Soc.* **63**, 117–148.

WOODHOUSE, M. J., HOGG, A. J., PHILLIPS, J. C. & SPARKS, R. S. J. 2013 Interaction between volcanic plumes and wind during the 2010 Eyjafjallajökull eruption, Iceland. *J. Geophys. Res. Solid Earth* **118**, 92–109.

WOODS, A.W. 1988 The fluid dynamics and thermodynamics of eruption columns. *Bull. Volcanol.* **50**, 169–193.

WOODS, A. W. 1995 The dynamics of explosive volcanic eruptions. *Rev. Geophys.* **33**, 495–530.

WOODS, A. W. & BOWER, S. M. 1995 The decompression of volcanic jets in a crater during explosive eruptions. *Earth Planet. Sci. Lett.* **131**, 189–205.

WOODS, A. W. & BURSIK, M. I 1991 Particle fallout, thermal disequilibrium and volcanic plumes. *Bull. Volcanol.* **53**, 559–570.

WOODS, A. W. & CAULFIELD, C. P. 1992 A laboratory study of explosive volcanic eruptions. *J. Geophys. Res.* **97** (B5), 6699–6712.

Chapter 4

Wind entrainment in reversing buoyant jets: laboratory constraints and implications for volcanic plumes

Michaud-Dubuy A., Carazzo G., and Kaminski E. *Submitted.*

Table of contents

Résumé du chapitre 4

Le modèle présenté dans le chapitre précédent permet d'expliquer la transition entre les régimes stable et d'effondrement de plusieurs éruptions historiques. Nous montrons dans ce chapitre qu'il ne peut pourtant pas expliquer le déroulement des éruptions historiques du Tambora (Indonésie) en 1815, du Nevado del Ruiz (Colombie) en 1985 et du Pinatubo (Philippines) en 1991. Ces éruptions sont particulièrement célèbres à cause de leurs puissances, de leurs conséquences climatiques ressenties dans de nombreuses régions du globe, et de leurs bilans humains particulièrement lourds. L'étude des dépôts de ces éruptions a révélé qu'elles se sont toutes produites sous des vents puissants allant jusqu'à $30 \, \mathrm{m \, s^{-1}}$. Or, le vent peut avoir un fort effet sur la dynamique d'une colonne volcanique, en augmentant l'efficacité du mélange entre celle-ci et l'atmosphère. Notre modèle PPM présenté en chapitre 3 ne prenant pas en compte l'effet du vent, cela pourrait expliquer le manque de cohérence entre les prédictions du modèle et les conditions éruptives du Tambora, du Nevado del Ruiz et du Pinatubo.

Afin d'incorporer l'effet du vent dans le modèle, il est tout d'abord nécessaire de quantifier son impact sur le mélange turbulent entre colonne volcanique et atmosphère. Ce dernier est généralement pris en compte dans les modèles 1D par un coefficient d'entrainement β dont la valeur est actuellement mal contrainte et varie entre 0.1 et 1 dans la littérature. Dans ce chapitre, nous réalisons des expériences en laboratoire inédites permettant de simuler des jets turbulents se formant dans un environnement soumis au vent, et reproduisant l'inversion de flottabilité caractérisant les colonnes volcaniques naturelles. En comparant nos observations avec les prédictions théoriques d'un modèle 1D, nous montrons qu'une valeur de $\beta = 0.5$ permet d'expliquer nos résultats obtenus en laboratoire. Une autre série d'expériences reproduisant des fontaines en effondrement dont les trajectoires sont ensuite comparées à des trajectoires théoriques calculées par un modèle 1D confirme que cette valeur peut également être utilisée pour des jets à flottabilité négative ou positive.

En incorporant cette valeur universelle de β dans notre modèle 1D complet PPM, nous sommes capables d'expliquer le déroulement des éruptions historiques du Pinatubo, du Nevado del Ruiz et du Tambora. Nous montrons donc que le vent fort soufflant durant ces éruptions a retardé voire empêché l'effondrement de la colonne éruptive, épargnant ainsi les populations vivant au pied de ces volcans. Nos résultats permettent également de créer une nouvelle loi de transition basée sur le flux de masse de l'éruption et le rapport vitesse de vent / flux de masse. Ce rapport peut être déterminé par des mesures de la vitesse du vent et de la hauteur maximale atteinte par la colonne éruptive pour les éruptions observées, ou par la distribution des fragments lithiques sur le terrain pour des éruptions plus anciennes. Ainsi, la forme des isoplètes déterminées sur le terrain pourrait être un critère déterminant pour l'étude de la dynamique des éruptions passées. Cette étude montre donc l'importance primordiale du vent à chaque étape d'une éruption, de la dynamique du panache à la dispersion des produits volcaniques dans l'atmosphère (et donc sur l'évaluation de l'aléa).

1   Introduction

The historical eruptions of Tambora (Indonesia) in 1815, Pinatubo (Philippines) in 1991, and Nevado del Ruiz (Colombia) in 1985, respectively ranked 7, 6, and 3 in the VEI (Volcanic Explosivity Index, Newhall & Self 1982), were powerful and led to huge casualties making them almost legendary. Death tolls generally assumed for these eruptions indeed reach a total of 65,000 for the Tambora eruption, 23,000 for the Nevado del Ruiz event (caused by volcanic mudflows), and 1,200 only for the Pinatubo eruption (thanks to early warning indicators and effective evacuations) (Tanguy *et al.*, 1998; Oppenheimer, 2003). In addition, all three eruptions ejected huge amounts of sulfure dioxide in the atmosphere leading to drastic decrease of global temperatures (about 0.5 °C for the Tambora and Pinatubo eruptions, D'Arrigo *et al.* 2009; Self *et al.* 1996) causing famine and epidemic diseases all around the globe. The Tambora, Pinatubo and Nevado del Ruiz eruptions were characterized by a strong explosion propelling a column of hot gas and pyroclasts up to a maximum height of 43, 39, and 31 km in the atmosphere, respectively (Sigurdsson & Carey, 1989; Costa *et al.*, 2016; Naranjo *et al.*, 1986). While the Nevado del Ruiz eruptive column remained stable, those of the Tambora and the Pinatubo partially collapsed during the eruption and produced deadly pyroclastic density currents (PDC) (Figure 1a).
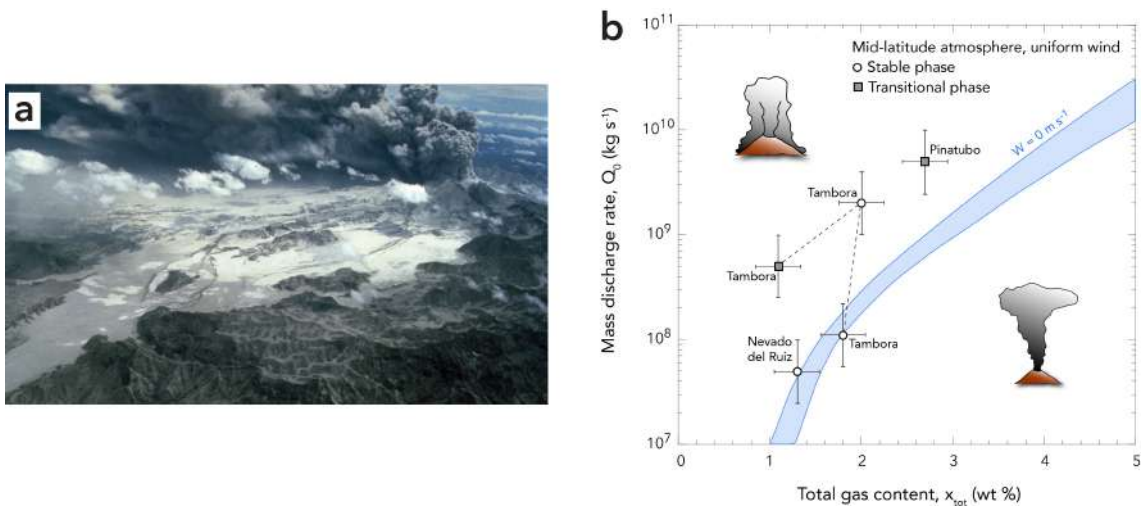

Figure 1: a Aerial view of the Marella valley filled with pyroclastic flow deposits (in foreground) and the ash plume (in distance) produced by the Mount Pinatubo eruption in 1991, *Ed Wolfe, USGS*. **b** Eruptive conditions of the Tambora 1815, Nevado del Ruiz 1985 and Pinatubo 1991 eruptions in terms of source mass discharge rate (in $kg\,s^{-1}$) and total gas content (wt%). The blue envelope accounts for the effect of the power-law exponent D (see Michaud-Dubuy *et al.* 2018 and main text). We consider a mid-latitude atmosphere, a magma temperature taken as the average of andesitic magma (T_0=1200 K), and an open porosity of 65% (Michaud-Dubuy *et al.*, 2018). All the geological data are summarized in Table 1.

Since the 1970's, numerous 1D, 2D and 3D theoretical models have allowed to reach a good knowledge of the overall physics of these eruptions and to study the conditions leading to column collapse (Sparks, 1986; Woods, 1988; Valentine & Wohletz, 1989; Neri & Dobran, 1994; Suzuki *et al.*, 2005; Esposti Ongaro *et al.*, 2008). As in Michaud-Dubuy *et al.* (2018) and Chapter 3, we define here the transition between the stable and collapse regimes as a critical mass discharge (MDR, in $kg\,s^{-1}$) before collapse for a given gas mass fraction (in wt%), two key parameters controlling the stability of a volcanic column (Wilson *et al.*, 1980; Woods & Caulfield, 1992). The blue envelope in Figure 1b shows the threshold mass discharge rate calculated by the 1D Paris Plume Model (PPM, Michaud-Dubuy *et al.* 2018). Comparing this transition law with the Tambora, Pinatubo and Nevado del Ruiz eruptions

shows that the transition conditions between the stable (white dots) and partial collapse (grey squares) regimes are not reproduced by the model (Figure 1b).

Table 1: Eruption conditions of the 1815 Tambora, 1985 Nevado del Ruiz and 1991 Pinatubo eruptions. (1) Sigurdsson & Carey 1989; (2) Kandlbauer & Sparks 2014; (3) Melson *et al.* 1990; (4) Wallace 2005; (5) Naranjo *et al.* 1986; (6) Borisova *et al.* 2005; (7) Koyaguchi & Ohno 2001; (8) Costa *et al.* 2013; (9) Costa *et al.* 2016; (10) Holasek *et al.* 1996; (11) Wiesner *et al.* 2004; (12) Fero *et al.* 2009. As in Michaud-Dubuy *et al.* (2018), we retain an uncertainty of a factor of 2 for the mass discharge rate (MDR), which corresponds to the change in MDR required to reach the same column height when using the model of Sparks (1986) or a more recent one (Girault *et al.*, 2014). * Values corrected for the presence of crystals and lithic fragments, which do not contain volatiles, as in Kaminski & Jaupart (2001). We assume complete degassing. ** Mass discharge rate of 1.5×10^9 $\mathrm{kg\,s^{-1}}$ (Costa *et al.*, 2013, 2016) corrected with a F factor of 0.7 (Carazzo *et al.*, 2015) to take into account both the air fall deposit and flow deposit masses.

Eruption (deposit)	Initial gas content, (corrected for crystals and lithics, wt%)	Mass discharge rate, MDR $(\mathrm{kg\,s^{-1}})$	Plume maximum height (km a.s.l.)	Estimated wind speed $(\mathrm{m\,s^{-1}})$
Tambora (F2)	1.8 ± 0.25 (1)*	1.1×10^8 (1)	33 (1)	5 (1)
Tambora (F4)	2.0 ± 0.25 (1)*	2.0×10^9 (2)	43 (1)	25 (1)
Tambora (F5)	1.1 ± 0.25 (1)*	5.0×10^8 (2)	25 (2)	25 (1)
Nevado del Ruiz (1985)	1.3 ± 0.25 (3,4,5)*	5.0×10^7 (5)	31 (5)	30 (1)
Pinatubo (C1)	2.7 ± 0.25 (6,7)*	5.0×10^9 (8, 9)**	39 (7, 8, 9, 10)	20 (7, 11, 12)

The non-consistency between the theoretical predictions and field data may be due to the absence of wind in PPM. All three Tambora, Pinatubo and Nevado del Ruiz eruptions indeed occurred under strong winds (between 20 and 30 $\mathrm{m\,s^{-1}}$, Sigurdsson & Carey 1989; Koyaguchi & Ohno 2001; Wiesner *et al.* 2004; Fero *et al.* 2009). Wind can cause, for example, a distortion of the plume trajectory by addition of horizontal momentum, which will have a strong impact on both the column maximum height (Woods, 1988; Bursik, 2001; Costa *et al.*, 2016) and the main dispersal axis of the volcanic products (Carey & Sigurdsson, 1986; Michaud-Dubuy *et al.*, 2019). But it can also enhance the turbulent entrainment and mixing between the rising volcanic column and the atmospheric air. In the classical entrainment parameterization for a turbulent jet rising in an environment with a horizontal crossflow, the radial entrainment velocity u_e introduced in Chapter 3 becomes (Hewett *et al.*, 1971):

$$u_e = \alpha |u - w\cos(\theta)| + \beta |w\sin(\theta)|, \tag{1}$$

where α is the entrainment coefficient of Morton *et al.* (1956), u is the vertical velocity of the column, θ is the inclination of the plume centerline relative to the horizontal, and β is the wind entrainment coefficient. This latter coefficient is currently not well constrained, and experimental estimates in the literature vary between 0.1 and 1.0 (Bursik, 2001; Degruyter & Bonadonna, 2013; Woodhouse *et al.*, 2013; Suzuki & Koyaguchi, 2015). This range of values leads to important discrepancies in predictions of maximum column heights and plume trajectories (Costa *et al.*, 2016).

In this chapter, we present laboratory experiments designed to evaluate β and improve our theoretical model by accounting for the effect of turbulent entrainment due to wind. The experiments reproduce the column collapse transition of volcanic eruptions and allow to reduce the discrepancy between the model and field data in Figure 1b.

2   Laboratory experiments

2.1   Experimental set up

Natural volcanic jets have the ability to reverse their buoyancy: if the entrainment and heating of cold atmospheric air into the jet is efficient enough, the column may become buoyant; otherwise the jet collapses to the ground producing deadly PDC. We performed laboratory experiments to fully reproduce collapsing jets with reversing buoyancy rising in a windy environment. All experiments were conducted at ambient temperature in a large Plexiglas tank filled with fresh water, without stratification. Prior to an experiment, a constant head tank was filled with a mixture of pure (not diluted) colored ethanol and ethylene glycol (EEG, Kaminski *et al.* 2005) using a pump connected to a larger reservoir (Figure 2). EEG is less dense than fresh water but becomes denser when mixed with more than 60% of water, and thus can reproduce accurately the behavior of a natural volcanic column (Figure 3).
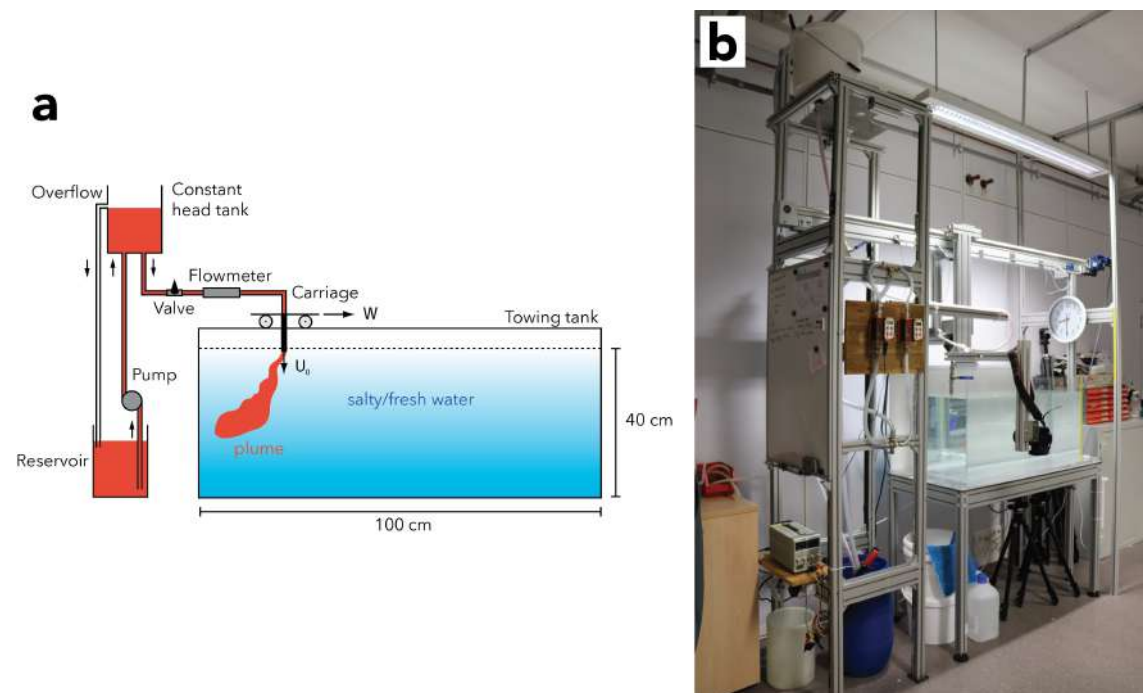
Figure 2: a Schematic diagram and **b** photograph of the experimental apparatus.

At the start of the experiment, we towed the jet source at a constant speed through the stationary fluid, and we opened the valve allowing the jet fluid to be released downward from the water surface. Every injection lasted between 10 and 60 sec and was recorded using a video camera. The volumetric flow rate (Q_0; and thus the volume flux u_0), the lateral speed of the injector (i.e., the speed of the crossflow w), and the inner radius of the source (r_0) were varied during the experiments in order to cover the full range of conditions appropriate to reproduce the main forces acting on the dynamics of a volcanic plume. Run

conditions are given in Appendix A.

Figure 3: Evolution of the measured density of the mixture between EEG and water (in $\mathrm{kg\,m^{-3}}$, purple dots) as a function of the water content in the mixture (in wt%). Dashed line corresponds to Eq. (10).

2.2 Scaling analysis

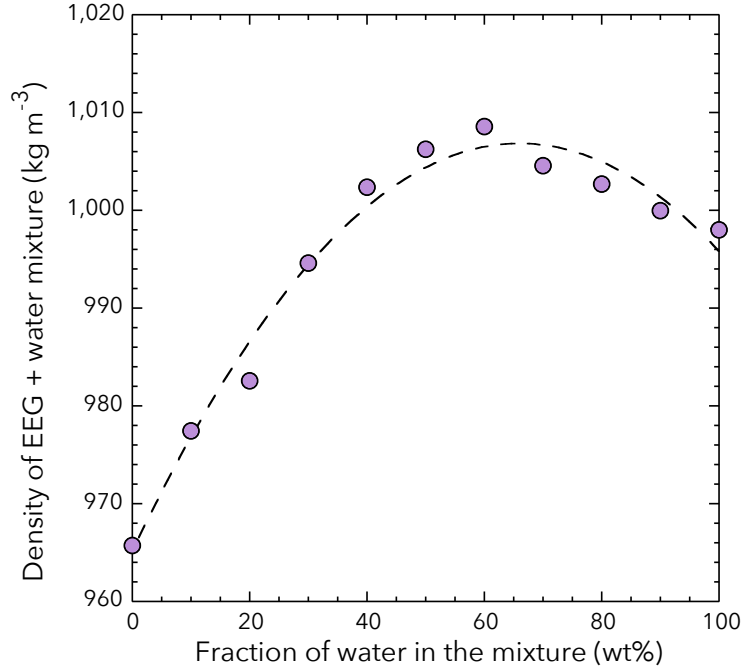Our laboratory experiments are at reduced scale compared to the natural phenomenon. In order to ensure that our experiments adequately scale to volcanic plumes, we present a scaling analysis related to the dynamics of the particle-gas mixture and the particles in the flow.

The Reynolds number (Re_0) characterizes the ratio between inertial to viscous forces,

$$\mathrm{Re}_0 = \frac{u_0 r_0}{\nu}, \tag{2}$$

where u_0 and r_0 are the jet velocity and radius at the source, respectively, and ν is the kinematic viscosity of the fluid. In explosive eruptions, $10^7 \leq \mathrm{Re}_0 \leq 10^9$, which is unattainable under laboratory conditions. We note, however, that our flows are at high-Re (Appendix A), fully turbulent and conducted under Re conditions comparable to many published studies (Burgisser *et al.*, 2005; Carazzo & Jellinek, 2012).

The Richardson number at the source (Ri_0) characterizes the balance between the buoyancy and inertial forces in the jet and can be written as,

$$\mathrm{Ri}_0 = \frac{g_0' r_0}{u_0^2}, \tag{3}$$

where $g_0' = g(\rho_a - \rho_0)/\rho_a$ is the jet reduced gravity at the source, with g the acceleration of gravity, and ρ_0 and ρ_a the densities of the jet and ambient fluid at the source, respectively.

The presence of a crossflow introduces a velocity scale (W^*), which defines the wind

velocity ratio (Hewett *et al.*, 1971; Yang & Hwang, 2001),

$$W^* = \frac{w}{u_0},\qquad\qquad(4)$$

where w is the velocity of the crossflow.

Figure 4 shows that our experimental range of wind velocity ratio (W^*) is consistent with values calculated for volcanic plumes (Carazzo *et al.*, 2014). The Richardson number at the base of volcanic jets is negative because the eruptive mixture is denser than the atmosphere at the vent. Our experimental range of Ri_0 is consistent with values calculated for the source of volcanic plumes (Figure 4). We note that all previous studies designed to investigate the behavior of a turbulent jet in a crossflow were performed at $Ri_0 > 0$ at the source, which prevents to reproduce the buoyancy inversion that controls the column collapse transition.
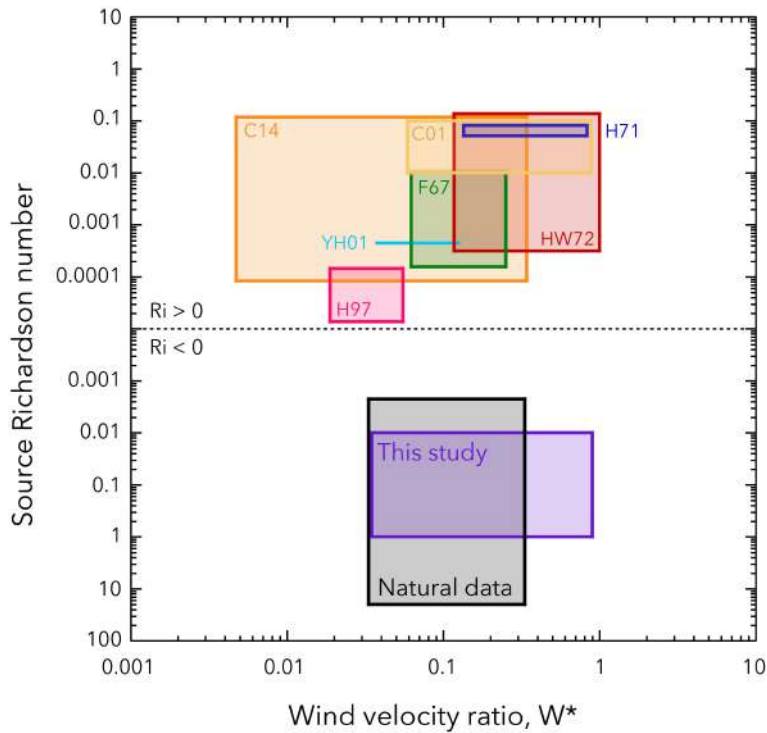
Figure 4: a Review of source Richardson number (Ri_0) and wind velocity ratio (W^*) for natural volcanic plumes and experimental works published in relation with positively buoyant jets (upper boxes) and negatively buoyant jets (lower boxes) in a crossflow. The values of Ri_0 for natural data correspond to those at the volcanic vent. C01: Contini & Robins (2001), C14: Carazzo *et al.* (2014), F67: Fan (1967), H71: Hewett *et al.* (1971), HW72: Hoult & Weil (1972), H97: Huq (1997), YH01: Yang & Hwang (2001).

3   A model for the laboratory experiments

3.1   Conservation equations

We now present a 1D model of a turbulent jet in a windy environment in order to compare our experimental results with theoretical ones. Following Morton *et al.* (1956) and Hoult *et al.* (1969), we use a plume-centered system, where s denotes the curvilinear abscissa along the plume centerline, and θ is the local inclination of the mixture. For "top-hat"

radial dependence of the plume properties, the conservation equations of volume flux, axial and radial momentum fluxes, and volume flux of EEG in the mixture are:

$$\frac{\mathrm{d}}{\mathrm{d}s}\left(ur^2\right) = 2ru_e, \tag{5}$$

$$\frac{\mathrm{d}}{\mathrm{d}s}\left(u^2r^2\right) = \frac{(\rho - \rho_a)}{\rho_a}gr^2\sin(\theta) + w\cos(\theta)\frac{\mathrm{d}}{\mathrm{d}s}\left(ur^2\right), \tag{6}$$

$$\left(u^2r^2\right)\frac{\mathrm{d}\theta}{\mathrm{d}s} = \frac{(\rho - \rho_a)}{\rho_a}gr^2\cos(\theta) - w\sin(\theta)\frac{\mathrm{d}}{\mathrm{d}s}\left(ur^2\right), \tag{7}$$

$$\frac{\mathrm{d}}{\mathrm{d}s}\left(xur^2\right) = 0, \tag{8}$$

where r is the mixture radius, u is the mixture velocity, g is the acceleration of gravity, ρ is the mixture density, ρ_a is the ambient density, x is the volume fraction of EEG in the mixture, w is the wind speed, and u_e is the entrainment velocity at the edge of the mixture, calculated using Eq. (1).

Here, we use a simplified version of the formula proposed by Kaminski *et al.* (2005) for α,

$$\alpha = 0.0675 + \left(1 - \frac{1}{A}\right)\text{Ri}, \tag{9}$$

where $\text{Ri} = g'r/u^2$ is the local Richardson number, with $g' = g(\rho - \rho_a)/\rho_a$ the local reduced gravity of the jet. The dimensionless parameter A depends on the structure of the flow (Carazzo *et al.*, 2006) and can be calculated using Eqs. (A1) to (A4) in Michaud-Dubuy *et al.* (2018) (Chapter 3, and Appendix A).

The density of the water-EEG mixture is given by (Woods & Caulfield, 1992; Kaminski *et al.*, 2005),

$$\Delta\rho = \left[1 - (1 - X)^2\right]\Delta\rho_m, \tag{10}$$

where $\Delta\rho = \rho - \rho_a$, $\Delta\rho_m = \rho_m - \rho_a$, and $X = x/x_m$, with ρ_m the maximum density the mixture may attain, which occurs when $x = x_m$. This simple parameterization models relatively well the density measurements in Figure 3.

This theoretical model fully describes the motion of a turbulent mixture of water and EEG rising in a windy uniform environment, and it can be used to calculate the conditions for the collapse of the mixture and the trajectory of the mixture. For this, we rewrite Eqs. (5) to (10) by using a new set of dimensionless variables:

$$\zeta = \frac{s}{r_0}, \tag{11}$$

$$W^* = \frac{w}{u_0}, \tag{12}$$

$$Q = \frac{ur^2}{u_0r_0^2}, \tag{13}$$

$$M = \frac{u^2r^2}{u_0^2r_0^2}, \tag{14}$$

$$\text{Ri}_0 = \frac{r_0g}{u_0^2}\frac{(\rho_a - \rho_0)}{\rho_a}, \tag{15}$$

where the subscript $_0$ denotes values at the source. Eq. (8) can then be written:

$$XQ = X_0, \tag{16}$$

which gives the volume flux of EEG in the mixture at any dimensionless distance from the source ζ.

Combining Eqs. (5) to (8), and injecting Eqs. (10) and (16) gives two dimensionless conservation equations:

$$\frac{\mathrm{d}Q}{\mathrm{d}\zeta} = 2\alpha M^{1/2} - 2W^* \frac{Q}{M^{1/2}} \left[\alpha \cos(\theta) - \beta \sin(\theta) \right], \tag{17}$$

$$\cos(\theta) M \frac{\mathrm{d}\theta}{\mathrm{d}\zeta} + \sin(\theta) \frac{\mathrm{d}M}{\mathrm{d}\zeta} = -\mathrm{Ri}_0 \frac{\Delta\rho_m}{\Delta\rho_0} \frac{Q^2}{M} \left[1 - \left(1 - \frac{X_0}{Q} \right)^2 \right]. \tag{18}$$

Eqs. (17) and (18) can be used to calculate the plume dynamics at any dimensionless height ζ.

3.2   No wind case

In the absence of wind, $W^* = 0$ and the inclinaison of the mixture remains at $\theta = \pi/2$. Eqs. (17) and (18) may then be reduced to:

$$\frac{\mathrm{d}Q}{\mathrm{d}\zeta} = 2\alpha M^{1/2}, \tag{19}$$

$$\frac{\mathrm{d}M}{\mathrm{d}\zeta} = -\mathrm{Ri}_0 \frac{\Delta\rho_m}{\Delta\rho_0} \frac{Q^2}{M} \left[1 - \left(1 - \frac{X_0}{Q} \right)^2 \right]. \tag{20}$$

By combining these two equations, we obtain:

$$\left(M(\zeta)^{5/2} - 1 \right) = -\frac{5\mathrm{Ri}_0}{4\alpha} \frac{\Delta\rho_m}{\Delta\rho_0} \left[X_0 \left(Q(\zeta)^2 - 1 \right) - X_0^2 \left(Q(\zeta) - 1 \right) \right], \tag{21}$$

which describes the motion of the water-EEG mixture at any distance from the vent. If the mixture is to collapse before becoming buoyant, then $M = 0$ and $\mathrm{d}M/\mathrm{d}\zeta = 0$ at the collapsing height (Woods & Caulfield, 1992). Injecting these conditions in Eqs. (20) and (21) gives a criterion for the collapse of the mixture:

$$\frac{5\mathrm{Ri}_0}{4\alpha} \frac{\Delta\rho_m}{\Delta\rho_0} \left[X_0 \left(\frac{X_0^2}{4} - 1 \right) - X_0^2 \left(\frac{X_0}{2} - 1 \right) \right] = 1, \tag{22}$$

which may be rewritten as

$$\mathrm{Ri}_0 = -\frac{4\alpha}{5} \frac{\Delta\rho_0}{\Delta\rho_m} \left[\frac{1}{X_0 \left(\frac{X_0}{4} - 1 \right)^2} \right]. \tag{23}$$

In the no wind case, the criterion for the collapse of the mixture corresponds to a critical Richardson number, a result consistent with previous studies (Woods & Caulfield,

1992; Kaminski *et al.*, 2005). The value of this critical Richardson number is given by the entrainment coefficient and the properties of the water-EEG mixture. In our experiments, $\Delta\rho_0 = 31\,\text{kg}\,\text{m}^{-3}$, $\Delta\rho_m = 9\,\text{kg}\,\text{m}^{-3}$, $X_0 = 2.86$ (Figure 3), and $\alpha \approx 0.05$ (Kaminski *et al.*, 2005). The theoretical critical Richardson number in our experiments is therefore

$$\text{Ri}_0 \approx -0.26, \tag{24}$$

that we use in Figure 5 to draw the plume/fountain transition in the absence of wind.
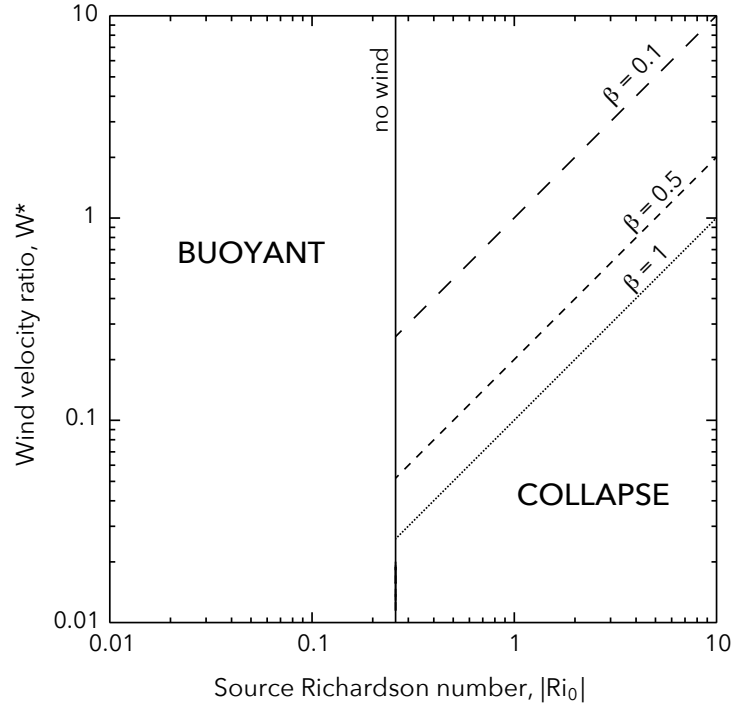

Figure 5: Theoretical criterion for the collapse of the mixture. Solid, long dashed, dashed, and dotted lines correspond to predictions made for the no wind case (Eq. (24)), and the highly negatively buoyant jets in a windy environment with $\beta = 0.1$, 0.5, and 1 (Eq. (30)), respectively.

3.3   Negatively buoyant jets in a windy environment

We now consider the case of highly negatively buoyant jets (i.e., with a high Ri_0), for which the value of the radial entrainment coefficient is predicted to fall to zero (Kaminski *et al.*, 2005), in a windy environment but with a low inclinaison angle such as $\theta \approx \pi/2$. Eqs. (17) and (18) may then be reduced to:

$$\frac{\mathrm{d}Q}{\mathrm{d}\zeta} = 2\beta W^* \frac{Q}{M^{1/2}}, \tag{25}$$

$$\frac{\mathrm{d}M}{\mathrm{d}\zeta} = -\text{Ri}_0 \frac{\Delta\rho_m}{\Delta\rho_0} \frac{Q^2}{M} \left[1 - \left(1 - \frac{X_0}{Q} \right)^2 \right]. \tag{26}$$

By combining these two equations, we obtain:

$$\left(M(\zeta)^{3/2} - 1\right) = -\frac{3\mathrm{Ri}_0}{4\beta W^*}\frac{\Delta\rho_m}{\Delta\rho_0}\left[X_0\left(Q(\zeta)-1\right) - X_0^2\ln\{Q(\zeta)\}\right],\qquad(27)$$

which describes the motion of the water-EEG mixture at any distance from the vent. If the mixture is to collapse before becoming buoyant, then $M = 0$ and $\mathrm{d}M/\mathrm{d}\zeta = 0$ at the maximum collapsing height. Injecting these conditions in Eqs. (26) and (27) gives a criterion for the collapse of the mixture:

$$-\frac{4}{3}\beta W^* = -\mathrm{Ri}_0\frac{\Delta\rho_m}{\Delta\rho_0}\left[X_0^2\left(1 - \ln\left\{\frac{X_0}{2}\right\}\right) - 2X_0\right],\qquad(28)$$

which may be rewritten as

$$\mathrm{Ri}_0 = \frac{4}{3}\beta W^*\frac{\Delta\rho_0}{\Delta\rho_m}\left[\frac{1}{X_0^2\left(1 - \ln\left\{\frac{X_0}{2}\right\}\right) - 2X_0}\right].\qquad(29)$$

In the case of highly negatively buoyant jets in a windy environment, the criterion for the collapse of the mixture is given by both a critical Richardson number and a critical wind to plume speed ratio. The exact values of these numbers are given by the wind entrainment coefficient and the properties of the water-EEG mixture. In our experiments, $\Delta\rho_0 = 31\,\mathrm{kg\,m^{-3}}$, $\Delta\rho_m = 9\,\mathrm{kg\,m^{-3}}$, and $X_0 = 2.86$ (Figure 3, Kaminski *et al.* 2005). The theoretical critical Richardson number in our experiments is therefore:

$$\mathrm{Ri}_0 \approx -10\beta W^*,\qquad(30)$$

that we report in Figure 5 for $\beta = 0.1$, 0.5, and 1.

4   Results

4.1   Qualitative observations

Our experiments investigate the different phenomena that occur when we vary both the crossflow rate and the Richardson number (which involves the exit velocity, vent radius and density difference with ambient). Although the EEG mixture is lighter than the environment, its density increases as a result of turbulent entrainment and dilution to values higher than the ambient density. Resultant buoyancy forces augment the momentum flux imparted at the source to drive the plume to the bottom of the tank. This behaviour is shown in Figure 6a and is analog for the formation of a strong plume (Wilson, 1976).

For high density difference at the source and low flow rates, there is less entrainment and mixing of the ambient fluid. The injected mixture remains too light to undergo a buoyancy inversion and returns to the top of the tank as a turbulent fountain feeding radial gravity current. This behaviour is shown in Figure 6b and is an analog to a volcanic collapsing fountain with associated PDC (Sparks & Wilson, 1976).

For high wind velocity, the jet mixes more efficiently than in the strong plume case by ingesting significant quantities of ambient fresh water through the action of wind. The centerline of the jet bends over in the wind field, and reaches the bottom of the tank. This behaviour is shown in Figure 6c and is analog for the formation of a weak plume

([Bonadonna & Phillips](), 2003). We observed that the formation of a turbulent fountain could not be reached under high wind speed conditions.
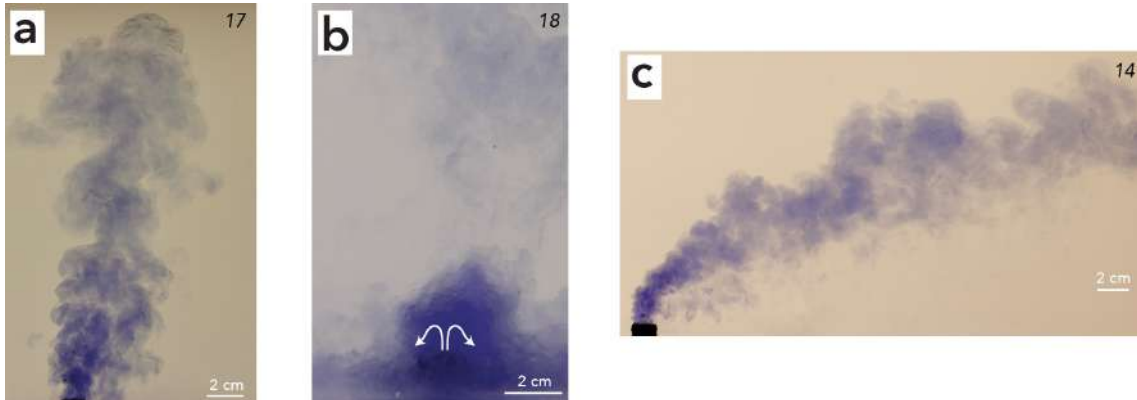

Figure 6: a, b, c Photographs of experiments illustrating the effect of wind on the plume regime with **a** a strong plume, **b** a collapsing column, and **c** a weak plume. All scale bars are 2 cm long. Numbers correspond to the experiment numbers reported in [Appendix A]().

4.2 The plume/fountain transition

Combining the methodology of [Kaminski *et al.* (2005)]() and [Carazzo *et al.* (2014)](), we performed 27 laboratory experiments (numbered from 1 to 27 in [Appendix A]()) and we observed during the experiment whether the mixture formed a buoyant jet or a collapsing fountain.
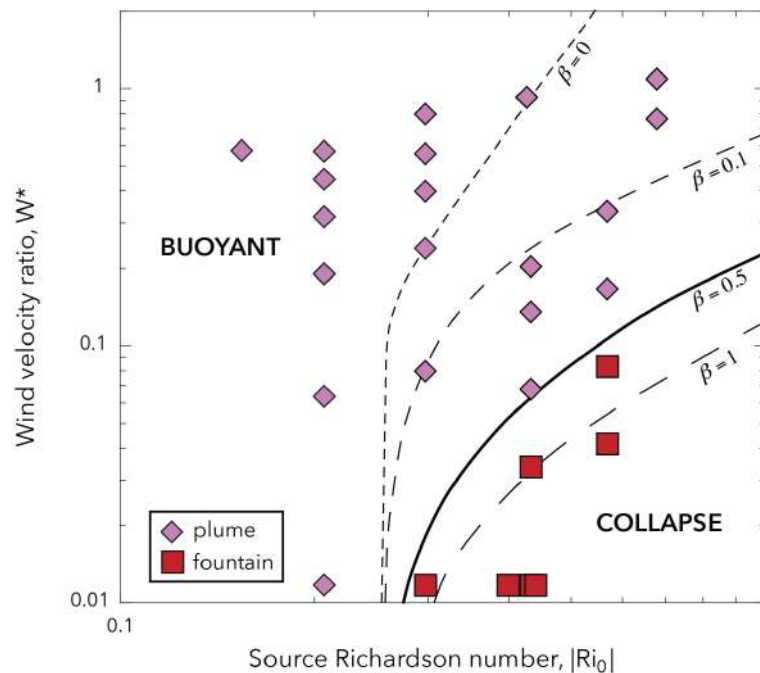
Figure 7: Theoretical threshold wind velocity ratio (W^*) at the transition between buoyant and collapse regimes as a function of the source Richardson number Ri_0, for $\beta = 0$ (small dashed line), $\beta = 0.1$ (medium dashed line), $\beta = 0.5$ (solid line), $\beta = 1$ (large dashed line), compared with experiments of jets with reversing buoyancy (purple and red symbols).

The results are presented in [Figure 7]() (purple and red symbols) using a theoretical threshold $W^*(= w/u_0)$ as a function of the source Richardson number Ri_0 (black lines) calculated

by a 1D model of turbulent jet that takes into account Eqs. (5) to (10) in Section 3.1. W^* and Ri_0 are indeed two key parameters for the jet dynamics (see Section 3.1 and Figure 5). This diagram has also been used in several previous studies on the effect of wind on volcanic column dynamics (Degruyter & Bonadonna, 2013; Aubry & Jellinek, 2018). Several theoretical thresholds are shown, each accounting for a different value of β (Devenish *et al.*, 2010; Mastin, 2014). Not surprisingly, increasing the value of β (and thus the entrainment due to wind) increase the range of stability conditions to form a buoyant jet.

We can note in Figure 7 that the theoretical threshold calculated for $\beta = 0.5$ shows the best agreement with the experimental observations.

4.3   Trajectory of negatively buoyant jets

To refine the quantification of the coefficient β, we performed a second set of laboratory experiments to reproduce jets with negative buoyancy (i.e., collapsing) by filling the tank with an aqueous NaCl solution, and by using colored fresh water as the injected fluid. We further used these experiments to measure the flow and constrain the value of β in our model (Section 3.1). We performed 6 experiments (numbered I to VI in Appendix A) in which we varied the volume flux of the injected fluid Q_0, the density of the ambient fluid ρ_a (i.e., salty water), and the crossflow speed w from one experiment to another. For each experiment, a series of recorded images was extracted and averaged to give a final image on which we drew the central trajectory.
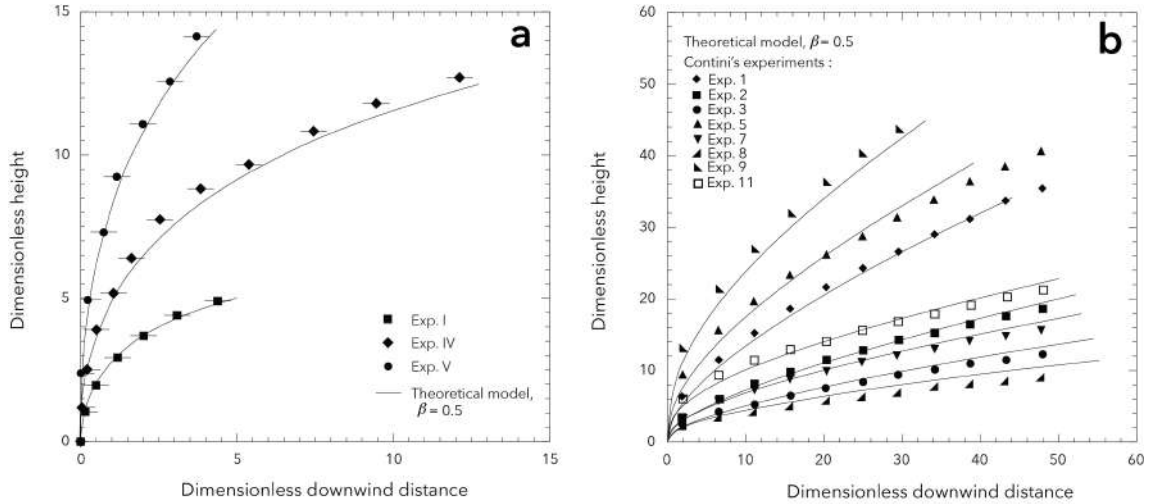

Figure 8: a Single plumes trajectories derived from ensemble averaged video images of three experiments (black symbols) of jets with negatively buoyancy, compared with theoretical predictions. Every theoretical predictions were made using a 1D theoretical model accounting for a wind entrainment parameter $\beta = 0.5$ (black line). **b** Comparison between predictions from a 1D theoretical model (Section 3) for a wind entrainment parameter $\beta=0.5$ (black lines), and the trajectories of positively buoyant plumes measured by Contini & Robins (2001).

Trajectories of single jets (black symbols) are plotted in Figure 8a for three experiments (I, IV and V), where the dimensionless height corresponds to $z/2r_0$ and the dimensionless downwind distance stands for $x/2r_0$, where $r_0 = 3$ mm. We show that the experiments are in good agreement with the theoretical predictions made for a parameter $\beta = 0.5$ (black lines). This is an interesting result as it is the same constant value found by Aubry *et al.* (2017) for positively buoyant jets. To further strengthen the hypothesis that a single value of β could be used to describe the wind entrainment both for negatively and positively buoyant

jets, we compared the single plume trajectories obtained by Contini & Robins (2001) to our theoretical predictions, and also found a good agreement for $\beta = 0.5$ (Figure 8b).

This constant value is thus valid for negatively and positively buoyant jets and for jets with reversing buoyancy, provided that α varies as in Kaminski *et al.* (2005) (see Eq. (9) in Section 3.1).

5 Volcanological implications

5.1 Collapsing regimes of historical eruptions

We now use this constant value of wind entrainment parameter β to parameterize our 1D model (PPM, see Girault *et al.* 2016 for details) and confront it to the historical eruptions of Tambora, Pinatubo and Nevado del Ruiz. We show in Figure 9 how the strong winds blowing during the eruptions $(20-30 \text{ m s}^{-1})$ prevented the total collapse of the eruptive columns and maintained them in the transitional (i.e., partial collapse) regime.
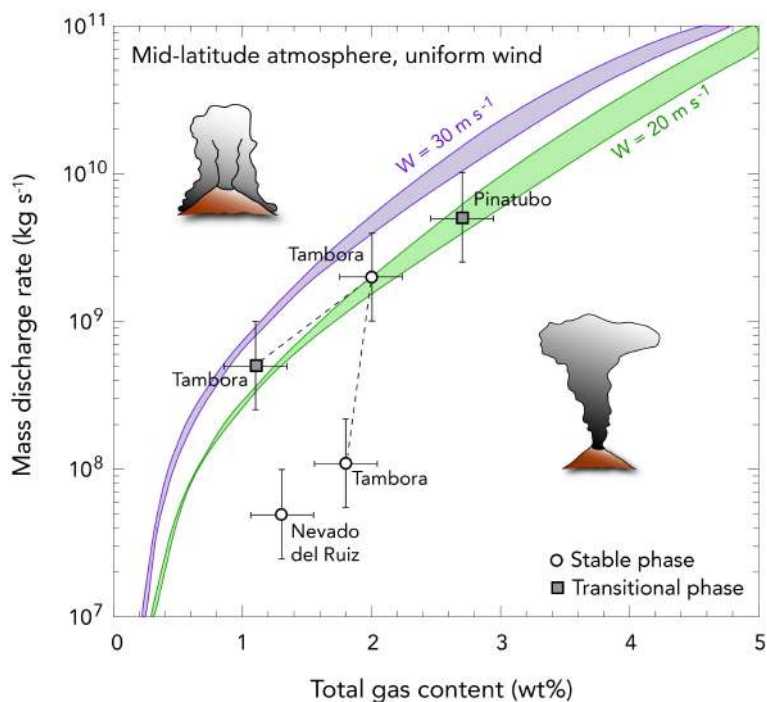

Figure 9: Eruptive conditions of several eruptions in terms of source mass discharge rate (in kg s^{-1}) and gas content (in wt%). The curves give the threshold mass discharge rate for column collapse when accounting for a uniform wind speed with altitude of 20 m s^{-1} (green envelope) and 30 m s^{-1} (purple envelop). The amount of gas at the vent depends on the fragmentation of magma occurring in the conduit before the eruption, and therefore on the pyroclast size that will be ejected during the eruption represented in PPM by the power-law exponent D (Michaud-Dubuy *et al.*, 2018). The envelopes account for the effect of this exponent D, taken here as $D = 3.2$ (upper limit of the envelope) and as $D = 2.8$ (lower limit of the envelope). We consider a mid-latitude atmosphere, a magma temperature taken as the average of andesitic magma ($T_0 = 1200$ K), and an open porosity of 65% (Michaud-Dubuy *et al.*, 2018).

When comparing the theoretical predictions in Figure 9 and field data for all historical eruptions (white dots and grey squares), we observe a good consistency between them. The transitional phase of the Pinatubo eruption, which occurred under 20 m s^{-1} winds, is well explained by the corresponding green transition envelope. The two stables phases of the Tambora eruption are in the stable domain, while the transitional stage of the eruption

(characterized by 25 m s^{-1} winds) is well located in the collapse domain. Finally, the Nevado del Ruiz eruption, characterized by the formation of a stable plume previously on the theoretical threshold (Figure 1b), is now far in the stable domain as > 30 m s^{-1} winds blew during the event. We can thus suggest that the strong winds blowing during these famous historical eruptions prevented or delayed total volcanic column collapses, possibly saving many people from dying into the massive pyroclastic density currents that could have been produced. The F4 phase of the Tambora eruption, for example, is characterized by a strong MDR that could have produced pyroclastic density currents with a run-out distance of approximately 30 km (Bursik & Woods, 1996); while a total column collapse during the Nevado del Ruiz eruption would have added a huge mass of deposits on the volcano flanks and may have increased the number of lahars.

5.2   New regime diagram for column collapse in case of wind

In order to go further, we calculated the wind speed w required to prevent a volcanic column to collapse and therefore propose a new transition curve based on the relationship between the mass discharge rate (MDR) and $w/\log(\text{MDR})$ (Figure 10), the latter of which can be easily determined from wind and maximum column height measurements for historical eruptions (Mastin *et al.*, 2009), or from the downwind to crosswind ratio of the distribution of lithic fragments (isopleths) for past eruptions (Carey & Sigurdsson, 1986).
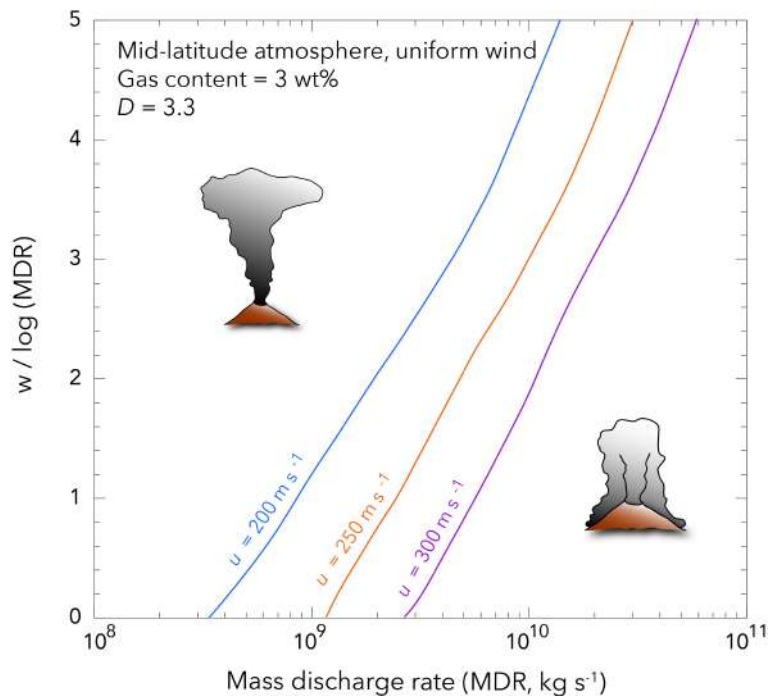
Figure 10: Ratio of the threshold wind speed (in m s^{-1}) and mass discharge rate at the transition between buoyant and collapse regimes, as a function of the mass discharge rate (in kg s^{-1}). Each color represents a different value of the plume velocity at the vent. Calculations are made with an initial exsolved gas content of 3 wt%, and a power-law exponent $D = 3.3$. We consider a mid-latitude atmosphere, a magma temperature taken as the average of andesitic magma ($T_0 = 1200$ K), and an open porosity of 65% (Michaud-Dubuy *et al.*, 2018).

The threshold ratio $w/\log(\text{MDR})$ is calculated as a function of MDR for different plume velocities at the vent and all calculations were made using a gas content of 3 wt% and a power-law exponent $D = 3.3$. In no wind conditions, a volcanic plume will be buoyant

regardless of its initial velocity as long as the MDR is smaller than 3×10^8 $\mathrm{kg\,s^{-1}}$, thus defining a minimal mass discharge rate below which there is no column collapse. If wind blows during the eruption, the threshold ratio $w/\log(\mathrm{MDR})$ steadily increases with the MDR. Our new transition diagram involves physical parameters (w and MDR) that are much easier to estimate from field data than the dimensionless numbers (e.g., Richardson number or overpressure ratio) involved in previous regime diagrams (Degruyter & Bonadonna, 2013; Valentine & Wohletz, 1989). This simplified diagram may thus help to compare easily the results from physical models and field studies on the collapse of explosive plumes.

Our results show that isopleth shapes determined in the field could be a dominant criterion for investigating the column behavior of past eruptions. Fine and elongated isopleths would mean that $w/\log(\mathrm{MDR})$ was high and that the Plinian column could have been rather stable; while wide and shortened isopleths would correspond to low $w/\log(\mathrm{MDR})$ and possibly to a more unstable column. This conclusion has strong implications for the reconstruction of past eruptive histories of active volcanoes, and thus on the prevision of future events.

6   Conclusion

We presented new laboratory experiments simulating turbulent jets with a reversing buoyancy rising in a windy environment. The results on plume/fountain transition and jet trajectory show that the entrainment coefficient due to wind is $\beta = 0.5$, provided that α varies as in Kaminski *et al.* (2005). Using this constant value in our 1D model of volcanic plume (PPM) allows to reconcile field data and theoretical predictions for the 1815 Tambora, 1985 Nevado del Ruiz, and 1991 Pinatubo eruptions. Strong winds can indeed favor volcanic plume stability, and prevent the formation of deadly PDC on the volcano flanks. This study opens a new perspective on the strong importance of wind at every stage of an eruption, from the inner column dynamics to the dispersion of volcanic products in the atmosphere, and thus on the volcanic hazard assessment.

We thus demonstrated, in the second part of this PhD thesis manuscript, the importance of both the total grain-size distribution and the wind on volcanic column collapse. In the last part, we will focus on the effect of wind on tephra dispersion and perform 2D simulations for two of the newly discovered/revisited eruptions of Mount Pelée volcano in Martinique. The results will then be integrated to produce new hazard maps.

Appendix A

Table A1: Experimental conditions.

Run	Q_0 $(\mathrm{m^3\,s^{-1}})$	r_0 (m)	u_0 $(\mathrm{m\,s^{-1}})$	w $(\mathrm{m\,s^{-1}})$	$\Delta\rho/\rho_a$	W^*	Ri_0	Re_0	Observation
1	1.2×10^{-5}	0.0075	0.066	0	0.026	0	-0.439	495	Fountain
2	1.2×10^{-5}	0.0075	0.069	0	0.026	0	-0.399	520	Fountain
3	1.7×10^{-5}	0.0075	0.096	0	0.026	0	-0.207	722	Plume
4	1.7×10^{-5}	0.0075	0.096	0.006	0.026	0.064	-0.207	722	Plume
5	1.7×10^{-5}	0.0075	0.096	0.018	0.026	0.191	-0.207	722	Plume
6	1.7×10^{-5}	0.0075	0.096	0.031	0.026	0.318	-0.207	722	Plume
7	1.7×10^{-5}	0.0075	0.096	0.043	0.026	0.445	-0.207	722	Plume
8	1.7×10^{-5}	0.0075	0.096	0.055	0.026	0.572	-0.207	722	Plume
9	1.0×10^{-5}	0.0075	0.056	0.061	0.029	1.089	-0.678	421	Plume
10	1.0×10^{-5}	0.0075	0.056	0.043	0.029	0.762	-0.678	421	Plume
11	1.2×10^{-5}	0.0075	0.066	0.061	0.025	0.925	-0.426	495	Plume
12	1.9×10^{-5}	0.0075	0.106	0.061	0.024	0.575	-0.154	797	Plume
13	1.3×10^{-5}	0.0075	0.076	0.061	0.024	0.797	-0.297	575	Plume
14	1.3×10^{-5}	0.0075	0.076	0.043	0.024	0.558	-0.297	575	Plume
15	1.3×10^{-5}	0.0075	0.076	0.031	0.024	0.399	-0.297	575	Plume
16	1.3×10^{-5}	0.0075	0.076	0.018	0.024	0.239	-0.297	575	Plume
17	1.3×10^{-5}	0.0075	0.076	0.006	0.024	0.080	-0.297	575	Plume
18	1.3×10^{-5}	0.0075	0.076	0	0.024	0	-0.297	575	Fountain
19	5.2×10^{-5}	0.0135	0.090	0.018	0.027	0.203	-0.432	1218	Plume
20	5.2×10^{-5}	0.0135	0.090	0.012	0.027	0.135	-0.432	1218	Plume
21	5.2×10^{-5}	0.0135	0.090	0.006	0.027	0.068	-0.432	1218	Plume
22	5.2×10^{-5}	0.0135	0.090	0.003	0.027	0.034	-0.432	1218	Fountain
23	5.2×10^{-5}	0.0135	0.090	0	0.027	0	-0.432	1218	Fountain
24	4.2×10^{-5}	0.0135	0.073	0.024	0.023	0.333	-0.568	990	Plume
25	4.2×10^{-5}	0.0135	0.073	0.012	0.023	0.167	-0.568	990	Plume
26	4.2×10^{-5}	0.0135	0.073	0.006	0.023	0.083	-0.568	990	Fountain
27	4.2×10^{-5}	0.0135	0.073	0.003	0.023	0.042	-0.568	990	Fountain
I	0.8×10^{-5}	0.003	0.283	0.061	0.020	0.216	-0.007	849	Fountain
II	0.8×10^{-5}	0.003	0.283	0.031	0.020	0.108	-0.007	849	Fountain
III	0.8×10^{-5}	0.003	0.283	0	0.020	0	-0.007	849	Fountain
IV	1.5×10^{-5}	0.003	0.542	0.061	0.010	0.113	-0.001	1627	Fountain
V	1.5×10^{-5}	0.003	0.542	0.031	0.010	0.056	-0.001	1627	Fountain
VI	1.5×10^{-5}	0.003	0.542	0	0.010	0	-0.001	1627	Fountain

$Q_0 = \pi u_0 r_0^2$: volume flux; r_0: vent radius; u_0: exit velocity; w: ambient velocity; $\Delta\rho = \rho_a - \rho_0$: density gradient; ρ_0: jet density; ρ_a: ambient density; $W^* = w/u_0$: wind velocity ratio; $\mathrm{Ri}_0 = g_0' r_0/u_0^2$: source Richardson number; $g'_0 = g \times \Delta\rho/\rho_a$: reduced gravity; g: acceleration of gravity; $\mathrm{Re}_0 = u_0 r_0/\nu$: source Reynolds number; ν: kinematic viscosity. For experiments 1 to 27, we injected a mixture of EEG into a tank filled with fresh water; for experiments I to VI, we injected fresh water into a tank filled with salty water.

References

AUBRY, T.J., CARAZZO, G. & JELLINEK, A.M. 2017 Turbulent Entrainment Into Volcanic Plumes: New Constraints From Laboratory Experiments on Buoyant Jets Rising in a Stratified Crossflow. *Geophys. Res. Lett.* **44**, 10,198–10,207.

Aubry, T.J. & Jellinek, A.M. 2018 New insights on entrainment and condensation in volcanic plumes: Constraints from independent observations of explosive eruptions and implications for assessing their impacts. *Earth Plan. Sci. Lett.* **490**, 132–142.

Bonadonna, C. & Phillips, J.C. 2003 Sedimentation from strong volcanic plumes. *J. Geophys. Res. Solid Earth* **108**, 1–28.

Borisova, A.Y., Pichavant, M., Beny, J.-M., Rouer, O. & Pronost, J. 2005 Constraints on dacite magma degassing and regime of the June 15, 1991, climactic eruption of Mount Pinatubo (Philippines): New data on melt and crystal inclusions in quartz. *J. Volcanol. Geotherm. Res.* **145**, 35–67.

Burgisser, A., Bergantz, G. W. & Breidenthal, R. E. 2005 Addressing complexity in laboratory experiments: The scaling of dilute multiphase flows in magmatic systems. *J. Volcanol. Geotherm. Res.* **141**, 245–265.

Bursik, M. 2001 Effect of wind on the rise height of volcanic plumes. *Geophys. Res. Lett.* **28**, 3621–3624.

Bursik, M.I. & Woods, A.W. 1996 The dynamics and thermodynamics of large ash flows. *Bull. Volcanol.* **58**, 175–193.

Carazzo, G., Girault, F., Aubry, T., Bouquerel, H. & Kaminski, E. 2014 Laboratory experiments of forced plumes in a density-stratified crossflow and implications for volcanic plumes. *Geophys. Res. Lett.* **41**, 8759–8766.

Carazzo, G. & Jellinek, A. M. 2012 A new view of the dynamics, stability and longevity of volcanic clouds. *Earth Planet. Sci. Lett.* **325-326**, 39–51.

Carazzo, G., Kaminski, E. & Tait, S. 2006 The route to self-similarity in turbulent jets and plumes. *J. Fluid Mech.* **547**, 137–148.

Carazzo, G., Kaminski, E. & Tait, S. 2015 The timing and intensity of column collapse during explosive volcanic eruptions. *Earth Planet. Sci. Lett.* **411**, 208–217.

Carey, Steven & Sigurdsson, Haraldur 1986 The 1982 eruptions of El Chichon volcano, Mexico (2): Observations and numerical modelling of tephra-fall distribution. *Bull. Volcanol.* **48**, 127–141.

Contini, D. & Robins, A. 2001 Water tank measurements of buoyant plume rise and structure in neutral crossflows. *Atmospheric Environment* **35**, 6105–6115.

Costa, A., Folch, A. & Macedonio, G. 2013 Density-driven transport in the umbrella region of volcanic clouds: implications for tephra dispersion models. *Geophys. Res. Lett.* **40**, 4823–4827.

Costa, A., Suzuki, Y. J., Cerminara, M., Devenish, B. J., Esposti Ongaro, T., Herzog, M., Van Eaton, A. R., Denby, L. C., Bursik, M., de' Michieli Vitturi, M., Engwell, S., Neri, A., Barsotti, S., Folch, A., Macedonio, G., Girault, F., Carazzo, G., Tait, S., Kaminski, E., Mastin, L. G., Woodhouse, M. J., Phillips, J. C., Hogg, A. J., Degruyter, W. & Bonadonna, C. 2016 Results of the eruptive column model inter-comparison study. *J. Volcanol. Geotherm. Res.* **326**, 2–25.

D'Arrigo, R., Wilson, R. & Tudhope, A. 2009 The impact of volcanic forcing on tropical temperatures during the past four centuries. *Nat. Geosci.* **2**.

Degruyter, W. & Bonadonna, C. 2013 Impact of wind on the condition for column collapse of volcanic plumes. *Earth Planet. Sci. Lett.* **377-378**, 218–226.

Devenish, B.J., Rooney, G.G., Webster, H.N. & Thomson, D.J. 2010 The entrainment rate for buoyant plumes in a crossflow. *Boundary-Layer Meteorol.* **134**, 411–439.

Esposti Ongaro, T., Neri, A., Menconi, G., de'Michieli Vitturi, M., Marianelli, P., Cavazzoni, C., Erbacci, G. & Baxter, P. J. 2008 Transient 3D numerical simulations of column collapse and pyroclastic density current scenarios at Vesuvius. *J. Volcanol. Geotherm. Res.* **178** (3), 378–396.

Fan, L.-N. 1967 Turbulent buoyant jets into stratified or flowing ambient fluids. *Tech. Rep.* KH-R-15. W.M. Keck Laboratory of Hydrology and Water Resources, California Institute of Technology, Pasadena, CA, USA.

Fero, J., Carey, S.N. & Merrill, J.T. 2009 Simulating the dispersal of tephra from the 1991 Pinatubo eruption: Implications for the formation of widespread ash layers. *J. Volcanol. Geotherm. Res.* **186**, 120–131.

Girault, F., Carazzo, G., Tait, S., Ferrucci, F. & Kaminski, E. 2014 The effect of total grain-size distribution on the dynamics of turbulent volcanic plumes. *Earth Planet. Sci. Lett.* **394**, 124–134.

Hewett, T.A., Fay, J.A. & Hoult, D.P. 1971 Laboratory experiments of smokestack plumes in a stable atmosphere. *Atmos. Environ.* **5**, 459–461.

Holasek, R.E., Self, S. & Woods, A.W. 1996 Satellite observations and interpretation of the 1991 Mount Pinatubo eruption plumes. *J. Geophys. Res.* **101**, 27,635–27,655.

Hoult, D. P., Fay, J. A. & Forney, L. J. 1969 A theory of plume rise compared with field observations. *J. Air Pollut. Contr. Assoc.* **19**, 585–590.

Hoult, D. P. & Weil, J. C. 1972 Turbulent plume in a laminar cross flow. *Atmos. Environ.* **6**, 513–531.

Huq, P. 1997 Observations of jets in density stratified crossflows. *Atmos. Environ.* **31**, 2011–2022.

Kaminski, E. & Jaupart, C. 2001 Marginal stability of atmospheric eruption columns and pyroclastic flow generation. *J. Geophys. Res.* **106** (B10), 21785–21798.

Kaminski, E., Tait, S. & Carazzo, G. 2005 Turbulent entrainment in jets with arbitrary buoyancy. *J. Fluid Mech.* **526**, 361–376.

Kandlbauer, J. & Sparks, R.S.J. 2014 New estimates of the 1815 Tambora eruption volume. *J. Volcanol. Geotherm. Res.* **286**, 93–100.

Koyaguchi, T. & Ohno, M. 2001 Reconstruction of eruption column dynamics on the basis of grain size of tephra fall deposits. 2. Application to the Pinatubo 1991 eruption. *J. Geophys. Res.* **106**, 6513–6533.

Mastin, L. G. 2014 Testing the accuracy of a 1-D volcanic plume model in estimating mass eruption rate. *J. Geophys. Res.* **119**, 2474–2495.

Mastin, L. G., Guffanti, M., Servranckx, R., Webley, P., Barsotti, S., Dean, K., Durant, A., Ewert, J.W., Neri, A., Rose, W.I., Schneider, D., Siebert, L., Stunder, B., Swanson, G., Tupper, A., Volentik, A. & Waythomas, C. F. 2009 A multidisciplinary effort to assign realistic source parameters to models of volcanic ash-cloud transport and dispersion during eruptions. *J. Volcanol. Geotherm. Res.* **186**, 10–21.

Melson, W.G., Allan, J.F., Jerez, D.R., Nelen, J., Calvache, M.L., Williams, S.N., Fournelle, J. & Perfit, M. 1990 Water contents, temperatures and diversity of the magmas of the catastrophic eruption of Nevado del Ruiz, Colombia, November 13, 1985. *J. Volcanol. Geotherm. Res.* **41**, 91–126.

Michaud-Dubuy, A., Carazzo, G., Kaminski, E. & Girault, F. 2018 A revisit of the role of gas entrapment on the stability conditions of explosive volcanic columns. *J. Volcanol. Geotherm. Res.* **357**, 349–361.

Michaud-Dubuy, A., Carazzo, G., Tait, S., Le Hir, G., Fluteau, F. & Kaminski, E. 2019 Impact of wind direction variability on hazard assessment in Martinique (Lesser Antilles): The example of the 13.5 ka cal BP Bellefontaine Plinian eruption of Mount Pelée volcano. *J. Volcanol. Geotherm. Res.* **381**, 193–208.

Morton, B.R., Taylor, G.I. & Turner, J.S. 1956 Turbulent gravitational convection from maintained and instantaneous sources. *Philos. Trans. R. Soc. A* **234**, 1–23.

Naranjo, J.L., Sigurdsson, H., Carey, S.N. & Fritz, W. 1986 Eruption of the Nevado del Ruiz volcano, Colombia, on 13 November 1985: Tephra fall and lahars. *Science* **233**, 961–963.

Neri, A. & Dobran, F. 1994 Influence of eruption parameters on the thermofluid dynamics of collapsing volcanic columns. *J. Geophys. Res.* **99** (B6), 11833–11857.

Newhall, Christopher G. & Self, Stephen 1982 The volcanic explosivity index (VEI) an estimate of explosive magnitude for historical volcanism. *J. Geophys. Res.* **87** (C2), 1231–1238.

OPPENHEIMER, C. 2003 Climatic, environmental and human consequences of the largest known historic eruption: Tambora volcano (Indonesia) 1815. *Prog. Phys. Geogr.* **27** (2), 230–259.

SELF, S., ZHAO, J.-X., HOLASEK, R.E., TORRES, R.C. & KING, A.J. 1996 The atmospheric impact of the 1991 Mount Pinatubo eruption. In *Fire and Mud: Eruptions and Lahars of Mount Pinatubo, Philippines* (ed. C.G. Newhall & R.S. Punongbayan), pp. 1089–1115. Philippine Institute of Volcanology and Seismology, Queen City and University of Washington Press, Seattle.

SIGURDSSON, H. & CAREY, S. 1989 Plinian and co-ignimbrite tephra fall from the 1815 eruption of Tambora volcano. *Bull. Volcanol.* **51**, 243–270.

SPARKS, R. S. J. 1986 The dimensions and dynamics of volcanic eruption columns. *Bull. Volcanol.* **48**, 3–15.

SPARKS, R. S. J. & WILSON, L. 1976 A model for the formation of ignimbrite by gravitational column collapse. *J. Geol. Soc. Lond.* **132**, 441–451.

SUZUKI, Y. & KOYAGUCHI, T. 2015 Effects of wind on entrainment in volcanic plumes. *J. Geophys. Res. B.* **120**, 6122–6140.

SUZUKI, Y. J., KOYAGUCHI, T., OGAWA, M. & HACHISU, I. 2005 A numerical study of turbulent mixing in eruption clouds using a three-dimensional fluid dynamics model. *J. Geophys. Res.* **110**, B08201.

TANGUY, J.C., RIBIÈRE, CH., SCARTH, A. & TJETJEP, W.S. 1998 Victims from volcanic eruptions: A revised database. *Bull. Volcanol.* **60**, 137–144.

VALENTINE, G. A. & WOHLETZ, K. H. 1989 Numerical Models of Plinian Eruption Columns and Pyroclastic Flows. *J. Geophys. Res.* **94** (B2), 1867–1887.

WALLACE, P.J. 2005 Volatiles in subduction zone magmas: concentrations and fluxes based on melt inclusion and volcanic gas data. *J. Volcanol. Geotherm. Res.* **140**, 217–240.

WIESNER, M.G., WETZEL, A., CATANE, S.G., LISTANCO, E.L. & MIRABUENO, H.T. 2004 Grain size, area thickness distribution and controls on sedimentation of the 1991 Mount Pinatubo tephra layer in the South China Sea. *Bull. Volcanol.* **66**, 226–242.

WILSON, L. 1976 Explosive Volcanic Eruptions: III. Plinian Eruption Columns. *J. R. Astron. Soc.* **45**, 543–556.

WILSON, L., SPARKS, R. S. J. & WALKER, G. P. L. 1980 Explosive volcanic eruptions - IV. The control of magma properties and conduit geometry on eruption column behaviour. *Geophys. J. R. Astron. Soc.* **63**, 117–148.

WOODHOUSE, M. J., HOGG, A. J., PHILLIPS, J. C. & SPARKS, R. S. J. 2013 Interaction between volcanic plumes and wind during the 2010 Eyjafjallajökull eruption, Iceland. *J. Geophys. Res. Solid Earth* **118**, 92–109.

WOODS, A.W. 1988 The fluid dynamics and thermodynamics of eruption columns. *Bull. Volcanol.* **50**, 169–193.

WOODS, A. W. & CAULFIELD, C. P. 1992 A laboratory study of explosive volcanic eruptions. *J. Geophys. Res.* **97** (B5), 6699–6712.

YANG, W.-C. & HWANG, R. R. 2001 Vertical buoyant jets in a linearly stratified ambient cross-stream. *Environ. Fluid Mech.* **1**, 235–256.

Part 3

Volcanic hazard assessment in Martinique

Chapter 5

Modeling volcanic tephra dispersion in Martinique

Table of contents

Résumé du chapitre 5

Nous avons étudié dans le chapitre précédent l'effet du vent sur la stabilité des colonnes volcaniques. Dans ce chapitre, nous étudions en détail l'importance du vent en Martinique pour la dispersion des cendres volcaniques durant une éruption et donc sur la distribution des dépôts sur le terrain. Dans la majorité des études, des profils de vents moyennés sont utilisés pour simuler la dispersion des produits volcaniques et quantifier les risques associés. Ici, nous présentons une réinterprétation des deux éruptions peu comprises de la montagne Pelée, Bellefontaine et Balisier, permettant de démontrer que l'utilisation exclusive des profils de vent moyennés peut mener à une mauvaise représentation du risque volcanique.

Ces deux éruptions, tout comme celles de Carbet et d'Etoile, sont caractérisées par une distribution des dépôts dont l'axe principal est orienté en direction du sud de l'île, et donc de Fort-de-France (chef-lieu de la Martinique), vers des zones considérées comme sécurisées dans les cartes actuelles et comportant des infrastructures décisionnelles majeures pour la gestion de crise (telle que la préfecture). Cette direction est surprenante car elle n'est pas cohérente avec les directions moyennes de vents d'est (jusqu'à environ 6 km d'altitude) et d'ouest (de 7 km à la tropopause) caractérisant les Petites Antilles, alors même que ces vents permettent d'expliquer les dispersions des éruptions plus récentes P1 et P2 (Carazzo *et al.*, 2012, 2019). Des études précédentes ont suggéré que cet axe de dispersion inhabituel pourrait être dû à des conditions météorologiques très particulières éventuellement liées à un cyclone passant proche de la Martinique au moment de l'éruption de Bellefontaine (Roobol & Smith, 1976; Westercamp & Traineau, 1983; Traineau *et al.*, 1989). Ces conditions particulières seraient donc similaires pour les éruptions d'Etoile, du Carbet, et de Balisier dont le panache secondaire issu de la rencontre d'une coulée de densité pyroclastique avec une barrière topographique a également dispersé des dépôts en direction du sud de l'île.

Grâce à des simulations 2D faites en utilisant le modèle de dispersion de cendres volcaniques HAZMAP (Macedonio *et al.*, 2005), nous cherchons à tester ces hypothèses. Nos résultats montrent que les profils de vents moyennés sur une saison ne peuvent pas expliquer les dispersions au sud des dépôts de ces éruptions de Bellefontaine et Balisier (et donc également de celles de Carbet et d'Etoile). Pour comprendre l'origine de ces axes de dispersion inhabituels, nous utilisons quarante ans de données de vent sur la Martinique issues des réanalyses de climat global par l'ECMWF (European Centre for Medium-Range Weather Forecasts). Grâce à ces bases de données nommées ERA-Interim (Dee *et al.*, 2011) et ERA-5 (Hersbach *et al.*, 2019), nous démontrons que l'éruption de Bellefontaine ne s'est pas nécessairement produite sous des conditions météorologiques extrêmes associées au passage d'un cyclone, mais plutôt dans des contextes atmosphériques plus particuliers durant lesquels le trajet du "jet-stream" tropical est modifié. Cette situation produit des vents de faibles vitesses venant du nord dans la haute troposphère jusque sur l'île de la Martinique. Nos résultats ont également montré que notre estimation de hauteur maximale du panache secondaire de Balisier (i.e. 13 km) est cohérente avec nos simulations. Pour finir, nous avons calculé que la probabilité d'occurrence mensuelle de tels vents peut atteindre presque 5% aux mois de mai et novembre marquant la transition entre les saisons humide et sèche.

Ces résultats démontrent que l'utilisation de profils saisonniers moyens ne fournissant que des informations sur les cas les plus probables peut entrainer de fortes sous-estimations dans l'évaluation de l'aléa volcanique. Il apparaît donc nécessaire de considérer la variabilité journalière des vents, à la fois pour ce qui est de la vitesse et de l'orientation, dans la prévision des catastrophes volcaniques.

1   Introduction

We saw in the previous chapter the strong effect of wind on the collapse of volcanic columns, but the wind also has a paramount importance for tephra dispersal during an eruption and therefore on the distribution of deposits in the field (Figure 1). In this chapter, we investigate this effect by performing tephra dispersal simulations of the Plinian eruptions of the Mount Pelée volcano that we revisited/discovered during this PhD work.
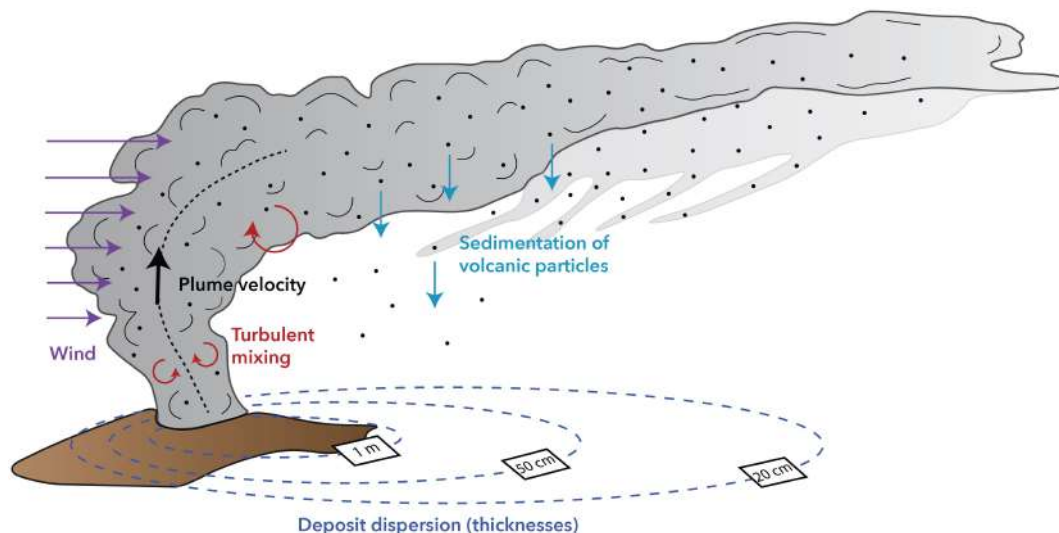

Figure 1: Sketch of a volcanic plume illustrating the effect of wind on turbulent mixing and tephra dispersion.

The Bellefontaine, Carbet and Etoile events are characterized by a striking southward distribution of the isopachs and isopleths (Chapter 2, Section 2.2). This direction is surprising because it is not consistent with the mean directions of easterly (up to ≈ 6 km high) and westerly (between 7 km and the tropopause) winds (Chapter 1, Figure 5b and Dunion 2011). Furthermore, these directions explain well the dispersion of the recent P1 and P2 eruption deposits (Carazzo *et al.*, 2012, 2019). Previous studies suggested that this southward dispersion could be related to very specific wind conditions during the Bellefontaine eruption (and thus to similar conditions during the Carbet and Etoile events), perhaps due to a hurricane passing over or close to Martinique (Roobol & Smith, 1976; Westercamp & Traineau, 1983; Traineau *et al.*, 1989). Here we test this possibility by performing 2D simulations of volcanic tephra dispersal, using the HAZMAP tephra dispersion model (Macedonio *et al.* 2005; version 2.4.2 released in 2014). As the Bellefontaine, Carbet, and Etoile eruptions exhibit more or less the same dispersal axis, we run the simulations for the Bellefontaine eruption only, whose eruptive parameters are better constrained. Our conclusions have however similar implications for the three Plinian eruptions.

The Balisier event is a rather unique Pelean event in Martinique. As described in Chapter 2, it is characterized by the destruction of a lava dome that induced the formation of a pyroclastic density current (PDC) rushing down the southern volcano flanks. But as the PDC encountered the topographical barrier created by a large flank collapse, at least one co-PDC plume rose above the PDC and deposited a thick fallout deposit up to 6 km away from the vent. This deposit further displays a southward dispersal axis. In Chapter 2, we estimated a maximum column height of ≈ 13 km for the co-PDC plume, using field data and published relationships between mass discharge rate and column height. We now use this value as input parameter in the HAZMAP model to infer the wind regime that

occurred during the eruption.

First, we describe the HAZMAP model, its constitutive equations and the inputs parameters needed to run tephra dispersal simulations. We then determine the likely wind conditions that prevailed during the Bellefontaine and Balisier eruptions using the global atmospheric reanalyses ERA-Interim (Dee *et al.*, 2011) and ERA5 (Hersbach *et al.*, 2019), together with the HAZMAP software. We conclude the chapter by a discussion of the consequences of this study on volcanic hazard assessment in Martinique.

2   The HAZMAP model

HAZMAP is a semi-analytical model that solves the advection-diffusion-sedimentation equation for fine particles in the umbrella cloud. This model is commonly used for volcanic hazard assessment to predict Plinian deposit characteristics as a function of eruptive source parameters and wind datasets (e.g., Macedonio *et al.* 2008, 2016; Costa *et al.* 2009; Bonasia *et al.* 2011, 2012). This model does not take into account particle aggregation, a phenomenon that we did not observed in the field.

2.1   Constitutive equations

The HAZMAP model describes the dispersion and sedimentation of volcanic tephra in two dimensions from vertically distributed point sources. The dispersion of particles is governed mainly by wind transport and turbulent diffusion, whereas the fallout is controlled by the particle free fall velocity set by the balance of gravity and air drag. The model assumes that the horizontal wind components and horizontal turbulent diffusion are uniform and constant with time, whereas the vertical wind component and vertical turbulent diffusion are negligible with respect to the horizontal ones (Armienti *et al.*, 1988; Macedonio *et al.*, 2005; Pfeiffer *et al.*, 2005; Costa *et al.*, 2006; Folch *et al.*, 2009; Macedonio & Costa, 2014).

In this first-order approach, the motion of particles is described by the mass conservation equations as follows:

$$\frac{\partial C_\phi}{\partial t} + W_x \frac{\partial C_\phi}{\partial x} + W_y \frac{\partial C_\phi}{\partial y} - \frac{\partial V_\phi C_\phi}{\partial z} = K_x \frac{\partial^2 C_\phi}{\partial x^2} + K_y \frac{\partial^2 C_\phi}{\partial y^2} + S \qquad (1)$$

where C_ϕ denotes the concentration of particle class ϕ, t is time, x, y, z are the spatial coordinates, W_x and W_y are the horizontal components of the wind velocity vector, K_x and K_y are the horizontal atmospheric eddy diffusion coefficients assumed equal (i.e., $K_x = K_y = K$), V_ϕ is the terminal settling velocity for particle class ϕ, and S is a source function.

The source term in Eq. (1) is described using an empirical formula modified from Suzuki (1983):

$$S(x, y, z, t) = S_0 \left\{ 1 - \frac{z}{H} \exp \left[A (z/H - 1) \right] \right\}^\lambda \times \delta (t - t_0) \, \delta (x - x_v) \, \delta (y - y_v) \qquad (2)$$

where x_v and y_v are the coordinates of the vent, $S_0 \left\{ 1 - \frac{z}{H} \exp \left[A (z/H - 1) \right] \right\}^\lambda$ is the vertical mass distribution function describing the eruption column, S_0 is a normalisation factor, H is the maximum plume height, A and λ are two dimensionless parameters, and δ is the Dirac's function. Eq. (2) considers a filiform and instantaneous release of particles with a maximum concentration centered at $H(A - 1)/A$ and a mass concentration vertically

distributed around the maximum according to the value of λ.

2.2　Input parameters

2.2.1　Volcanological parameters

HAZMAP introduces a horizontal atmospheric diffusion coefficient that we set at 3,000 $m^2\,s^{-1}$ for all Bellefontaine simulations, a value consistent with the ones used in the literature (Macedonio *et al.*, 1988; Bonadonna *et al.*, 2002; Pfeiffer *et al.*, 2005) and calibrated with our deposits by using 25 preliminary tests. As suggested by Costa *et al.* (2009), we take a smaller diffusion coefficient of 1,000 $m^2\,s^{-1}$ for all Balisier simulations, as this Pelean eruption is of smaller magnitude than a Plinian one. The simplification of the eruptive column in the model requires two additional empirical parameters, the Suzuki parameters A and λ, that describe geometrically the vertical mass distribution within the eruption column and define the shape of the column (see Figure 1 in Pfeiffer *et al.* 2005 and Macedonio *et al.* 1988 or Suzuki 1983 for calculation details). Here we use A = 4 and $\lambda = 1$, commonly chosen values in the literature (Pfeiffer *et al.*, 2005; Costa *et al.*, 2009; Macedonio *et al.*, 2016). We finally consider a deposit density of 1,070 $kg\,m^{-3}$ based on previous estimates for Mount Pelée deposits (Traineau *et al.*, 1989), and use this value to convert mass loads in $kg\,m^{-2}$ given by HAZMAP into thickness values.

In the Bellefontaine simulations, the total erupted mass for Unit B is taken as 4.6 × 10^{11} kg, the maximum column height is set at 20 km (see Chapter 2, Section 3.2), and we use the total grain–size distribution reconstructed in Chapter 2 (Figure 11b). The eruptive source is the volcanic vent at the summit (orange triangle in Figure 4).

In the Balisier simulations, the total erupted mass for Unit C is taken as 3.9 × 10^{10} kg, the maximum column height is set at 13 km (see Chapter 2, Section 3.3), and we use the total grain-size distribution reconstructed in Chapter 2 (Figure 13b). In that case, we consider that the source was located where the co-PDC rose above the PDC generated by the destruction of the lava dome (i.e., close to the location 200 which is the Mont Parnasse section in Chapter 1, purple star in Figure 5). For simplicity, we consider the co-PDC plume to act like a Plinian plume.

2.2.2　Wind profiles from ERA Interim and ERA 5

HAZMAP being used in its "deposit mode", the computation of the mass distribution requires a given single wind profile giving wind velocity components (u, v) as a function of altitude. In this study, we mainly use wind velocity profiles based on the European Centre for Medium-Range Weather Forecasts ERA-Interim reanalysis (ERA-Interim) for the years 1979-2017 (Dee *et al.*, 2011). We further use ERA5 (Hersbach *et al.*, 2019) for hurricane simulations for which higher temporal and horizontal resolutions are necessary to capture the detailed time evolution of these non-linear and quickly evolving events. Note that the atmospheric reanalysis of ERA-Interim is now offline and no longer updated.

The initial content of ERA-Interim files consists of six-hourly global fields of zonal and meridional winds at a horizontal resolution of 0.75° × 0.75° ($\approx$ 79 km) and vertically distributed on 37 pressure levels from 110 m (1000 hPa) to $\approx$ 48 km (1 hPa). These wind fields have been interpolated to match HAZMAP format by converting each of the 37 pressure levels into an altitude level using the altitude model in Figure 2. We calculate the wind components over Martinique at each time step and each pressure level in an area
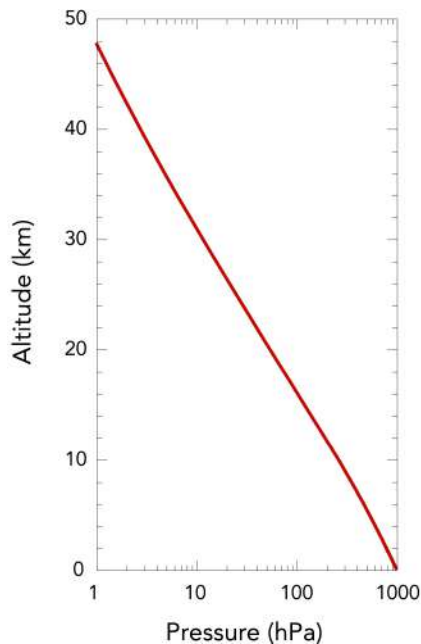
Figure 2: Altitude model used to convert the 37 pressure levels of the original ERA-Interim and ERA5 files into the altitude levels required by HAZMAP.

ranging from 14.4°N to 14.8°N and from 60.8°W to 61.2°W. Our final dataset, used in the following section and shown in Figure 3, is composed of 56,984 vertical wind profiles from January 1979 to December 2017.
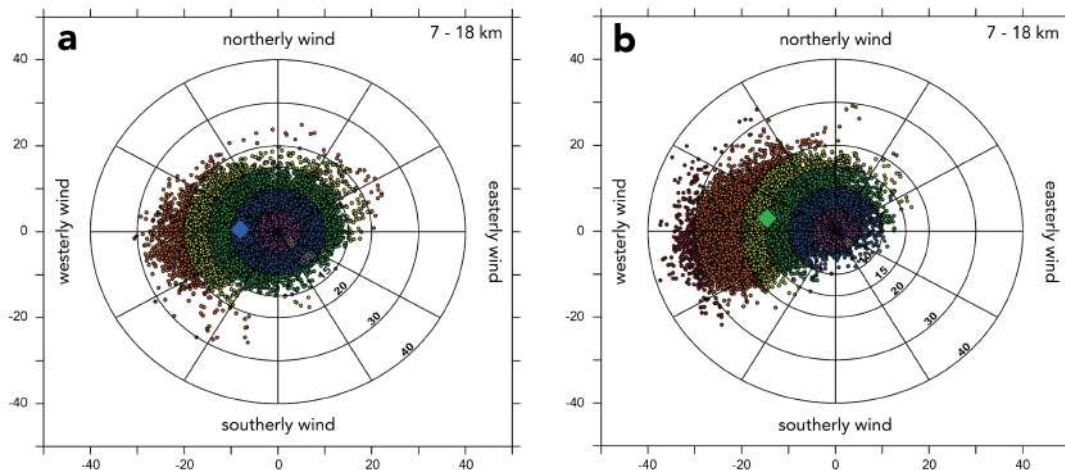

Figure 3: Compass roses representing the 40-year wind database for the **a** wet and **b** dry season, respectively. Horizontal wind vectors (intensity and direction) are averaged over the high tropospheric layers (from 7 to 18 km of altitude). The wind speed is discretized into 6 levels, respectively < 5 m s^{-1}, 5-10 m s^{-1}, 10-15 m s^{-1}, 15-20 m s^{-1}, 20-30 m s^{-1}, and 30-40 m s^{-1}, from the center to the rose boundary (and from purple to red). The large colored diamonds represent the mean value of each database.

The ERA5 dataset (Hersbach *et al.*, 2019) released in early 2019 uses the same 37 pressure levels as ERA-Interim but has higher horizontal (0.25° × 0.25°, ≈ 31 km) and temporal (hourly analysis fields) resolutions, the latter of which is smaller than the duration of the Bellefontaine eruption (i.e., 2h30). Hurricane simulations using ERA5 are reported in Section 4.2.

3   Predictions using mean seasonal wind profiles

We first use the eruptive source parameters inferred from our field study, and the dominant seasonal wind profiles in the Lesser Antilles (large colored diamonds in Figure 3) to analyze their consequences for the fallout isopach maps. Figure 4a (inset) presents the wind profile, averaged over the duration of the wet season (June to November), while Figure 4b (inset) corresponds to the dry season (December to May). The averaged wind profile for the wet season is characterized by easterlies from the surface to 350 hPa ($\approx$ 7 km) with a highest speed of 7.8 m s^{-1} at 850 hPa ($\approx$ 1 km), and westerlies from 300 hPa ($\approx$ 8.8 km) to 125 hPa ($\approx$ 15.3 km) with wind speed not exceeding 7 m s^{-1} at 150 hPa ($\approx$ 13 km). This wind profile for the wet season compares remarkably well with the one determined by Dunion (2011) (their Figure 8e and f) using 8 years of rawinsonde observations from four Caribbean stations. During the dry season, we observe two noticeable differences compared with the wet season: the change in wind direction within the troposphere occurs at a lower elevation (550 hPa or $\approx$ 4.5 km) in the dry season, and westerlies within the upper troposphere becomes much faster with 20 m s^{-1} at 175 hPa ($\approx$ 12 km).

3.1   The Bellefontaine eruption (13,516 yr cal BP)
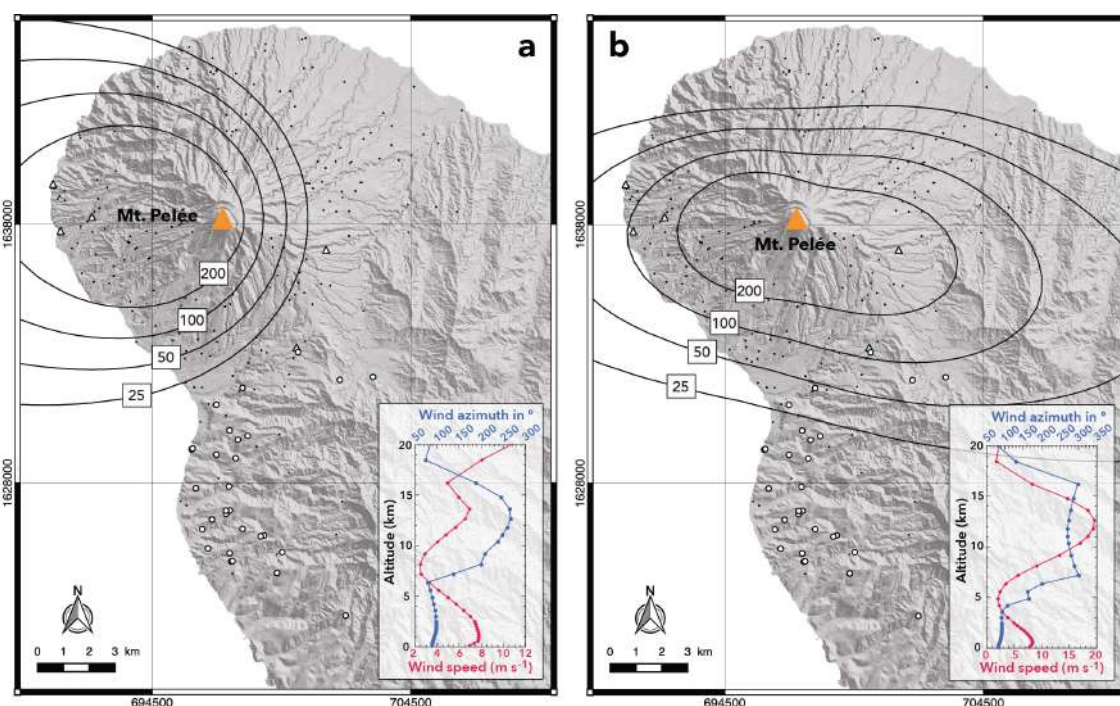

Figure 4: Isopach maps (in centimeters) of the Bellefontaine eruption calculated using the HAZMAP model (Macedonio *et al.*, 2005) for **a** wet and **b** dry season, respectively. The white dots correspond to locations where Bellefontaine deposits are present. Seasonal average wind speed (pink) and azimuth (blue) profiles used for the HAZMAP simulations are given in inset. See Chapter 2 for volcanic input details. All maps were generated using the open source QGIS software. Coordinates are in WGS 84 − UTM Zone 20 system.

The main dispersal axes obtained with HAZMAP using mean wind profiles of the wet (Figure 4a) and dry (Figure 4b) seasons are clearly inconsistent with the dispersion axis inferred for the Bellefontaine eruption (Chapter 2, Figure 5b).

For the wet season, the direction of the dispersal axis (Figure 4a) is mainly westward which corresponds to the direction of the most rapid easterlies found within the lower

stratosphere and within the troposphere below an elevation of 9 km. During the dry season, the model predicts fallout deposits west and east of Mount Pelée volcano (Figure 4b). The amount of deposits is larger to the east than to the west, highlighting the effect of strong westerlies within the upper troposphere. We also note that the direction of the dispersal axis during the wet season (Figure 4a) is consistent with the isopachs determined in the field for the P1 eruption (Figure 5 in Carazzo *et al.* 2012).

3.2   The Balisier eruption (14,072 yr cal BP)

Figure 5 shows the main dispersal axes obtained with HAZMAP using the same seasonal mean wind profiles as for the Bellefontaine eruption (insets in Figure 4). We note that predictions based on wet (Figure 5a) and dry (Figure 5b) season wind profiles are clearly inconsistent with the field data obtained for the Balisier eruption (Chapter 2, Figure 8). For both seasons, the direction of the dispersal axis is mainly westward which corresponds to the direction of the most rapid easterlies found within the troposphere below an altitude of 9 km. Because the maximum co-PDC plume height is only 13 km, the strong westerlies within the upper troposphere cannot counterbalance the effect of these lower easterlies.
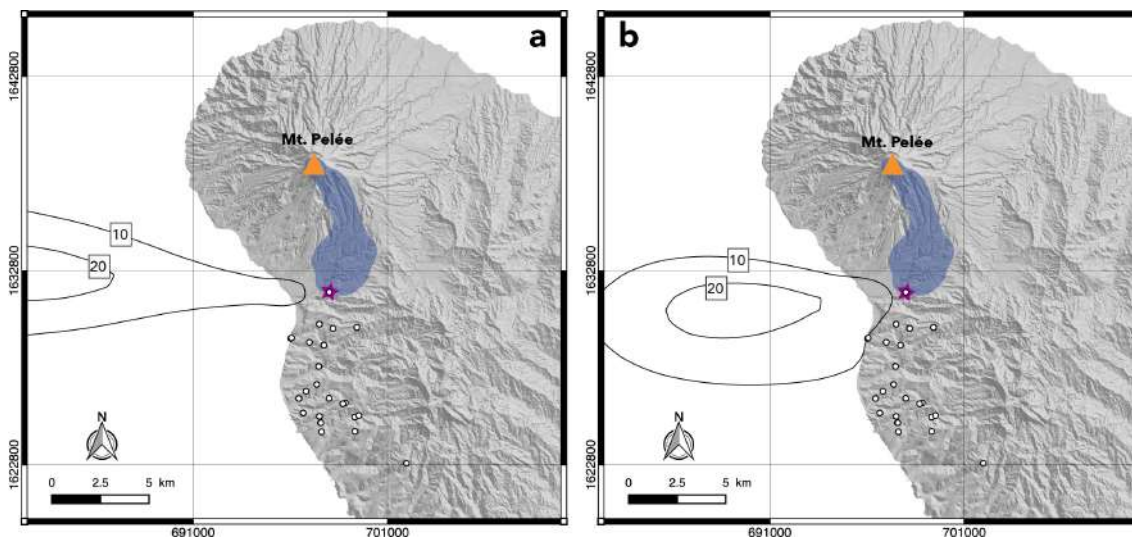

Figure 5: Isopach maps (in centimeters) of the Balisier eruption calculated using HAZMAP for **a** wet and **b** dry season, respectively. The white dots correspond to locations where Balisier deposits are present. Location of the eruptive source given as an input for HAZMAP is shown by the purple star, corresponding to the Mont Parnasse section in Chapter 1. The blue patch represents the extrapolated global extent of the PDC deposits (see Chapter 2, Section 2.2.2).

These results suggest that small co-PDC plume always spread fine volcanic material towards the sea, as observed in 1902 by Lacroix (1904) (Chapter 1, Figure 1b) and in 1929 by Perret (1937) (his Figure 4a). The exceptional preservation of the Balisier deposits in the field thus results from particular wind conditions, with a main direction towards the south, at the time of the eruption.

4   Dispersal modeling of eruption products

Averaged wind profiles, such as those used in Section 3, represent the typical values for a dataset, i.e. the most probable case. Unfortunately, a "statistical" forecasting based solely

on average values hides by definition the variability observed at shorter timescales (months, days, or hours). In this section, we first seek to understand the unusual southward dispersal axis of the Bellefontaine, Balisier, Carbet and Etoile eruptions by using high frequency wind profiles in HAZMAP. All simulations of Plinian eruptions are done for the Bellefontaine eruption only, as this event is the better constrained one (Section 4.1 and Section 4.2). We then perform calculations for the Balisier eruption in order to test the consistency of the maximum column height inferred from field data in Chapter 2 (Section 4.3).

4.1   Northerly winds in Martinique (1979–2017)

In order to interpret the unusual southward direction of tephra dispersion during the Bellefontaine eruption, we analyzed the high frequency (i.e., six-hourly) wind dataset over Martinique from ERA-Interim. Among the 56,984 vertical wind profiles available (1979-2017), we observed a relatively weak variability of wind in the lower troposphere, which is strongly dominated by easterlies throughout the year. The upper troposphere between 400 hPa ($\approx$ 7 km high) and the tropopause ($\approx$ 18 km high) are, however, characterized by a notable variability of both wind speed and direction (Figure 3a and b), which can impact the direction of tephra dispersion. Consequently, we sampled a few cases where upper tropospheric mean winds blow from N310 to N30, a configuration that was likely to counterbalance the effect of lower tropospheric easterlies and provide isopach maps consistent with the Bellefontaine deposits. Cases with upper tropospheric mean winds from N30 to N50 were discarded since their trend would tend to align with lower tropospheric easterlies and spread tephra to the southwest at sea. Among 54 of such wind profiles (see Table 1), used as input in HAZMAP together with the same volcanic input parameters as in Section 3, 45 produce isopach maps similar to that inferred for Bellefontaine eruption (Chapter 2, Figure 5b) (cases marked "O" in Table 1), including those shown in Figure 6a,b and c. Hence this preliminary criterion accounts for the location of the Bellefontaine deposits in the field in a very large majority of cases (83%), and highlights the importance of the wind direction heterogeneity when considered at a finer time-scale (few hours maximum).

Table 1: The 54 wind profiles selected because of their N310 to N30 mean direction in the upper troposphere, that we tested using HAZMAP. The two first columns give the date and time of each wind profile, the third column gives the main dispersal axis of the isopach map calculated using HAZMAP, and the last column indicates whether the calculated isopach map is consistent with the Bellefontaine deposit pattern (O) or not (x). Based on these results, conditions for northerly winds last between 6 hours and 2.5 days.

Date	Time (UTC)	Dispersal axis	Comparison with field data
October 14, 2017	6:00 AM	SW	x
August 28, 2017	12:00 PM	SW	x
October 4, 2003	12:00 PM	SSE	O
October 4, 2003	6:00 AM	SE	O
October 3, 2003	12:00 PM	SE	O
September 27, 2000	6:00 PM	S	O
September 1, 1999	6:00 PM	SW	x
September 20, 1998	6:00 PM	SSW	O
December 21, 1996	12:00 AM	SSE	O
November 29, 1996	6:00 PM	SSE	O
November 29, 1996	12:00 PM	SSE	O
November 29, 1996	6:00 AM	SSE	O
November 29, 1996	12:00 AM	S	O

Continued on next page

Table 1 – *Continued from previous page*

Date	Time (UTC)	Dispersal axis	Comparison with field data
November 28, 1996	12:00 AM	SSE	O
November 27, 1996	6:00 PM	SSE	O
November 27, 1996	12:00 PM	SSE	O
October 24, 1996	12:00 PM	SW	x
September 13, 1996	6:00 AM	SSE	O
September 12, 1996	12:00 AM	S	O
September 2, 1996	6:00 AM	SW	x
May 2, 1996	12:00 AM	SSE	O
May 1, 1996	6:00 PM	SSE	O
January 26, 1996	6:00 PM	SSE	O
January 25, 1996	12:00 AM	SE	O
September 19, 1995	6:00 AM	SW	x
April 13, 1995	6:00 PM	SSE	O
November 12, 1994	12:00 PM	S	O
November 3, 1994	12:00 AM	SSE	O
November 2, 1994	6:00 PM	SSE	O
May 31, 1993	6:00 AM	SSE	O
May 23, 1993	6:00 AM	SSE	O
November 21, 1992	12:00 AM	Circular	O
November 8, 1992	6:00 PM	SW	x
October 21, 1992	12:00 AM	SSE	O
October 20, 1992	6:00 PM	SSE	O
October 20, 1992	12:00 PM	SSE	O
October 20, 1992	6:00 AM	SSE	O
October 20, 1992	12:00 AM	SSE	O
October 7, 1991	6:00 AM	SSE	O
December 8, 1990	6:00 PM	S	O
October 9, 1990	6:00 PM	SE	O
October 9, 1990	6:00 AM	SE	O
March 14, 1988	12:00 PM	SSE	O
March 29, 1987	6:00 AM	S	O
March 29, 1987	12:00 AM	S	O
October 6, 1986	6:00 PM	W	x
October 27, 1985	12:00 AM	S	O
October 26, 1985	6:00 PM	SSE	O
September 16, 1985	6:00 PM	SW	x
September 16, 1984	6:00 PM	Circular	O
January 2, 1984	12:00 AM	SE	O
November 17, 1979	12:00 PM	SE	O
October 11, 1979	12:00 PM	S	O
October 10, 1979	6:00 PM	SSE	O

To enhance the robustness of our selection, we further looked for common features shared by these 45 successful simulations, and found that a specific combination of factors − made explicit below as four criteria − leads to a successful reproduction of the Bellefontaine southward ash dispersion. First, in the high tropospheric layers (from 7 to 18 km of altitude), the wind azimuth has to be limited to a narrow band of directions: from 310°N to 350°N
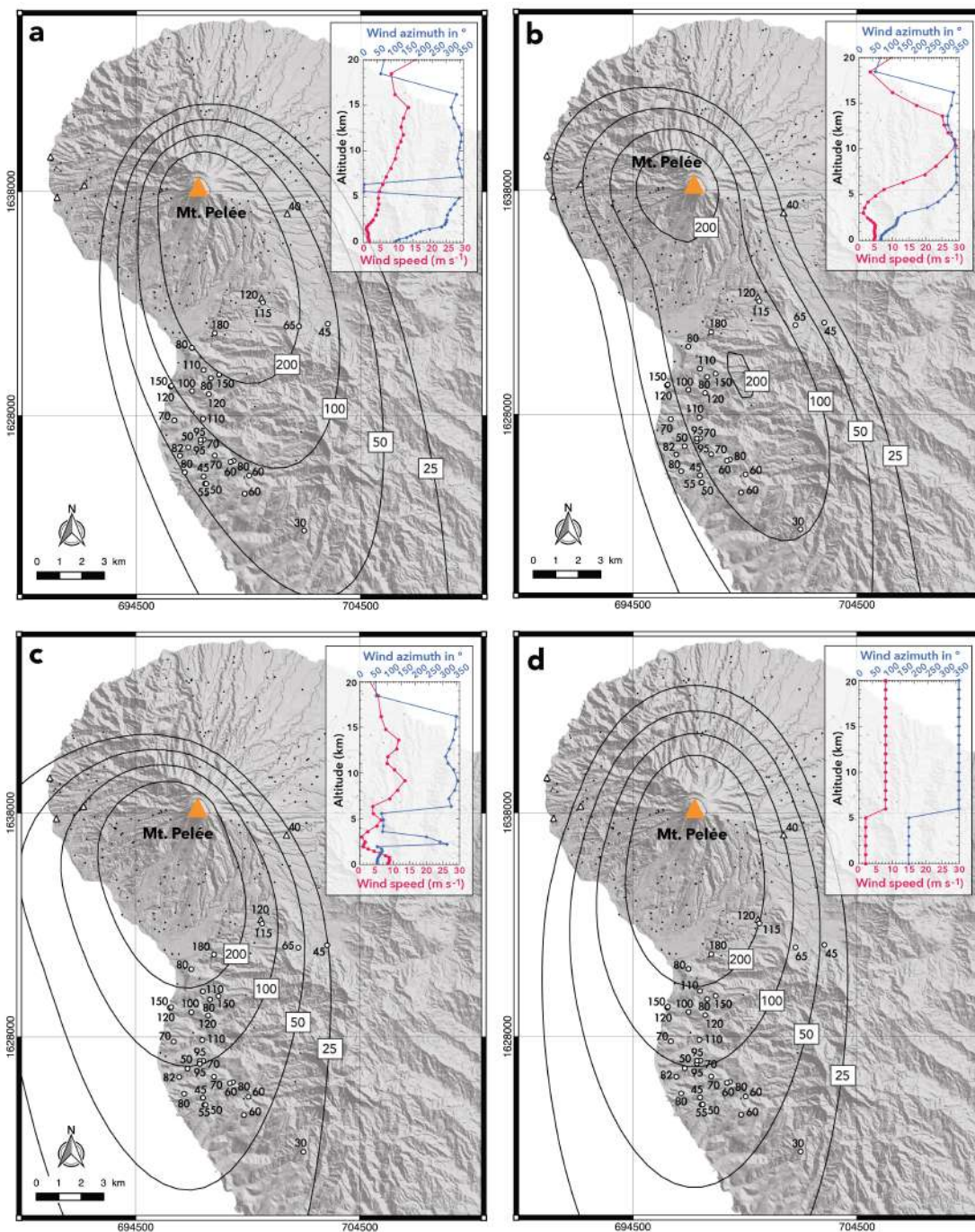
Figure 6: Isopach maps (in centimeters) from HAZMAP simulations, using the wind profiles given in inset, from **a** 4 October 2003, 12 pm UTC; **b** 27 November 1996, 6 pm UTC; **c** 29 March 1987, 6 am UTC; and **d** a theoretical wind profile, compared with the thicknesses (in centimeters) measured in the field. These Bellefontaine-like cases illustrate the possibility of northerly winds over Martinique in the last forty years.

(criterion **C1**). Second, these upper tropospheric winds also have to be dominant with a speed ≥ 7 m s^{-1} (**C2**). Third, wind speed ratio between the high and mid- troposphere (from 2 to 7 km of altitude) must be larger than 2 (i.e., high/mid > 2, **C3**). Finally, lower tropospheric wind speeds (below 2 km of altitude) have to be low enough (≤ 4 m s^{-1}) to avoid tephra dispersion in multiple directions (**C4**). We note that no specific condition for the lowest stratospheric layers (from 18 to 20 km of altitude) is required to reproduce
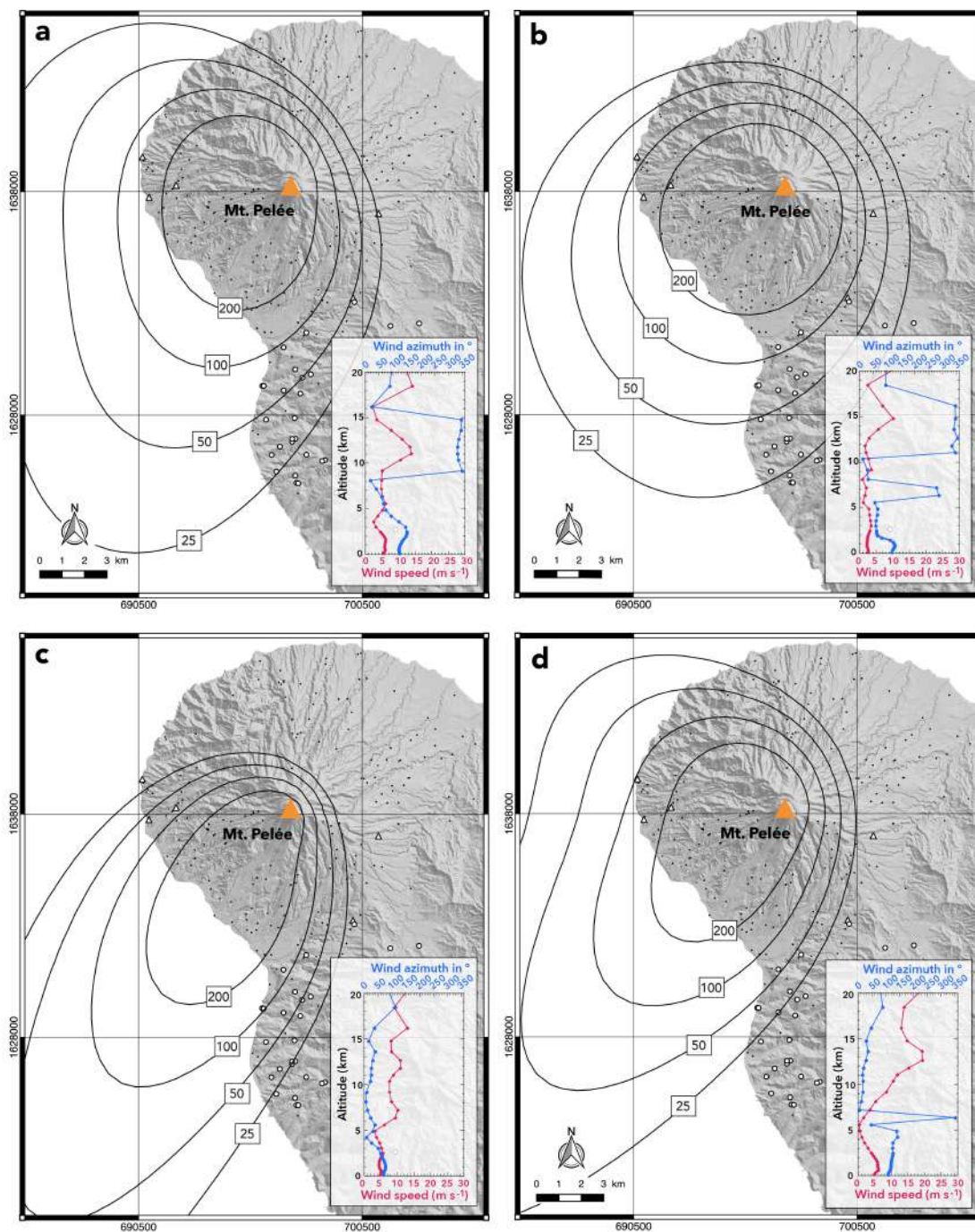
Figure 7: Isopach maps (in centimeters) from HAZMAP simulations using the wind profiles given in inset from **a** August 28, 2017, 12 pm UTC (verified criteria: C1 and C2); **b** October 14, 2017, 6 am UTC (verified criteria: C1 and C4); **c** November 8, 1992, 6 pm UTC (verified criterion: C2); and **d** September 2, 1996, 6 am UTC (verified criteria: C2 and C3). These "unsuccessful" cases illustrate the importance of the criteria required to reproduce the Bellefontaine southward ash dispersion.

the Bellefontaine eruption dispersion axis, because the winds at those levels are generally weaker than in the high troposphere.

Figure 6a shows that for a simulation using a wind profile fulfilling all the above criteria, we obtain a dispersal axis oriented to the SSE, thus covering the entire area where Bellefontaine deposits were found. When all the criteria but **C4** are satisfied, the simulated

dispersal axis remains similar (SSE and S, respectively, in Figure 6b and c). The "bulge" to the west in Figure 6c however shows the impact of strong easterly winds in the low troposphere, which can reach a maximum speed of 9 m s^{-1} in the first km of altitude. One can also note a secondary maximum in the simulated isopach map shown in Figure 6b, which is not present in any of the other results of this study. Considering the proximity to the vent and the simple modeling approach taken, this feature is probably not caused by volcanic plume effects (Manzella *et al.*, 2015) or topographic effects (Watt *et al.*, 2015). It could rather be due, as suggested by Poulidis *et al.* (2018), to the low wind speed layer associated to wind shear present at $\approx$ 4 km of altitude (inset in Figure 6b), which traps ash and thus can act as an elevated secondary source.

Four of the 9 unsuccessful cases (marked "x" in the Table 1) are presented in Figure 7. We show that when only one or two criteria are fulfilled, the tephra dispersion axis is always oriented to the southwest. In case of stronger winds in low to mid-troposphere (i.e., only **C1** and **C2** are satisfied) mostly blowing from the southeast to east, the tephra dispersion axis is oriented to the southwest, with a "bulge" to the northwest (Figure 7a). If stronger easterly winds in mid-troposphere are combined with weaker winds in high troposphere (i.e., only **C1** and **C4** are fulfilled), the isopachs are more circular with a dispersal axis oriented to the southwest (Figure 7b). If only **C2** is satisfied, the isopachs are strongly stretched to the southwest (Figure 7c). Finally, if **C2** and **C3** are fulfilled, a similar result is found, but with a "bulge" to the northwest due to south-easterlies in the low troposphere (Figure 7d).

Figure 6a, b and c thus shows that the combination of all the criteria given above leads to model predictions consistent with the main direction of tephra dispersion observed for the Bellefontaine eruption. However, the thicknesses and global shape of isopachs are not completely equivalent to those in the Chapter 2, Figure 5b. Based on these results, we further optimized the wind conditions in order to better reproduce the isopach map inferred from the field data. We determined the wind profile yielding the best agreement between simulated isopachs and those measured in the field (Figure 6d and Figure 5b in Chapter 2), in both downwind and crosswind directions. This idealized wind profile, fulfilling all the criteria, consists of southerlies blowing at 2 m s^{-1} up to an altitude of 5 km, and northerlies blowing at speed of 8 m s^{-1} above an altitude of 5 km up to the tropopause (inset in Figure 6d). Such conditions prevent the formation of elongated isopachs (Figure 6a and b) and the shift of volcanic deposit pattern towards the sea (Figure 6c).

4.2   Can hurricanes explain the Bellefontaine pattern of deposition?

We now test the hypothesis originally proposed by Westercamp & Traineau (1983) that strong hurricane winds blowing over Martinique during the eruption could explain the southward dispersion of the Bellefontaine deposits. As a hurricane is a synoptic scale weather system (i.e., corresponding to a large horizontal length scale of about 1,000 kilometers), it can affect the meteorological state (and thus wind speed and direction) up to 250 kilometers from the eye. Using the Atlantic hurricane database HURDAT2 maintained by the National Oceanic and Atmospheric Administration (NOAA) National Hurricane Center (Landsea & Franklin, 2013), we identified 11 hurricanes that passed within less than 250 kilometers from Mount Pelée in the past 40 years (Figure 8). In the northern hemisphere, northerly winds can only be observed to the west of the hurricane eye. We thus focused only on the 8 hurricanes that passed to the east and then to the north of Martinique (labeled 1, 2, 3, 4, 7, 8, 9, and 10 in Figure 8). We retrieved the wind profiles corresponding to these hurricanes from the atmospheric reanalysis ERA5, and found that only 5 of them produced northerly winds, and did so during a short period of time ($\approx$ 2h): hurricanes David in 1979, Hugo in
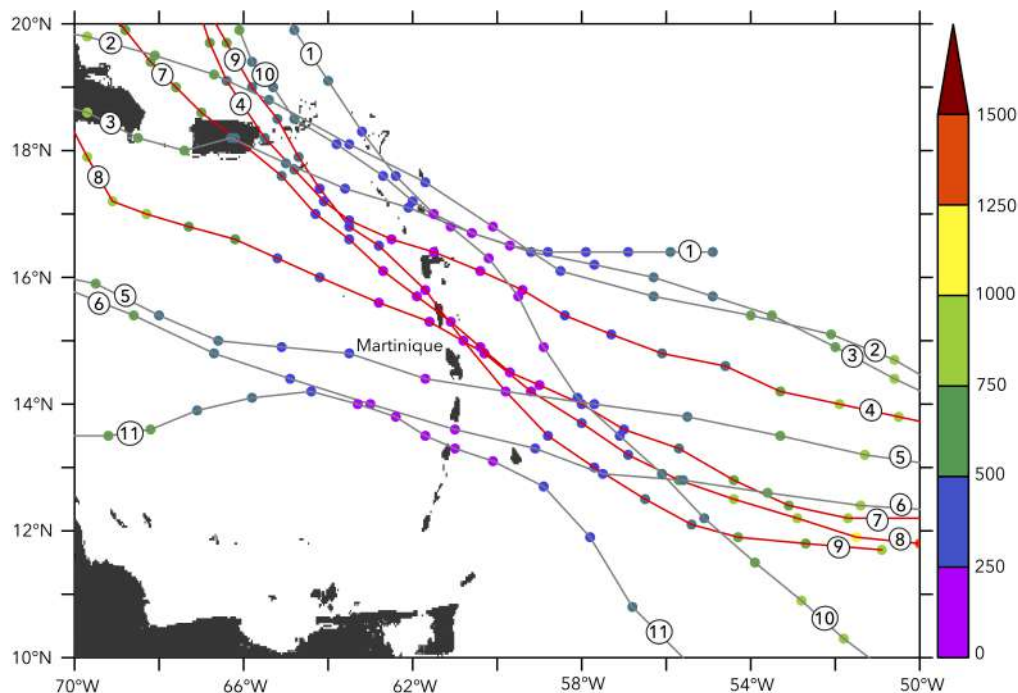
Figure 8: Tracks of the North Atlantic hurricanes that passed within 250 km of Mount Pelée during the period 1979-2017: **1** Gonzalo in 2014, **2** Debby in 2000, **3** Georges in 1998, **4** Hugo in 1989, **5** Dean in 2007, **6** Allen in 1980, **7** Maria in 2017, **8** David in 1979, **9** Marilyn in 1995, **10** José in 1999, and **11** Tomas in 2010. The colored dots show for each hurricane track the distance to Mount Pelée in kilometers, given by the colored scale on the right. The red tracks refer to the hurricanes used for the simulations in Figure 10.

1989, Marilyn in 1995, Georges in 1998, and Maria in 2017. These 5 events all belong to the cluster 3 defined by Kossin *et al.* (2010), in which hurricanes originate from the eastern part of the central Atlantic Ocean (defined as Cape Verde hurricanes). Because of its high temporal and spatial resolution, hurricane tracks and wind speed profiles are better captured by ERA5 than by ERA-Interim dataset. Using this approach implies to neglect gusts associated with hurricanes (which can reach speeds up to 80 m s^{-1}; Murakami 2014). This type of event is, however, generally too brief (about one minute long) to significantly influence tephra dispersion and to be preserved in the deposits.

Using the HAZMAP model, we then performed 2 simulations for each hurricane, each considering two different (and consecutive in time) wind profiles from ERA5 dataset (Figure 9). These wind profiles differ from those described in Section 4.1, and illustrate the changes of air mass circulation as the hurricane is passing by. In particular, hurricane Maria exhibits a decreasing speed with height, a characteristic generally observed during a hurricane (Franklin *et al.*, 2000). Comparing these wind profiles with our criteria defined in the previous section, reveals that whereas **C1**, **C3**, and **C4** are not fulfilled, the wind speed is however > 7 m s^{-1} in the high troposphere (**C2**). Wind directions are rather homogeneous along the entire tropospheric column with an azimuth between N315 and N35, with strongest winds up to 22 m s^{-1} in the low to mid-troposphere. These conditions are likely to promote a southward dispersion of the volcanic products. As each wind profile presents the state of the atmosphere for one hour (temporal resolution of ERA5) and as the Bellefontaine eruption lasted for approximately 2 hours, each simulation was made using as HAZMAP input half of the total erupted volume of the Bellefontaine eruption (i.e., 2.3 × 10^{11} kg). The lack of pronounced grading in the deposits (the grain sizes are broadly homogeneous throughout the deposit thickness) is consistent with the hypothesis of a sta-
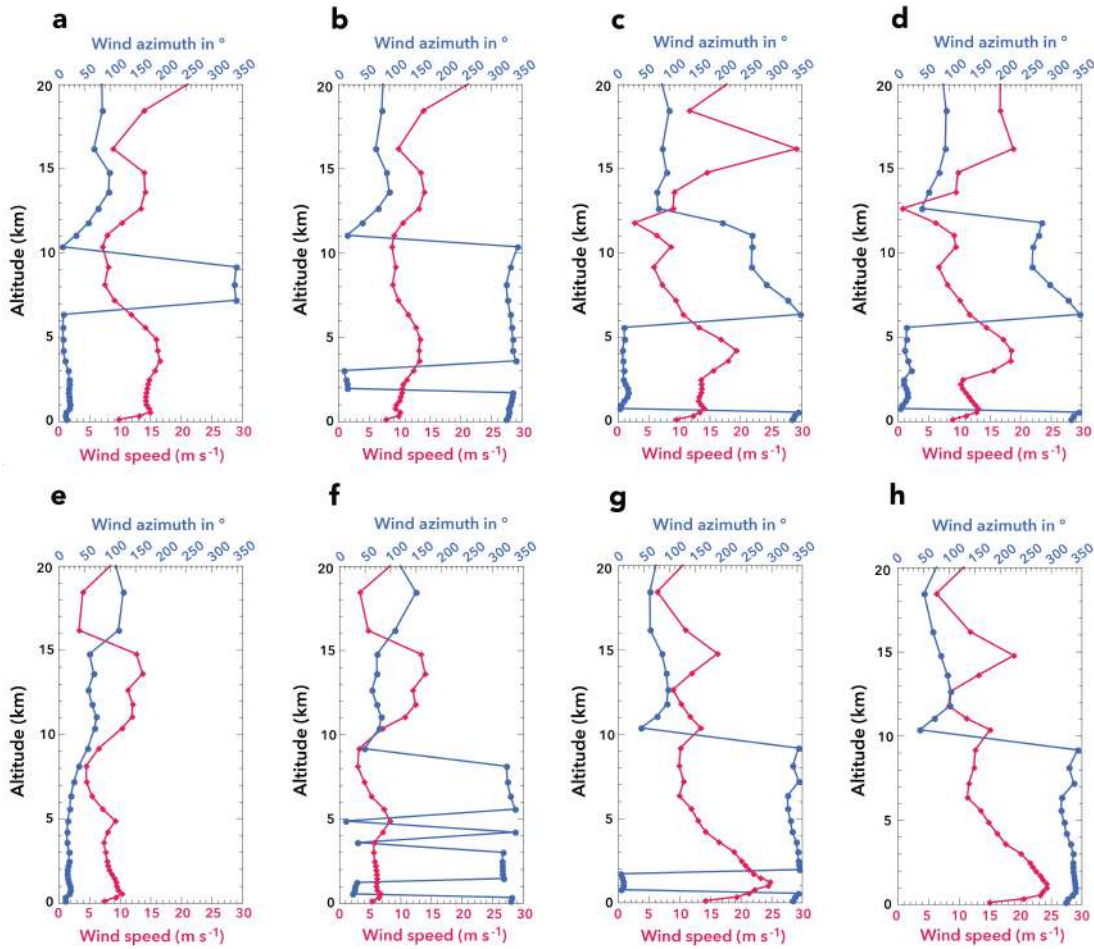
Figure 9: Wind profiles used for HAZMAP simulations shown in Figure 10. Two simulations were made for each hurricane, using **a** August 29, 1979, 12 pm UTC and **b**, August 29, 1979, 1 pm UTC for the hurricane David; **c** September 17, 1989, 2 pm UTC and **d** September 17, 1989, 3 pm UTC for the hurricane Hugo; **e** September 14, 1995, 3 pm UTC and **f** September 14, 1995, 4 pm UTC for the hurricane Marilyn; and **g** September 18, 2017, 3 pm UTC and **h** September 18, 2017, 4 pm UTC for the hurricane Maria.

ble mass discharge rate during the entire eruption, which makes this approximation valid. Other volcanic input parameters are the same as described in Section 2.2.1.

Figure 10 shows the isopach map obtained for each hurricane by adding the two simu-lations consecutive in time. The model predicts a southward dispersal axis for hurricanes David (Figure 10a), Hugo (Figure 10b), and Maria (Figure 10d), while the simulations for hurricane Marilyn (Figure 10c) result in a main dispersal axis oriented to the southwest. This difference can be explained by the N13-N23 oriented low tropospheric winds (< 2 km) of hurricane Marilyn (at 4 pm UTC, Figure 9e). A similar orientation (N13-N22) can be observed for hurricane David (12 pm UTC, Figure 9 a) but the prevailing orientation arising from these low tropospheric winds was counterbalanced by northerly winds (N345-N348) in the higher tropospheric layers (from 7 to 9 kilometers), thus resulting in a southward dis-persal axis. Similar N315 to N360 winds are systematically observed for hurricanes David, Hugo and Maria, either in the low, mid- or high troposphere (Figure 9a, b, c, d, g and h). As in the previous section, this N315-N360 orientation is thus the main criterion to obtain a southward dispersal axis. Finally, hurricane Georges displays a main southeastward dis-persal axis (thus not consistent with the Bellefontaine dispersion axis) in response to low
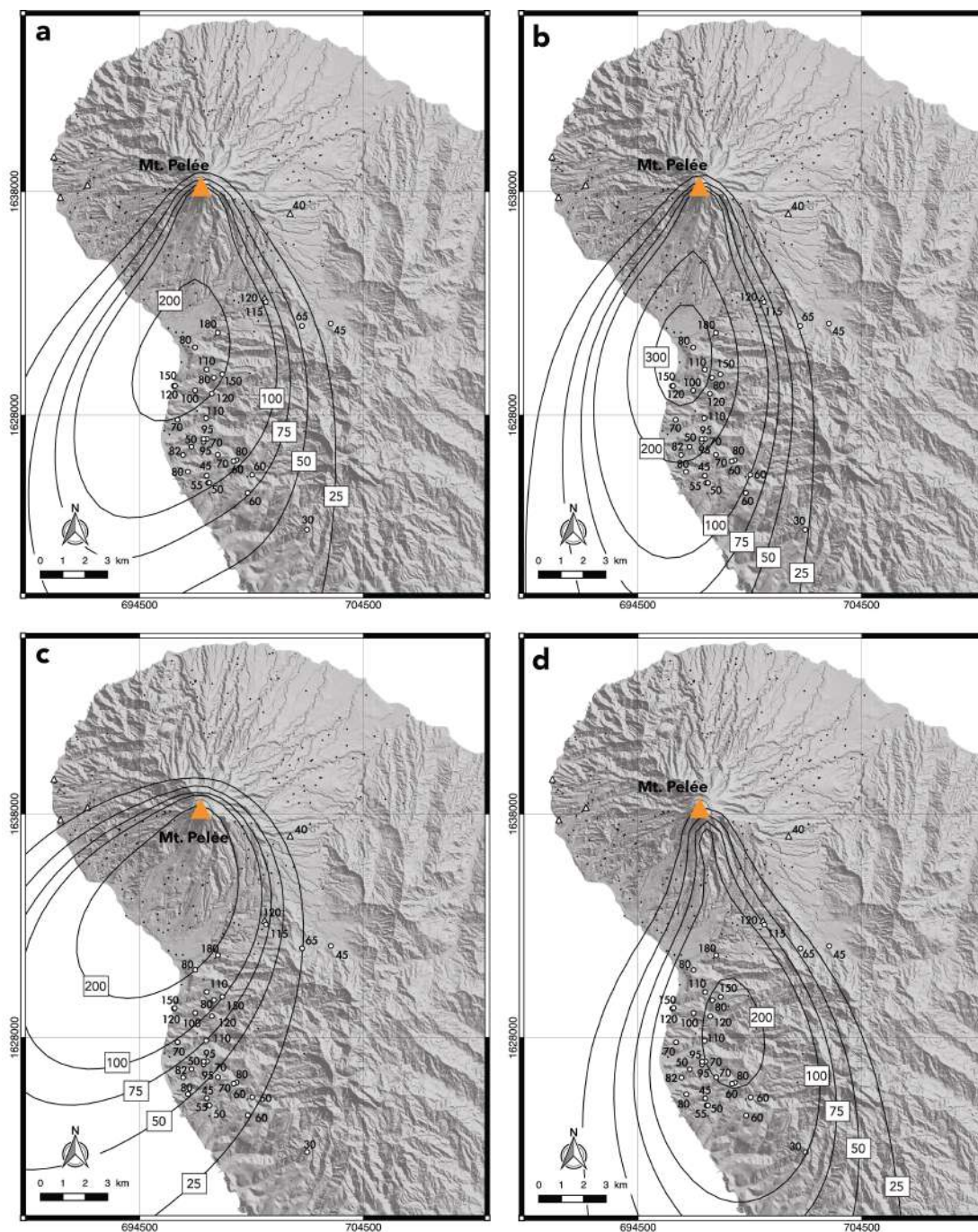
Figure 10: Isopach maps (in centimeters) from HAZMAP simulations for **a** hurricane David in 1979; **b** hurricane Hugo in 1989; **c** hurricane Marilyn in 1995; and **d** hurricane Maria in 2017. The wind profiles used for these simulations are shown in Figure 9.

tropospheric winds oriented N278 to N288.

   The main southward dispersal axis is retrieved from these hurricane simulations (Figure 10), but some differences can be noted when compared to the Bellefontaine isopach map inferred from field data (Chapter 2, Figure 5b). In the first place, the dispersion induced by the hurricanes appears more elongated than in the Bellefontaine case, and the thicknesses do not match those measured in the field (especially on the eastern flanks of the volcano). This difference could be due to strong winds present within the entire tropospheric column

during the hurricanes. In the second place, an interesting feature is that the maximum thickness is shifted from the vent for hurricanes David (Figure 10a), Hugo (Figure 10b) and Maria (Figure 10d). Such a pattern was never observed at Mount Pelée volcano, and could be a response to the change in wind speed noted between 3 to 5 km of altitude for hurricanes David and Hugo (Figure 9a, b, c and d), and between 0 and 2 km of altitude for hurricane Maria (Figure 9g and h).

We can thus conclude that a hurricane passing to the north of Martinique can indeed produce northerly winds. However, it remains difficult to prove convincingly that a hurricane can explain the dispersion of the Bellefontaine products, mainly because of the simulated maximum thickness shifted from the vent, and because the elongated isopachs produced are significantly different from the Bellefontaine deposit pattern measured in the field.

4.3 Dispersion of the Balisier deposits

Our simulations for the Bellefontaine eruption showed that northerly winds are possible in Martinique and can explain the dispersal axis of all the newly discovered eruptions (Bellefontaine, Balisier, Carbet and Etoile) at Mount Pelée. We now test these northerly winds on the Balisier eruption by simulating the dispersal of the co-PDC products, in order to test the maximum column height of 13 km estimated in Chapter 2, Section 3.3.
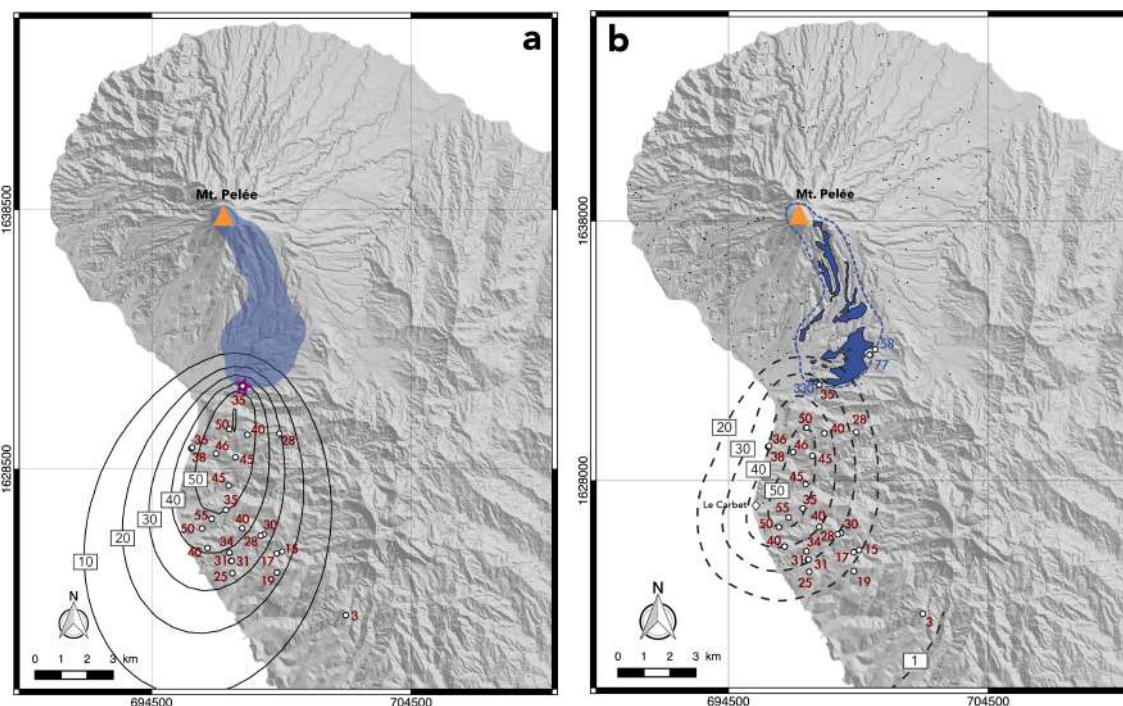

Figure 11: a Isopach map (in centimeters) from the best-fit HAZMAP simulation for the Balisier eruption, compared with the thicknesses (in centimeters) measured in the field. Location of the eruptive source given as an input for HAZMAP is shown by the purple star, corresponding to the Mont Parnasse section in Chapter 1, Section 4.1.1. The blue patch represents the extrapolated global extent of the PDC deposits (see Chapter 2, Section 2.2.2). The wind profile used for this simulation is described in the main text. **b** Isopach map (in centimeters) determined from field measurements and presented in Chapter 2, given for comparison.

We performed 40 simulations by varying the maximum column height from 2 to 16 km, and wind profile with a maximum speed ranging from 1 to 16 m s^{-1}. As the results strongly depend on lower tropospheric wind speeds (Figure 5), we chose a constant wind

speed throughout the entire atmospheric column (from 0 to 20 km-high), and a constant azimuth of N13 for the sake of simplicity. Figure 11a shows the best-fit simulation obtained for a wind speed of 1.5 m s^{-1} and a maximum column height of 13 km (corresponding to the estimated one in Chapter 2), and for which the simulated isopachs are consistent with the thicknesses measured in the field.

We note that the "peanut-shape" of the isopachs inferred from field data (Figure 11b) is not reproduced by our HAZMAP simulations nor is the shift in maximum thickness from the source (represented by the purple star in Figure 11a). Moreover, our simulations produce a small 60-cm isopach, which is greater than the maximum thickness measured in the field. We suggest that the strong erosion processes occurring on tropical islands such as Martinique could explain this difference, especially for an event that took place 14 ka ago.

Our maximum column height is estimated from the MDR feeding the co-PDC plume, which strongly depends on the elutriation factor that we measured at 25% (see Chapter 2, Section 3.3). Assuming a lower (10%) or higher (40%) elutriation factor gives a source MDR for the co-PDC plume of 1 or 4 $\times$ 10^7 kg s^{-1}, corresponding to a co-PDC plume height of about 9 or 16 km, respectively (Woods & Wohletz, 1991). We thus performed two simulations to investigate the effect of this critical parameter on tephra dispersal for the Balisier eruption, whose results are given in Figure 12. We used the same constant wind profile as in Figure 11a, with an azimuth N13 and a speed of 1.5 m s^{-1}.
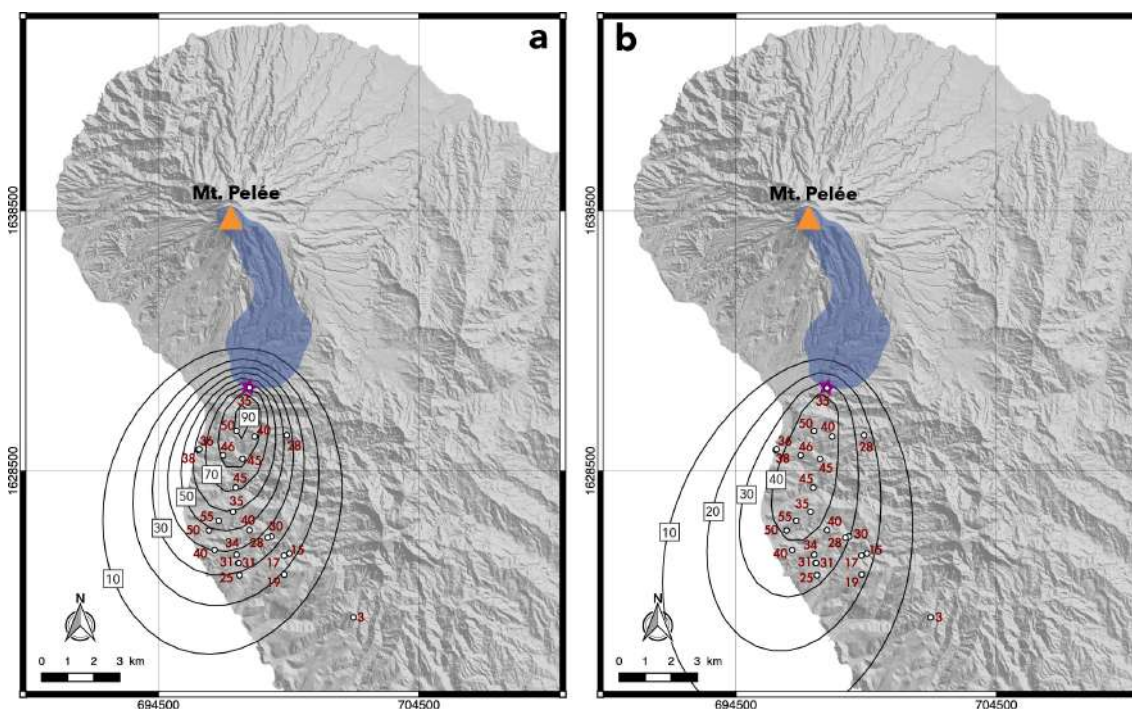

Figure 12: Isopach map (in centimeters) from HAZMAP simulations for the Balisier eruption, and considering a maximum column height of **a** 9 km and **b** 16 km. Location of the eruptive source given as an input for HAZMAP is shown by the purple star, corresponding to the Mont Parnasse section in Chapter 1, Section 4.1.1. The blue patch represents the extrapolated global extent of the PDC deposits (see Chapter 2, Section 2.2.2). The wind profile used for this simulation is described in the main text.

We observe that a maximum column height of 9 km (Figure 12a), produces more tightened isopachs with thicknesses ranging from 10 to 90 cm, much larger than those measured in the field. When considering a maximum column height of 16 km (Figure 12b), the simulated isopachs are more elongated and the maximum thickness is too small (40 cm) compared

to observations (55 cm). Both of these maximum column heights, when considering weak tropospheric winds of 1.5 m s^{-1}, are thus not consistent with our field data. We tested other wind profiles (characterized by higher wind speed and/or a reversal in wind direction), but none of them allowed to reproduce the isopachs inferred from thicknesses measured in the field.

These results could be enlarged by performing a full probabilistic calculation in which we could test more precise wind profiles together with a larger range of maximum column heights, TGSD, and volume (as in Bonadonna *et al.* 2002); but such work is beyond the scope of this study. Overall, these results show that a 13-km high co-PDC plume (along with weak northerly winds) can produce isopachs consistent with our field observations, which reinforce the confidence in our estimated value.
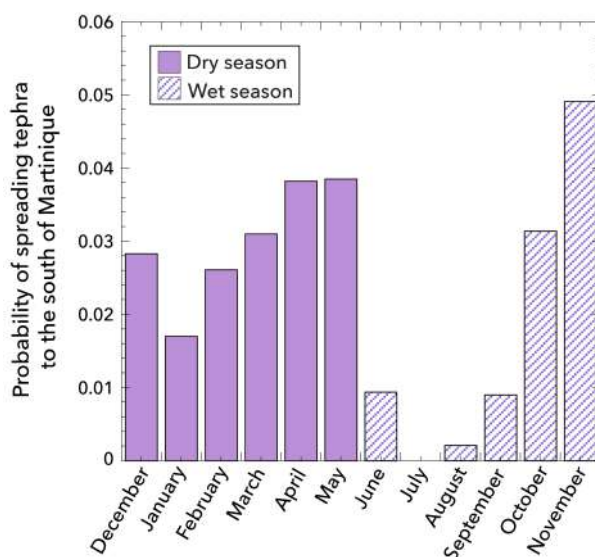
5   Impact of wind on volcanic hazard assessment

Figure 13: Monthly distribution of the probability to reach wind conditions consistent with the Bellefontaine eruption tephra dispersal axis.

In many volcanic hazard studies using tephra dispersion models, the impact of wind is investigated by considering mean wind profiles typically averaged over a season (Komorowski *et al.*, 2008; Lindsay & Robertson, 2018). This may be taken as a valid assumption for most eruptions in the Lesser Antilles as the trade and anti-trade winds are considered to enforce a largely invariable regime, especially during the dry season (from December to May). However, we show in this study that for both the Bellefontaine and the Balisier eruptions, considering a mean wind profile cannot reproduce the dispersion deposits as they are found in the field (Figures 4 and 5). While exploring the 1979-2017 ERA-Interim dataset to estimate the number of occurrences of wind configuration that could have produced tephra deposits similar to those observed for the Bellefontaine eruption, we noticed that although the trade wind regime is ubiquitous, exceptional circumstances indeed exist and need to be taken into account. Contrary to the dry season during which the wind directions are remarkably stable, they are quite variable during the wet season, i.e. from June to November (Figure 3a and b). The wind speed also remains uniform in the troposphere during the dry season, whereas it fluctuates during the wet season. Above 20 km, the wind speed can
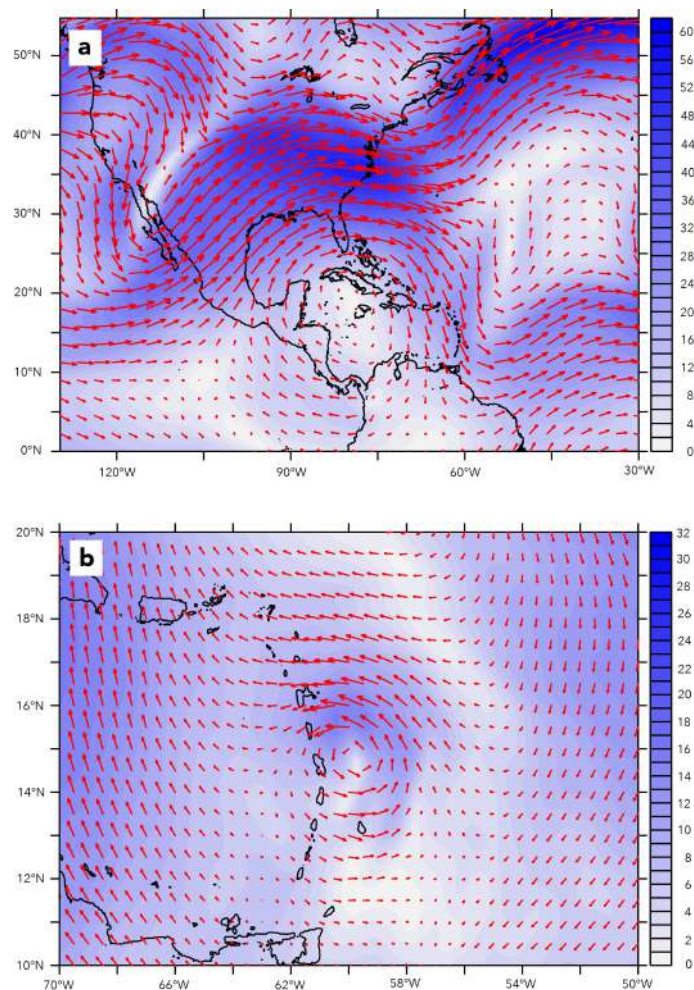
Figure 14: Atmospheric circulation in the high troposphere (i.e., from 7 to 18 km of altitude) described by wind vectors (red arrows) and speed (colored gradient in $\mathrm{m\,s^{-1}}$) **a** for a Bellefontaine-like configuration on November 27, 1996 at 6 pm UTC (see Section 4.1) and **b** during the hurricane Maria at 3 pm UTC (see Section 4.2). These data are extracted from the ERA-Interim database (for November 27, 1996) and from the ERA5 database (for the hurricane Maria).

strongly vary during the whole year. These results can explain the discrepancy between the simulations presented in Figure 4a and b, and our field measurements.

Applying the four criteria required to produce Bellefontaine-like dispersion axes (described in Section 4.1) on our complete ERA-Interim wind database (1979-2017), we have detected 1,327 (out of 56,984 cases) northerly wind profiles blowing over Martinique that could have produced southward deposit dispersion similar to the Bellefontaine eruption. We thus calculate that the monthly probability of spreading tephra to the south of the island including the city of Fort-de-France lies between 0 and 5% during the wet season, and between 2 and 4% during the dry season (Figure 13). We note that there is a non-negligible probability of spreading tephra towards the south of Martinique during most part of the year, and that the highest probabilities correspond to seasonal transitions in November (4.7%) and May (3.8%). One can note that northerly winds due to a hurricane passing by Martinique can be hidden in the wind profiles likely to reproduce the Bellefontaine deposit dispersion during the wet season. Our results however strongly support that most of the northerly winds (99.9%) are the result of a particular atmospheric circulation lasting between $\approx$ 6h and $\approx$ 3 days.

The atmospheric pattern linked to Bellefontaine-like events (Section 4.1) is indeed a result of a peculiar situation wherein the path of the subtropical jet-stream is spitted into two branches: a northern branch flowing from the West to the East (standard behavior), and a southern branch meandering toward the South before flowing to the East (Figure 14a). Reasons leading to this change are beyond the scope of this study, but the common feature seems to be a drifting to the North (> 30°N latitude) of the high/low-pressure zone at the surface/tropopause in the central Atlantic Ocean. In contrast, a hurricane is a transient and local system (Figure 14b), and thus, the chance of it passing close enough to Martinique, along an appropriate path, during an eruption is less probable than northerly winds such as those presented in Section 4.1. This probability should nonetheless be taken into account into a future multi-hazard assessment in Martinique.

These results highlight the scarcity of the cases in Martinique yielding Bellefontaine-like southward tephra dispersion. The Bellefontaine, Carbet and Etoile events are, however, the proof that such a scenario (impacting half of the island) remains possible for future eruptions in Martinique as well as other Caribbean volcanoes (e.g., Brazier *et al.* 1982; Poret *et al.* 2017; Poulidis *et al.* 2018). Such wind conditions are of crucial importance for hazard assessment as our HAZMAP calculations show that a Bellefontaine-like eruption would spread over 2 cm of ash on the city of Fort-de-France, a situation not currently represented on the hazard map (Stieltjes & Mirgon 1998, see Introduction, Figure 7). Moreover, Fort-de-France and its surrounding area are densely populated (more than 123,000 inhabitants), which increase their vulnerability – and therefore the volcanic risk – to a future eruption. We thus conclude that models must include the daily variability of wind profiles instead of using season-averaged ones to depict volcanic hazard and risk in Martinique (and in other similar settings) more accurately.

6   Conclusion

In this chapter, we investigated the unusual southward dispersion of all the newly discovered eruptions in Martinique: the Bellefontaine, Balisier, Carbet and Etoile events, by using the 2D HAZMAP model. Simulations of tephra dispersion using the HAZMAP model suggest that the Bellefontaine eruption (and thus the Balisier, Carbet and Etoile events) probably did not occur during a hurricane, but rather under weak northerlies in upper troposphere (7-18 km) occasionally measured over Martinique, and could have spread volcanic tephra as far as the city of Fort-de-France. We also demonstrated that the distribution of the co-PDC deposits from the Balisier eruption can be explained by a 13-km high plume rising under weak northerly winds, which is consistent with our estimated value based on an elutriation factor of 25%.

These findings identify a major caveat when using mean seasonal wind profiles, which provide information about the most probable case only, to assess hazard-prone areas with a high degree of confidence. To improve volcanic disaster forecasting, especially in regions like small tropical islands, the daily variability of winds in terms of speed and direction must be taken into account. In the following chapter, we refine the volcanic hazard assessment for tephra fallout in Martinique by accounting for a more detailed wind variability.

References

Armienti, P., Macedonio, G. & Pareschi, M.T. 1988 A numerical model for simulation of tephra transport and deposition: Application to May 18, 1980, Mount St. Helens eruption. *J. Geophys. Res.*

93 (B6), 6463–6476.

BONADONNA, C., MAYBERRY, G.C., CALDER, E.S., SPARKS, R.S.J., CHOUX, C., JACKSON, P., LEJEUNE, A.M., LOUGHLIN, S.C., NORTON, G.E., ROSE, W.I., RYAN, G. & YOUNG, S.R. 2002 Tephra fallout in the eruption of Soufriere Hills Volcano, Montserrat. In *The Eruption of Soufriere Hills Volcano, Montserrat from 1995 to 1999* (ed. T.H. Druitt & B.P. Kokelaar), pp. 483–516. Geological Society, London, Memoirs.

BONASIA, R., CAPRA, L., COSTA, A., MACEDONIO, G. & SAUCEDO, R. 2011 Tephra fallout hazard assessment for a Plinian eruption scenario at Volcán de Colima (Mexico). *J. Volcanol. Geotherm. Res.* **203**, 12–22.

BONASIA, R., COSTA, A., FOLCH, A., MACEDONIO, G. & CAPRA, L. 2012 Numerical simulation of tephra transport and deposition of the 1982 El Chichón eruption and implications for hazard assessment. *J. Volcanol. Geotherm. Res.* **231-232**, 39–49.

BRAZIER, S., DAVID, A.N., SIGURDSSON, H. & SPARKS, R.S.J. 1982 Fall-out and deposition of volcanic ash during the 1979 explosive eruption of the Soufriere of St. Vincent. *J. Volcanol. Geotherm. Res.* **14**, 335–359.

CARAZZO, G., TAIT, S. & KAMINSKI, E. 2019 Marginally stable recent Plinian eruptions of Mt. Pelée volcano (Lesser Antilles): The P2 AD 280 eruption. *Bull. Volcanol.* **81**, 1–17.

CARAZZO, G., TAIT, S., KAMINSKI, E. & GARDNER, J. E. 2012 The recent Plinian explosive activity of Mt. Pelée volcano (Lesser Antilles): The P1 AD 1300 eruption. *Bull. Volcanol.* **74**, 2187–2203.

COSTA, A., DELL'ERBA, F., VITO, M. A., ISAIA, R., MACEDONIO, G., ORSI, G. & PFEIFFER, T. 2009 Tephra fallout hazard assessment at the Campi Flegrei caldera (Italy). *Bull. Volcanol.* **71**, 259–273.

COSTA, A., MACEDONIO, G. & FOLCH, A. 2006 A three-dimensional Eulerian model for transport and deposition of volcanic ashes. *Earth Planet. Sci. Lett.* **241** (3-4), 634–647.

DEE, D. P., UPPALA, S. M., SIMMONS, A. J., BERRISFORD, P., POLI, P., KOBAYASHI, S., ANDRAE, U., BALMASEDA, M. A., BALSAMO, G., BAUER, P., BECHTOLD, P., BELJAARS, A. C.M., VAN DE BERG, L., BIDLOT, J., BORMANN, N., DELSOL, C., DRAGANI, R., FUENTES, M., GEER, A. J., HAIMBERGER, L., HEALY, S. B., HERSBACH, H., HÓLM, E. V., ISAKSEN, L., KÅLLBERG, P., KÖHLER, M., MATRICARDI, M., MCNALLY, A. P., MONGE-SANZ, B. M., MORCRETTE, J. J., PARK, B. K., PEUBEY, C., DE ROSNAY, P., TAVOLATO, C., THÉPAUT, J. N. & VITART, F. 2011 The ERA-Interim reanalysis: Configuration and performance of the data assimilation system. *Q. J. R. Meteorol. Soc.* **137**, 553–597.

DUNION, J.P. 2011 Rewriting the climatology of the tropical North Atlantic and Caribbean Sea atmosphere. *J. Clim.* **24**, 893–908.

FOLCH, A., COSTA, A. & MACEDONIO, G. 2009 FALL3D: A computational model for transport and deposition of volcanic ash. *Comput. Geosci.* **35**, 1334–1342.

FRANKLIN, J.L., BLACK, M.L. & VALDE, K. 2000 Eyewall wind profiles in hurricanes determined by GPS dropwindsondes. *Preprints 24th Conf. on Hurricanes and Tropical Meteorology, Amer. Meteor. Soc., Fort Lauderdale, FL* pp. 446–447.

HERSBACH, H., BELL, B., BERRISFORD, P., HORÁNYI, A., MUÑOZ SABATER, J., NICOLAS, J., RADU, R., SCHEPERS, D., SIMMONS, A., SOCI, C. & DEE, D. 2019 Global reanalysis: goodbye ERA-Interim, hello ERA5. *ECMWF Newslett.* **159**, 17–24.

KOMOROWSKI, J. C., LEGENDRE, Y., CARON, B. & BOUDON, G. 2008 Reconstruction and analysis of sub-plinian tephra dispersal during the 1530 A.D. Soufriere (Guadeloupe) eruption: Implications for scenario definition and hazards assessment. *J. Volcanol. Geotherm. Res.* **178**, 491–515.

KOSSIN, J.P., CAMARGO, S.J. & SITKOWSKI, M. 2010 Climate modulation of North Atlantic hurricane tracks. *J. Climate* **23**, 3057–3076.

LACROIX, A. 1904 *La Montagne Pelée et ses éruptions*. Masson, Paris.

References

Landsea, C.W. & Franklin, J.L. 2013 Atlantic hurricane database uncertainty and presentation of a new database format. *Mon. Weather Rev.* **141**, 3576–3592.

Lindsay, J.M. & Robertson, R.E.A. 2018 Integrating Volcanic Hazard Data in a Systematic Approach to Develop Volcanic Hazard Maps in the Lesser Antilles. *Frontiers in Earth Science* **6** (42), 1–17.

Macedonio, G. & Costa, A. 2014 *HAZMAP-2.4.2: User Manual*. Istituto Nazionale di Geofisica e Vulcanologia (INGV).

Macedonio, G., Costa, A. & Folch, A. 2008 Ash fallout scenarios at Vesuvius: Numerical simulations and implications for hazard assessment. *J. Volcanol. Geotherm. Res.* **178** (3), 366–377.

Macedonio, G., Costa, A. & Longo, A. 2005 A computer model for volcanic ash fallout and assessment of subsequent hazard. *Comput. Geosci.* **31**, 837–845.

Macedonio, Giovanni, Costa, Antonio, Scollo, Simona & Neri, Augusto 2016 Effects of eruption source parameter variation and meteorological dataset on tephra fallout hazard assessment: Example from Vesuvius (Italy). *J. Appl. Volcanol.* **5** (1).

Macedonio, G., Pareschi, M.T. & Santacroce, R. 1988 A Numerical Simulation of the Plinian Fall Phase of 79 A.D. Eruption of Vesuvius. *J. Geophys. Res.* **93** (B12), 14817–14827.

Manzella, I., Bonadonna, C., Phillips, J.C. & Monnard, H. 2015 The role of gravitational instabilities in deposition of volcanic ash. *Geology* **43**, 211–214.

Michaud-Dubuy, A., Carazzo, G., Tait, S., Le Hir, G., Fluteau, F. & Kaminski, E. 2019 Impact of wind direction variability on hazard assessment in Martinique (Lesser Antilles): The example of the 13.5 ka cal BP Bellefontaine Plinian eruption of Mount Pelée volcano. *J. Volcanol. Geotherm. Res.* **381**, 193–208.

Murakami, H. 2014 Tropical cyclones in reanalysis data sets. *Geophys. Res. Lett.* **41**, 2133–2141.

Perret, F.A. 1937 *The Eruption of Mt. Pelée 1929-1932*. Carnegie Institution of Washington.

Pfeiffer, T., Costa, A. & Macedonio, G. 2005 A model for the numerical simulation of tephra fall deposits. *J. Volcanol. Geotherm. Res.* **140** (4), 273–294.

Poret, M., Costa, A., Folch, A. & Martí, A. 2017 Modelling tephra dispersal and ash aggregation: The 26th April 1979 eruption, La Soufrière St. Vincent. *J. Volcanol. Geotherm. Res.* **347**, 207–220.

Poulidis, A.P., Phillips, J.C., Renfrew, I.A., Barclay, J., Hogg, A., Jenkins, S.F., Robertson, R. & Pyle, D.M. 2018 Meteorological controls on local and regional volcanic ash dispersal. *Scientif. Rep.* **8** (6873).

Roobol, M.J. & Smith, A.L. 1976 Mount Pelée, Martinique: A pattern of alternating eruptive styles. *Geology* **4**, 521–524.

Stieltjes, L. & Mirgon, C. 1998 Approche méthodologique de la vulnérabilité aux phénomènes volcaniques : Test d'application sur les réseaux de la Martinique. In *Unpublished Internal Report No. R40098*. Bureau de Recherches Géologiques et Minières, Marseille.

Suzuki, T. 1983 A Theoretical Model for Dispersion of Tephra. In *Arc Volcanism: Physics and Tectonics*, pp. 95–113. Terra Scientific Publishing Company (TERRAPUB), Tokyo.

Traineau, H., Westercamp, D., Bardintzeff, J. M. & Miskovsky, J. C. 1989 The recent pumice eruptions of Mt. Pelée volcano, Martinique. Part I: Depositional sequences, description of pumiceous deposits. *J. Volcanol. Geotherm. Res.* **38**, 17–33.

Watt, S.F.L., Gilbert, J.S., Folch, A., Phillips, J.C. & Cai, X.M. 2015 An example of enhanced tephra deposition driven by topographically induced atmospheric turbulence. *Bull. Volcanol.* **77** (35).

Westercamp, D. & Traineau, H. 1983 The past 5,000 years of volcanic activity at Mt. Pelée Martinique (F.W.I.): Implications for assessment of volcanic hazards. *J. Volcanol. Geotherm. Res.* **17**, 159–185.

Woods, A. W. & Wohletz, K. 1991 Dimensions and dynamics of co-ignimbrite eruption columns. *Nature* **350**, 225–227.

Chapter 6

Refined hazard maps for tephra fallout in Martinique

Table of contents

Résumé du chapitre 6

Nous avons vu dans les chapitres précédents que l'histoire éruptive de la montagne Pelée est bien plus riche que nous ne le pensions auparavant, et que la dynamique d'une éruption explosive dépend fortement des paramètres éruptifs dont la distribution totale des tailles de grains, mais aussi des vents au moment de l'événement éruptif. La carte d'aléa volcanique pour les retombées de cendres en Martinique construite par Stieltjes & Mirgon (1998) et utilisée actuellement dans le plan ORSEC de gestion de crise s'appuie sur une histoire éruptive limitée à 5 000 ans. De plus, celle-ci ne prend pas en compte l'effet du vent sur la dispersion des cendres, mais seulement l'extension maximale des dépôts retrouvés sur le terrain en ignorant les processus d'érosion qui auront fait disparaître les dépôts les plus fins et les plus distaux. Dans ce chapitre, dédié à une première réévaluation de l'aléa volcanique en Martinique, nous utilisons le modèle 2D HAZMAP de dispersion des produits volcaniques pour construire une nouvelle carte d'aléa pour les retombées de cendres en Martinique en considérant les éruptions pliniennes passées de la montagne Pelée depuis 24 000 ans, ainsi que la variabilité des vents.

Nous proposons une méthode basée sur la considération de 16 scénarii éruptifs, cohérents avec les éruptions passées de la montagne Pelée. Chaque scénario considère une masse de dépôts et un flux de masse, et possède une probabilité d'occurrence en fonction de l'histoire éruptive de la montagne Pelée déterminée en Chapitre 1. Grâce à la base de données de vents ERA-Interim (présentée dans le chapitre précédent), nous considérons la variabilité des vents saisonnière puis mensuelle.

Notre première série de résultats, considérant chacun de ces 16 scénarii avec deux profils de vents moyens saisonniers (approche classique pour l'estimation de l'aléa volcanique), montrent que ces profils lissent la variabilité des vents ce qui a un impact sur la caractérisation de l'aléa volcanique, confirmant donc les conclusions du Chapitre 5. Notre seconde série de résultats, basée sur les mêmes 16 scénarii éruptifs mais considérant cette fois la variabilité mensuelle des vents, montre des changements importants dans la carte d'aléa obtenue. Ces changements concernent principalement la partie sud de l'île de la Martinique qui était jusqu'à présent considérée comme sécurisée mais qui pourrait être menacée par des vents venant du NNO dans la haute troposphère, principalement durant la saison sèche (de décembre à mai).

La carte d'aléa volcanique pour les retombées pliniennes obtenue à la fin de cette étude, et combinant les cartes mensuelles d'aléa, est basée sur des épaisseurs de dépôts ou sur des charges de dépôts (en $\mathrm{kg\,m^{-2}}$). Afin de faciliter sa lecture pour les autorités compétentes en gestion de crise, nous la combinons avec des seuils critiques d'épaisseurs de dépôts déterminés dans la littérature, et obtenons une carte affichant seulement 4 niveaux de couleurs, chacun associé à un degré d'endommagement potentiel des bâtis ou des réseaux de communication. Cette étude n'est qu'une première étape dans la réévaluation de l'aléa volcanique à la Martinique mais permet de proposer une nouvelle carte d'aléa intégrant tous les aléas volcaniques connus en Martinique. Dans le futur, il sera nécessaire de considérer la variabilité journalière des vents afin de produire des cartes probabilistes.

1   Introduction

We saw in previous chapters that the contribution of Plinian eruptions to the past eruptive history of Mount Pelée volcano is much richer than previously thought (Chapters 1 and 2), and that the eruption dynamics strongly depends on total grain-size distribution (TGSD, Chapter 3) and winds blowing during the eruption (Chapters 4 and 5). This chapter is dedicated to the production of a refined volcanic hazard assessment in Martinique using the 2D HAZMAP model described in the previous chapter. Considering past Plinian eruptions at Mount Pelée volcano as well as wind variability over Martinique allows us to build a new hazard map for tephra fallout that can be compared to the actual one. This work paves the way for an improved integrated volcanic hazard map in Martinique.

First, we present previous studies on volcanic hazard assessment in Martinique and discuss the caveats of their results. Then, we describe the method used to identify reference volcanic scenarii based on past Plinian eruptions at Mount Pelée volcano, later used to provide input parameters for the HAZMAP model. A first set of results is obtained by using the classical approach for volcanic hazard assessment related to tephra fallout (i.e., using mean seasonal wind profiles), then we present the improved predictions obtained when using a refined method accounting for the monthly variability of winds. Finally, we compare the newly obtained hazard map for tephra fallout with the one used in the current evacuation plan (ORSEC, Organisation de la réponse de la sécurité civile) by using relationships between deposit thickness, tephra mass load and their impact on infrastructures. We also investigate what future steps must be taken to move forward towards a new integrated volcanic hazard map, which would be of essential necessity in case of a future eruption at Mount Pelée volcano.

2   Current volcanic hazard assessment in Martinique

Mount Pelée is one of the most active volcanoes in the Lesser Antilles arc with more than 34 magmatic events in the last 24,000 years (Chapter 1), including the deadliest eruption of the XXe century in 1902 (see Introduction). Our field study revealed that all eruptive magmatic events (Pelean and Plinian) occurring at Mount Pelée volcano could result into tephra dispersal towards the south of Martinique, where most of the population lives. Today, about 400,000 people live in Martinique and are thus more or less threatened by volcanic hazards, making crucial the improvement of volcanic hazard assessment (and consequently risk assessment).

During the last few decades, various approaches have been proposed to improve the management of volcanic crisis. Traditionally, volcanic hazard assessment for tephra fallout was based on volcano monitoring and geological records (Baker, 1985; Houghton *et al.*, 1987; Stieltjes & Mirgon, 1998; Newhall & Hoblitt, 2002; Orsi *et al.*, 2004; Macías *et al.*, 2008). This method may be sufficient for volcanic environments where only a few information are available on the past eruptive history of the volcano, but it can often hide crucial informations about the weakest (and more frequent) events as their deposits are rapidly eroded or buried beneath those of more voluminous eruptions.

Since the 1990's, GIS (Geographic Information System) tools and numerical simulations allow to quantify volcanic hazard with a much better precision. Numerical modeling, together with field studies, indeed allows to explore much wider range of possible scenarii (Bonadonna *et al.*, 2002). Previous studies focused on either one eruptive scenario (usually

the largest one or the more likely to happen within a given time window) along with a large set a wind profiles (Komorowski *et al.*, 2008; Bonasia *et al.*, 2011), or considered instead one or several eruptive scenarii together with a single wind profile (commonly averaged over a season or estimated to be the most probable one, Barberi *et al.* 1992). The best (and widely used) method most likely consists in considering several eruptive scenarii along with a wide set of wind profiles (Cioni *et al.*, 2003; Bonadonna *et al.*, 2005; Macedonio *et al.*, 2008; Costa *et al.*, 2009; Bonasia *et al.*, 2012). The results of these studies take generally the form of probabilistical maps, showing probabilities of reaching a tephra loading (in $\mathrm{kg\,m^{-2}}$) greater than a given threshold.

In Martinique, the current volcanic hazard map used in the ORSEC plan (Introduction, Figure 7) was built by Stieltjes & Mirgon (1998). To produce it, these authors mapped the hazard zoning of each volcanic phenomenon considered in Martinique (i.e., tephra fallout, pyroclastic flows, lava intrusions/flows, gas emissions, lahars, landslides, and tsunamis), by using "exposure" matrices. These matrices combine both the intensity (I) and the frequency (F) of each volcanic phenomenon over the entire area exposed to it. Five classes of intensity and frequency are proposed by Stieltjes & Mirgon (1998), from I0/F0 for the lowest one to I4/F4 for the highest one, based on the past eruptive history of the Mount Pelée volcano known at that time (i.e., the last 5,000 years; Westercamp & Traineau 1983). Seven hazard zoning maps were created, one for each of the seven volcanic phenomenon considered, and combined into the final integrated volcanic hazard map (Introduction, Figure 7).

As the final goal of this work is to re-assess the tephra fallout hazard in Martinique, we only describe in detail the current hazard map for tephra fallout produced by Stieltjes & Mirgon (1998) and presented in Figure 1. Four classes of intensity (from I0, very low to non-existent, to I4, very high) and one class of frequency are taken into account into this map; the color scale thus depends on the product I $\times$ F defining five levels of exposure to tephra fallout hazard. Figure 1 shows that the northern part of the island is the most exposed to tephra fallout, and that the exposure level decreases with the distance from the Mount Pelée summit. The southern half of Martinique is considered to be safe, as the exposure level is null (white color) beyond the Lamentin plain.

This map was built on the eruptive history determined by Westercamp & Traineau (1983) for the last 5,000 years, and thus on the maximum extent of Plinian deposits found in the field. As the erosion processes are strongly active in tropical islands such as Martinique, much of the finest deposits must have long disappeared and thus reduced this maximum extent. To produce a more precise hazard map for tephra fallout, one must take into account this lack of geological data. We propose in the following sections of this chapter to re-assess the tephra fallout hazard in Martinique by using the 2D HAZMAP model (described in Chapter 5) and thus to simulate tephra dispersion (including the finest particles) while taking into account the wind variability, another key parameter for volcanic hazard assessment (Michaud-Dubuy *et al.*, 2019). As this work is a preliminary one, we first use a deterministic approach instead of a probabilistic one, which would require a longer computing time.

3   Input parameters for HAZMAP

HAZMAP (Macedonio *et al.*, 2005) is a semi-analytical model solving the advection-diffusion-sedimentation equation for volcanic tephra now commonly used for volcanic hazard assessment. Two sets of input parameters are required to run the simulations: eruptive source parameters and wind fields. A full description of the model is presented in Chapter 5, Section 2.
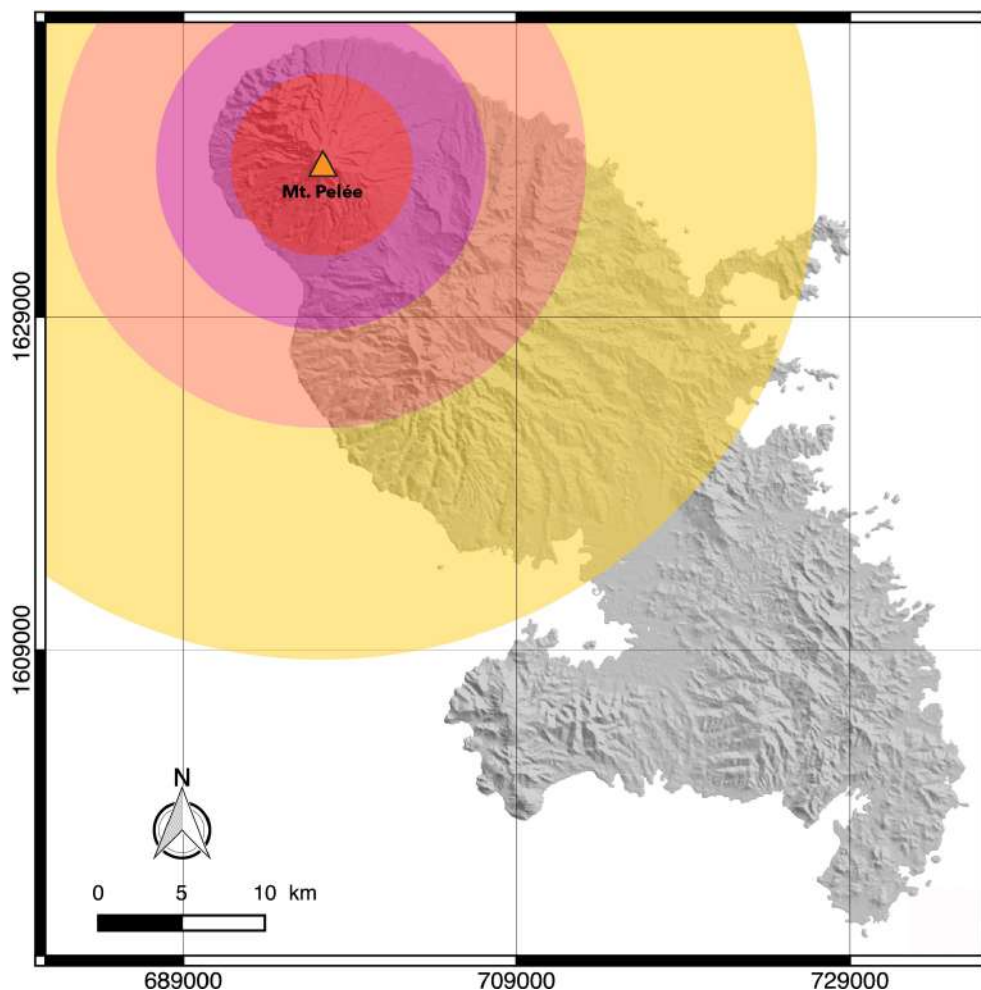
Figure 1: Hazard map for tephra fallout in Martinique, based on data from BRGM and built by Stieltjes & Mirgon (1998). Colors correspond to the exposure level with red: very high; pink: high; orange: intermediate; yellow: low; and white: very low to null. All maps were generated using the open source QGIS software. Coordinates are in WGS 84 − UTM Zone 20 system.

3.1   Volcanological parameters: matrix of correlation

As in Chapter 5, we use in all simulations a horizontal atmospheric diffusion coefficient set at 3,000 $m^2\,s^{-1}$, together with Suzuki parameters A = 4 and λ = 1. We further use a deposit density of 1,070 $kg\,m^{-3}$ to convert the mass loads in $kg\,m^{-2}$ given by HAZMAP into deposit thicknesses. In all simulations, the source location is the Mount Pelée summit, and we use the TGSD of the P1 eruption (Figure 7a in Carazzo *et al.* 2012). This TGSD is characterized by a power-law exponent D (Kaminski & Jaupart, 1998) of 3.2, a value consistent with almost all past Plinian eruptions at Mount Pelée volcano (see Table 3 in Chapter 2).

HAZMAP also requires volcanological inputs such as the total mass of deposits and the maximum height reached by the volcanic column. Based on our refined eruptive history of the volcano, we concluded in Chapter 2 (Section 4.2) that the most probable future eruptive scenarii in Martinique would be characterized by a mass discharge rate (MDR) comprised between $\sim 10^6$ and $\sim 10^8$ $kg\,s^{-1}$, and a volume ranging from ~ 0.01 to ~ 1 km^3 DRE. Such a volume range corresponds to a mass of deposits ranging from $\sim 10^{10}$ to $\sim 10^{12}$ kg. We translate these MDR and mass ranges into the matrix 4×4 presented in Table 1 showing

the 16 eruptive scenarii that are consistent with the past eruptive history of the Mount Pelée volcano and later used in our simulations. An eruptive scenario is thus defined by a MDR/Mass couple.

Table 1: Matrix of correlation used for the HAZMAP simulations, showing the relative probabilities of occurence of each eruptive scenario.

Log_{10} Mass / Log_{10} Flux	$10-10.5$	$10.5-11$	$11-11.5$	$11.5-12$
$7.5-8$	0.9 %	2.6 %	5.3 %	10.5 %
$7-7.5$	2.6 %	7 %	14 %	10.5 %
$6.5-7$	5.3 %	7 %	14 %	5.3 %
$6-6.5$	5.3 %	2.6 %	5.3 %	1.8 %

We then calculate the probability of each eruptive scenario based on several assumptions:

- The probability of scenarii characterized by a mass of deposits between 10^{11} and 10^{12} kg is twice the probability of cases between 10^{10} and 10^{11} kg, from our stratigraphical record (see Table 3 in Chapter 2).

- Following the general observation that MDR and total mass of deposits are positively correlated in Plinian eruptions, we set a lower probability for scenarii with high MDR/low total mass as well as those for scenarii with low MDR/high total mass, compared to scenarii characterized by a simultaneous increase or decrease in MDR and total mass.

- Finally, we set a higher probability for the scenarii that are closer to the P1/P2/Bellefontaine characteristics as they represent the most frequent eruptive scenario at Mount Pelée (see Figure 17 in Chapter 2).

The calculated probabilities of occurence for each of the 16 eruptive scenarii are reported in Table 1. Finally, as HAZMAP requires a maximum height reached by the volcanic column, we use the relations presented in Table 4 of Carazzo *et al.* (2008) for a tropical atmosphere to convert the MDR values shown in Table 1 into maximum heights. According to these authors' scaling law, a log(MDR) of $7.5-8$ gives a maximum height of ≈ 23.7 km, while a log(MDR) of $6-6.5$ corresponds to a maximum height of ≈ 13.5 km.

3.2 Wind profiles from ERA Interim

HAZMAP being used in its "deposit mode", it requires a given single wind profile including wind velocity components (u, v) as a function of altitude. As in Chapter 5, we use in all simulations wind velocity profiles based on the European Centre for Medium-Range Weather Forecasts ERA-Interim reanalysis (ERA-Interim) for the years 1979-2017 (Dee *et al.*, 2011). Note that this atmospheric reanalysis is now offline and no longer updated, and replaced by ERA5 (Hersbach *et al.*, 2019).

The initial content of ERA-Interim files consists of six-hourly global fields of zonal and meridional winds at a horizontal resolution of $0.75° \times 0.75°$ and vertically distributed on 37 pressure levels from 110 m to ≈ 48 km. These wind fields have been interpolated to match HAZMAP format by converting each of the 37 pressure levels into an altitude level using the altitude model in Chapter 5 (Figure 2). We calculate the wind components over

Martinique at each time step and each pressure level in an area ranging from 14.4°N to 14.8°N and from 60.8°W to 61.2°W. Our final dataset is thus composed of 56,984 vertical wind profiles from January 1979 to December 2017.

We first re-assess the tephra fallout hazard assessment in Martinique by using mean seasonal wind profiles, which is the classical approach in volcanic hazard assessment (Section 4.1). The oceanic tropical climate of Martinique can be splitted into two main seasons: the dry season extending from December to May, and the wet season extending from June to November (see Section 2.4 in Chapter 1). Figure 2a presents the wind profile averaged over the wet season, while Figure 2b corresponds to the dry season.
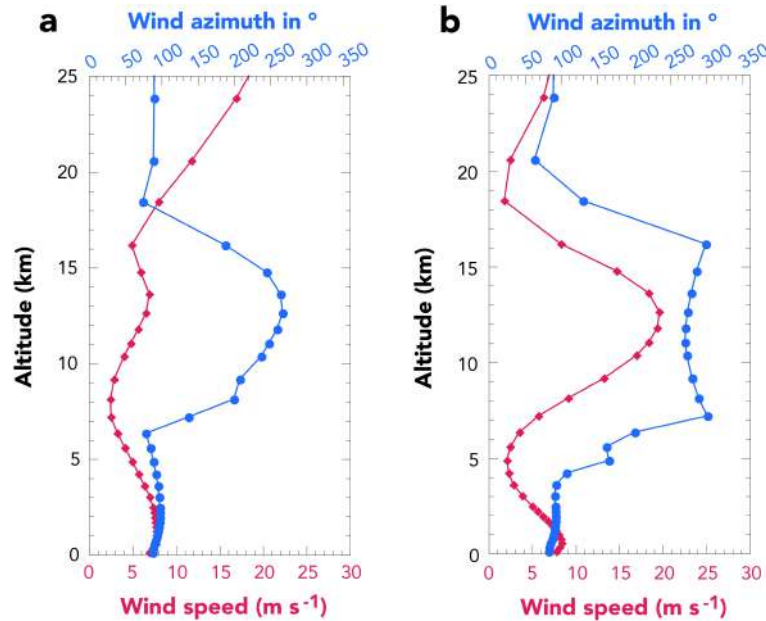

Figure 2: Seasonal average wind speed (pink) and azimuth (blue) profiles from the ERA-Interim dataset for **a** wet season and **b** dry season, used for the HAZMAP simulations in Section 4.1.

The averaged wind profile for the wet season is characterized by easterlies from the surface to ≈ 7 km with highest speed of 7.8 m s^{-1} at ≈ 1 km, and westerlies from ≈ 8.8 km to ≈ 15.3 km with wind speeds not exceeding 7 m s^{-1} at ≈ 13 km. In the stratosphere, wind blows from the east with speeds increasing from the tropopause (≈ 17 km) to > 25 km. During the dry season, the change in wind direction within the troposphere (from 0 to ≈ 17 km) occurs at a lower elevation (≈ 4.5 km), and westerlies within the upper troposphere become much faster, reaching a value of 20 m s^{-1} at ≈ 12 km.

We demonstrated in Chapter 5 (Michaud-Dubuy *et al.*, 2019) the paramount importance of taking into account the daily variability of winds in volcanic hazard assessment, as mean seasonal wind profiles represent the most probable case only and tend to hide less frequent wind orientation. To re-assess the tephra fallout hazard while accounting for the daily variability of winds would require a minimum of 5,840 simulations (365 days × 16 scenarii), and thus would take a considerable time. Here, we choose to test the monthly variability of winds, as a first step. Figure 3 and Figure 4 present the mean monthly wind profiles averaged over our entire 40-years ERA-Interim dataset and used in HAZMAP, for the wet season (June to November) and the dry season (December to May), respectively.

The lower troposphere (from the surface to ≈ 7 km) is characterized by constant easterlies throughout the wet season, with a maximum wind speed varying from ≈ 6 m s^{-1} in September (at 1 km of altitude, Figure 3d) to ≈ 10 m s^{-1} in July (at 4 km of altitude, Figure
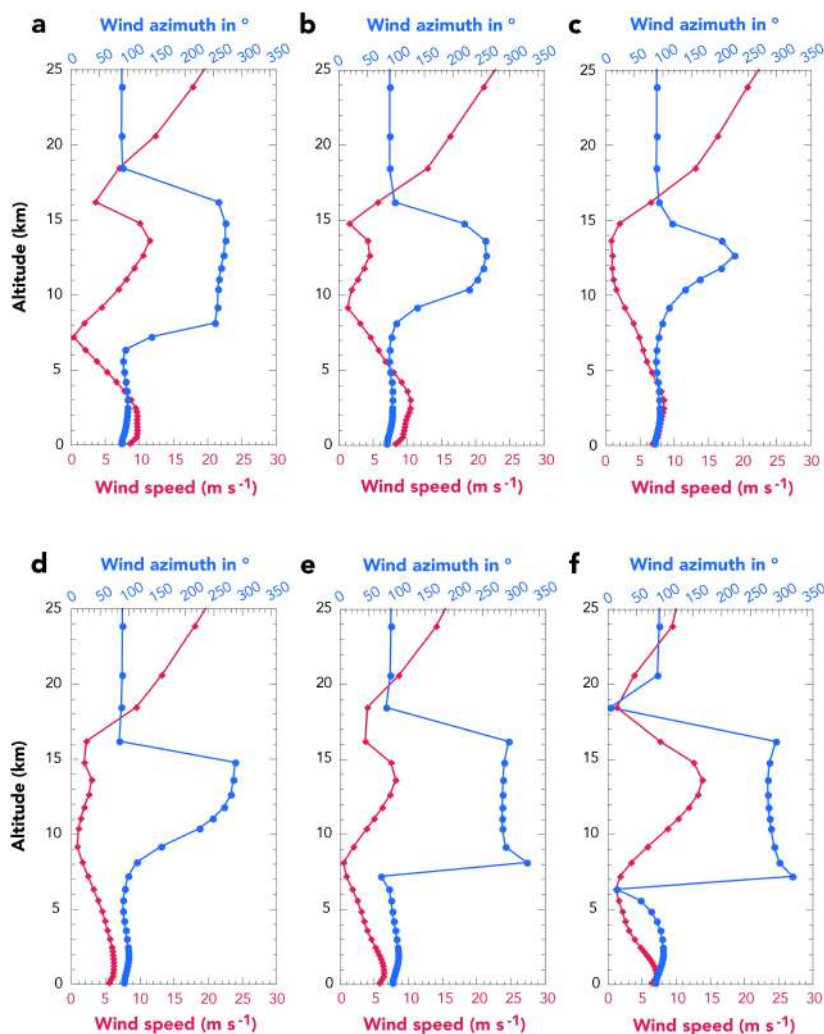
Figure 3: Monthly average wind speed (pink) and azimuth (blue) profiles from the ERA-Interim dataset for the wet season, with **a** June, **b** July, **c** August, **d** September, **e** October, and **f** November, used for the HAZMAP simulations in Section 4.2.

3b). Both wind speed and azimuth however strongly vary in the upper troposphere (from 7 to 17 km) throughout the wet season. Whereas wind mainly blows from the northwest in September, October and November (Figure 3d, e, and f), June, July and August are characterized by westerlies (Figure 3a, b, and c). Wind speed slighly increases (from $\approx 1-2$ m s^{-1} to $\approx 3-4$ m s^{-1}) in July, August and September (Figure 3b, c, and d), while wind speed can reach $12-14$ m s^{-1} in November (Figure 3f). In the stratosphere, wind blows from the east over the entire season, and wind speed strongly increases up to more than 20 m s^{-1} in June, July and August while it does not exceed 10 m s^{-1} in November (at ≈ 26 km). These stratospheric variations should not strongly influence tephra dispersal, as we saw in Chapter 5.

Tropospheric winds blowing during the dry season are much more stable than those blowing during the wet season (Figure 4). Esterlies blow in the lower troposphere (up to $4-6$ km) with a maximum wind speed reaching $8-9$ m s^{-1}, whereas the upper troposphere is characterized by strong westerlies with a maximum wind speed of $\approx 17-20$ m s^{-1}. In the stratosphere, wind blows from the east between the tropopause and up to > 25 km throughout the entire season; wind speed however varies depending on the month considered.
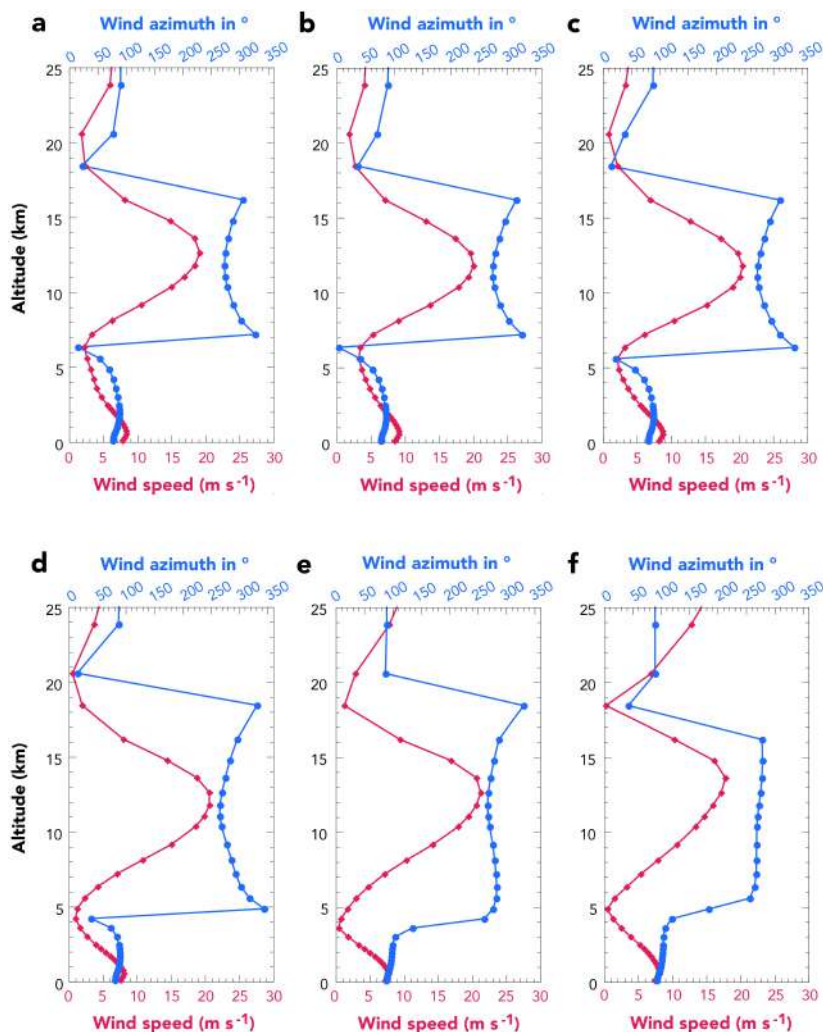
Figure 4: Monthly average wind speed (pink) and azimuth (blue) profiles from the ERA-Interim dataset for the dry season, with **a** December, **b** January, **c** February, **d** March, **e** April, and **f** May, used for the HAZMAP simulations in Section 4.2.

From December to March (Figure 4a, b, c, and d), wind speed slightly increases up to $\approx$ 5 m s^{-1} in the stratosphere, whereas April and May (Figure 4e, and f) are characterized by a wind speed strongly increasing from the tropopause to 25 km, with a maximum value reached in May ($\approx$ 12 m s^{-1}).

4 Results

4.1 Classical approach using mean seasonal wind profiles

4.1.1 Hazard maps for wet and dry seasons

We performed 32 simulations with the HAZMAP model, using the two mean seasonal wind profiles (Section 3.2) for each of the 16 eruptive scenarii described in Section 3.1. The 16 output files generated by HAZMAP for each season were weighted according to Table 1 by using the open source QGIS software (Chugiak 2.4), and combined into final seasonal hazard maps. In order to allow a rapid comparison with other field maps shown in this

manuscript, we first chose to define hazard levels based on deposit thickness simulated by HAZMAP. Therefore, the hazard maps presented in this section are only given as isopach maps in centimeters.
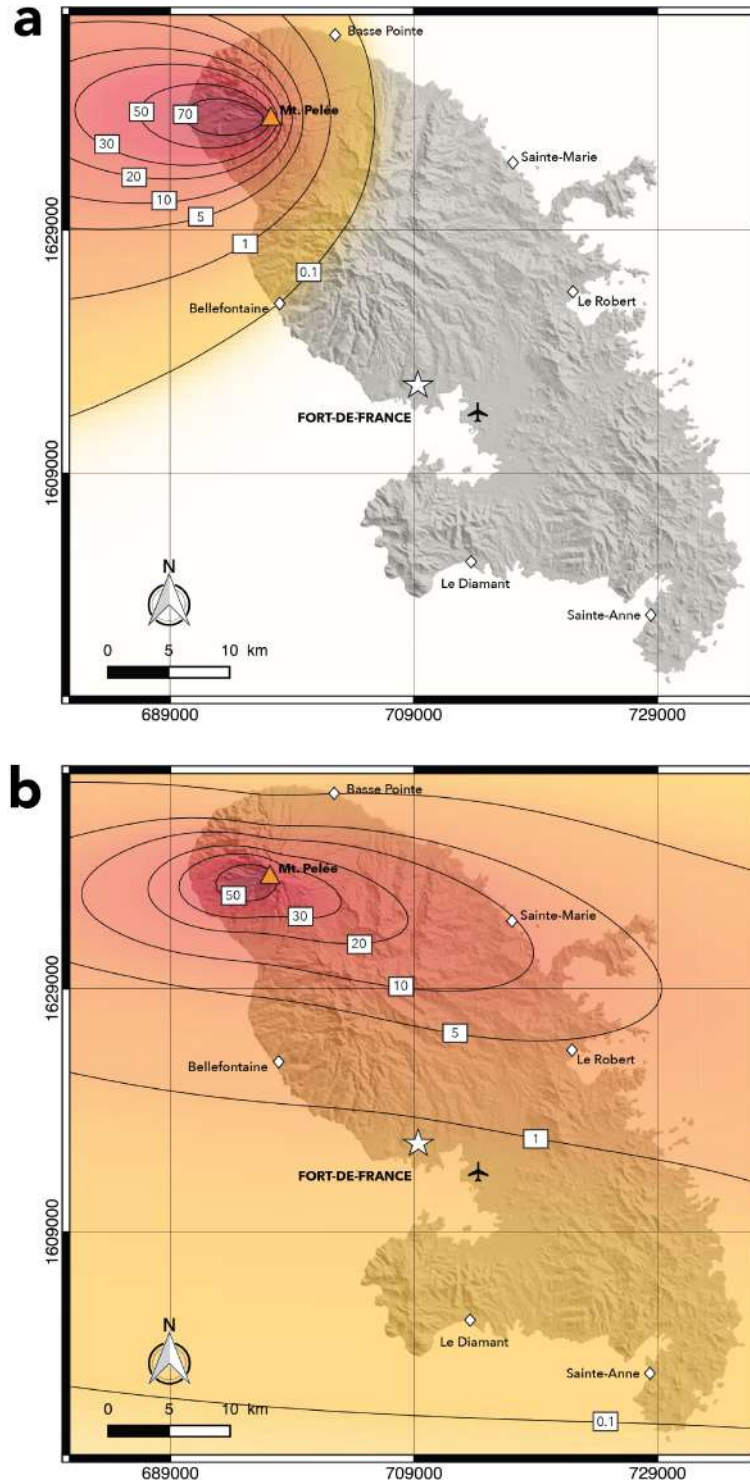

Figure 5: Hazard maps for tephra fallout in Martinique, when considering 16 eruptive scenarii (see Section 3.1) and a wind profile averaged over the entire **a** wet season (from June to November, see Figure 2a) and **b** dry season (from December to May, see Figure 2b). Hazard level is evaluated depending on deposit thickness, and shown using the color scale and isopachs in centimeters.

Figure 5a shows the hazard map for tephra fallout when considering a wind profile averaged over the entire wet season. In this case, only the northern part of the island is threatened by tephra fallout, especially on the western flanks of the volcano with more than $50-70$ centimeters of deposit simulated over Le Prêcheur. Basse-Pointe and Bellefontaine are the farthest cities impacted by tephra fallout, with a thickness ranging from 1 cm to 1 mm. This result highlights the importance of the lower tropospheric easterlies that cannot be counterbalanced by the weak westerlies in the upper troposphere, and thus strongly control the tephra dispersal towards the west throughout the entire wet season (Figure 2a).

Figure 5b shows the hazard map for tephra fallout when considering a wind profile averaged over the entire dry season. In this case, the entire island is threatened by tephra fallout resulting from a Plinian eruption. Up to 50 cm of deposits are simulated over the western flank of Mount Pelée volcano, which remains the most threatened coast of Martinique. In contrast to the wet season, the dry season winds allow tephra dispersal towards the Atlantic coast with 10 cm simulated over Sainte-Marie and 5 cm over Le Robert. The south of Martinique is also affected with ≈ 1 cm over Fort-de-France and the international airport (plane symbol in all figures), and even 1 mm of tephra simulated to the south of Sainte-Anne. Such a wide dispersal of volcanic products can be explained by the strong opposition between dominant lower tropospheric easterlies and strong (> 15 m s^{-1}) westerlies in the upper troposphere (Figure 2b).

4.1.2 Aggregated hazard map

We now combine Figure 5a and b into a single aggregated map for the whole year, presented in Figure 6. We can see that contrary to the hazard map for tephra fallout presented in Figure 1, the entire island of Martinique is threatened in this case, mainly because of the influence of the dry season winds (Figure 5b). A thickness of 50 cm is simulated by HAZMAP over Le Prêcheur (western flank of Mount Pelée volcano), while Saint-Pierre and Sainte-Marie are on the 5-cm isopach on each side of the island. Around 5 mm of tephra is simulated over Fort-de-France and the international airport, and less than 1 mm is forecasted south of the island.

We can compare these simulated thicknesses with some damage thresholds given in the literature in order to better illustrate the implication of this first aggregated hazard map. In the northern part of the island where the hazard level is highest, a thickness of 50 cm in Le Prêcheur would mean only a partial survival of vegetation (Bonadonna, 2006), severe roof collapses (Komorowski *et al.* 2008, their Table 4), severe contamination of water supply, road closures, and the need of extensive repair on electrical supply (Wilson *et al.* 2014, their Table 11). In Saint-Pierre and Sainte-Marie, where 5 cm-thick deposits are simulated, electrical and water supply networks would be damaged, as well as roads meaning dangerous driving conditions. Wilson *et al.* (2014) also indicates in their Table 11 that 5 mm of tephra over an airport corresponds to a reduced visibility and a possible abrasion of runway, leading to the airport closure. Finally, even if the south of Martinique would receive less than 1 mm of tephra, Horwell & Baxter (2006) indicate that masks should be worn as long as a 100 μg m^{-3} threshold of PM$_{10}$ in the air is exceeded.
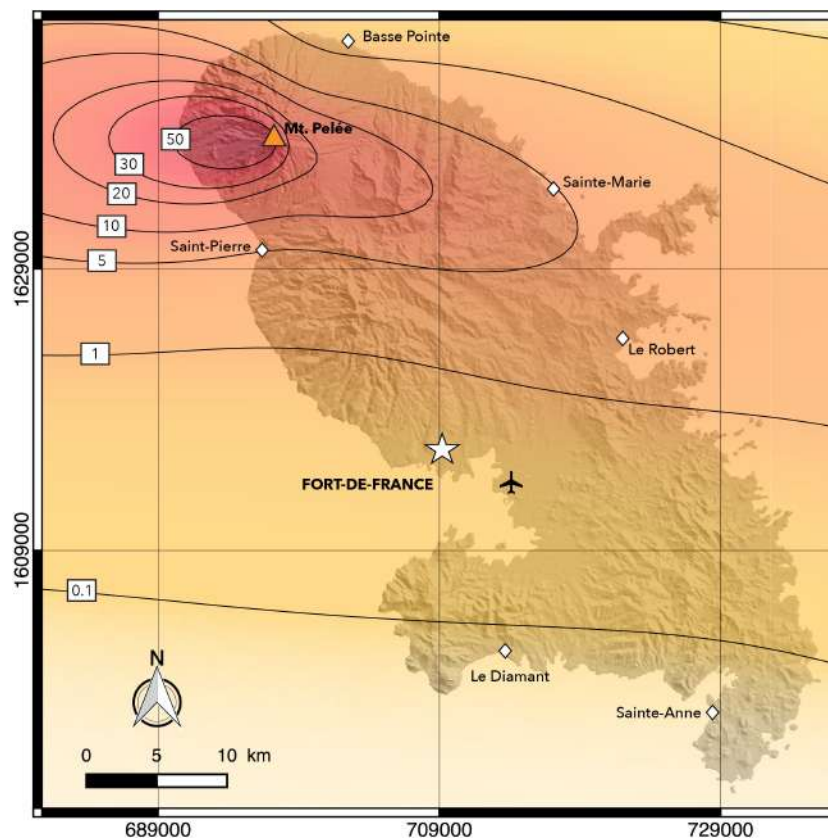
Figure 6: Aggregated hazard map for tephra fallout in Martinique, obtained by combining Figure 5a and b. Hazard level is evaluated depending on deposit thickness, and shown using the color scale and isopachs in centimeters.

4.2   Refined method accounting for wind variability

4.2.1   Monthly hazard maps

By taking into account winds and several eruptive scenarii, the aggregated hazard map presented in Figure 6 is already an improvement for tephra fallout hazard assessment in Martinique. To go further, we now perform 192 simulations to test each eruptive scenario along with 12 mean monthly wind profiles (Figure 3 and Figure 4). We obtain 16 maps for each month, that we combine into a single monthly map using the coefficients given in Table 1. We present in this section the 12 hazard maps for tephra fallout calculated for each month of the year.

Figure 7 shows the results for January and February, corresponding to the wind profiles in Figure 4b and c. The two maps present very similar thicknesses ranging from 50 cm simulated over the western flank of the Mount Pelée volcano to 1 cm-thick deposits over Fort-de-France bay, which reflects the strong resemblance between the two wind profiles averaged over January and February. The slight differences in the westerlies wind speed at ≈ 12 km of altitude can explain that the isopachs for February (Figure 7b) are more elongated towards the east than for January.

In March and April, the troposphere is almost entirely characterized by westerlies blowing from ≈ 5 to 18 km, with a wind speed reaching 20 m s^{-1} at ≈ 12 km (Figure 4d and e) counterbalancing the effect of low tropospheric easterlies. As a consequence, the hazard maps for these two months (Figure 8) exhibit strongly elongated isopachs covering the north-
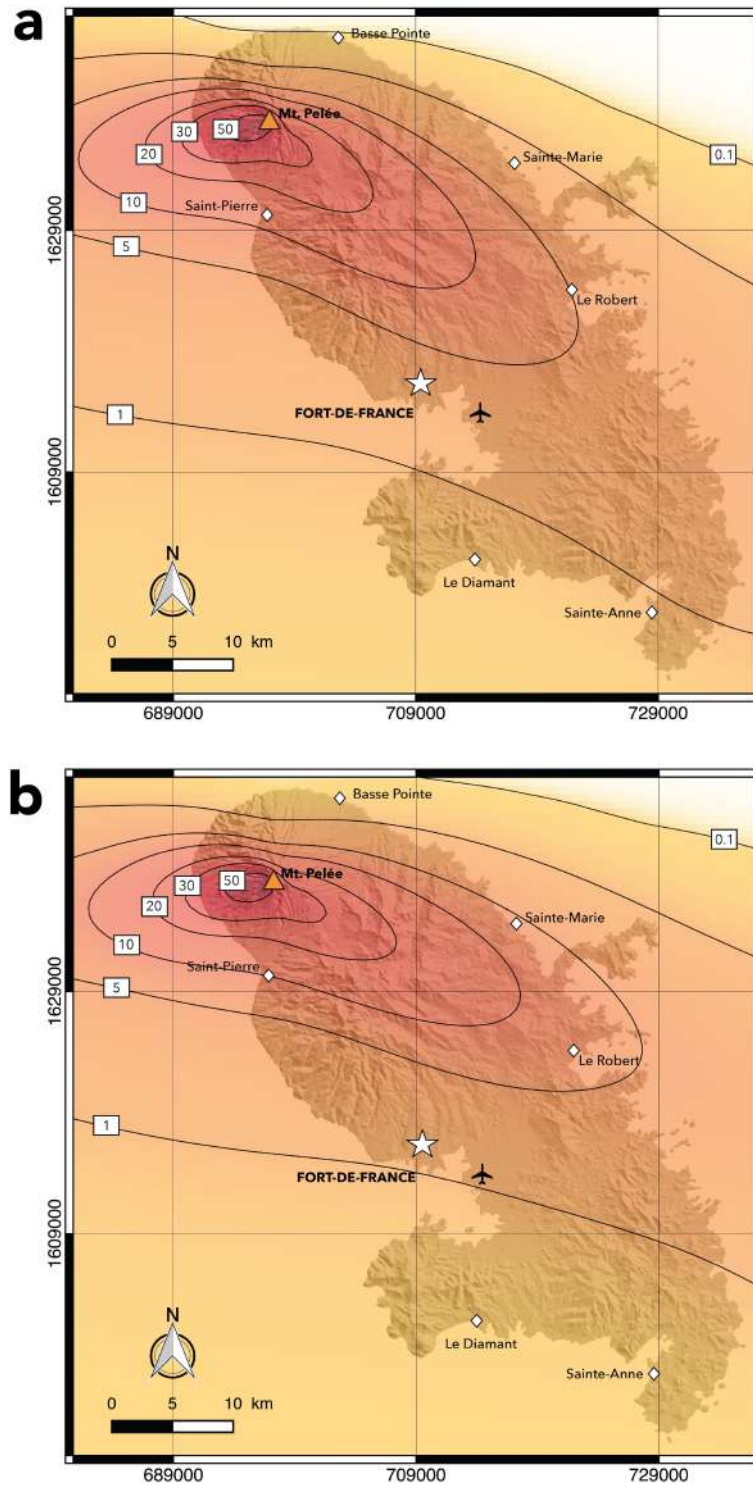
Figure 7: Hazard maps for tephra fallout in Martinique, when considering 16 eruptive scenarii (see Section 3.1) and a wind profile averaged over **a** January (see Figure 4b) and **b** February (see Figure 4c). Hazard level is evaluated depending on deposit thickness, and shown using the color scale and isopachs in centimeters.

ern part of the island on a W-E axis. All the island however remains subjected to tephra fallout hazard during March (Figure 8a), while the extreme south of Martinique would be spared in April (Figure 8b). This can be explained by the weak northerlies blowing at 5 and 20 km of altitude in March (Figure 4d), while easterlies blow at the same altitudes in

Figure 8: Hazard maps for tephra fallout in Martinique, when considering 16 eruptive scenarii (see Section 3.1) and a wind profile averaged over **a** March (see Figure 4d) and **b** April (see Figure 4e). Hazard level is evaluated depending on deposit thickness, and shown using the color scale and isopachs in centimeters.

April (Figure 4e).

Figure 9 gives the hazard maps produced when considering winds blowing in May and June, at the transition between the dry and wet seasons. May is characterized by stable westerlies (270-280°N) that can reach a speed of ≈ 18 m s^{-1} at 14 km (Figure 4f) yielding
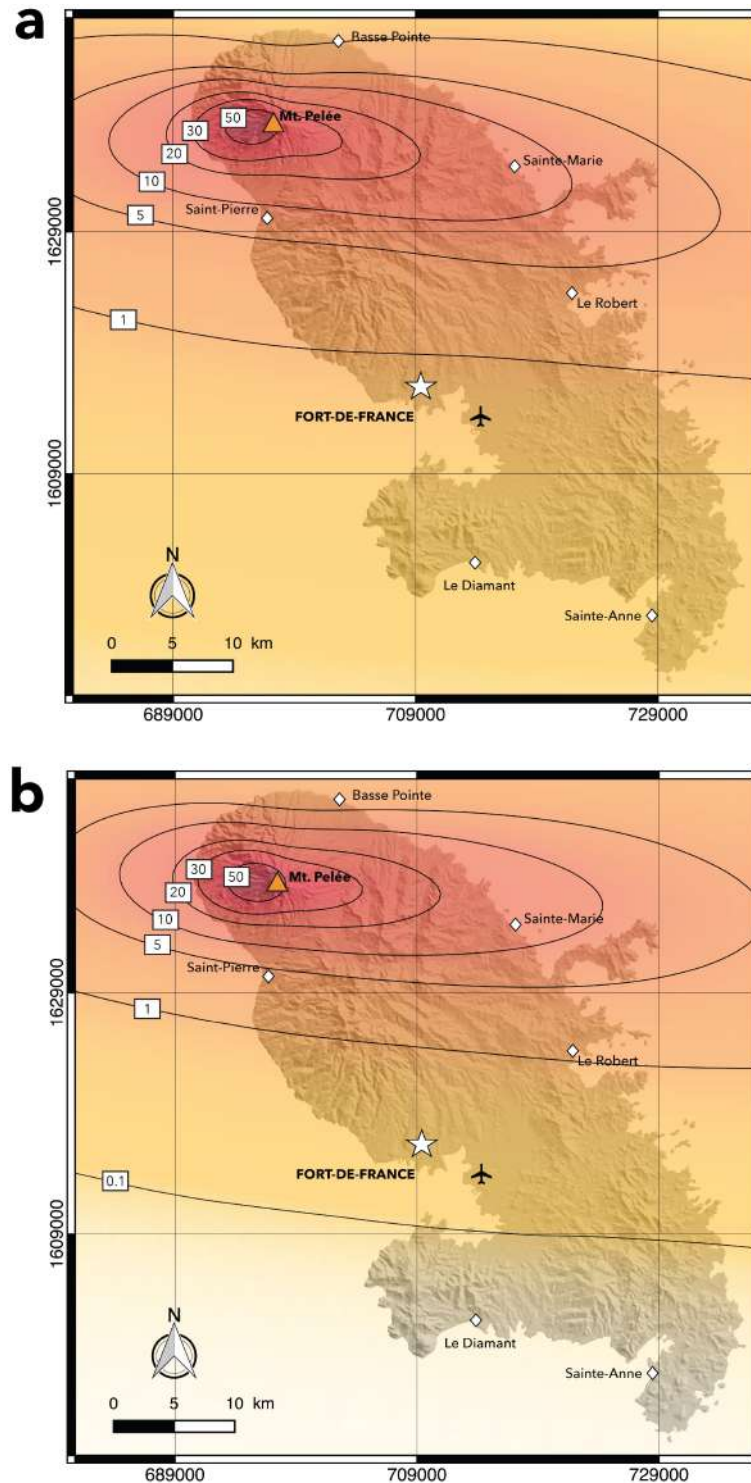
Figure 9: Hazard maps for tephra fallout in Martinique, when considering 16 eruptive scenarii (see Section 3.1) and a wind profile averaged over **a** May (see Figure 4f) and **b** June (see Figure 3a). Hazard level is evaluated depending on deposit thickness, and shown using the color scale and isopachs in centimeters.

elongated isopachs exclusively covering the north of Martinique (Figure 9a). In June, the upper tropospheric westerlies are weaker with a maximum speed reaching only ≈ 11 m s^{-1} (Figure 3a). In addition, low tropospheric easterlies are reinforced with a maximum wind speed of 10 m s^{-1}, thus changing considerably the resulting hazard map characterized by
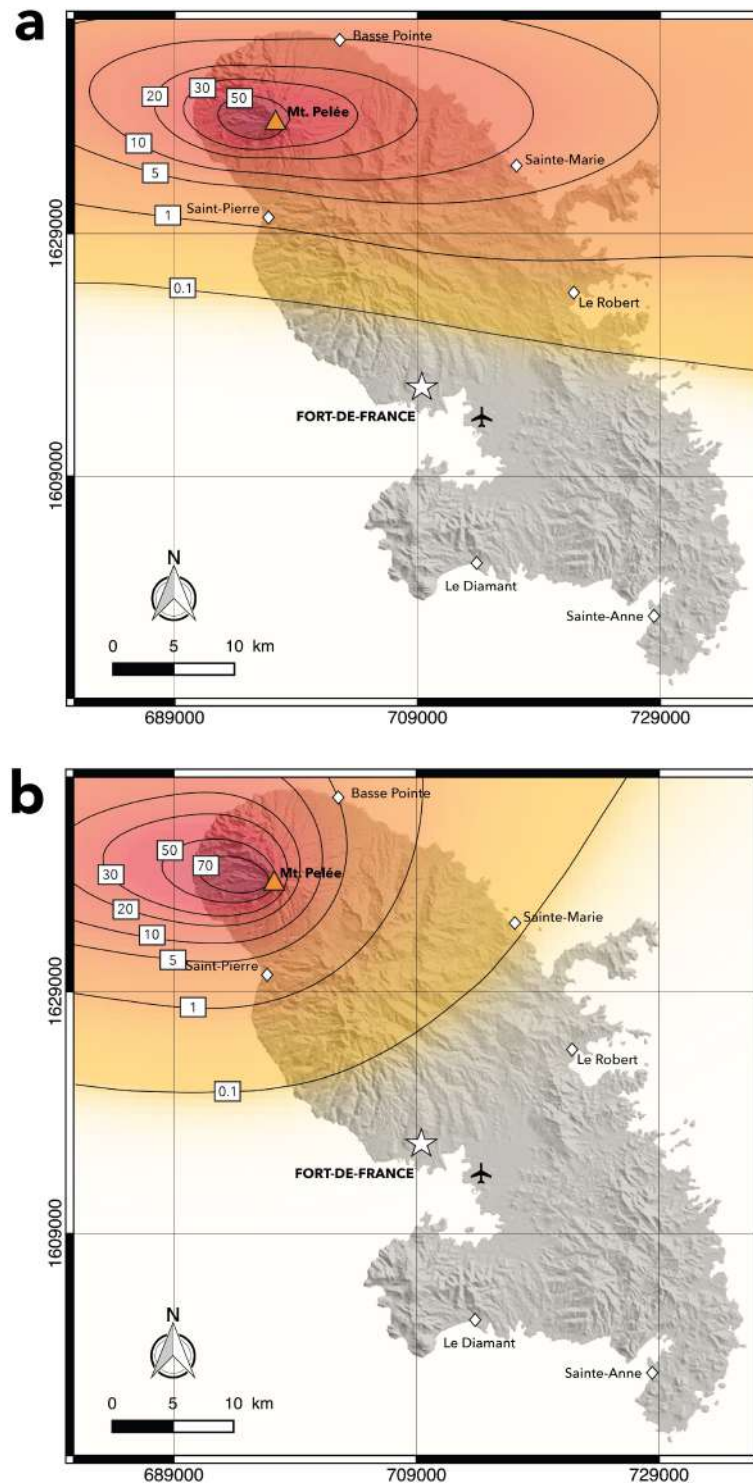
Figure 10: Hazard maps for tephra fallout in Martinique, when considering 16 eruptive scenarii (see Section 3.1) and a wind profile averaged over **a** July (see Figure 3b) and **b** August (see Figure 3c). Hazard level is evaluated depending on deposit thickness, and shown using the color scale and isopachs in centimeters.

more tightened isopachs with a main westward dispersal axis (Figure 9b).

Figure 10 and Figure 11a, produced for July, August and September, strongly resemble the hazard map produced for the wet season when considering a mean seasonal wind profile (Figure 5a). During these months, strong easterlies blowing in the lower troposphere (Figure
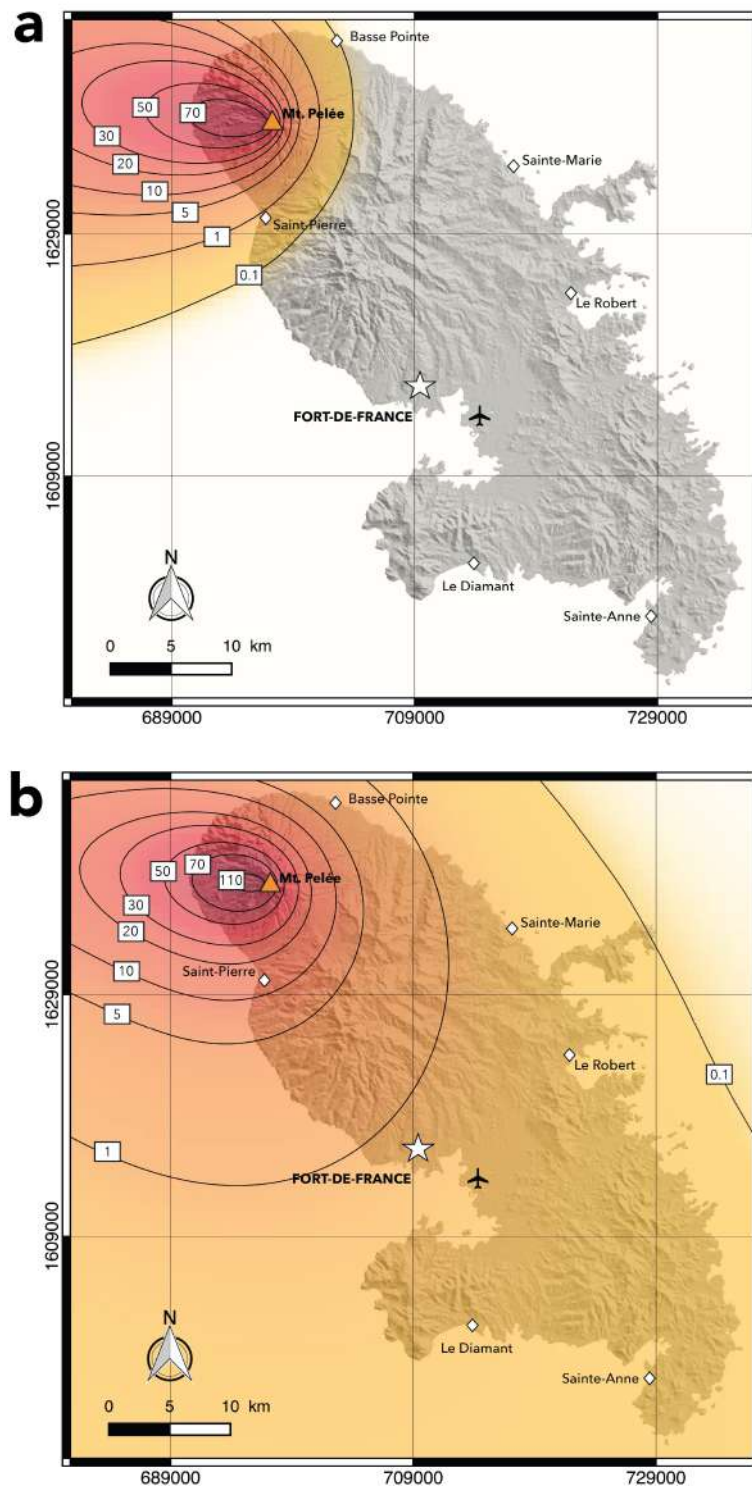
Figure 11: Hazard maps for tephra fallout in Martinique, when considering 16 eruptive scenarii (see Section 3.1) and a wind profile averaged over **a** September (see Figure 3d) and **b** October (see Figure 3e). Hazard level is evaluated depending on deposit thickness, and shown using the color scale and isopachs in centimeters.

3b, c, and d) yield tightened isopachs with a strong westward dispersal axis, leaving the Atlantic coast untouched.

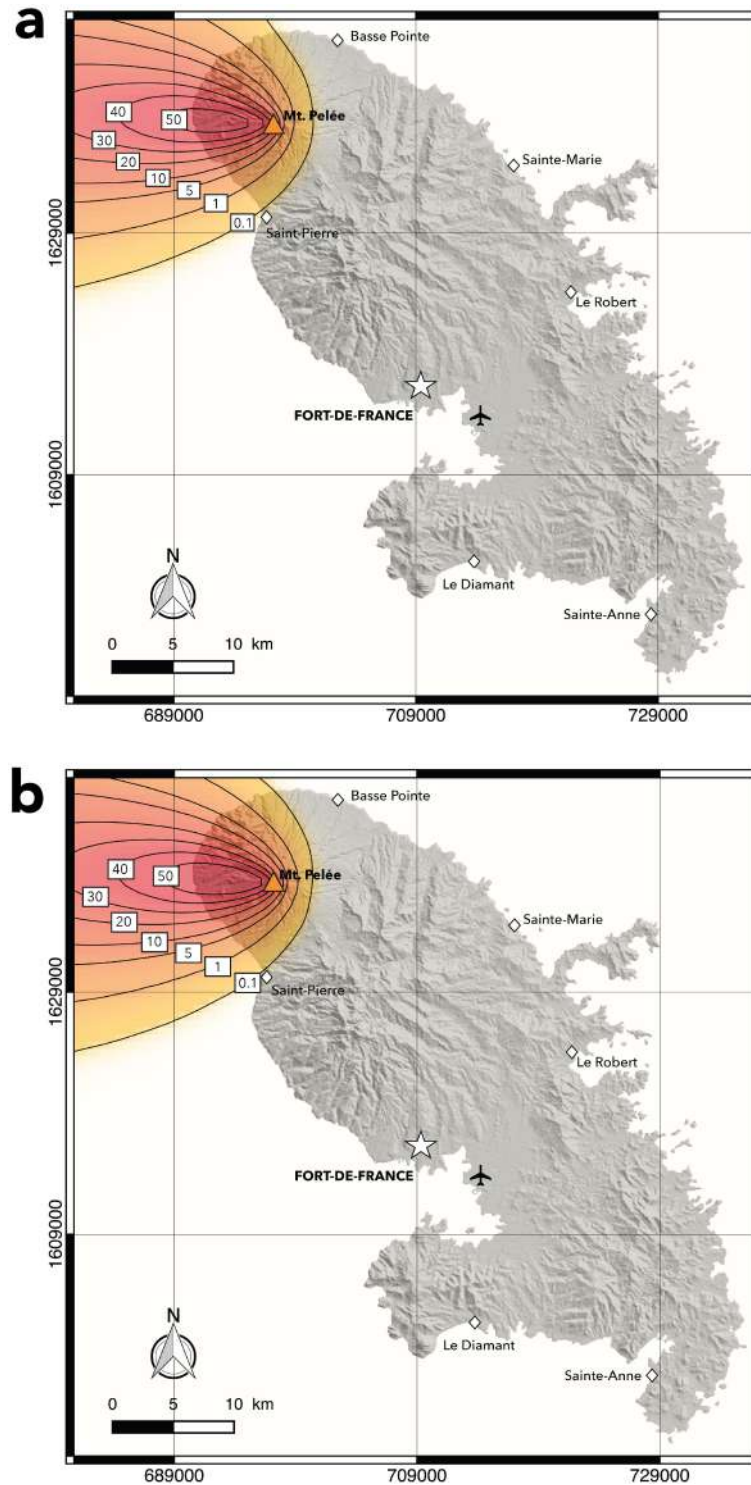Figure 11 shows a sharp transition between September, still characterized by a westward
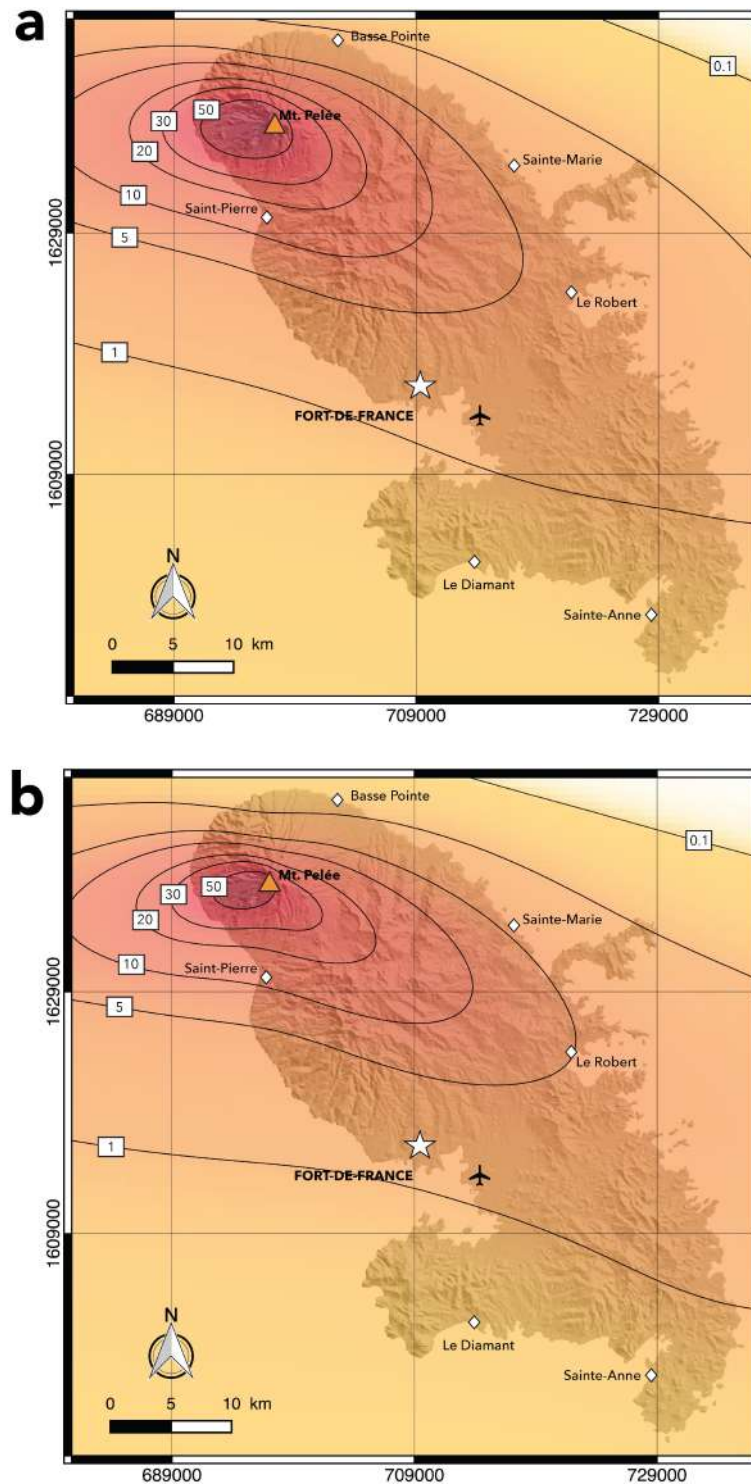
Figure 12: Hazard maps for tephra fallout in Martinique, when considering 16 eruptive scenarii (see Section 3.1) and a wind profile averaged over **a** November (see Figure 3f) and **b** December (see Figure 4a). Hazard level is evaluated depending on deposit thickness, and shown using the color scale and isopachs in centimeters.

dispersal axis, and October, for which the entire island is affected by tephra fallout hazard (even if less than 1 cm of tephra is simulated for the southern part of Martinique). This large difference can be explained by an increase in wind speed of the upper tropospheric

westerlies in October, compared to September (Figure 3d and e).

In November and December, marking the transition between the wet and dry season, the upper tropospheric wind speed still increases from 8 m s^{-1} in October, to 14 m s^{-1} in November and up to 18 m s^{-1} in December (Figure 3e and f; Figure 4a), increasing the tephra fallout hazard in Martinique (Figure 12). In December (Figure 12b), we obtain almost the exact same map as in January (Figure 7a).

These results show that while hazard maps obtained for the dry season months (from December to May) are really similar to each other, those obtained for the wet season months (from June to November) exhibit a strong variation of simulated thicknesses − and thus of tephra fallout hazard − in accordance with wind variability observed during these months (Figure 3). This variability is completely hidden in the hazard map for the wet season shown in Figure 5a, and thus in our first aggregated map (Figure 6).

4.2.2 New hazard map for tephra fallout in Martinique

We now combine these twelve monthly hazard maps into a new hazard map for tephra fallout in Martinique shown in Figure 13, either using isopachs in centimeters (Figure 13a), or iso-mass loads in kg m^{-2} as done for most hazard maps in the literature (Figure 13b).

Our results show that HAZMAP underestimates tephra fallout hazard when accounting solely for seasonal winds (Figure 6) compared to the monthly variability maps (Figure 13). Our new hazard map indeed simulates more than 1 mm of tephra over Sainte-Anne, whereas the level of exposure if null in the previous map (Stieltjes & Mirgon, 1998). The international airport is also more subjected to tephra fallout with ≈ 6.5 mm of tephra (7 kg m^{-2}) predicted near Fort-de-France. Up to the north, similar thicknesses to those obtained with seasonal winds are calculated, with ≈ 50 cm-thick deposits over Le Prêcheur and between 5 and 10 cm over Saint-Pierre.

Comparing Figure 13b with damage thresholds by tephra fallout in the literature, we find that the western flanks of the Mount Pelée volcano (north of Saint-Pierre and Le Prêcheur) would be sujected to heavy damages on buildings. Indeed, beyond 200 kg m^{-2}, there is a 50% probability of weak roof collapse (made of timber); beyond 300 kg m^{-2}, even rooftops made of massonry would have a 50-50 chance to collapse (Komorowski *et al.*, 2008). All villages built north and east of Saint-Pierre on the southwestern flanks of the volcano are beyond the 100 kg m^{-2} limit and are thus subjected to severe road, buildings and network damages (Wilson *et al.*, 2014). According to Komorowski *et al.* (2008), the 15 kg m^{-2} isoline represents the limit beyond which there is damage to cultivated croplands. Figure 13b shows that half of the island is beyond this boundary, but the actual consequences of harvest losses would be felt by the entire island as the northeastern atlantic coast, characterized by a more temperate and rainy climate (Chapter 1, Figure 4a), is a favorable environment for farming. Finally, the southern half of Martinique has a tephra fallout hazard comprised between 15 kg m^{-2} in Fort-de-France and 1 kg m^{-2} on the south of Sainte-Anne peninsula. This range of mass loads corresponds to the Level 1 described by Wilson *et al.* (2014) for which cleaning is required to avoid permanent damage on all networks (electrical, water supply, wastewater, communications, roads, etc). In addition, the airport should be closed as soon as a thickness of 1 mm (≈ 1 kg m^{-2}) is reached. These results indicate that the entire island would be impacted by a future Plinian eruption at Mount Pelée volcano.

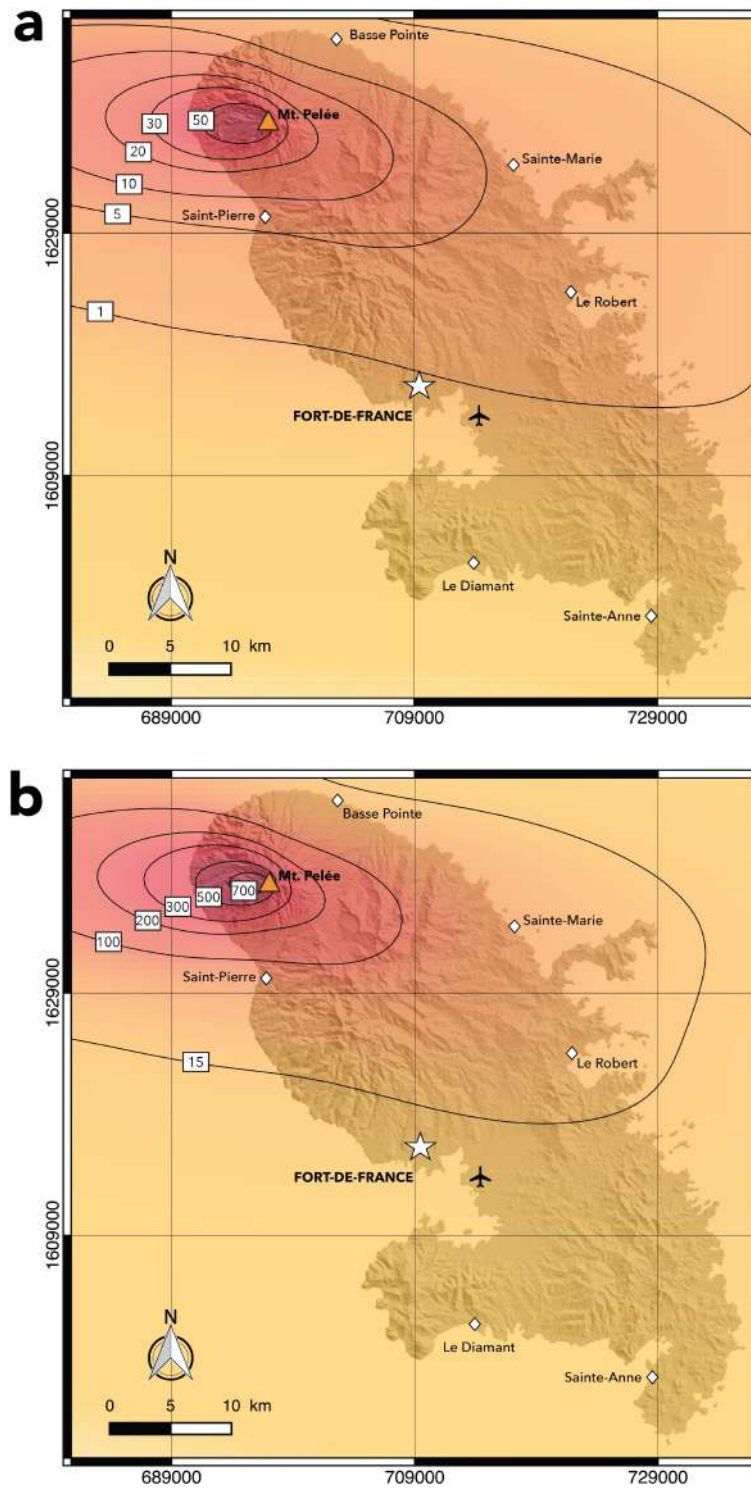**Figure 13:** New hazard maps for tephra fallout in Martinique, obtained by combining all monthly hazard maps (Figures 7, 8, 9, 10, 11, and 12). Hazard level is evaluated depending on **a** deposit thickness (in centimeters), and **b** mass load in kg m^{-2}. Color scale begins at 0.1 cm or 1 kg m^{-2}, which corresponds to the threshold for minor damage on health, agriculture and infrastructures (Wilson *et al.*, 2014).

5   Discussion

5.1   Comparison with previous hazard map for tephra fallout

Cartography is a precious tool for hazard and risk assessment (Leone & Lesales, 2009), and can facilitate discussions with competent authorities managing eruptive crises. For a "friendly" reading of our new tephra fallout hazard map by the authorities, and to compare it more easily with the previous one built by Stieltjes & Mirgon (1998), we combine our simulated thicknesses (Figure 13a) with damage threshold found in the literature. To this purpose, we adapt the intensity levels of Stieltjes & Mirgon (1998) ranging from I0 (no exposure) to I4 (very high exposure) and give them a thickness value corresponding to a degree of damage (Table 2).

Table 2: Intensity levels (I_0 to I_4) used to build the hazard map for tephra fallout in Figure 14, with their corresponding exposure, tephra thickness thresholds (Th) and damages on infrastructures.

I_0	null	Th < 1 mm	No damage
I_1	low	1 mm < Th < 1 cm	Maintenance required on supply networks, airport closing
I_2	intermediate	1 cm < Th < 15 cm	Extensive repair required on supply networks
I_3	high	15 cm < Th < 30 cm	Replacement required on supply networks; severe weak roof collapse (timber)
I_4	very high	Th > 30 cm	Severe roof collapse (timber, massonry, concrete...)

Level 0 (I0, < 1 mm, white) corresponds to no damage; level 1 (I1, 1 mm − 1 cm, yellow) corresponds to the level 1 described by Wilson *et al.* (2014) at which maintenance is required for all kind of supply networks (electricity, water, roads,...) in order to prevent further damage, and at which the airport should be closed; level 2 (I2, 1 cm − 15 cm, orange) corresponds to damages on supply networks requiring repair (Wilson *et al.*, 2014); level 3 (I3, 15 cm − 30 cm, pink) corresponds to complete destruction of infrastructures (Wilson *et al.*, 2014), and to severe roof collapse for buildings made of timber (Komorowski *et al.*, 2008); level 4 (I4, > 30 cm, red) corresponds to the highest degree of building damages. By applying these thresholds on Figure 13a, we obtain Figure 14 that summarizes both hazard levels determined in previous section, and the consequences of the exposure. Comparing this map with Figure 1, we note that the concentric circles drawn from maximum extent of Plinian deposits by Stieltjes & Mirgon (1998) are here replaced by large ellipses accounting for the effect of winds. Moreover, there is no level 0 of tephra fallout hazard in our newly built map, as even the southern parts of Martinique could be damaged. It is nonetheless important to note that the northern part of the island, especially the western flanks of Mount Pelée volcano, remains the most hazardous area in Martinique, as in Figure 1. Only the northern Atlantic coast is retrograded into a Level 2 hazard area, while Basse Pointe was at Level 3 in the previous map. This is, once again, due to the strong effects of wind that blows from east to west in the lower troposphere throughout the whole year.
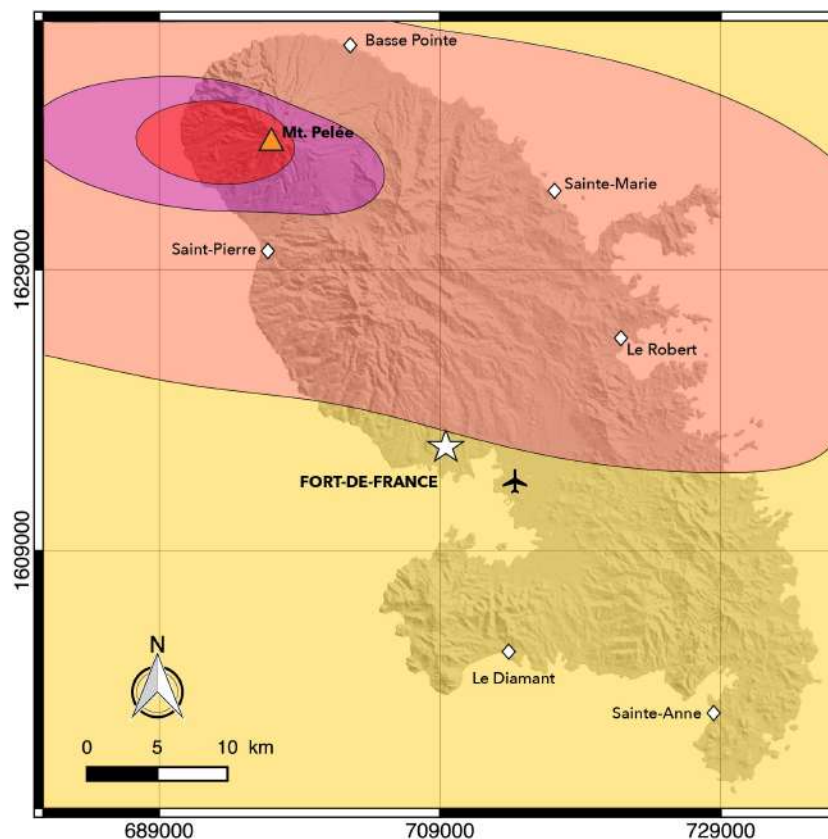
Figure 14: Tephra fallout hazard/exposure map for Martinique based on Figure 13a and showing four levels of intensity with red: very high, (I4); pink: high, (I3); orange: intermediate, (I2); yellow: low, (I1). These levels depend on thickness thresholds for infrastructure damage (see main text and Table 2).

5.2   Other volcanic hazards in Martinique

Although this chapter is dedicated to tephra fallout hazard assessment, six other volcanic hazards should be considered in Martinique, as done by Stieltjes & Mirgon (1998): pyroclastic flows, lava intrusions/flows, gas emissions, lahars, landslides and tsunamis (we could also add volcano-tectonic earthquakes induced by magma injection or withdrawal). In order to produce a new integrated volcanic hazard map for Mount Pelée volcano, a complete re-assessment of each hazard should be done in the future. We indeed showed in Chapter 1 that the Plinian eruptive history of Mount Pelée was much richer than previously thought, and we can argue that many phreatic and Pelean eruptions also remain unknown. A careful revisit of this eruptive history is crucial, as hazard assessment strongly relies on eruption frequency and intensity. In addition, we saw with the Balisier event in Chapters 2 and 5 that even a Pelean eruption can have a strong impact far beyond the source if a co-PDC plume forms.

To get a preliminary insight on what could resemble a revisited integrated volcanic hazard map in Martinique, we combine our Figure 14 together with the hazard zoning made by Stieltjes & Mirgon (1998) for other volcanic phenomena (pyroclastic flows, lava intrusion/flow, gas emissions, lahars, and landslides, see Introduction, Figure 7) in Figure 15. This resulting map highlights the high level of exposure of the northern part of the island as all these other volcanic phenomena mainly occur near the vent. Close to the volcano summit, where all volcanic hazards overlap, appears a fifth intensity level (in purple) corresponding to the area where destruction would be total.
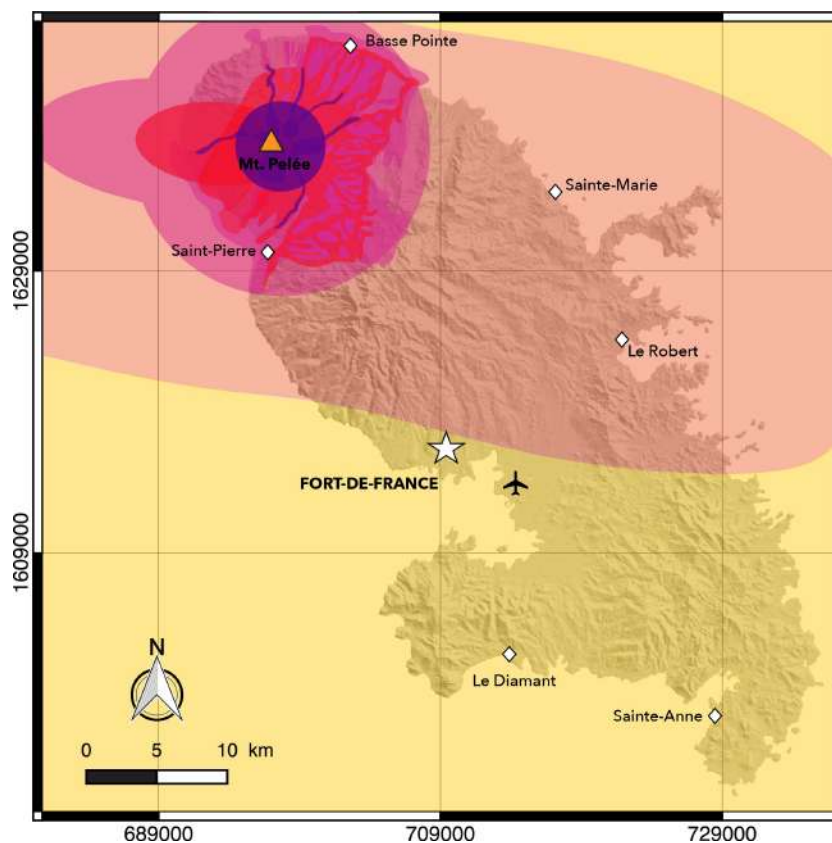
Figure 15: Integrated volcanic hazard/exposure map for Martinique combining Figure 14 and other volcanic hazards as assessed by Stieltjes & Mirgon (1998) (see Introduction, Figure 7). Five levels of intensity are shown with purple: major; red: very high; pink: high; orange: intermediate; yellow: low.

6 Conclusion

In this chapter, we propose an approach that refines tephra fallout hazard assessment in Martinique based on 16 eruptive scenarii determined and weighted according to our revisited eruptive history of Mount Pelée volcano (Chapter 1), and considering seasonal and monthly wind variability. We show, in agreement with our conclusions from Chapter 5, that mean seasonal wind profiles strongly smooth wind variability and thus have a large impact on volcanic hazard assessment. When considering monthly wind variability, drastic changes are observed in the resulting hazard map, especially for the southern part of Martinique which was until now considered as safe from tephra fallout. As a final step in this preliminary study, we combine the newly built hazard map with tephra thresholds found in the literature in order to produce a final user-friendly map designed for the competent authorities. This map, thanks to four intensity levels, shows both a degree of exposure to tephra fallout as well as corresponding damages that could be expected in each area considered.

This work represents a first step in the volcanic hazard re-assessment in Martinique, as we only use a deterministic approach with multiple volcanic scenarii. In the future, the methodology presented here will be refined to account for the daily variability of winds in order to produce probabilistic maps. To go even further, it would be necessary to revisit the phreatic and Pelean eruptive history of Mount Pelée to re-assess the corresponding hazards and move towards a new integrated volcanic hazard map in Martinique. It is important to remind that these hazard maps are not risk maps, which would require an additional vulnerability assessment of the elements that may be affected during an eruption

(population, buildings, networks...).

References

BAKER, P.E. 1985 Volcanic hazards on St Kitts and Montserrat, West Indies. *J. Geol. Soc. London* **142**, 279–295.

BARBERI, F., GHIGLIOTTI, M., MACEDONIO, G., ORELLANA, H., PARESCHI, M.T. & ROSI, M. 1992 Volcanic hazard assessment of Guagua Pichincha (Ecuador) based on past behaviour and numerical models. *J. Volcanol. Geotherm. Res.* **49**, 53–68.

BONADONNA, C. 2006 Probabilistic modelling of tephra dispersion. In *Statistics in Volcanology* (ed. H.M. Mader, S.G. Coles, C.B. Connor & L.J. Connor), pp. 243–259. Geological Society, London.

BONADONNA, C., CONNOR, C.B., HOUGHTON, B.F., CONNOR, L., BYRNE, M., LAING, A. & HINCKS, T.K. 2005 Probabilistic modeling of tephra dispersal: Hazard assessment of a multiphase rhyolitic eruption at Tarawera, New Zealand. *J. Geophys. Res.* **110** (B03203).

BONADONNA, C., MAYBERRY, G.C., CALDER, E.S., SPARKS, R.S.J., CHOUX, C., JACKSON, P., LEJEUNE, A.M., LOUGHLIN, S.C., NORTON, G.E., ROSE, W.I., RYAN, G. & YOUNG, S.R. 2002 Tephra fallout in the eruption of Soufriere Hills Volcano, Montserrat. In *The Eruption of Soufriere Hills Volcano, Montserrat from 1995 to 1999* (ed. T.H. Druitt & B.P. Kokelaar), pp. 483–516. Geological Society, London, Memoirs.

BONASIA, R., CAPRA, L., COSTA, A., MACEDONIO, G. & SAUCEDO, R. 2011 Tephra fallout hazard assessment for a Plinian eruption scenario at Volcán de Colima (Mexico). *J. Volcanol. Geotherm. Res.* **203**, 12–22.

BONASIA, R., COSTA, A., FOLCH, A., MACEDONIO, G. & CAPRA, L. 2012 Numerical simulation of tephra transport and deposition of the 1982 El Chichón eruption and implications for hazard assessment. *J. Volcanol. Geotherm. Res.* **231-232**, 39–49.

CARAZZO, G., KAMINSKI, E. & TAIT, S. 2008 On the rise of turbulent plumes: Quantitative effects of variable entrainment for submarine hydrothermal vents, terrestrial and extra terrestrial explosive volcanism. *J. Geophys. Res. Solid Earth* **113**, 1–19.

CARAZZO, G., TAIT, S., KAMINSKI, E. & GARDNER, J. E. 2012 The recent Plinian explosive activity of Mt. Pelée volcano (Lesser Antilles): The P1 AD 1300 eruption. *Bull. Volcanol.* **74**, 2187–2203.

CIONI, R., LONGO, A., MACEDONIO, G., SANTACROCE, R., SBRANA, A., SULPIZIO, R. & ANDRONICO, D. 2003 Assessing pyroclastic fall hazard through field data and numerical simulations: Example from Vesuvius. *J. Geophys. Res* **108** (B22063).

COSTA, A., DELL'ERBA, F., VITO, M. A., ISAIA, R., MACEDONIO, G., ORSI, G. & PFEIFFER, T. 2009 Tephra fallout hazard assessment at the Campi Flegrei caldera (Italy). *Bull. Volcanol.* **71**, 259–273.

DEE, D. P., UPPALA, S. M., SIMMONS, A. J., BERRISFORD, P., POLI, P., KOBAYASHI, S., ANDRAE, U., BALMASEDA, M. A., BALSAMO, G., BAUER, P., BECHTOLD, P., BELJAARS, A. C.M., VAN DE BERG, L., BIDLOT, J., BORMANN, N., DELSOL, C., DRAGANI, R., FUENTES, M., GEER, A. J., HAIMBERGER, L., HEALY, S. B., HERSBACH, H., HÓLM, E. V., ISAKSEN, L., KÅLLBERG, P., KÖHLER, M., MATRICARDI, M., MCNALLY, A. P., MONGE-SANZ, B. M., MORCRETTE, J. J., PARK, B. K., PEUBEY, C., DE ROSNAY, P., TAVOLATO, C., THÉPAUT, J. N. & VITART, F. 2011 The ERA-Interim reanalysis: Configuration and performance of the data assimilation system. *Q. J. R. Meteorol. Soc.* **137**, 553–597.

HERSBACH, H., BELL, B., BERRISFORD, P., HORÁNYI, A., MUÑOZ SABATER, J., NICOLAS, J., RADU, R., SCHEPERS, D., SIMMONS, A., SOCI, C. & DEE, D. 2019 Global reanalysis: goodbye ERA-Interim, hello ERA5. *ECMWF Newslett.* **159**, 17–24.

HORWELL, C. J. & BAXTER, P. J. 2006 The respiratory health hazards of volcanic ash: A review for volcanic risk mitigation. *Bull. Volcanol.* **69** (1), 1–24.

HOUGHTON, B. F., LATTER, J.H. & HACKETT, W.R. 1987 Volcanic hazard assessment for Ruapehu composite volcano, Taupo Volcanic Zone, New Zealand. *Bull. Volcanol.* **49**, 737–751.

References

Kaminski, E. & Jaupart, C. 1998 The size distribution of pyroclasts and the fragmentation sequence in explosive volcanic eruptions. *J. Geophys. Res.* **103**, 29759–29779.

Komorowski, J. C., Legendre, Y., Caron, B. & Boudon, G. 2008 Reconstruction and analysis of sub-plinian tephra dispersal during the 1530 A.D. Soufriere (Guadeloupe) eruption: Implications for scenario definition and hazards assessment. *J. Volcanol. Geotherm. Res.* **178**, 491–515.

Leone, F. & Lesales, T. 2009 The interest of cartography for a better perception and management of volcanic risk: From scientific to social representations, the case of Mt. Pelée volcano, Martinique (Lesser Antilles). *J. Volcanol. Geotherm. Res.* **186**, 186–194.

Macedonio, G., Costa, A. & Folch, A. 2008 Ash fallout scenarios at Vesuvius: Numerical simulations and implications for hazard assessment. *J. Volcanol. Geotherm. Res.* **178** (3), 366–377.

Macedonio, G., Costa, A. & Longo, A. 2005 A computer model for volcanic ash fallout and assessment of subsequent hazard. *Comput. Geosci.* **31**, 837–845.

Macías, J., Capra, L., Arce, J., Espíndola, J., García-Palomo, A. & Sheridan, M. 2008 Hazard map of El Chichón volcano, Chiapas, Mexico: Constraints posed by eruptive history and computer simulations. *J. Volcanol. Geotherm. Res.* **175**, 444–458.

Michaud-Dubuy, A., Carazzo, G., Tait, S., Le Hir, G., Fluteau, F. & Kaminski, E. 2019 Impact of wind direction variability on hazard assessment in Martinique (Lesser Antilles): The example of the 13.5 ka cal BP Bellefontaine Plinian eruption of Mount Pelée volcano. *J. Volcanol. Geotherm. Res.* **381**, 193–208.

Newhall, C. G. & Hoblitt, R.P. 2002 Constructing event trees for volcanic crises. *Bull. Volcanol.* **64**, 3–20.

Orsi, G., Di Vito, M.A. & Isaia, R. 2004 Volcanic hazard assessment at the restless Campi Flegrei caldera. *Bull. Volcanol.* **66**, 514–530.

Stieltjes, L. & Mirgon, C. 1998 Approche méthodologique de la vulnérabilité aux phénomènes volcaniques : Test d'application sur les réseaux de la Martinique. In *Unpublished Internal Report No. R40098*. Bureau de Recherches Géologiques et Minières, Marseille.

Westercamp, D. & Traineau, H. 1983 The past 5,000 years of volcanic activity at Mt. Pelée Martinique (F.W.I.): Implications for assessment of volcanic hazards. *J. Volcanol. Geotherm. Res.* **17**, 159–185.

Wilson, G., Wilson, T. W., Deligne, N. I. & Cole, J. W. 2014 Volcanic hazard impacts to critical infrastructure: A review. *J. Volcanol. Geotherm. Res.* **286**, 148–182.

Conclusion générale et perspectives

Une nouvelle histoire éruptive pour la montagne Pelée

Les résultats de la première partie de ce manuscrit, entièrement consacrée aux deux études de terrain effectuées en Martinique durant cette thèse, ont permis d'aboutir à une nouvelle chronologie des éruptions de la montagne Pelée sur les vingt-quatre derniers milliers d'années. En effet, nos travaux de reconnaissance et de corrélation de dépôts éruptifs pliniens, nos mesures et prélèvements de dépôts sur le terrain, ainsi que leurs datations ont permis l'identification de six nouvelles éruptions dont les âges sont calibrés de -12 000 à -24 000 ans (cal AP). Parmi ces éruptions, les dépôts des éruptions pliniennes que nous avons nommées P10 (11 334 cal AP) et Bellefontaine (13 516 cal AP) ainsi que ceux des éruptions péléennes nommées NMC (13 132 cal AP) et Balisier (14 072 cal AP) avaient déjà été partiellement identifiés par les précédents auteurs ayant travaillé dans cette région (Roobol & Smith, 1976; Westercamp & Traineau, 1983; Traineau, 1982; Boudon *et al.*, 2005), mais aucune étude poussée ne leur avait été consacrées. Les éruptions pliniennes que nous avons nommées Carbet (18 711 cal AP) et Etoile (21 450 cal AP) étaient par contre totalement inconnues jusqu'à ce jour.

L'histoire éruptive reconstruite à partir de ces nouvelles données permet de conclure que la montagne Pelée a produit un minimum de 34 éruptions magmatiques (dont 21 éruptions péléennes et 13 éruptions pliniennes) dans les derniers 24 000 ans, et qu'une éruption plinienne se produit environ tous les 1 800 ans à la Martinique. Il semble important de rappeler que ce ne sont que des estimations minimales car d'anciennes éruptions péléennes ou pliniennes de plus petite ampleur peuvent encore nous être inconnues. De plus, cette histoire éruptive ne prend pas en compte les très nombreuses éruptions phréatiques s'étant produites dans le passé, comme en 1792 et 1851. Ces incertitudes mettent en lumière l'importance primordiale d'étudier plus précisément dans le futur ces éruptions péléennes et phréatiques, de plus petite ampleur mais représentant également un grand risque pour les populations environnantes de par leur fréquence plus élévée (Boudon *et al.*, 2005).

Nous avons ici comparé notre nouvelle histoire éruptive avec des données de tephrochronologie issues d'un forage en mer au nord de la Martinique (Boudon *et al.*, 2013), et avons pu constater que trois des quatre éruptions pliniennes identifiées sur le terrain (Bellefontaine, Carbet et Etoile) correspondent à des événements datés dans la carotte de forage. L'acquisition d'autres données de forage, à plusieurs endroits autour de la côte nord de l'île, pourraient confirmer ou infirmer notre chronologie éruptive, voire permettre l'identification de nouveaux événements volcaniques dont les dépôts auraient été érodés à terre mais préservés en mer.

Scenarii éruptifs à la montagne Pelée

Par rapport aux carottes en mer potentiellement plus complètes, le grand avantage des études à terre est de pouvoir interpréter les dépôts volcaniques en termes de paramètres éruptifs, c'est-à-dire de quantifier le volume, la hauteur maximale de colonne, le flux de masse, la durée, etc., de chaque éruption. Grâce à des modèles physiques de colonnes volcaniques, nous avons pu reconstruire les paramètres éruptifs de quatre des six éruptions nouvelles/revisitées (Bellefontaine, Balisier, Carbet et Etoile) et les comparer à ceux quantifiés par Carazzo *et al.* (2012, 2019, 2020) pour les éruptions pliniennes plus récentes de la montagne Pelée, P1 (650 AP), P2 (1 670 AP) et P3 (2 010 AP). Il est ressorti de cette comparaison que la montagne Pelée semble produire des éruptions pliniennes très semblables les unes par rapport aux autres depuis 24 000 ans, puisqu'elles sont toutes caractérisées par un flux de masse compris entre 10^7 et 10^8 kg s^{-1}, et un volume entre 0.04 et 1 km^3 DRE (ce qui correspond à des VEI 4−5). Leurs hauteurs maximales de colonnes (entre 19 et 30 km), ainsi que leurs durées (de 1 à 11h) sont également comparables, ainsi que leurs distributions

totales de tailles de grains avec un exposant D compris entre 3.0 et 3.5 suggérant une bonne efficacité de fragmentation du magma avant éruption (voir la note en bas de page 193 pour la signification de D). Ces fortes similitudes ont permis de distinguer des scenarii potentiels de futures éruptions pliniennes à la montagne Pelée dont le plus probable est une éruption produisant une colonne d'environ 20 km de haut, caractérisée par un flux de masse entre 10^7 et 10^8 kg s^{-1} et des dépôts assez finement fragmentés ($D > 3.3$).

Deux éruptions se distinguent malgré tout de ce schéma : l'éruption plinienne P3 et l'éruption péléenne Balisier. La première semble être l'éruption plinienne la plus puissante enregistrée dans la dernière étape d'activité de la montagne Pelée puisqu'elle est caractérisée par un volume supérieur à 1 km^3 (ce qui en fait une des seules éruptions pliniennes VEI 5 connues dans les Petites Antilles), un flux de masse supérieur à 10^8 kg s^{-1} et une hauteur de colonne atteignant 30 km. L'éruption péléenne Balisier est tout aussi remarquable. La coulée de densité pyroclastique résultant de la destruction d'un dôme de lave a été stoppée par la barrière topographique créée par un effondrement de flanc antérieur (à l'est de Saint-Pierre dans les hauteurs). Cette interaction entre relief et coulée de densité pyroclastique a généré un panache secondaire ("co-PDC plume") qui aurait atteint 13 km de hauteur et répandu des cendres très fines ($D = 4.6$) de Saint-Pierre à Bellefontaine, zone en général hors d'atteinte des éruptions péléennes historiques. Les analyses de tailles de grains et la comparaison avec d'autres éruptions ayant produit des panaches secondaires (i.e., éruptions du Tungurahua en 2006, Engwell & Eychenne 2016; de Soufriere Hills à Montserrat en 1997, Bonadonna *et al.* 2002; du Mount Redoubt en 1990, Woods & Kienle 1994) nous ont permis d'étayer notre hypothèse d'un panache secondaire pour expliquer ces dépôts, mais d'autres études plus poussées restent à faire pour totalement éclaircir les mécanismes de formation de ce dépôt. Des analyses de cendres par microscopie électronique à balayage en électrons rétrodiffusés, par exemple, pourraient permettre d'identifier des fragments lithiques provenant de la coulée de densité pyroclastique originelle et donc de renforcer l'hypothèse d'un panache secondaire.

Aperçu des processus magmatiques mis en oeuvre

La teneur en gaz dans le magma et le flux de masse maximum durant une éruption sont les paramètres clés de la stabilité d'une colonne volcanique (Wilson *et al.*, 1978; Woods, 1988; Sparks *et al.*, 1997). Les teneurs en gaz permettent ainsi très souvent de comprendre l'évolution de la dynamique d'une éruption plinienne, car de cette teneur en gaz dépend notamment la vitesse d'éjection des produits volcaniques à l'évent. Pour un flux de masse donné, la colonne volcanique sera d'autant plus stable que la teneur en gaz, et donc la vitesse, seront élevées. Pour une teneur en gaz donnée, une augmentation du flux de masse favorisera l'effondrement de colonne et la production de coulées de densité pyroclastiques. Aucune estimation de teneur de gaz dissous dans le magma n'a été réalisée durant cette thèse, nous n'avons donc aucune indication sur les vieilles éruptions étudiées ici. Cependant, les estimations de vitesses à l'évent faites pour les éruptions anciennes (Bellefontaine, Carbet et Etoile) combinées aux estimations de teneur en gaz exsolvé faites sur les éruptions pliniennes récentes (P1, 1.6−2.1 wt%; P2, 1.7−2.1 wt% et P3, 2−2.9 wt%; Carazzo *et al.* 2012, 2019, 2020) nous indiquent que les éruptions Bellefontaine et Carbet pourraient avoir des teneurs élévées de gaz similaires à celle de P3, tandis que Etoile aurait plutôt une teneur en gaz proche de celles de P1 et P2. Toutes ces valeurs restant globalement proches les unes des autres, et considérant la régularité des éruptions pliniennes de la montagne Pelée (volumes similaires, fréquence régulière...), la chambre magmatique alimentant les éruptions de la montagne Pelée semble avoir des caractéristiques stables dans le temps.

Cette hypothèse a déjà été formulée par des résultats expérimentaux d'équilibre de phase dans les produits récents du volcan issus des éruptions péléennes de 1902 et 1929, et

de l'éruption plinienne P1 (Pichavant *et al.*, 2002). En effet, les températures et pressions pré-éruptives de magma déterminées dans ces produits se sont révélées constantes pour les trois éruptions (875−900°C et 2 ± 0.5 kbar). Cette température est très probablement restée stable (ou n'a pas augmenté au-delà de 875°C) dans la chambre magmatique car il n'y a aucune preuve minéralogique de réchauffement dans les andésites émises (Martel *et al.*, 1998; Pichavant *et al.*, 2002). La pression pré-éruptive déterminée correspondant à une profondeur d'environ 6−9 km, les auteurs suggèrent que la chambre magmatique est dans un état quasi stationnaire depuis 13 500 ans (début de la dernière phase d'activité de la montagne Pelée). Dans leur étude, Annen *et al.* (2008) ont utilisé un modèle analytique décrivant l'évolution thermique d'une chambre magmatique sphérique pour essayer de déterminer les conditions requises pour le maintien d'une chambre stable sous la montagne Pelée expliquant l'homogénéité remarquable des produits du volcan. La solution la plus envisageable d'après leur modèle et d'après les caractéristiques d'un arc de subduction, est que la chambre magmatique de la montagne Pelée se construise par accumulation d'intrusions magmatiques sous forme de sills à un taux d'environ quelques centimètres par an. À ce taux, et considérant un refroidissement par conduction de la chambre magmatique, le magma se refroidit rapidement et seulement 10 à 20 % de son volume total atteint une température de 875°C et est capable de produire une éruption correspondant aux produits retrouvés sur le terrain.

De nombreuses pistes sont cependant encore à explorer afin de comprendre la dynamique du réservoir et les temps de résidence du magma dans ce réservoir avant éruption. La méthode d'analyse systématique des compositions des cristaux ("Crystal system analysis", Kahl *et al.* 2011, 2013, 2015) par exemple, alliée à l'utilisation de la diffusion intracristalline (Morgan *et al.*, 2004; Allan *et al.*, 2013; Solaro, 2017) pourra permettre d'aboutir à une telle vision dynamique du système d'alimentation. Les différentes zonations observées dans un cristal permettent en effet de définir des environnements magmatiques caractérisés par des conditions de cristallisation (P, T, fO_2, fluides) suffisamment stables pour être enregistrées dans le cristal. Les passages d'un environnement magmatique à un autre, indiqués par un changement de composition du cristal (une zonation), donnent ainsi des indices sur la survenue d'un événement perturbateur (tel qu'un réchauffement/refroidissement/mélange/décompression du magma) et permettent éventuellement de le dater par rapport au moment du déclenchement de l'éruption.

Cette méthode a récemment été appliquée sur des ponces issues des éruptions pliniennes P1, P2 et P3 de la montagne Pelée (Lyonnet *et al.*, 2017). La modélisation de l'interdiffusion du Fe-Mg dans des orthopyroxènes contenus dans ces ponces permet d'aboutir à des temps de diffusion (et donc de délai entre l'événement perturbateur et l'éruption) de moins de 6 mois, voire même de moins de 4 mois pour la plupart des échantillons (Figure 1). Trois environnements magmatiques ont été définis à partir de l'étude des zonations dans les orthopyroxènes considérés. Ainsi, les auteurs ont pu déterminer à partir des passages successifs d'un environnement à un autre que l'éruption P3 a probablement été déclenchée par une injection de magma plus basique venu d'un réservoir plus profond, qui aurait provoqué le réchauffement du magma dans le réservoir enregistré par les cristaux. L'éruption P2 aurait plutôt été déclenchée par la saturation progressive des éléments volatils au cours du refroidissement du magma. L'éruption P1, quant à elle, a été plus complexe à analyser. Elle aurait débuté par une montée lente de magma aboutissant à la formation d'un dôme de lave, ce dernier générant par la suite deux grosses explosions dirigées latéralement (Villemant & Boudon, 1998; Boudon *et al.*, 2015). Les différents temps de résidence pourraient correspondre (i) à la forte décompression associée à la deuxième explosion latérale aboutissant à une dépressurisation du conduit et du toit du réservoir et (ii) à l'ascension rapide du magma

résultant de cette perturbation. Même si les phénomènes déclencheurs de ces trois éruptions sont différents, la faible diversité des temps enregistrés par les cristaux montrent que la réponse éruptive aux perturbations du réservoir est reproductible. Elle pourrait donc être utilisée pour de futurs modèles destinés à une meilleure détermination de l'aléa volcanique, par exemple afin de voir si les perturbations dans le réservoir (comme une réinjection de magma) donnent lieu à des signaux géophysiques détectables (e.g. sismicité).
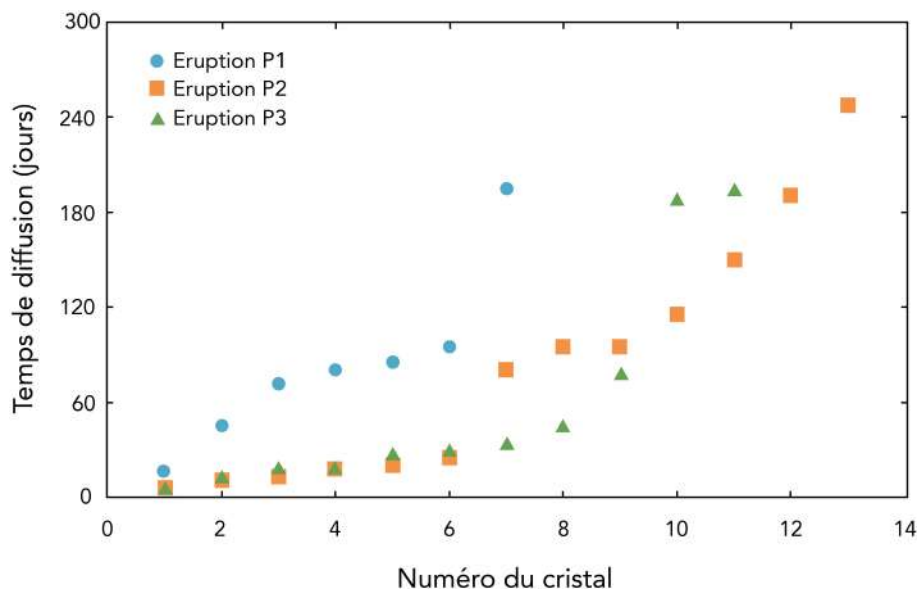

Figure 1: Temps de diffusion modélisés pour les éruptions pliniennes récentes P1 (cercles bleus), P2 (carrés oranges) et P3 (triangles verts) de la montagne Pelée. Les barres d'erreur sont comprises dans les figurés. *Modifiée d'après* Lyonnet et al. *(2017)*.

Les travaux menés dans le cadre de cette thèse montrent que les éruptions pliniennes de la montagne Pelée des 24 000 dernières années sont très similaires en volumes (ainsi qu'en teneurs de gaz), ce qui suggère que la chambre magmatique est dans un état quasi stationnaire depuis bien plus longtemps que ce que l'on pensait jusqu'à présent. Ces caractéristiques communes suggèrent donc un réservoir stable à la dynamique reproductible, ce que de futurs travaux sur les temps de diffusion pour les éruptions anciennes devraient permettre de confirmer.

Piégeage de gaz et libération par porosité ouverte

Nous avons expliqué en introduction de ce manuscrit le fonctionnement d'une éruption plinienne. Lors de la remontée du magma dans le conduit, des bulles de gaz se forment par exsolution. Au niveau de fragmentation, le gaz présent dans le magma se scinde entre une phase continue, séparant le magma et les clastes, et une phase gazeuse dispersée contenue dans des bulles à l'intérieur des clastes (Figure 2). L'efficacité de la fragmentation, et donc la taille des fragments (ponces et cendres) obtenus après celle-ci, joue ainsi un rôle critique dans la quantité de gaz disponible pour l'éruption. Les gros fragments (ponces) vont en effet conserver une grande partie du gaz piégé dans les bulles qu'ils contiennent, alors que les petits fragments (cendres) ne retiendront pas de gaz (Kaminski & Jaupart, 1998). Ainsi, une distribution de tailles de grains grossière (et donc un piégeage de gaz conséquent) pourra contribuer à l'effondrement d'une colonne volcanique, tandis qu'une distribution plus fine favorisera la formation d'une colonne volcanique stable. Parce que les roches volcaniques se fragmentent en suivant une loi puissance[1] (Kaminski & Jaupart, 1998; Kueppers *et al.*,

---

[1]le nombre de fragments de taille $R_P \geq r_p$ vaut λr_p^{-D} avec λ une constante de normalisation.

2006), nous utilisons l'exposant de loi puissance D pour décrire la distribution de tailles de grains. Si D est inférieur à 3, la population de tailles de grains est majoritairement grossière (démontrant une fragmentation peu efficace), tandis que si D est supérieur à 3, la population de tailles de grains est majoritairement fine (caractérisant une fragmentation efficace). Cet exposant D peut être calculé précisément en analysant la granulométrie des dépôts volcaniques échantillonnés sur le terrain (Kaminski & Jaupart, 1998).
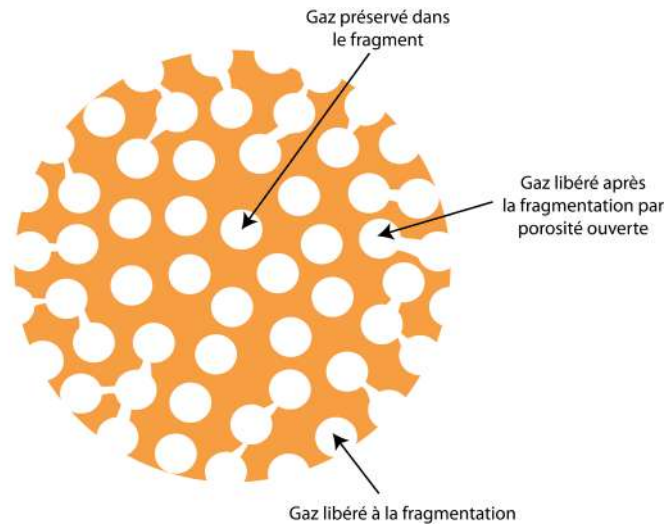

Figure 2: Schéma d'une ponce illustrant le devenir du gaz piégé dans les bulles du magma originel (voir texte).

Dans le chapitre 3 de ce manuscrit, nous avons revisité le rôle de ce piégeage de gaz sur la dynamique de colonne volcanique en considérant cette fois l'effet de la porosité ouverte. Les bulles de gaz présentes dans le magma peuvent en effet se connecter entre elles, et ainsi former un accès vers l'extérieur de la ponce qui libérera du gaz et le rendra disponible pour l'éruption (Figure 2). Nous avons ainsi amélioré le modèle 1D PPM créé dans notre équipe en prenant en compte le piégeage de gaz modulé par la porosité ouverte, mais aussi la sédimentation des particules au fur et à mesure de l'ascension du panache et la réduction de l'entraînement d'air atmosphérique à la base de la colonne. En effet, dans cette zone du panache nommée "gas-thrust region", la dynamique est contrôlée par la quantité de mouvement injectée à la source et sa flottabilité négative (la colonne est ici plus dense que l'environnement), ce qui contribue à la fois à diminuer la vitesse d'ascension et l'efficacité de l'entraînement de l'air extérieur (Carazzo *et al.*, 2008). Nous avons montré dans notre étude que l'effet combiné du piégeage de gaz, de la sédimentation et de l'entraînement réduit à la base de la colonne est drastique sur la stabilité des colonnes volcaniques et peut même empêcher la formation de colonnes stables si la population de tailles de grains est grossière ($D < 2.8$). La modulation du piégeage de gaz par la porosité ouverte permet de diminuer cet effet, mais seulement à partir d'un ratio ξ (fraction de gaz libérée par porosité ouverte sur fraction de gaz initialement piégé dans les bulles) supérieur à 65%. Cette valeur correspond par ailleurs à la moyenne de porosité ouverte mesurée dans les échantillons naturels, ce qui témoigne de la cohérence du modèle (Michaud-Dubuy *et al.*, 2018).

Cette nouvelle version du modèle PPM a permis de déterminer les caractéristiques des fontaines volcaniques (c'est-à-dire des colonnes en effondrement) à leur hauteur maximale, ce qui contraint en retour les caractéristiques des coulées de densité pyroclastiques générées au sol par cet effondrement. Nous avons pu déterminer que pour une teneur de gaz et un flux de masse donnés, une fontaine volcanique sera d'autant plus haute que sa distribution totale

de tailles de grains est dominée par des particules fines (D grand). De la même manière, pour une teneur de gaz et un flux de masse donnés, une fontaine volcanique propulsera à sa hauteur maximale majoritairement des cendres fines (inférieures à $\approx 8\ \mu$m) si sa distribution totale de tailles de grains était fine à l'évent, et des bombes volcaniques (supérieures à ≈ 12 cm) si sa distribution totale de tailles de grains était grossière à l'évent.

Pour finir, nous avons également montré que ce modèle prenant en compte la porosité ouverte permet également d'expliquer les différents stades (stable, puis transitionnel, puis effondrement) de l'éruption du Taupo qui s'est déroulée autour de l'année 186 de notre ère en Nouvelle-Zélande, mais également les régimes successifs des éruptions pliniennes récentes de la montagne Pelée P1, P2, et P3 (Figure 3, issue de Carazzo *et al.* 2020). Par contre, notre modèle ne permet pas d'expliquer le déroulement de la célèbre éruption du Vésuve en 79 en Italie. Dans ce cas, nous montrons qu'il faudrait sûrement prendre en compte le déséquilibre thermique entre les ponces et la phase gazeuse de la colonne volcanique pour expliquer son effondrement. En effet, si la distribution totale de tailles de grains est strictement dominée par des particules grossières ($D < 3$) ou fines ($D > 3$), l'équilibre thermique est maintenu dans la colonne car soit les particules grossières auront sédimenté rapidement, soit les cendres sont assez fines pour maintenir de toute manière l'équilibre thermique avec le gaz au cours de son expansion. Dans le cas du Vésuve, la distribution totale de tailles de grains est parfaitement répartie entre particules grossières et fines ($D = 3$), l'équilibre thermique n'est donc pas atteint, ce qui favorise l'effondrement de colonne (Woods & Bursik, 1991).
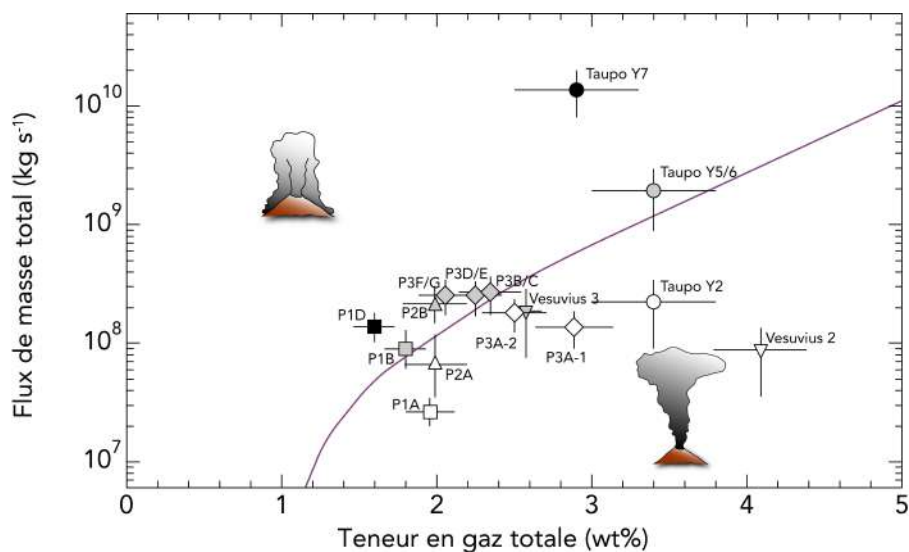

Figure 3: Diagramme de transition calculé par le modèle 1D PPM (Michaud-Dubuy *et al.*, 2018) montrant les différents stades (stable en blanc, transitionnel en gris et effondrement en noir) des éruptions P3 (losanges), P2 (triangles), P1 (carrés), Taupo (cercles), and Vesuvius (triangles inversés). La courbe violette correspond au flux de masse maximum avant effondrement en fonction de la quantité de gaz totale à l'évent. Nous considérons dans le calcul une atmosphère tropicale et un exposant $D = 3.3$ pour la distribution de tailles des fragments pyroclastiques. *Modifiée d'après* Carazzo *et al.* (2020).

Pour ces éruptions du Taupo et du Vésuve, nous avons montré que le vent soufflant durant l'éruption ne pouvait pas avoir d'incidence sur la dynamique de la colonne car le débit de l'éruption était bien supérieur à la vitesse du vent. Mais ce n'est pas le cas pour toutes les éruptions, l'étape suivante de notre étude théorique a donc été de prendre en compte l'effet du vent dans notre modèle.

L'effet du vent sur la stabilité des colonnes volcaniques

Nous avons montré au début du chapitre 4 que le modèle PPM prenant en compte les effets de la sédimentation, du piégeage de gaz modulé par la porosité ouverte, et de l'entraînement réduit à la base de la colonne ne peut pas expliquer le déroulement des éruptions historiques puissantes et bien connues du Tambora (Indonésie) en 1815, du Nevado del Ruiz (Colombie) en 1985 et du Pinatubo (Philippines) en 1991. Or, ces éruptions se sont toutes les trois produites sous un vent fort d'après les estimations tirées des études de terrain.

Le principal effet du vent sur la colonne volcanique est d'augmenter l'efficacité du mélange entre celle-ci et l'atmosphère, ce qui modifie les bilans dans les équations de conservation de la masse et de l'énergie dans la colonne. La vitesse d'entraînement dans un environnement sans vent ne dépend que d'un coefficient d'entraînement α et de la vitesse d'ascension de la colonne (Morton *et al.*, 1956). En cas de vent, cette vitesse d'entraînement va également dépendre d'un second coefficient d'entraînement lié au vent et nommé β (Hewett *et al.*, 1971). Ce coefficient est très mal contraint et sa valeur varie largement dans la littérature (entre 0.1 et 1). Afin de le quantifier, nous avons développé en laboratoire des expériences permettant de simuler des colonnes volcaniques. Pour cela, nous utilisons un montage se composant de deux réservoirs remplis d'un mélange d'éthanol et d'éthylène glycol (EEG) et de colorant, reliés à un injecteur représentant le volcan qui déverse ce mélange coloré dans une grande cuve remplie d'eau douce représentant l'atmosphère. Afin de simuler l'effet du vent, l'injecteur est déplacé le long d'un rail à une vitesse constante plus ou moins grande. Le mélange d'EEG a été choisi pour ses propriétés permettant de reproduire l'inversion de flottabilité de la colonne volcanique se produisant naturellement au cours du mélange avec le milieu ambiant. Le dimensionnement de ces expériences est réalisé de telle sorte que les nombres sans dimension caractérisant le système expérimental reproduisent convenablement l'équilibre des forces d'une véritable éruption volcanique.

Nous avons fait varier d'une expérience à l'autre les paramètres clés de la dynamique de ces jets expérimentaux : le rayon de la source, la densité du mélange EEG injecté et son débit d'injection, et la vitesse à laquelle se déplace le robinet le long du rail. À chaque expérience, nous avons observé si le jet obtenu était stable ou bien s'il s'effondrait. Ces résultats de jet à flottabilité réversible, comparés à des prédictions théoriques faites grâce à un modèle simplifié de jet turbulent, nous ont permis de déterminer que le coefficient d'entraînement dû au vent β devait être proche de 0.5 pour expliquer nos observations. Nous avons également mené une autre série d'expériences simulant des jets à flottabilité négative (en injectant de l'eau douce dans une cuve remplie d'eau salée plus dense). Les trajectoires des fontaines obtenues lors de ces expériences sont également reproduites numériquement si nous prenons en compte un coefficient $\beta = 0.5$ dans le modèle. Nous aboutissons à la même conclusion pour les trajectoires de panaches stables obtenus lors des expériences de Contini & Robins (2001). Nous démontrons donc qu'une valeur fixe de $\beta = 0.5$ peut être utilisée pour tout type de jet (à flottabilité réversible, négative, ou positive) à condition de considérer un coefficient α variable comme dans Kaminski *et al.* (2005).

Ces résultats novateurs issus d'expériences analogiques en laboratoire nous ont donc permis de prendre en compte l'effet du vent dans le modèle 1D PPM. En considérant un vent uniforme sur toute l'atmosphère, cette dernière version de PPM reproduit les différents régimes de stabilité ou d'effondrement partiel des éruptions historiques du Tambora, du Nevado del Ruiz et du Pinatubo. Jusqu'ici, nous avons représenté la transition entre les régimes stable et d'effondrement par un flux de masse maximal avant effondrement en fonction de la teneur en gaz à l'évent (comme en Figure 3). Mais les résultats du chapitre 4 nous ont amenés à proposer une nouvelle loi de transition basée sur des mesures plus facilement quantifiables après une éruption. En effet, nous avons calculé grâce à PPM la

vitesse de vent w nécessaire pour empêcher une colonne volcanique de s'effondrer et tracé une courbe de transition basée sur la relation entre le flux de masse de l'éruption (MDR) et le rapport $w/\log(\text{MDR})$. Ce rapport peut être facilement mesuré à partir de mesures de vitesse du vent et de hauteur maximale de colonne pour des éruptions contemporaines observées, ou à partir du rapport grand axe / petit axe des isoplèthes tracées à partir de la distribution des fragments lithiques sur le terrain pour des éruptions plus anciennes. En cas de vent, le rapport $w/\log(\text{MDR})$ maximal avant effondrement augmente avec le flux de masse. Ainsi, les isoplèthes construites à partir des données de terrain pourraient être un indice fort de la stabilité des colonnes volcaniques des éruptions passées: des isoplèthes fines et allongées signifiraient un rapport $w/\log(\text{MDR})$ élevé et donc probablement une colonne plutôt stable, alors que des isoplèthes plus circulaires correspondraient à un rapport $w/\log(\text{MDR})$ plus faible et donc une colonne plus instable.

Ainsi, le travail théorique détaillé dans la partie 2 du manuscrit a révélé que le piégeage de gaz, modulé par la porosité ouverte, ainsi que le vent ont tous les deux un impact fort sur la dynamique de l'effondrement ce qui permet d'expliquer le déroulement de plusieurs éruptions historiques telles que celles du Taupo ou du Tambora. Le déséquilibre thermique entre le gaz et les particules au sein du panache ainsi que d'autres effets, tels que la forme et la taille du cratère du volcan (Koyaguchi *et al.*, 2010), n'ont pas été étudiés ici et ont également une incidence sur la stabilité des colonnes. Des travaux futurs visant à intégrer ces effets au modèle PPM permettraient d'atteindre une version de plus en plus robuste capable d'expliquer des éruptions historiques particulières telle que celle du Vésuve en 79.

La montagne Pelée et la dispersion des cendres par le vent

Le vent, en plus d'influencer la dynamique de la colonne, a également un impact sur la dispersion des produits volcaniques dans l'atmosphère (Carey & Sigurdsson, 1986) et donc sur l'aléa volcanique associé (Michaud-Dubuy *et al.*, 2019). La partie 3 de ce manuscrit est consacrée à des simulations numériques de dispersion de cendres en utilisant le modèle 2D HAZMAP (Macedonio *et al.*, 2005) et des profils de vents moyennés sur 6h ou 1h tirés respectivement des bases de données ERA-Interim (Dee *et al.*, 2011) et ERA-5 (Hersbach *et al.*, 2019) afin (i) de comprendre la dispersion au sud inhabituelle des éruptions de la montagne Pelée (re)découvertes dans cette étude (celles de Bellefontaine, Balisier, Carbet et Etoile) et (ii) de ré-évaluer l'aléa volcanique "retombées de cendres" associé aux éruptions pliniennes pour la Martinique.

Les résultats du chapitre 5 montrent que la dispersion des cendres vers le sud des éruptions pliniennes de Bellefontaine, Carbet et Etoile est très probablement le résultat d'une circulation atmosphérique spécifique pouvant durer entre 6h et 3 jours et identifiée plusieurs fois au cours des 40 dernières années dans la base de données de vents ERA-Interim. Dans ces cas-là, le parcours du jet-stream (courant d'air rapide et étroit) sub-tropical est scindé en deux branches : au lieu d'être caractérisé seulement par des vents allant de l'ouest vers l'est, un deuxième courant provoque la formation de vents allant du nord vers le sud sur les îles des Petites Antilles. Ces vents du nord, quand ils se produisent en même temps qu'une éruption plinienne, peuvent alors disperser les cendres vers le sud de l'île. Nous avons calculé que la probabilité d'observer des vents venant du nord en Martinique (en se basant sur les données des 40 dernières années) varie selon les mois entre 0% en juillet et $\approx 5\%$ en novembre. Ces probabilités semblent faibles mais les éruptions étudiées dans cette thèse démontrent que cette situation est possible, et qu'elle pourrait menacer les zones les plus peuplées de Martinique principalement localisées dans le sud de l'île. Une telle dispersion de cendres vers le sud, bien que considérée inhabituelle, a été également observée lors de l'éruption de la Soufrière de Saint-Vincent en 1979 par exemple (Poulidis *et al.*, 2018).

Très récemment, le vent soufflant inhabituellement vers le nord a dévié le panache de gaz s'échappant de Soufrière Hills à Montserrat, l'envoyant vers l'observatoire volcanologique de Montserrat (Figure 4). Ces deux exemples sur d'autres îles de la Caraïbe illustrent bien nos conclusions du chapitre 5 : ne prendre en compte que des profils de vents moyennés sur une saison est insuffisant pour capturer précisément la haute variabilité journalière des vents dans cette région. D'ailleurs ces profils de vents moyennés sur une saison n'expliquent la dispersion que de peu d'éruptions pliniennes connues de la montagne Pelée (P1 et P2, Carazzo *et al.* 2012, 2019).
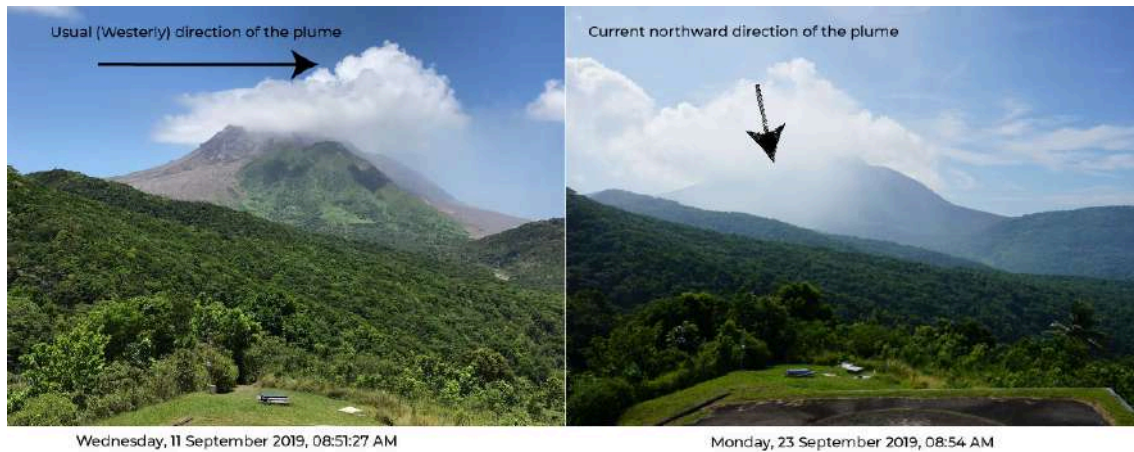

Figure 4: Photographies de Soufrière Hills à Montserrat montrant la trajectoire habituelle du panache de gaz lorsque les vents venant d'ouest dominent (à gauche) et la trajectoire déviée du panache le 23 septembre 2019 alors qu'un vent venant du sud souffle sur l'île (à droite). *Crédit: Montserrat Volcano Observatory.*

Nous avons également montré dans le chapitre 5 que la dispersion des cendres provenant du panache secondaire produit à partir de la coulée de densité pyroclastique de l'éruption Balisier pourrait également être le résultat de ces vents particuliers venant du nord. De plus, les simulations HAZMAP ont permis de confirmer que l'estimation de la hauteur du panache faite à partir des données de terrain dans la première partie de la thèse est compatible avec les cartes d'iso-épaisseur de dépôts tracées sur le terrain. Des simulations plus complètes, prenant en compte plusieurs profils de vents réels, pourraient permettre d'avoir une idée plus précise du vent soufflant durant cette éruption.

Enfin, nous avons également testé dans le chapitre 5 l'hypothèse d'un cyclone pour expliquer les dépôts de l'éruption de Bellefontaine. Nos simulations ont montré qu'un cyclone passant sur l'île de la Martinique (ou proche d'elle) ne peut pas expliquer les variations d'épaisseurs mesurées sur le terrain pour ces dépôts. Cependant, ces simulations nous ont démontré qu'un cyclone venant de l'Atlantique et passant à moins de 250 km au nord de la Martinique peut produire des vents allant au sud sur l'île. Cette conclusion est d'une importance capitale pour l'évaluation d'aléas croisés puisqu'un tel cyclone passant proche de l'île au moment d'une éruption plinienne pourrait provoquer une forte dispersion de cendres en direction du sud de la Martinique, possiblement jusqu'à Sainte-Lucie. Une telle étude n'a pas pu être menée durant la thèse mais nous avons tout de même débuté une réévaluation de l'aléa volcanique plinien lié aux retombées de cendres, en se basant toujours sur des simulations de dispersion avec HAZMAP.

L'aléa volcanique à la Martinique

La carte d'aléa volcanique intégrée actuellement utilisée dans le plan ORSEC est celle construite par Stieltjes & Mirgon (1998) et présentée en introduction. Dans le chapitre 6, nous nous sommes surtout intéressés à la carte que les mêmes auteurs ont créée pour l'aléa

"retombées de cendres" (chapitre 6, Figure 1). Cette carte n'étant basée que sur les éruptions pliniennes récentes de la montagne Pelée et ne prenant pas en compte l'effet du vent, il était intéressant de voir quels changements seraient visibles en considérant les scénarii éruptifs exposés dans le chapitre 2 (basés sur notre nouvelle histoire éruptive) et en considérant plusieurs profils de vents issus de la base de données ERA-Interim.

Nos résultats (en accord avec ceux du chapitre 5) montrent que les profils moyennés sur une saison cachent la variabilité des vents. Durant cette première étape, nous avons construit une carte d'aléa pour chacune des deux saisons caractéristiques aux Antilles (saison sèche et saison humide), que nous avons combinées ensuite en une carte d'aléa volcanique plinien. Dans ce cas, nous avons obtenu que presque toute la Martinique était concernée par un aléa "retombées de cendres", sauf l'extrême sud de l'île. Par la suite, nous avons considéré des profils de vents moyennés sur un mois et construit douze nouvelles cartes d'aléa que nous avons de nouveau combinées en une carte intégrée d'aléa volcanique plinien. Nous avons constaté que dans ce cas, contrairement à la première carte construite en utilisant les profils saisonniers, même le sud de la Martinique est concerné par l'aléa "retombées de cendres". Le "lissage" des vents saisonniers provoqué par la moyenne effectuée sur plusieurs mois a donc pour conséquence une sous-estimation de l'aléa volcanique, et ce principalement dans des zones considérées comme sécurisées dans le plan ORSEC actuel et où la conscience des dangers liés au volcan est souvent moindre par rapport aux régions du nord de l'île. Finalement, afin de rendre cette carte intégrée issue des simulations mois par mois plus facilement utilisable par les autorités compétentes en gestion de crise, nous l'avons interprétée grâce à des seuils de masses de cendres au-delà desquels des dégradations (de bâtiments par exemple) sont à prévoir, pour aboutir à une carte finale. Cette dernière montre, grâce à quatre niveaux d'intensité, le degré d'exposition à l'aléa "retombées de cendres" de chaque zone et donc les dommages associés auxquels on peut s'attendre dans ces zones.

Le chapitre 6 consiste essentiellement en un travail préparatoire vers une nouvelle carte d'aléa volcanique complète considérant plusieurs aléas (retombées de cendres, coulées de densité pyroclastiques, etc.). Avant cela, il faudra revoir notre méthodologie pour la carte d'aléa "retombées de cendres" en considérant des profils de vents journaliers et/ou en considérant d'autres scénarii éruptifs (ici nous en avons utilisé 16) afin de produire des cartes probabilistes plus aisées à interpréter. Par la suite, une réévaluation de l'histoire éruptive péléenne et phréatique est nécessaire à la Martinique, même si les faibles volumes de ces éruptions complexifient ce type d'études. Nous pourrions par exemple utiliser des dépôts mieux conservés d'éruptions phréatiques sur d'autres îles (telles que celles des Canaries) afin d'en savoir plus sur la dynamique de ces éruptions, de les modéliser et donc de simuler des éruptions phréatiques à la Martinique. Ces futurs développements de la carte d'aléa et de cartes de risques réactualisées seront effectués en accord et en concertation avec l'Observatoire Volcanologique et Sismologique de la Martinique, le BRGM et la Préfecture de la Martinique. Il serait d'ailleurs intéressant d'utiliser les résultats de cette thèse pour apporter dès aujourd'hui de nouveaux moyens de prédiction aux observatoires, en intégrant par exemple un outil de simulation de dispersion de cendres dans le WebObs des observatoires français. Ce dispositif, couplé à des données météorologiques, permettrait de simuler une éruption (en se basant sur une scénario précis) et d'obtenir une carte de dispersion en temps réel.

En conclusion, ce travail s'inscrit dans un effort collectif de mieux caractériser l'histoire éruptive des volcans actifs des îles des Petites Antilles (comme à la Guadeloupe: Boudon et al. 2008; Komorowski et al. 2008; Legendre 2012; ou à la Dominique: Boudon et al. 2017) et de mieux connaître la dynamique des éruptions puissantes des volcans de ces zones de subduction, dans le but de pouvoir évaluer le plus précisément possible l'aléa et le risque

volcanique dans ces milieux insulaires où les populations sont déjà vulnérables face aux aléas sismique et cyclonique.

Bibliographie

ALLAN, A.S.R., MORGAN, D.J., WILSON, C.J.N. & MILLET, M-A. 2013 From mush to eruption in centuries: Assembly of the super-sized oruanui magma body. *Contrib. Mineral. Petrol.* **166**, 143–164.

ANNEN, C., PICHAVANT, M., BACHMANN, O. & BURGISSER, A. 2008 Conditions for the growth of a long-lived shallow crustal magma chamber below Mount Pelée volcano (Martinique, Lesser Antilles Arc). *J. Geophys. Res.* **113** (B07209).

BONADONNA, C., MAYBERRY, G.C., CALDER, E.S., SPARKS, R.S.J., CHOUX, C., JACKSON, P., LEJEUNE, A.M., LOUGHLIN, S.C., NORTON, G.E., ROSE, W.I., RYAN, G. & YOUNG, S.R. 2002 Tephra fallout in the eruption of Soufriere Hills Volcano, Montserrat. In *The Eruption of Soufriere Hills Volcano, Montserrat from 1995 to 1999* (ed. T.H. Druitt & B.P. Kokelaar), pp. 483–516. Geological Society, London, Memoirs.

BOUDON, G., BALCONE-BOISSARD, H., SOLARO, C. & MARTEL, C. 2017 Revised chronostratigraphy of recurrent ignimbritic eruptions in Dominica (Lesser Antilles arc): Implications on the behavior of the magma plumbing system. *J. Volcanol. Geotherm. Res.* **343**, 135–154.

BOUDON, G., BALCONE-BOISSARD, H., VILLEMANT, B. & MORGAN, D. 2015 What factors control superficial lava dome explosivity? *Sci. Rep.* **5** (14551).

BOUDON, G., KOMOROWSKI, J.C., VILLEMANT, B. & SEMET, M.P. 2008 A new scenario for the last magmatic eruption of La Soufrière of Guadeloupe (Lesser Antilles) in 1530 A.D. Evidence from stratigraphy radiocarbon dating and magmatic evolution of erupted products. *J. Volcanol. Geotherm. Res.* **178**, 474–490.

BOUDON, G., LE FRIANT, A., VILLEMANT, B. & VIODE, J.P. 2005 Martinique. In *Volcanic Hazard Atlas of the Lesser Antilles* (ed. J.M. Lindsay, R.E.A. Robertson, J.B. Sheperd & S. Ali), pp. 127–146. Seismic Research Unit, The University of the West Indies, Trinidad and Tobago, W.I.

BOUDON, G., VILLEMANT, B., LE FRIANT, A., PATERNE, M. & CORTIJO, E. 2013 Role of large flank-collapse events on magma evolution of volcanoes: Insights from the Lesser Antilles Arc. *J. Volcanol. Geotherm. Res.* **263**, 224–237.

CARAZZO, G., KAMINSKI, E. & TAIT, S. 2008 On the dynamics of volcanic columns: A comparison of field data with a new model of negatively buoyant jets. *J. Volcanol. Geotherm. Res.* **178**, 94–103.

CARAZZO, G., TAIT, S. & KAMINSKI, E. 2019 Marginally stable recent Plinian eruptions of Mt. Pelée volcano (Lesser Antilles): The P2 AD 280 eruption. *Bull. Volcanol.* **81**, 1–17.

CARAZZO, G., TAIT, S., KAMINSKI, E. & GARDNER, J. E. 2012 The recent Plinian explosive activity of Mt. Pelée volcano (Lesser Antilles): The P1 AD 1300 eruption. *Bull. Volcanol.* **74**, 2187–2203.

CARAZZO, G., TAIT, S., MICHAUD-DUBUY, A., FRIES, A. & KAMINSKI, E. 2020 Transition from stable column to partial collapse during the 79 cal CE P3 Plinian eruption of Mt Pelée volcano (Lesser Antilles). *J. Volcanol. Geotherm. Res. In press.* https://doi.org/10.1016/j.jvolgeores.2019.106764.

CAREY, STEVEN & SIGURDSSON, HARALDUR 1986 The 1982 eruptions of El Chichon volcano, Mexico (2): Observations and numerical modelling of tephra-fall distribution. *Bull. Volcanol.* **48**, 127–141.

CONTINI, D. & ROBINS, A. 2001 Water tank measurements of buoyant plume rise and structure in neutral crossflows. *Atmospheric Environment* **35**, 6105–6115.

DEE, D. P., UPPALA, S. M., SIMMONS, A. J., BERRISFORD, P., POLI, P., KOBAYASHI, S., ANDRAE, U., BALMASEDA, M. A., BALSAMO, G., BAUER, P., BECHTOLD, P., BELJAARS, A. C.M., VAN DE BERG, L., BIDLOT, J., BORMANN, N., DELSOL, C., DRAGANI, R., FUENTES, M., GEER, A. J., HAIMBERGER, L., HEALY, S. B., HERSBACH, H., HÓLM, E. V., ISAKSEN, L., KÅLLBERG, P., KÖHLER, M., MATRICARDI, M., MCNALLY, A. P., MONGE-SANZ, B. M., MORCRETTE, J. J., PARK, B. K., PEUBEY, C., DE ROSNAY, P., TAVOLATO, C., THÉPAUT, J. N. & VITART, F. 2011 The ERA-Interim reanalysis: Configuration and performance of the data assimilation system. *Q. J. R. Meteorol. Soc.* **137**, 553–597.

ENGWELL, S. & EYCHENNE, J. 2016 Contribution of Fine Ash to the Atmosphere From Plumes Associated With Pyroclastic Density Currents. In *Volcanic Ash: Hazard Observation*. Elsevier.

HERSBACH, H., BELL, B., BERRISFORD, P., HORÁNYI, A., MUÑOZ SABATER, J., NICOLAS, J., RADU, R., SCHEPERS, D., SIMMONS, A., SOCI, C. & DEE, D. 2019 Global reanalysis: goodbye ERA-Interim, hello ERA5. *ECMWF Newslett.* **159**, 17–24.

HEWETT, T.A., FAY, J.A. & HOULT, D.P. 1971 Laboratory experiments of smokestack plumes in a stable atmosphere. *Atmos. Environ.* **5**, 459–461.

KAHL, M., CHAKRABORTY, S., COSTA, F. & POMPILIO, M. 2011 Dynamic plumbing system beneath volcanoes revealed by kinetic modeling, and the connection to monitoring data: An example from Mt. Etna. *Earth Planet. Sci. Lett.* **308**, 11–22.

KAHL, M., CHAKRABORTY, S., COSTA, F., POMPILIO, M., LIUZZO, M. & VICCARO, M. 2013 Compositionally zoned crystals and real-time degassing data reveal changes in magma transfer dynamics during the 2006 summit eruptive episodes of Mt. Etna. *Bull. Volc.* **692**, 1—14.

KAHL, M., CHAKRABORTY, S., POMPILIO, M. & COSTA, F. 2015 Constraints on the Nature and Evolution of the Magma Plumbing System of Mt. Etna Volcano (1991-2008) from a Combined Thermodynamic and Kinetic Modeling of the Compositional Record of Minerals. *J. Petrol.* **56** (10), 2025–2068.

KAMINSKI, E. & JAUPART, C. 1998 The size distribution of pyroclasts and the fragmentation sequence in explosive volcanic eruptions. *J. Geophys. Res.* **103**, 29759–29779.

KAMINSKI, E., TAIT, S. & CARAZZO, G. 2005 Turbulent entrainment in jets with arbitrary buoyancy. *J. Fluid Mech.* **526**, 361–376.

KOMOROWSKI, J. C., LEGENDRE, Y., CARON, B. & BOUDON, G. 2008 Reconstruction and analysis of sub-plinian tephra dispersal during the 1530 A.D. Soufriere (Guadeloupe) eruption: Implications for scenario definition and hazards assessment. *J. Volcanol. Geotherm. Res.* **178**, 491–515.

KOYAGUCHI, T., SUZUKI, Y. J. & KOZONO, T. 2010 Effects of the crater on eruption column dynamics. *J. Geophys. Res.* **115** (7), 1–26.

KUEPPERS, U., PERUGINI, D. & DINGWELL, D. B. 2006 "Explosive energy" during volcanic eruptions from fractal analysis of pyroclasts. *Earth Planet. Sci. Lett.* **248** (3-4), 800–807.

LEGENDRE, Y. 2012 Reconstruction fine de l'histoire éruptive et scenarii éruptifs à la Soufrière de Guadeloupe : vers un modèle intégré de fonctionnement du volcan. PhD thesis, Université de Paris 7.

LYONNET, E., BOUDON, G. & BALCONE-BOISSARD, H. 2017 Dynamique des réservoirs magmatiques à l'origine des dernières éruptions pliniennes de la Montagne Pelée, Martinique. Master's thesis, Institut de Physique du Globe de Paris.

MACEDONIO, G., COSTA, A. & LONGO, A. 2005 A computer model for volcanic ash fallout and assessment of subsequent hazard. *Comput. Geosci.* **31**, 837–845.

MARTEL, C., PICHAVANT, M., BOURDIER, J.L., TRAINEAU, H., HOLTZ, F. & SCAILLET, B. 1998 Magma storage conditions and control of eruption regime in silicic volcanoes: Experimental evidence from Mt. Pelée. *Earth Planet. Sci. Lett.* **156** (1-2), 89–99.

MICHAUD-DUBUY, A., CARAZZO, G., KAMINSKI, E. & GIRAULT, F. 2018 A revisit of the role of gas entrapment on the stability conditions of explosive volcanic columns. *J. Volcanol. Geotherm. Res.* **357**, 349–361.

MICHAUD-DUBUY, A., CARAZZO, G., TAIT, S., LE HIR, G., FLUTEAU, F. & KAMINSKI, E. 2019 Impact of wind direction variability on hazard assessment in Martinique (Lesser Antilles): The example of the 13.5 ka cal BP Bellefontaine Plinian eruption of Mount Pelée volcano. *J. Volcanol. Geotherm. Res.* **381**, 193–208.

MORGAN, D.J., BLAKE, S., ROGERS, N.W., DE VIVO, B., ROLANDI, G., MACDONALD, R. & HAWKESWORTH, C.J. 2004 Time scales of crystal residence and magma chamber volume from modelling of diffusion profiles in phenocrysts: Vesuvius 1944. *Earth Planet. Sci. Lett.* **222**, 933–946.

MORTON, B.R., TAYLOR, G.I. & TURNER, J.S. 1956 Turbulent gravitational convection from maintained and instantaneous sources. *Philos. Trans. R. Soc. A* **234**, 1–23.

PICHAVANT, M., MARTEL, C., BOURDIER, J. & SCAILLET, B. 2002 Physical conditions, structure, and dynamics of a zoned magma chamber: Mount Pelée (Martinique, Lesser Antilles arc). *J. Geophys. Res.* **107** (B52093).

POULIDIS, A.P., PHILLIPS, J.C., RENFREW, I.A., BARCLAY, J., HOGG, A., JENKINS, S.F., ROBERTSON, R. & PYLE, D.M. 2018 Meteorological controls on local and regional volcanic ash dispersal. *Scientif. Rep.* **8** (6873).

ROOBOL, M.J. & SMITH, A.L. 1976 Mount Pelée, Martinique: A pattern of alternating eruptive styles. *Geology* **4**, 521–524.

SOLARO, C. 2017 Storage conditions and dynamics of magma reservoirs feeding the major pumiceous eruptions of Dominica (Lesser Antilles arc). PhD thesis, Université Paris Diderot.

SPARKS, R. S. J., BURSIK, M., CAREY, S., GILBERT, J. S., GLAZE, L. S., SIGURDSSON, H. & WOODS, A. W. 1997 *Volcanic Plumes*. John Wiley, New York.

STIELTJES, L. & MIRGON, C. 1998 Approche méthodologique de la vulnérabilité aux phénomènes volcaniques : Test d'application sur les réseaux de la Martinique. In *Unpublished Internal Report No. R40098*. Bureau de Recherches Géologiques et Minières, Marseille.

TRAINEAU, H. 1982 Contribution à l'étude géologique de la Montagne Pelée (Martinique) : Evolution de l'activité éruptive au cours de la période récente. PhD thesis, Université Paris XI.

VILLEMANT, B. & BOUDON, G. 1998 Transition from dome-forming to plinian eruptive styles controlled by H$_2$0 and Cl degassing. *Letters to Nature* **392**, 65–69.

WESTERCAMP, D. & TRAINEAU, H. 1983 The past 5,000 years of volcanic activity at Mt. Pelée Martinique (F.W.I.): Implications for assessment of volcanic hazards. *J. Volcanol. Geotherm. Res.* **17**, 159–185.

WILSON, L., SPARKS, R. S. J., HUANG, T. C. & WATKINS, N. D. 1978 The Control of Volcanic Column Heights by Eruption Energetics and Dynamics. *J. Geophys. Res.* **83** (B4), 1829–1836.

WOODS, A.W. 1988 The fluid dynamics and thermodynamics of eruption columns. *Bull. Volcanol.* **50**, 169–193.

WOODS, A. W. & BURSIK, M. I. 1991 Particle fallout, thermal disequilibrium and volcanic plumes. *Bull. Volcanol.* **53**, 559–570.

WOODS, A. W. & KIENLE, J. 1994 The dynamics and thermodynamics of volcanic clouds: Theory and observations from the April 15 and April 21, 1990 eruptions of Redoubt volcano, Alaska. *J. Volcanol. Geotherm. Res.* **62** (1-4), 273–299.

MADE IN JURA FRANCE

Dynamique des éruptions pliniennes : réévaluation de l'aléa volcanique en Martinique

Résumé : Les panaches volcaniques produits par les éruptions explosives représentent un aléa majeur dans les zones à proximité de volcans. Les modèles physiques développés ces quarante dernières années ont eu pour but de mieux comprendre ces éruptions et de quantifier les aléas associés. Les tests de robustesse de ces modèles prédictifs doivent reposer sur des données de terrain précises et détaillées sur les éruptions passées des volcans actifs. Nous proposons dans cette thèse de revisiter l'histoire éruptive plinienne de la montagne Pelée en Martinique (Petites Antilles) sur les vingt-quatre derniers milliers d'années. Nos résultats combinant travaux de terrain et datations au ^{14}C nous permettent d'établir une nouvelle chronologie des éruptions passées en accord avec les observations réalisées sur un carottage des fonds sous-marins. Nous reconstruisons par la suite l'évolution dynamique des éruptions nouvellement découvertes de Bellefontaine (13 516 ans cal A.P.), Balisier (14 072 cal A.P.), Carbet (18 711 cal A.P.) et Étoile (21 450 cal A.P.) dont le grand intérêt réside dans leur axe de dispersion vers le sud, inhabituel et englobant des zones considérées comme sécurisées sur les cartes d'aléa actuelles. Les fortes similitudes observées entre toutes les éruptions pliniennes documentées de la montagne Pelée permettent de dresser un portrait du scénario éruptif le plus susceptible de se produire dans le futur. Ce scénario pouvant inclure un effondrement de la colonne éruptive et la production de coulées de densité pyroclastiques, nous modifions un modèle physique 1D de panache volcanique afin d'en améliorer les prédictions. Nous étudions dans un premier temps l'impact de la distribution de taille des fragments volcaniques sur la transition d'une colonne plinienne stable à une fontaine en effondrement. L'effet du vent est ensuite pris en compte grâce à des expériences en laboratoire inédites permettant de simuler des jets turbulents se formant dans un environnement soumis au vent. Nous proposons ainsi un nouveau modèle théorique validé par les expériences qui remet en cohérence les données de plusieurs éruptions pliniennes historiques majeures. Nous étudions ensuite la dispersion des cendres volcaniques lors des éruptions de Bellefontaine et Balisier à l'aide d'un modèle physique 2D pour comprendre l'origine de leur direction préférentielle vers le sud, et donc vers Fort-de-France, chef-lieu de la Martinique. Nos résultats permettent d'identifier des contextes atmosphériques particuliers durant lesquels le trajet du « jet-stream » subtropical est modifié, produisant alors des vents venant du nord sur la Martinique et pouvant disperser des cendres volcaniques sur les zones les plus peuplées. Cette approche intégrée, mêlant études de terrain, simulations numériques et expériences en laboratoire, nous permet alors de dresser une nouvelle carte d'aléa volcanique pour la Martinique considérant pour la première fois les éruptions pliniennes passées de la montagne Pelée depuis 24 000 ans, ainsi que la variabilité mensuelle des vents atmosphériques.

Mots clefs : montagne Pelée, éruption plinienne, dynamique éruptive, dispersion de cendres, aléa volcanique, tephrostratigraphie

Dynamics of Plinian eruptions: re-assessment of volcanic hazard in Martinique

Abstract: Volcanic plumes produced by explosive eruptions represent a major threat in areas located near volcanoes. Physical models have been developed over the past forty years with an aim of better understanding these eruptions and assessing associated hazards. To test these models, we need robust and detailed field data from past and historical eruptions at active volcanoes. In this PhD work, we revisit the Plinian eruptive history of the Mount Pelée volcano in Martinique (Lesser Antilles) for the last 24,000 years. Our results combining new extensive field studies and carbon-dating measurements allow us to establish a new chronology of past eruptions, consistent with volcanic deposits identified in a deep-sea sediment core. We then reconstruct the dynamical evolution of the newly discovered eruptions of Bellefontaine (13,516 years cal BP), Balisier (14,072 cal BP), Carbet (18,711 cal BP) and Étoile (21,450 cal BP), whose great interest stems from their unusual southward dispersal axis encompassing areas that are considered to be safe in current hazard maps. The strong similarities observed between all documented Plinian eruptions of Mount Pelée volcano allow us to draw an accurate picture of the Plinian eruptive scenario most likely to occur in the future. This scenario may include a column collapse and the production of deadly pyroclastic density currents; we thus upgrade a 1D physical model of volcanic plume in order to improve its predictions. We first study the impact of the total grain-size distribution on the transition from a stable Plinian plume to a collapsing fountain. The effect of wind is then taken into account using laboratory experiments simulating turbulent jets rising in a windy environment. This new theoretical model, validated by laboratory experiments, is consistent with field data from several major historical Plinian eruptions. We then study the southward dispersal axis of the Bellefontaine and Balisier eruptions using a 2D physical model, in order to better understand this unusual dispersion towards Fort-de-France, capital of Martinique. Our results allow identifying peculiar atmospheric circulations associated to a modification of the subtropical jet-stream path, thus producing northerly winds over Martinique and spreading tephra towards the most populated areas of the island. This integrated approach, combining field studies, theoretical predictions and laboratory experiments, allows us to build a new volcanic hazard map for Martinique by taking into account for the first time the Plinian eruptions of the Mount Pelée volcano of the last 24,000 years, together with monthly variability of atmospheric winds.

Keywords: Mount Pelée, Plinian eruption, eruptive dynamics, tephra dispersal, volcanic hazard, tephrostratigraphy